Title
Atomic Layer Deposition Enabled Integration of Multiferroic Composites

Author
Chang, Jeffrey

Publication Date
2018

Peer reviewed|Thesis/dissertation

UNIVERSITY OF CALIFORNIA

Los Angeles

Atomic Layer Deposition Enabled Integration of Multiferroic Composites

A dissertation submitted in partial satisfaction of the

requirements for the degree Doctor of Philosophy

in Chemical Engineering

by

Jeffrey Chang

2018

ABSTRACT OF THE DISSERTATION

Atomic Layer Deposition Enabled Integration of Multiferroic Composites

by

Jeffrey Chang

Doctor of Philosophy in Chemical Engineering

University of California, Los Angeles, 2018

Professor Jane Pei-Chen Chang, Chair

This work focuses on the design, synthesis, characterization and integration of multiferroic composite materials via radical-enhanced atomic layer deposition (RE-ALD). Specifically, ferrimagnetic $CoFe_2O_4$ is integrated with multiferroic $BiFeO_3$ and ferroelectric HfO_2 (FE-HfO_2), respectively, to create two distinct composite systems. The use of multiferroic $BiFeO_3$ as the ferroelectric phase offers the potential of employing two interfacial coupling phenomena simultaneously. On the other hand, desirable ferroelectric property and superior Si-compatibility that FE-HfO_2 can offer make it an intriguing material system for further implementation into device processing at an industrial scale.

In the $CoFe_2O_4$/$BiFeO_3$ system, high-quality $CoFe_2O_4$ and $BiFeO_3$ were synthesized on $SrTiO_3$ (001) substrates via RE-ALD using TMHD-based metalorganic precursors (TMHD = 2,2,6,6-tetramethylheptane-3,5 dione) and atomic oxygen. With post-deposition thermal treatments, $BiFeO_3$ exhibited epitaxial single-crystalline growth in its $(001)_{pc}$ orientation. Ferroelectric switching and measurable ferromagnetism confirmed the multiferroicity of $BiFeO_3$. $CoFe_2O_4$ exhibited textured-polycrystalline growth with a ~10-nm epitaxial transition layer, which led to tunable ferrimagnetism with a thickness-related strain relaxation process. The $CoFe_2O_4$ thin films exhibited magnetic behavior that is comparable with the ones synthesized by other processing techniques as well as bulk crystals. Nano-laminates of

$CoFe_2O_4/BiFeO_3$ in 2D-2D configuration were synthesized on $SrTiO_3$ (001) and Si (001) substrates. By fixing the nanolaminate total thickness at 55 nm and $CoFe_2O_4$-$BiFeO_3$ ratio at a constant of $CoFe_2O_4$:$BiFeO_3$ = 15:40 while increasing the number of alternating layers up to 5 layers, the tri-layer $BiFeO_3/CoFe_2O_4/BiFeO_3$ structure exhibits the most promising functional properties with an optimized polarization ~17 μC/cm^2 and saturation magnetism (M_s) ~125 emu/cm^3. Both strain and magnetic interactions were observed at the interface for the nano-laminates due to the multiferroic nature of $BiFeO_3$. The tri-layer structure exhibited a converse magnetoelectric coupling coefficient ($\alpha_{converse}$) of ~22 Oe cm/kV. By scaling the nano-laminate from ~55 nm to ~16 nm in total thickness, $\alpha_{converse}$ is further improved to ~64 Oe cm/kV, comparable with systems reported with much higher thicknesses. As the first demonstration of a fully ALD-synthesized multiferroic composite, this part of the work reveals the possibility to utilize ALD to optimize multiferroic nano-laminates for further integrations into magnetoelectric devices.

For $CoFe_2O_4$/FE-HfO_2 composites, HfO_2 thin films were synthesized with tetrakis(dimethylamido)hafnium(IV) (TDMAH) and atomic oxygen. In this design, $CoFe_2O_4$ served not only as the mechanical confinement layer but also as an active magnetic layer that contributed to overall magnetism. For ~6nm HfO_2 annealed at ~700 °C, the $CoFe_2O_4$/FE-HfO_2 composites exhibited a remnant polarization (P_r) ~5.5 μC/cm^2 and an electrical coercivity (E_c) ~2000 kV/cm as well as an out-of-plane magnetic anisotropy with a saturation magnetization (M_s) of ~155 emu/cm^3 and a magnetic coercivity (H_c) ranging from ~1000-3400 Oe. Magnetoelectric characterization revealed promising magnetoelectric coupling, with $\alpha_{converse}$ ranged 55-168 Oe cm/kV at room-temperature, once again is comparable with other systems reported with much higher thicknesses. It is believed that the $CoFe_2O_4$/FE-HfO_2 system here opens many new avenues for developing future magnetoelectric composites and related devices.

The dissertation of Jeffrey Chang is approved

Gregory P. Carman

Harold G. Monbouquette

Dante Simonetti

Jane Pei-Chen Chang, Committee Chair

University of California, Los Angeles

2018

TABLE OF CONTENTS

LIST OF FIGURES

LIST OF TABLES

ACKOWLEDGEMENT

My graduate school experience would not be possible without the guidance, support, and companionship from many people, and in thinking back on the last five years have realized how grateful I am.

My first and foremost acknowledgement goes to Prof. Chang, who had faith in me and gave me the opportunity to be a part of her lab at UCLA. Her continued mentorship and drive to achieve excellence over the past five years has not only transformed me into a capable scientific researcher, but also an individual that can communicate effectively and think critically, both of which would otherwise never happen. I also want to thank Prof. Monbouquette, Prof. Carman, and Prof. Simonetti for making themselves available to advise my thesis research as well as the full funding support from the FAME center.

I am very fortunate to work closely with Chang lab people that are not only intelligent and motivated but also fun to be with. I must start from my mentor, Dr. Calvin Pham, who was patient enough to guide me through both the ALD system and his scientific research when I was absolutely overwhelmed by all the wrenches and flanges. He helped me establish a solid foundation that deeply benefitted my graduate study. I also want to thank Dr. Jay Cho, who almost became my mentor, for his great knowledge on ALD chemistry and dark grad school jokes. Thanks to the great Dr. Jack Chen for his numerous plasma science 101 sessions when I was working on the plasma-surface interaction paper. Lastly, Dr. Colin Rementer and Dr. Cyrus Cheung, thank you for your love and leadership as the senior students at the time.

I would like to wish the best of luck for the current, or remaining, lab members as well. Ryan, thank you for all the insightful discussions about ALD and, of course, craft beers and sneakers. Ernest and Kevin, I admire all the knowledge you guys have regarding the field we are in, keep it up! I should also thank my mentee Adrian, your dedication and willingness to learn is truly impressive, and I am sure you will have a successful experience here. Most

importantly, Nick, thank you for being extremely helpful as the go-to person for the lab, I cannot describe how glad I feel to have you around and to finish together.

Thank you to all the collaborators and research center participants that have assisted the completion of this thesis. Prof. Kathryn Moler and Dr. Aaron Rosenberg, thank you for spending the time to measure my samples with your one and only scanning SQUID setup. Prof. Sarah Tolbert, Dr. Abraham Buditama, and Ty, thank you for allowing me to use your electrical poling station and SSRL beamline time. Thank you Prof. Charles Ahn, Dr. Lior Kornblum, and Eric for supplying STO/Si substrates for the Si-integration study. Special thanks to all the brilliant FAME theme 1 researchers, Shuchi, Christina, and James for spending the time to discuss and construct the massive materials matrices with me for our annual reviews.

I would also want to thank all my friends who have provided me support and entertainment when I needed it the most. Sammy, my one and only roommate, thank you for being an extremely nice roommate and a great friend simultaneously. To my "research" group, Yachin, John, Shanon, and Shane, thank you for all the intellectual discussions and literal round the clock support. Ping-Wei, thank you for being a good pal, it is beyond what words can describe. To Michelle, we have been friends for 15 years, thank you for everything. Rose, thank you for what we have experienced together and your companionship, please remember that I will always be there for you.

Finally, this dissertation is dedicated to my family. To my parents Rita and Edward, thank you for all the love and sacrifices; I would not be able to become who I am today without what you have provided. To my brother Shane, thank you for all the humorous jokes and support despite the fact that we are never in the same city after high school. I am truly fortunate to be a part of my family, and the past five years and the completion of this dissertation would not have been possible without the endless love.

VITA

2012	B.S., Chemical Engineering National Taiwan University Taipei, Taiwan
2013-2018	Ph.D. Candidate Graduate Student Researcher Department of Chemical and Biomolecular Engineering University of California, Los Angeles Los Angeles, CA

AWARDS

2017	James Harper Award Finalist Thin Film Division Graduate Student Award AVS 64th International Symposium & Exhibition Tampa, FL
2016	Best Poster Presenter Award 4th FAME Center Annual Review Los Angeles, CA
2012	Valedictorian Presidential Award Department of Chemical Engineering National Taiwan University Taipei, Taiwan

PUBLICATIONS AND PRESENTATIONS

Jeffrey Chang and J. P. Chang, "Achieving Atomistic Control in Materials Processing by Plasma-Surface Interactions", *J. of Phys. D Appl. Phys.* 50 (2017) 253001 (23pp) *(Invited Research Review)*

C. D. Pham*, Jeffrey Chang*, M. A. Zurbuchen, and J. P. Chang, "Magnetic Properties of $CoFe_2O_4$ Thin Films Synthesized by Radical Enhanced Atomic Layer Deposition", *ACS Appl. Mater. Interfaces*, 2017, 9 (42), pp 38980-36988 (*Equal-contribution authors)

C. D. Pham., Jeffrey Chang, M. A. Zurbuchen, and J. P. Chang, "Synthesis and Characterization of $BiFeO_3$ Thin Films for Multiferroic Applications by Radical Enhanced Atomic Layer Deposition", *Chem. Mater.*, 2015, 27 (21), 7282-7288

Jeffrey Chang, C.-P. Lee, D. Kumar, P.-W. Chen, L.-Y. Lin, K. Thomas, and K.-C. Ho, "Co-Sensitization Promoted Light Harvesting for Organic DSSCs Using Unsymmetrical Squaraine Dye and Novel Pyrenoimidazole-Based Dye", *J. Power Sources* 240 (2013) 779-785

Jeffrey Chang*, A. Rosenberg, A. Buditama, E. Jin, L. Kornblum, C. Ahn, S. H. Tolbert, K. A. Moler, and J. P. Chang, "Atomic Layer Deposition Enabled Synthesis of Multiferroic

Composite Nanostructures", American Vacuum Society 64th International Symposium and Exhibition, Tampa, FL, USA, Oct. 30- Nov. 3 (2017) (Oral)

Jeffrey Chang* and J. P. Chang, "The Super-Power of Controlling Magnetism", American Vacuum Society 64th International Symposium and Exhibition, Tampa, FL, USA, Oct. 30-Nov. 3 (2017) (Oral) (Competition Talk for AVS Thin Film Division James Harper Award)

Jeffrey Chang*, and J. P. Chang, "ALD Enabled Synthesis of Nanostructured Multiferroics", 5th Function Accelerated nanoMateiral Engineering (FAME) Center Annual Review, Los Angeles, CA, USA, Feb. 14-15 (2017) (Poster)

Jeffrey Chang*, A. Buditama, A. Rosenberg, L. Kornblum, C. Ahn, K. A. Moler, S. H. Tolbert, and J. P. Chang, "Radical-Enhanced Atomic Layer Deposition Enabled Multiferroic Composite Synthesis", American Vacuum Society 63rd International Symposium and Exhibition, Nashville, TN, USA, Nov. 6-11 (2016) (Oral)

Cyrus Cheung*, Jeffrey Chang, and J. P. Chang, "Magnetic Anisotropy of CoFe2O4 Nanotubes Synthesized by Radical-Enhanced ALD", American Vacuum Society 63rd International Symposium and Exhibition, Nashville, TN, USA, Nov. 6-11 (2016) (Oral)

J. K.-C. Chen, Jeffrey Chang, C. D. Pham, T. Kim, and J. P. Chang*, "Enabling the Synthesis and Integration of Multiferroic Materials by Atomic Layer Processing", DPS 2016 – 38th International Symposium on Dry Process, Sapporo, Hokkaido, Japan, Nov. 21-22 (2016) (Oral)

Jeffrey Chang*, A. Rosenberg, L. Kornblum, C. Ahn, K. Moler, and J. P. Chang, "ALD Enabled Synthesis of Nanostructured Multiferroics", 12th International Nanotechnology Conference on Communication and Cooperation, Leuven, Belgium, May 10-12 (2016) (Poster)

Jeffrey Chang*, and J. P. Chang, "ALD Enabled Synthesis of Nanostructured Multiferroics", 4th Function Accelerated nanoMateiral Engineering (FAME) Center Annual Review, Los Angeles, CA, USA, Feb. 16-17 (2016) (Poster)

C. D. Pham, Jeffrey Chang*, and J. P. Chang, "Radical-Enhanced Atomic Layer Deposition Enabled Multiferroic Composite Synthesis", American Vacuum Society 62nd International Symposium and Exhibition, San Jose, CA, USA, Oct. 18-23 (2015) (Oral)

C. D. Pham*, Jeffrey Chang*, and J. P. Chang, "ALD Enabled Synthesis of Nanostructured Multiferroics", 3rd Function Accelerated nanoMateiral Engineering (FAME) Center Annual Review, Los Angeles, CA, USA, Feb. 10-11 (2015) (Poster)

Chapter 1. Introduction

In the past decades, the constant miniaturization of electronic devices has allowed the continuous improvement in its performance, feature density, and power efficiency. However, physical phenomena that emerge when such scaling enters the sub-10-nm region have posed great challenges in both the design and processing of future devices, and thus the development of functional materials and processing techniques are critical for further advancing current technologies. Here, backgrounds in next-generation magnetoelectric computer memories and the enabling multifunctional magnetoelectric multiferroic materials are introduced. Engineered multiferroic composites that are enabled by interfacial coupling effects are discussed to provide a thorough understanding of the materials aspect of this work. In addition, the quantification of converse magnetoelectric coupling coefficients $\alpha_{converse}$ is summarized, providing a framework for benchmarking the results obtained in this work. Lastly, atomic layer deposition technique is reviewed in detail to highlight its capabilities and potential for synthesizing multiferroic composites with complex geometries.

1.1. Motivation and Background

The development of computer semiconductor devices has always been driven by the famous Moore's law, proposed by Gordon Moore in 1965, which stated that the number of individual transistors on a fixed chip area will double every 12 months (Moore 1965). In terms of computer memories, they are organized into two main categories according to their corresponding tasks: working storage and permanent storage, which each have unique advantages. For instance, while working storage, like static random-access memory (SRAM) and dynamic random-access memory (DRAM), is faster in read/write speed, it consumes more energy and is more expensive. Mass storage like Flash and Solid-State Drives (SSD) are the

opposite (Flink 2014, Amiri 2015). It is the complementary behavior between the two distinct types of memories that comprises current computing devices. However, this is far from ideal as the power consumption and processing yield have become major problems as the Moore's law continues into the sub-10-nm range. For instance, in DRAM, fundamental physical limitations at nanoscale, such as source-to-drain leakage, increasing high power consumption, and limited material selection, have impeded the advancement of memory technology. As a result, new types of memory devices that work under different operational principles have been pursued to extend the success of Moore's law and serve as a single "universal memory" that could drastically reduce the complexity of computer devices and provide low-power switching, non-volatility, and fast read/write speed (Wang 2012, Amiri 2015).

Magnetoelectric random-access memory (MeRAM), which is similar to magnetic-random access memory (MRAM) but the switching of the magnetism is directly controlled using an electric field, is one of the most promising solutions for mitigating the aforementioned challenges (Bibes 2008). Prototypical MeRAM devices have recently been demonstrated and reveal great promise in practice (Heron 2014). A comparison between MeRAM and other memory technologies is shown in Table 1.1. It is shown that MeRAM exhibits a very fast switching and non-volatility with very high power efficiencies, which is >1000 times compared to DRAM and MRAM technologies (ITRS 2011, Wang 2012). Given all the advantages mentioned above, the biggest challenge in realizing the MeRAM design lies in the component that allows voltage-controlled magnetism – multiferroic materials. The voltage-controlled magnetism is also called the magnetoelectric coupling effect, where the coupling coefficient α provides a quantitative insight on how strongly the electric and magnetic degrees of freedom are coupled.

Table 1.1 Summary of memory technologies and their performance parameters (Kryder 2009, ITRS 2011)

Device	DRAM	MRAM	MeRAM
Switching mechanism	Charge accumulation	Current-controlled magnetism	Voltage-controlled magnetism
Density	8 Gb/chip	32 Mb/chip	N/A
Write energy	2 pJ	120 pJ	~1 fJ
Read/write time	10/10 ns	10/10 ns	~1/1 ns
Endurance	10^{16}	10^{16}	~MRAM
Non-volatility	No	Yes	Yes
Retention	64 ms	10 yr	~10 yr

1.2. Multiferroic Materials

Magnetic and electronic materials both play important roles in semiconductor technologies, especially in data storage devices such as RAM and Hard Disc Drives. The trend in device miniaturization and performance improvement have always been driven by the incorporation of functionally improved materials, which leads to an increased interest in utilizing electronic and magnetic behaviors simultaneously (Kim 2015). Multiferroic materials, discovered in 1982 by the Soviet scientists (Smolenskiĭ 1982), exhibit more than one ferroic ordering, including (anti)ferromagnetism, (anti)ferroelectricity, and ferroelasticity (Figure 1.1). These represent a new avenue for satisfying many of these emerging technological needs. Specifically, multiferroics that exhibit ferroelectricity and magnetism simultaneously (magnetoelectric multiferroics), have garnered significant interest. The magnetoelectric coupling effect in these materials is of particular value in the design of novel magnetoelectric data storage devices (Eerenstein 2006).

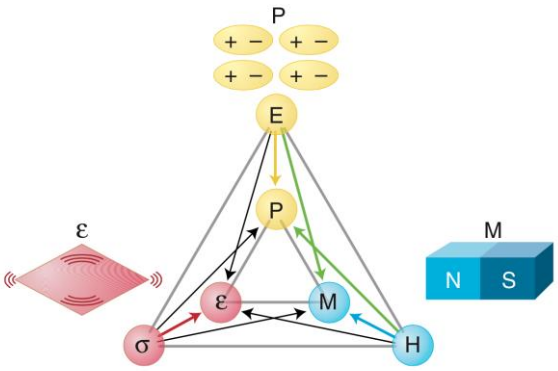

Figure 1.1 The relationship between electric field (*E*), magnetic field (*H*), stress (force field) (σ), and corresponding polarization (*P*), magnetization (*M*), strain (ε), respectively. Observing ferroelectricity or ferromagnetism accompanied by ferroelasticity is common, while the coexistence of ferroelectricity and ferromagnetism, represneted by the green arrows, is extremely rare. (Spaldin 2005)

In multiferroic materials, magnetoelectric coupling manifests itself in the induction of a magnetization upon application of an electric field as well as the generation of an electric polarization upon application of a magnetic field. The magnetoelectric interaction energy, F_{ME}, can then be expressed as (Lawes 2011):

$$F_{ME}(E,H) = \alpha_{ij}E_iH_j + \frac{1}{2}\beta_{ijk}E_iH_jH_k + \frac{1}{2}\gamma_{ijk}E_iE_jH_k + \frac{1}{6}\delta_{ijkl}E_iE_jH_kH_l + \cdots \quad (1.1)$$

E and *H* are the electric and magnetic fields respectively, while α_{ij}, β_{ijk}, γ_{ijkl}, and δ_{ijkl} are the magnetoelectric coupling coefficients of different orders. When studying magnetoelectric coupling in materials, above equation is often expressed in terms of electrical polarization, *P*, and magnetization, ***M,*** as the following (Fiebig 2005):

$$F_{ME}(E,H) = F_0 - P_{s,i}E_i - M_{s,i}H_i - \frac{1}{2}\varepsilon_0\varepsilon_{ij}E_iE_j - \frac{1}{2}\mu_0\mu_{ij}H_iH_j - \alpha_{ij}E_iH_j + \frac{1}{2}\beta_{ijk}E_iH_jH_k + \frac{1}{2}\gamma_{ijk}E_iE_jH_k + \cdots \quad (1.2)$$

where P_s, M_s, ε, and μ are spontaneous electric polarization, spontaneous magnetization, electric permittivity, and magnetic permeability, respectively. Polarization is obtained by taking the derivative of the equation with respect of the electric field:

$$P_i(E, H) = -\frac{\partial F_{ME}}{\partial E_i} = P_{s,i} + \varepsilon_0 \varepsilon_{ij} E_j + \alpha_{ij} H_j + \frac{1}{2}\beta_{ijk} H_j H_k + \gamma_{ijk} E_j H_k - \cdots \quad (1.3)$$

Likewise, magnetization is obtained by taking the derivative with respect to magnetic field:

$$M_i(E, H) = -\frac{\partial F_{ME}}{\partial H_i} = M_{s,i} + \mu_0 \mu_{ij} H_j + \alpha_{ij} E_j + \beta_{ijk} E_i H_j + \frac{1}{2}\gamma_{ijk} E_i E_j - \cdots \quad (1.4)$$

Although there are magnetoelectric couplings of different orders, the linear relationship defined by α_{ij} is sufficient enough to quantify the magnetoelectric coupling present in multiferroic materials in most cases. Thus, the majority of research on the magnetoelectric effect is devoted to this linear coupling, and the term "linear" is often omitted when describing the magnetoelectric effect. In general, the "direct" magnetoelectric effect is the induction of polarization with an external magnetic field, while the "converse" magnetoelectric effect is the induction of magnetization with an external electric field. It was reported that the two magnetoelectric effects are not equivalent because of the difference in resonating conditions between the ferroelectric and magnetic phases (Wu 2013). With the aim of achieving a voltage-controlled magnetism for MeRAM applications, only the "converse" magnetoelectric effect is of interest and discussed in this work.

The magnetoelectric effect can be observed by a variety of experimental setups. For example, it can be measured by either a superconducting quantum interference device (SQUID) magnetometer (Laukhin 2006) or a vibrating sample magnetometer (VSM) (Lou 2009) in conjunction with an *in situ* electrical biasing field. The effect can also be observed by using different modes of scanning probe microscopy (SPM) in the presence of external electric or magnetic fields (Caruntu 2012, Aimon 2015), or via x-ray photoemission electron microscopy

(X-ray PEEM) with X-ray linear dichroism (XLD) (Zhao 2006, Chu 2008). Ferromagnetic resonance provides a pathway to observe the magnetoelectric effects, especially in seeing the change in electron energy states between magnetic phases (Liu 2009, Lou 2009). Detailed discussion on the experimental setup for magnetoelectric coupling characterizations are provided in Section 1.3.

1.2.1. Single-phase multiferroics

Single-phase room-temperature magnetoelectric multiferroics are extremely scarce in nature due to the contradiction in physical origins for ferroelectricity and magnetism (Ramesh 2007). Ferroelectric polarization requires either an empty or full *d* orbital for the transition metal cation, while magnetic moments can only originate from partially filled asymmetric *d* orbitals (Hill 2000, Lawes 2011). As a result, the cation that contributes to polarization and magnetism must be different to allow multiferroic behavior in a single phase (Ramesh 2007). Single-phase multiferroicity is often achieved through an alternative mechanism for ferroelectricity, and it can be categorized into two types: type-1 and type-2 magnetoelectric multiferroics.

Ferroelectricity and magnetism originate from different atoms or different "subsystems" within type-1 multiferroics (van den Brink 2008). There are several possible microscopic origins that account for the occurrence of ferroelectricity in type-1 multiferroics (Khomskii 2006): As a result, they have distinct and relatively high ferroelectric and magnetic transition temperatures. However, the main challenge in type-1 multiferroics is to improve the magnetoelectric coupling without significantly compromising either of the individual properties. In type-2 multiferroics, ferroelectric behaviors only emerge from the magnetically ordered states. The transition temperature for ferroelectricity and magnetism in type-2 multiferroics are the same and often relatively low. For instance, spiral magnetic ordering and

charge ordering can give rise to single-phase multiferroicity (Mostovoy 2006, van den Brink 2008). The majority of type-2 multiferroics are rare-earth manganites (Mostovoy 2006). Low polarization values (mostly less than 10^{-1} $\mu C/cm^2$) and low transition temperatures limit the value of type-2 multiferroics for room-temperature applications.

1.2.2. Engineered multiferroic composites

Given the scarcity of single-phase multiferroic materials in nature and their weak magnetoelectric coupling (Fiebig 2005), composite approaches that utilize interfacial physical phenomena to combine and couple the ferroelectric and magnetic materials were made to achieve a robust magnetoelectric coupling effect. Compared to intrinsic multiferroics, composite multiferroics offers a widened material selection for an attainable magnetoelectric coupling as well as tailored functionality (schematic shown in Figure 1.2). Three strategies, namely charge-mediated coupling, exchange-bias coupling, and strain-mediated coupling, are employed to couple the ferroelectric and magnetic ordering of the constituent phases. To optimize the magnetoelectric coupling coefficient (α), a large interface within the composite nanostructure is needed. Multiple design geometries, including 0D-1D embedded nanopillars, 0D-3D filled mesoporous structures, and 2D-2D nano-laminates, where the number represents the connectivity in dimensionality of the phases, were utilized (Figure 1.3) to maximize the amount of interface and thus, magnetoelectric coupling (Nan 2005, Vaz 2010, Kim 2015).

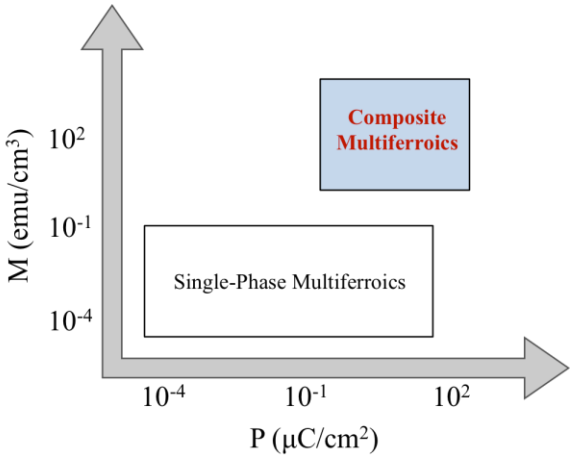

Figure 1.2 Schematic representation of the approximate magnitudes of the magnetization and polarization in composite multiferroics and single-phase multiferroics. (Figure adapted from (Lawes 2011))

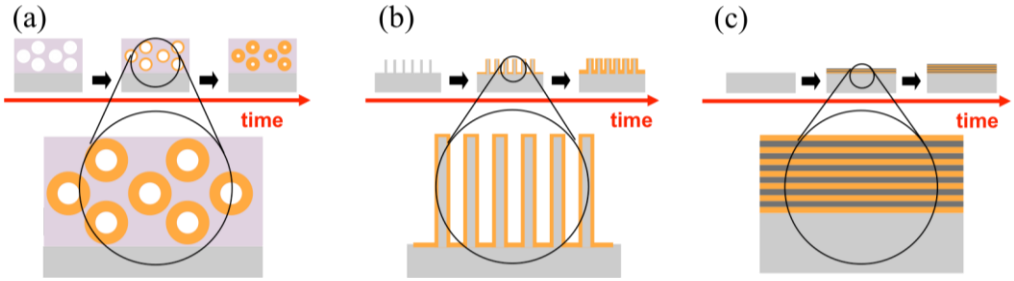

Figure 1.3 Schematic of (a) a 0D-3D filled mesoporous structure (b) a 1D-3D vertically embedded nanopillar structure, and (c) a 2D-2D nanolaminate composite structure.

In charge-mediated coupling systems, a combination of dielectric and ferromagnetic material is used. The charge accumulation upon *E*-field application breaks the space inversion symmetry at the dielectric/ferromagnetic interface and induces orbital reconstruction of the magnetic phase near the interface. This allows magnetoelectric behavior. This specific coupling mechanism has been demonstrated theoretically with density function theory (DFT) and has been experimentally identified (Weisheit 2007, Rondinelli 2008). Due to its interfacial nature, an ultra-thin magnetic phase, that is only a coupling unit cells thick, is required. $PbZr_{0.2}Ti_{0.8}O_3$ (250nm)/$La_{0.8}Sr_{0.2}MnO_3$ (4 nm) (PZT/LSMO) composite is an example of a charge-mediated multiferroic composite in which the annihilation of magnetism is induced when the PZT is electrically biased (Molegraaf 2009). Although intriguing, the fact that it is

only applicable to ultra-thin material systems (<5 nm) limits its potential to achieve a magnetoelectric coupling with a strong enough magnetic readout.

Exchange-bias coupling between antiferromagnetic/ferroelectric and ferromagnetic materials has been studied extensively as well. Due to the quantum mechanical exchange interaction and the canting effect between adjacent magnetic moments, the magnetic dipoles near the antiferromagnetic/ferromagnetic interface tends to be coupled even when they belong to different material phases (see Figure 1.4). Most of the time, the result of exchange-bias coupling is a shift, or bias, of the *M-H* hysteresis loop along the field axis. The offset is referred as the exchange bias field H_E. In some cases, depending on the material combination, film crystallinity, and the interfacial quality, a change in magnetic anisotropy would be observed instead of H_E (Gao 2017).

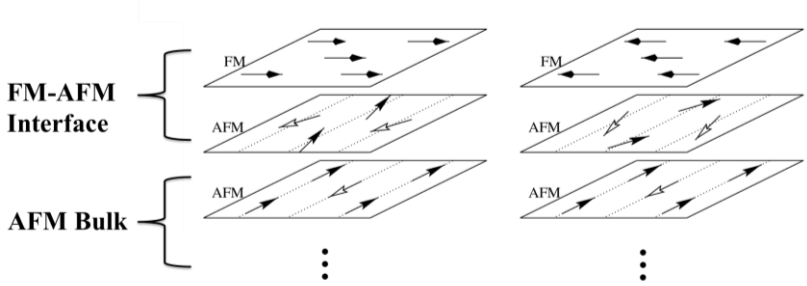

Figure 1.4 Schematic of different spin states in an exchange-bias coupled system at the ferromagnetic (FM)/antiferomagnetic (AFM) interface. Note that only the spins at the interface can be coupled; spins in the bulk remain the same due to coupling relaxation with increased distance from interface. Figure adopted from (Schulthess 1998)

In terms of the experimental demonstration of exchange-bias coupled multiferroic composites, combinations of a ferroelectric/antiferromagnetic multiferroic and a ferromagnetic metal were studied extensively (Morales 2015). Specifically, $BiFeO_3$ is used as the multiferroic of choice while magnetic metals such as CoFe (Heron 2014, Heron 2014) and Co (Gao 2017) were used as the ferromagnets. Since the switching of $BiFeO_3$ polarization is accompanied by its antiferromagnetic switching, exchange-bias coupling enables a direct control of the state

(direction) of the magnetic layer. Recent progress shows a direct coupling between multiferroic $BiFeO_3$ and ferromagnetic CoFe layers via exchange-bias coupling, and the bias can be further controlled by an external electric field (Trassin 2013, Heron 2014, Zhou 2015). More recently, $Co/BiFeO_3$ shows a reversible and controllable magnetic easy axis switching under exchange-bias coupling (Gao 2017). However, exchange bias coupling can only dominate under a relatively short range (up to ~10-20 nm) (Hu 2015), which is still far from ideal for device integrations. Furthermore, the fact that only BiFeO3 can be used as the ferroelectric phase for exchange-bias coupled multiferroic composites greatly limits the development of this coupling scheme.

Lastly, strain-mediated coupling utilizes the piezoelectric and magnetostrictive effect in ferroelectric and magnetic phases, respectively. An applied electric field can generate lattice strain in the ferroelectric phase, which can propagate through the ferromagnetic phase and thus change the magnetization state of the ferromagnetic material. The absolute magnetization and magnetic anisotropy could be changed since the overall magnetic energy landscape of the magnetic phase is changed (Martin 2010). Therefore, the magnetoelectric effect in strain-mediated multiferroic systems is generally weaker compared to the other two coupling schemes. However, in some cases, such strain interactions could lead to either a total removal of magnetization (Clarkson 2017) or a 180° switching in magnetic anisotropy (Li 2015) depending on the materials selection and composite geometry. Strain-mediated magnetoelectric coupling can be roughly described using the following relationship (Nan 1994):

$$ME\ Effect = \frac{Electrical}{Mechanical} \cdot \frac{Mechanical}{Magnetic} \tag{1.5}$$

Given the nature of strain propagation, the length scale of strain-mediated coupling can be up to mms, which is several magnitudes higher than the other two coupling schemes. A comparison between the three coupling schemes are shown in Figure 1.5. In addition, strain-mediated coupling

also offers the greatest degree of freedom in material selection, which eases the design of multiferroic composites. To develop undiscovered multiferroic material systems, strain-mediated coupling is the main coupling mechanism of choice in this work as it has the fewest limitations in the selection of materials.

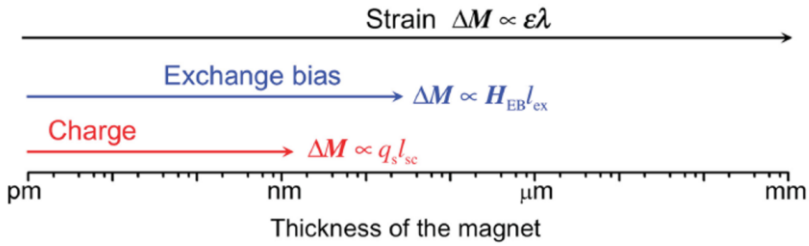

Figure 1.5 Schematic of the active thickness range of the magnetic layer correspoding to the coupling schemes in a multiferroic composite. (Hu 2015)

The possibility of employing multiple coupling schemes simultaneously was not recognized until recently, particularly for $BiFeO_3$-based multiferroic composites, due to the fact that $BiFeO_3$ itself is multiferroic. It is shown that the piezostrain and magnetic exchange interaction could yield a synergic effect by providing additional intermediate states to the $BiFeO_3$/CoFe composites when comparable (Heron 2014, Wang 2014). The first part of this work focuses on $BiFeO_3$-based multiferroic composites with the hope to better understand the effects of having both interfacial interactions within the composite.

By employing the abovementioned strain-mediated strategy, attempts to observe the magnetoelectric coupling were relatively successful with a wide spectrum of materials selections. Ferroelectric materials, such as $Pb(Zr_x, Ti_{1-x})O_3$ (PZT) (Zhai 2004), $Pb(Mg_{0.33}Nb_{0.67})O_3$-$PbTiO_3$ (PMN-PT) (Liu 2009), $BaTiO_3$ (Murugavel 2005), and $BiFeO_3$ (Zheng 2006, Zheng 2008, Aimon 2015), and magnetic materials, such as FeGaB (Liu 2009, Lou 2009), $NiFe_2O_4$ (Zhai 2004), Ni (Li 2015), FeRh (Clarkson 2017), and $CoFe_2O_4$ (Zheng 2004, Zheng 2006, Zheng 2008) were used due to their suitable piezoelectric and magnetostrictive properties. The individual properties of these constituent phases are listed in

Table 1.2. In terms of magnetoelectric coupling coefficients in composite systems, "direct" magnetoelectric coupling is more commonly reported due to the relatively simple characterization setup and the early interest in magnetoelectric sensors (Hu 2015).

Table 1.2 Ferroelectric materials that are used for strain-mediated multiferroic composites (P_r: remnant polarization, d_{33}: piezoelectric coeffficient)

Material	P_r (μC/cm^2)	d_{33} (pm/V)	Ref.
PZT	20	65	(Nguyen 2010)
PMN-PT	40	250	(Cao 2004)
$BaTiO_3$	10	105	(Park 2010)
$BiFeO_3$	60	85	(Wang 2003)

Table 1.3 Magnetic materials that are used for strain-mediated multiferroic composites (M_s: saturation magnetizaiton, λ_s: magnetostriction coefficient)

Material	M_s (emu/cm^3)	λ_s (ppm)	Ref.
$NiFe_2O_4$	200	-20	(Zeng 2004)
$CoFe_2O_4$	400	-110	(Thang 2007)
FeGaB	1000	80	(Liu 2013)
FeRh	200-400	-	(Clarkson 2017)

Attempts to observe direct magnetoelectric coupling in composites started from the nano-laminates with a 2D-2D geometry (Nan 2008, Wang 2010). However, although some of these experiments utilizing a strain-mediated strategy resulted in promising magnetoelectric coefficients, subsequent attempts in downscaling the 2D-2D geometry to a nanoscale was challenging (Kim 2015). Current theories suggest that the mechanical clamping from the substrate dominates the composite and limits magnetoelectric coupling by suppressing the induction of piezostrain when dimensions are down to the nanoscale (Bichurin 2003). Therefore, structures with 1D-3D and 0D-3D geometries were pursued to circumvent such issues. A summary of composite multiferroic systems with observable direct magnetoelectric coupling coefficients (α_{direct}) is provided in Table 1.4. α_{direct} is defined as the change in polarization P with a magnetic field H:

$$\alpha_{direct} = \frac{\Delta P}{\Delta H} \tag{1.6}$$

Table 1.4 Multiferroic composites reported with direct magnetoelectric coupling coefficients.

Material	Geometry	Thickness (nm)	α_{direct} (10^{-3} kV/Oe cm)	Ref.
PZT/$CoFe_2O_4$		Bulk	30	(Zhai 2003)
PZT/Terfenol-D	2D-2D	80	150	(Cibert 2013)
PZT/LSMO		270	300	(Tang 2013)
PLT/$CoFe_2O_4$		350	250	(Roy 2012)
PZT/$CoFe_2O_4$	0D-3D	1 mm	226	(Peng 2015)
$BaTiO_3$/Co		500	160	(Park 2008)
PZT/$CoFe_2O_4$		40	390	(Wan 2007)
BFO/$CoFe_2O_4$	1D-3D	150-2400	18	(Yan 2009)
BFO/$CoFe_2O_4$		300	60	(Oh 2010)

* Terfenol-D = $Tb_{0.3}Dy_{0.7}Fe_2$; LSMO = $La_{0.67}Sr_{0.33}MnO_3$; PLT = $Pb_{0.85}La_{0.15}TiO_3$

On the other hand, due to the renewed interest in obtaining voltage-controlled magnetism for MeRAMs and many other energy-efficient applications, characterization of converse magnetoelectric coupling coefficients ($\alpha_{converse}$) are also widely reported. $\alpha_{converse}$ is defined as the change in magnetization M with the application of an electric field E:

$$\alpha_{converse} = \frac{\Delta M}{\Delta E} \tag{1.7}$$

It is noteworthy that the two magnetoelectric coupling coefficients are neither reciprocal nor equivalent (Wu 2013). There are multiple methods for quantifying $\alpha_{converse}$, including the use of magnetic coercivity H_c instead of M. Detailed discussion on the quantification techniques and calculations are written in Section 1.3. Similarly, the effort started from 2D-2D geometries and quickly migrated to other nanostructures. 2D-2D strain-coupled $BaTiO_3$/$La_{0.3}Sr_{0.7}MnO_3$ composite is one of the earliest works on quantifying $\alpha_{converse}$ with a value ~230 Oe cm/kV (Eerenstein 2007). The high value is due to the use of a bulk crystal $BaTiO_3$ substrate, which mitigates the effects from substrate clamping fully. Efforts on exchange-bias and charge-mediated 2D-2D composites were also successful, yielding quantifiable coupling coefficients

up to ~100 Oe cm/kV (Molegraaf 2009, Heron 2014). Studies of self-assembled 1-3 embedded-nanopillar structures began with $CoFe_2O_4/BaTiO_3$ deposited via pulsed laser deposition (Zheng 2004), and migrated to other materials systems including $CoFe_2O_4/BiFeO_3$ (Aimon 2014, Aimon 2015, Ojha 2016). Due to the higher surface-area-to-volume ratio and the reduction/elimination of substrate clamping along *c*-axis, nanopillar structures exhibit an converse magnetoelectric coefficient up to ~125 Oe cm/kV (Zavaliche 2005, Aimon 2015). On the other hand, 0D-3D mesoporous structures are investigated as well; however, integrating such geometry into actual applications is extremely challenging due to processing limitations. PZT/CFO 0D-3D filling mesoporous were realized with a critical dimension of ~6-10 nm by incorporating atomic layer deposition and sol-gel synthesis together, exhibiting a $\alpha_{converse}$ of ~100 Oe cm/kV (Chien 2016). The strategies of utilizing complex geometries mentioned in this section are often only suitable for strain-mediated multiferroic composites due to the nature of strain interactions.

Multiferroic composites with converse magnetoelectric effects observed are summarized in Table 1.5, illustrating opportunities for device integrations based on multiferroic composite heterostructures. It is worth noting that the thicknesses for the reported multiferroic composites are usually <100 nm, where a nanoscale integration could effectively enhance the coupling as the interfaces dominate the systems more effectively. This work aims to achieve nanoscale integration for multiferroic composite heterostructures with a $\alpha_{converse}$ of ~50-100 Oe cm/kV, comparable with the values listed in Table 1.5.

Table 1.5 Multiferroic composites reported with converse magnetoelectric coupling effect

Material	Scheme	Structure	Thickness (nm)	$\alpha_{converse}$ (Oe cm/kV)	T (K)	Ref.
$BiFeO_3$/CoFe	Exchange	2D-2D	~100	100	RT*	(Heron 2014)
PZT/LSMO	Charge		~250	0.8	100	(Molegraaf 2009)
PMN-PT/Fe_2O_3	Strain		Bulk	67	RT	(Liu 2009)
PMN-PT/LCMO	Charge		~100	34	10	(Thiele 2007)
$BiFeO_3$/Co	Exchange		~100	H_c change	RT	(Gao 2017)
BTO/LSMO	Strain		Bulk	230	200	(Eerenstein 2007)
BFO/CFO	Strain	1D-3D	50-100	~45	RT	(Aimon 2015)
BFO/CFO	Strain		~200	~125	RT	(Zavaliche 2005)
PZT/CFO	Strain	0D-3D	1 mm	~12	RT	(Peng 2015)
PZT/CFO	Strain		100	~100	RT	(Chien 2016)

*RT = room temperature

1.2.2.1. Cobalt Ferrite, $CoFe_2O_4$

In this work, $CoFe_2O_4$ is the magnetic phase of choice for the integration of multiferroic composites due to its superior magnetic behavior among magnetic oxides. Among the family of ferrite films, $CoFe_2O_4$ has drawn significant interest due to its high magnetic anisotropy (K_1 ~10×10^6 erg/cm^3) and magnetostrictive behavior (λ_s up to -250 ppm) (Bozorth 1955, Fritsch 2012). Therefore it is a strong candidate for applications such as magnetic memory devices, antennas, and multiferroic composites. The negative magnetostriction value indicates that the magnetic easy axis will be induced in the direction parallel to the direction of compressive strain (Spaldin 2003). $CoFe_2O_4$ is also one of the strongest magnetic oxides (M_s up to ~500 emu/cm^3, H_c ~0.3-5 kOe (Ojha 2016)). The high magnetic ordering temperature (magnetic T_c ~870K), as well as its insulating behavior, adds on to the robustness and durability of $CoFe_2O_4$-based devices. $CoFe_2O_4$ possesses a body centered cubic (BCC) AB_2O_4 spinel structure with a lattice parameter a = 8.39 Å. As shown in Figure 1.6, the spin directions of magnetic iron and cobalt cations in ferrimagnetic $CoFe_2O_4$ are aligned in an antiparallel fashion, but the magnitude difference in the magnetic moments results in an overall uncompensated net magnetic moment.

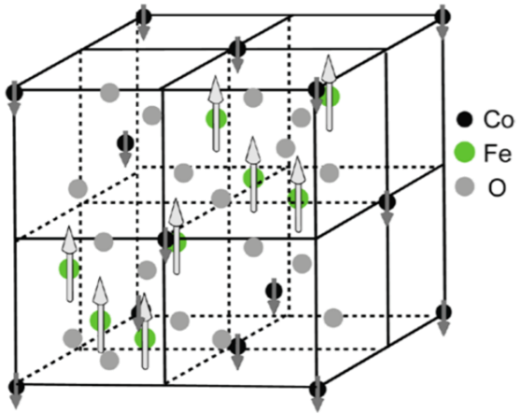

Figure 1.6 Ferrimagneitc spin structure of $CoFe_2O_4$. (Zaliznyak 2007)

Since the magnetic behavior of $CoFe_2O_4$ can be influenced greatly by chemical stoichiometry, research on $CoFe_2O_4$ is usually conducted via pulsed laser deposition (PLD) as it provides precise compositional control during deposition (Horng 2004, Thang 2007, Gao 2009, Gatel 2013). The influence of lattice strain on the overall magnetic behavior of $CoFe_2O_4$ is also receiving significant attention. It is showed that the magnetic anisotropy of $CoFe_2O_4$ could be controlled by strain induced by the lattice mismatch between the substrate and $CoFe_2O_4$ (Thang 2007). This was accomplished by comparing results of the epitaxial $CoFe_2O_4$ films on MgO and $SrTiO_3$ substrates. The magnetocrystalline anisotropy can influence its saturation magnetization (Gatel 2013). Therefore, considering the influence of lattice strain is vital to a proper analysis of the magnetic properties of $CoFe_2O_4$.

1.2.2.2. Bismuth Ferrite, $BiFeO_3$

Perovskite $BiFeO_3$ is the only room temperature single-phase magnetoelectric multiferroic that exhibits ferroelectricity (T_c ~1103K) and antiferromagnetism (T_N ~643K) simultaneously (Wang 2003, Zhao 2006, Akbashev 2014). Single crystal $BiFeO_3$ in the bulk is rhombohedral (a = 3.965 Å and α = 89.45°) with *R3c* space group and G-type antiferromagnetism (Kubel 1990). Its potential in multiferroic device integration has attracted great attention in the field of multiferroics. Ferroelectricity in $BiFeO_3$ originated from the *6s*

orbital lone pair electrons of A-site Bi^{3+} cations (Cheong 2007, Thomas 2010). On the other hand, the spin canting between the adjacent antiferromagnetic dipole moments induced by Dzyaloshinskii–Moriya interactions (see Figure 1.7) results in a weak net ferromagnetism (Ederer 2005).

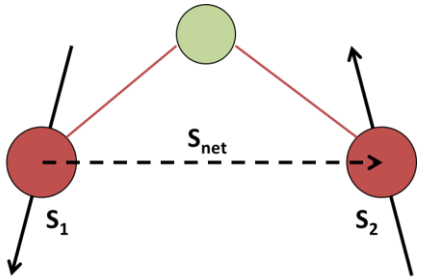

Figure 1.7 Schematic of the Dzyaloshinskii–Moriya interaction. The red circles, S_1 and S_2 are cations with antisymmetric spin directions. Due to the Dzyaloshinski–Moriya interaction, the spins are slightly tilted from perfect alignment directions. Therefore a net uncompensated spin is generated (dashed line).

$BiFeO_3$ polarization depends on the position Bi^{3+} lone pair electrons in the unit cell. Therefore, the value of polarization depends on the crystallographic directions. For example, in the [111] direction, the polarization value could be 90-95 $\mu C/cm^2$, while this value is 55-60 $\mu C/cm^2$ along the [001] direction. When switching the polarization direction by an external electric field, the orientation can be switched between three angles: 180°, 109°, and 71°, relative to the original polarization direction (Zhao 2006). Different switching directions relative to the pseudocubic $BiFeO_3$ structure are shown in Figure 1.8. Ferroelastic strain is accompanied by ferroelectric polarization and distorts the crystal shape.

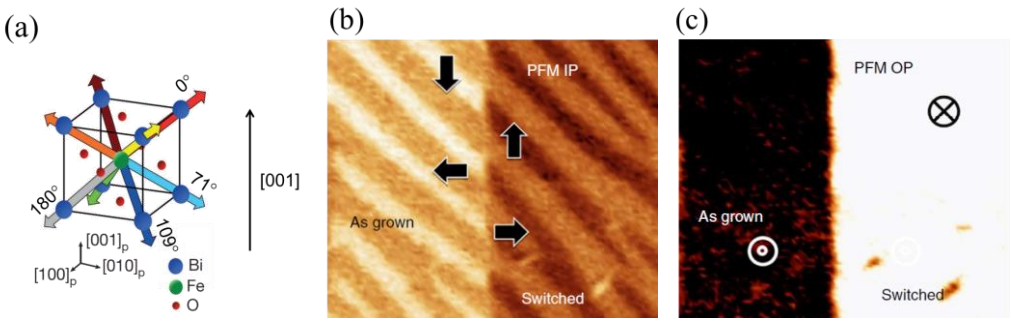

Figure 1.8 (a) schematic of ferroelectric polarization switching of (001) pseudocubic $BiFeO_3$ crystal. The different switching directions (108º, 109º, and 71º) are indicated. (b) In-plane and (c) out-of-plane piezoesponse force microscope (PFM) switching of $BiFeO_3$ ferroelectric domains. The arrows indicate polarizaiton directions. (Figures adapted from (Heron 2014, Zhou 2015)

G-type antiferromagnetism means that the magnetic moments of adjacent Fe^{3+} cations are aligned in an antiparallel fashion in all *a*, *b*, and *c* directions in a pseudocubic cell shown in Figure 1.8 (a). The overall configuration for the magnetic spins in $BiFeO_3$ is rather complicated, showing a cycloidal spiral with a 64-nm period (Cazayous 2008). The spiral propagation is along $[10\bar{1}]$, while the spin rotation is within the $(\bar{1}0\bar{2})$ plane. Figure 1.9 (a) and (b) show the pseudocubic $BiFeO_3$ crystal and the cycloidal spiral spin configuration. If the symmetry of the spin rotation is eliminated, both magnetization and ferroelectricity (Wang 2003) would enhance when compared to bulk $BiFeO_3$ crystals (Lebeugle 2008). A thin film strategy is a widely used approach to generate such asymmetry. Epitaxial strain generated from the substrate–film interface truncates the cycloid structure and in turn enhance the magnetic as well as the ferroelectric behaviors. It is known that different factors, such as the synthesis method, substrate orientation, and choice of substrate, could greatly influence the crystal structure of $BiFeO_3$ thin films and therefore its functionalities. It is also shown that epitaxial $BiFeO_3$ thin films synthesized via pulsed laser deposition (PLD) showed substantially increased remnant polarization and magnetism (P_r ~50-60 μC/cm^2, M_r ~150 emu/cm^3) compared to bulk $BiFeO_3$ (P_r ~6 μC/cm^2, M_r ~5 emu/cm^3) (Wang 2003).

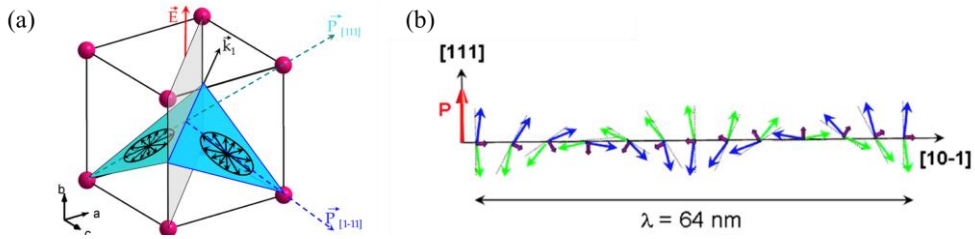

Figure 1.9 (a) Schematic of the planes of spin rotation, the cycloid $\vec{k}_1$ vector, and the polarization vectors relative to pseudocubic $BiFeO_3$ structure (only Bi cations are shown). (b) Schematic of the antiferromagnetic circular cycloid with a period of ~64 nm (Lebeugle 2008).

Antiferromagnetism in $BiFeO_3$ is coupled with its ferroelectricity, making $BiFeO_3$ a model material for studying single-phase magnetoelectric coupling effects (Ederer 2005). The magnetoelectric coupling has been illustrated theoretically (Ederer 2005, Kadomtseva 2006) and demonstrated experimentally through different characterization techniques (Chu 2006, Zhao 2006, Chu 2008). $BiFeO_3$ multiferroicity has been observed via ferromagnetic resonance (FMR), showing a non-volatile, repeatable, and robust voltage-induced 180° magnetization switching (Zhou 2015). However, quantification of a reliable magnetoelectric coefficient (α) value has been challenging since the $BiFeO_3$ magnetism is relatively weak. Therefore, a composite approach is required to further achieve a robust and pronounced ME coupling effect. In $BiFeO_3$-based multiferroic composites, both the strain and magnetic component were utilized as the coupling intermediate, depending on the material of choice (Heron 2014, Aimon 2015, Sone 2015, Gao 2017). $BiFeO_3$ serves as the ferroelectric phase in the first part of this work, where both the strain and magnetic component provide pathways for manipulating magnetic phase.

1.2.2.3. Ferroelectric HfO_2 Thin Films

Ferroelectricity has its own importance not only because it can be integrated into a multiferroic composite heterostructure as the ferroelectric component, but also because of its

wide range of electrical device applications such as high-k gate dielectrics, MEMS systems, and ferroelectric random-access memory (FeRAM) (Auciello 1998). However, one main obstacle in the development of ferroelectric materials is the fact that ferroelectricity can only emerge in a very limited group of perovskite oxides when they are crystalline (Benedek 2013). This not only limits the discovery of applicable ferroelectrics, but also places great difficulty in integrating ferroelectric materials into Si-based processing frameworks in current electronic industries (McDaniel 2015). Integration of ferroelectric perovskites can only be achieved with the help of a buffering layer of similar crystal orientation during film growth, usually $SrTiO_3$ grown via molecular beam epitaxy (MBE) (McDaniel 2013, Teherani 2017). Although some of the conventional ferroelectrics, such as $BaTiO_3$, can be epitaxially grown onto Si substrates directly, the interfacial quality is still inappropriate for device applications (Park 2015). Therefore, the complexity when processing those ferroelectric/multiferroic heterostructure composites has led to the need of a novel functional oxide material system that is easier to harness. Another main problem within those conventional perovskite ferroelectrics is the their small electrical band gap (E_g ~3-4eV) as it could lead to severe leakage problems when trying utilize their ferroelectric behaviors (Park 2015). As a result, the development of a new lead-free ferroelectric material that is not only compatible with Si substrates but also exhibits comparable ferroelectricity properties and high electrical band gaps has become one of the main tasks toward next-generation memory applications.

Ferroelectric HfO_2 (FE-HfO_2) thin films, with their well-studied atomic layer deposition (ALD) chemistry, outstanding Si-compatibility, large E_g values (~5-6 eV), and non-perovskite structure, show great promise in the development of future ferroelectric materials. HfO_2 is a dielectric material with dielectric constant ~17 when in the monoclinic structure (space group $P2_1/c$) at room temperature. When the temperature increases, the structure

transforms into tetragonal phase (space group $P4_2/nmc$) at 1973K and cubic phase (space group $Fm3m$) at 2773K under atmospheric pressure (Polakowski 2015). However, all the polymorphs mentioned above are not ferroelectric since all of them contain inversion symmetry. For the orthorhombic phases, only the metastable $Pca2_1$ and $Pmn2_1$ orthorhombic phases exhibit ferroelectric instability due to their non-centrosymmetric nature, verified by both first principle DFT calculations and experimental observations (Park 2015, Sang 2015, Künneth 2017). Figure 1.10 shows a schematic of different HfO_2 unit cell structures, with only $Pca2_1$ and $Pmn2_1$ orthorhombic phases being ferroelectric. Although the polar orthorhombic phases do not emerge in the bulk HfO_2 spontaneously, it is shown that several ways, including the use of dopants and the incorporation of structural confinement layers, are able to induce the its formation during post-deposition thermal annealing steps (Kim 2016, Karbasian 2017, Kozodaev 2017, Richter 2017). Table 1.6 shows a comparison between FE-HfO_2 and other conventional perovskite ferroelectrics.

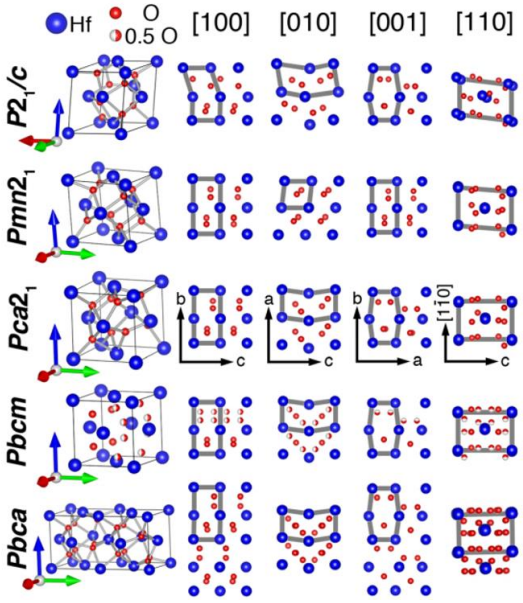

Figure 1.10 The crystal structure of five HfO_2 phases projected along four major zone axes. While $P2_1/c$ corresponds to the non-ferroelectric monoclinic phase, the other four phases are all orthorhombic phases. Only $Pca2_1$ and $Pmn2_1$ are ferroelectric due to their non-centrosymmetric nature. (Sang 2015)

Table 1.6 Comparison of perovskite and HfO_2-based ferroelectrics

Material	P_r (μC/cm^2)	E_g (eV)	Reference
PZT	25-100	3.4	(Moazzami 1992)
$BaTiO_3$	40	1.2	(Bang-Hung 2000)
$BiFeO_3$	6.1-90	2.8	(Wang 2003)
FE-HfO_2	10-30	5-6	(Park 2015)

Various dopants including Si (Martin 2014), Gd (Mueller 2012), Al (Mueller 2012), and La (Kozodaev 2017), were reported to induce ferroelectricity in HfO_2 thin films. In general, dopant concentrations ranging from 3% to 8% were demonstrated to be effective in generating ferroelectricity in HfO_2, however, the actual values are dopant-dependent. It is the differences in atomic radii between Hf and the dopants that distort the structure of HfO_2 cubic cells and thus give rise to the metastable orthorhombic phase. It is also worth noting that alloying HfO_2 and ZrO_2 into $Hf_{0.5}Zr_{0.5}O_2$ would lead to ferroelectricity in the film as well (Karbasian 2017). It is proven effective down to ~2.5 nm (Chernikova 2016). A summary of the dopants is listed in Table 1.7.

Table 1.7 Dopants for inducing ferroelectric in HfO_2

Dopant	Atomic radius (pm)	P_r (μC/cm^2)	Doping level (%)	Reference
Si	110	~24	~3-5	(Lomenzo 2016)
Al	120	~16	~4-7	(Mueller 2012)
Gd	180	~12	~2-3	(Mueller 2012)
Zr	230	~15-20	~20-80	(Karbasian 2017)
La	250	~10	~1-2	(Kozodaev 2017)

*atomic radius of Hf ~150 pm

Remnant polarization values of the doped-HfO_2 thin films can be up to ~30 μC/cm^2, which is comparable with the conventional lead-containing ferroelectric thin films, such as $Pb(Zr_{0.52}Ti_{0.48})O_3$. Besides Zr, another popular and well-studied dopant specie is Si since it is the fundamental material in the semiconductor industry. The polarization values of Si-doped HfO_2 can be up to ~25 μC/cm^2 at the doping level of ~4.4%(Lomenzo 2016). The influence of the concentration and atomic radii of different dopants to the remnant polarization of the doped HfO_2 thin films is summarized in Figure 1.11.

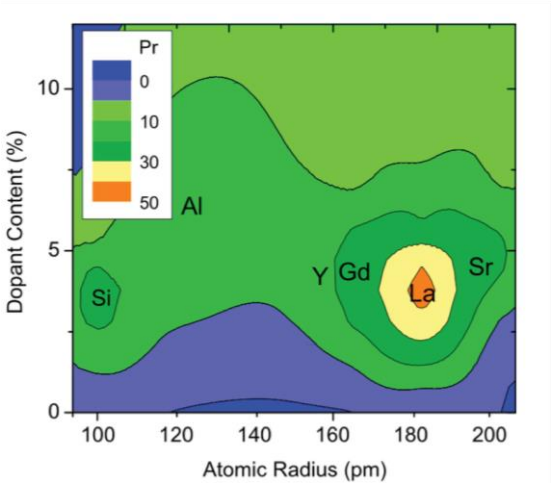

Figure 1.11 Contour plot of the remanent polarization as a function of crystal radius and dopant content in FE-HfO_2 thin films (Park 2015).

Mechanical confinement layers are often utilized in conjunction with dopant incorporations for orthorhombic phase stabilization. Conductive TiN electrode deposited via physical vapor deposition (PVD) is a widely used confinement layer for stabilizing ferroelectric orthorhombic phase of the sandwiched HfO_2 film (Lomenzo 2014, Karbasian 2017, Kim 2017). For the growth of confinement layers, low temperature film growth techniques such as sputtering and evaporation are more desirable because they can inhibit the structural relaxation of HfO_2 into its centrosymmetric phases during the growth process (Polakowski 2015). Figure 1.12 (a) and (b) show the *P-E* hysteresis loop obtained from $Hf_{0.5}Zr_{0.5}O_2$ thin films with and without top layers, highlighting the importance of confinement layer incorporation for film ferroelectricity (Kim 2017). To maximize the confinement/pinning effect and the resulting ferroelectricity, the thickness of the top pinning layer and the annealing conditions are the two major parameters to fine-tune and optimize. For the top layers, it is shown that the degree of pinning on the sandwiched $Hf_{0.5}Zr_{0.5}O_2$ layer is a function of top layer thickness. The confinement effect reached a maximum at thicknesses larger than ~90 nm, shown in Figure 1.12 (c).

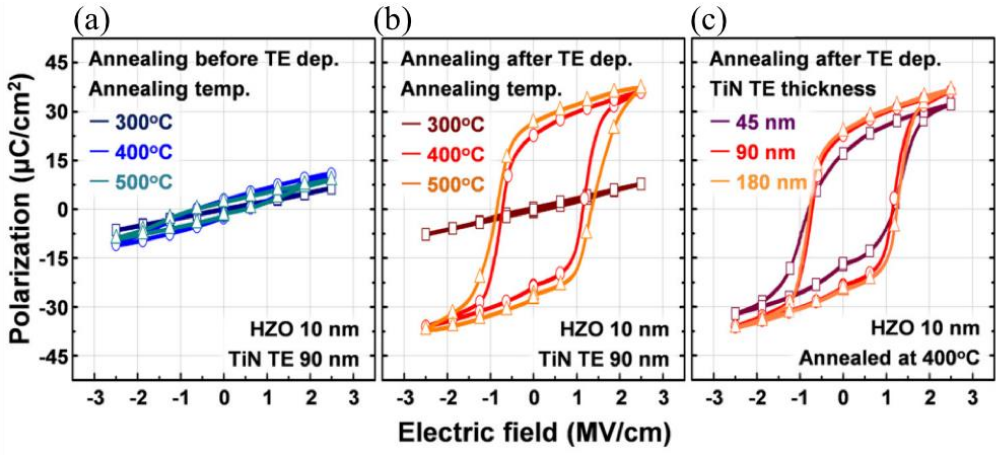

Figure 1.12 *P-E* hysteresis loops of a 10-nm thick $Hf_{0.5}Zr_{0.5}O_2$ (a) un-capped and (b) capped with TiN top electrodes. (c) shows the *P-E* hysteresis of the capped $Hf_{0.5}Zr_{0.5}O_2$ as a function of top TiN layer thicknesses (Kim 2017).

Structural analysis of the HfO_2-based ferroelectric thin films confirms the importance of orthorhombic phase stabilization to film ferroelectricity. A wide spectrum of temperatures and time durations for thermal annealing were reported for stabilizing the metastable ferroelectric orthorhombic phase, depending on the dopant concentration and film thickness (Mueller 2012, Park 2015, Sang 2015, Kozodaev 2017). Annealing temperature ranges from 400 to 1000 °C were reported, while the duration ranges from 1 to 60 seconds. In addition, since the strain state tends to relax along the *c*-axis of the film, film thickness is another important parameter to consider (Polakowski 2015). Since the XRD diffraction peaks of the centrosymmetric monoclinic and cubic phases are positioned closely to the ferroelectric orthorhombic phase, high-resolution grazing incidence X-ray diffraction (GI-XRD) is needed to observe and resolve the corresponding peaks. Figure 1.13 shows the GI-XRD analysis of an undpoed HfO_2 film of different thicknesses, accompanied with the resulted P_r values, highlighting the correlation between film orthorhombicity and ferroelectricity (Polakowski 2015).

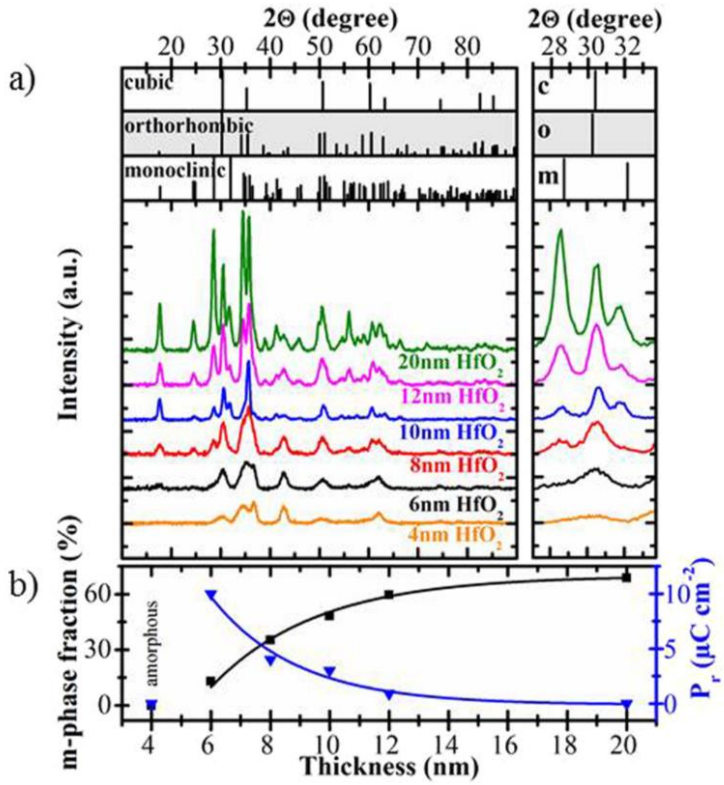

Figure 1.13 (a) GIXRD data for a thickness series of undoped HfO_2 crystallized in the presence a TiN top electrode. The inset shows an enlargement of the prominent reflexes for the monoclinic, orthorhombic, and cubic phase structure. (b) Calculated monoclinic phase fraction and corresponding values of remanent polarization P_r as a function of film thickness, exhibitng an inverse correlation. (Polakowski 2015)

Furthermore, the use of structural confinement layers such as TiN can induce FE-HfO_2 thin films even without any dopants (Lomenzo 2014, Polakowski 2015, Kim 2016). Besides, the link between HfO_2 film thickness and grain size also illustrates the relationship between the ferroelectricity and reducing grain size. The remnant polarization of the undoped HfO_2 thin films can be up to ~10.4 μC/cm^2 when HfO_2 thickness is ~4 nm (Polakowski 2015). It is believed that the pinning effect is arising from the difference in thermal expansion coefficient between the confinement layer and the HfO_2 thin films. Therefore, different materials with similar thermal expansion coefficients compared to TiN were also utilized for FE-HfO_2 thin films. It is shown that Ir (α_{Ir} = 6.4×10^{-6}/K) confinement layers also provides a similar effect on HfO_2 thin films besides TiN (α_{TiN} = 9.35×10^{-6}/K) (Lomenzo 2014). The possibility of using

other pinning layers is still under exploration. Recent reports include the use of W (Karbasian 2017), Au (Tian 2018), and Pt (Lin 2018) for pinning layers. In this work, structural confinement layer incorporation is the main pathway of achieving FE-HfO_2 thin films. Although the ferroelectricity in HfO_2 is studied intensively, most of the research was conducted with a focus of integrating ferroelectric HfO_2 into DRAMs (Florent 2017), ferroelectric random-access memories (FeRAMs) (Chatterjee 2017), ferroelectric field-effect transistors (FeFETs) (Mulaosmanovic 2017), and negative capacitance field-effect transistors (NC-FETs) (Kwon 2017). Integration of ferroelectric HfO_2 onto magnetoelectric electronics has been lacking thus far. Since Hf cations are not magnetic, the second part of this work aims to explore the possibility of achieving HfO_2-based multiferroic composites by implementing ferroelectric HfO_2 with magnetic $CoFe_2O_4$ as confinement layers due to its similar thermal expansion coefficient to TiN ($\alpha_{CFO} = 10\times10^{-6}$/K) (Zhou 2012).

1.3. Characterization Techniques for Converse Magnetoelectric Coupling Effects

With the objective of achieving a voltage-controlled magnetism, it is necessary to extract $\alpha_{converse}$ values while assessing the applicability of multiferroic composites systems since it is a quantifiable figure for comparison between cases. $\alpha_{converse}$ values can be determined by several methods (Zavaliche 2005, Eerenstein 2007, Thiele 2007, Evans 2013, Heron 2014). In this work, it can be determined by measuring the change in magnetization, especially remnant magnetization (M_r), after electrical poling. In addition, the change in anisotropy field (H_k) is considered also to provide the full picture of the magnetoelectric coupling effect. The magnetoelectric coupling coefficients are usually expressed in the forms of Oe cm/kV or s/m (SI units) with a conversion factor of 10^{-9} (100 Oe cm/kV = 1×10^{-7} s/m). The magnetoelectric coupling coefficient can be calculated by considering composite magnetization using Equation (1.7) with the following conversion:

$$\alpha_{converse} = \frac{\Delta M}{\Delta E} \text{ or } \alpha_{converse} = \mu_0 \frac{\Delta M}{\Delta E} \text{ (SI units)} \quad (1.8)$$

where M and E corresponds to the magnetization and electric field strength respectively, and μ_0 is the magnetic permeability of free space ($\mu_0 = 4\pi\times10^{-7}$ H/m = $4\pi\times10^{-7}$ V s/A m).

In some cases, especially when the magnetic anisotropy is the major parameter being altered upon electrical poling, $\alpha_{converse}$ is defined as the following and is expressed with a unit of Oe cm kV^{-1} (Aimon 2015):

$$\alpha_{converse} = \frac{\Delta H}{\Delta E} \quad (1.9)$$

where H is the magnetic coercivity of the material. $\alpha_{converse}$ obtained by using H_c correlates to the change in magnetic anisotropy since H_c represents how energetically favorable a sample is along a certain direction. Additionally, the use of anisotropy field H_k in $\alpha_{converse}$ calculations directly relates the change in magnetic anisotropy energy with applied electric field. H_k is defined as the following (Aimon 2012):

$$H_k = \frac{2K}{M_s} \quad (1.10)$$

where K is the anisotropy energy constant of the material, which directly correlates to a material's strain state (Fritsch 2012). One can also obtain K by considering the work W done in magnetizing the material along different directions. The work for magnetizing can be determined by an area method by calculating $\int H\, dM$, the area between the M-H hysteresis and the M-axis in the first quadrant (Cullity 2008). K can then be extracted by considering the absolute difference in W between in-plane (W_{ip}) and out-of-plane (W_{op}) as the following:

$$K = \left| W_{ip} - W_{op} \right| \quad (1.11)$$

In this work, with the goal of implementing the materials systems for memory devices, the converse magnetoelectric coupling coefficient $\alpha_{converse}$ is primarily calculated by using M_r as

the switching parameter to provide better perspective toward device applications. An example is shown in Figure 1.14.

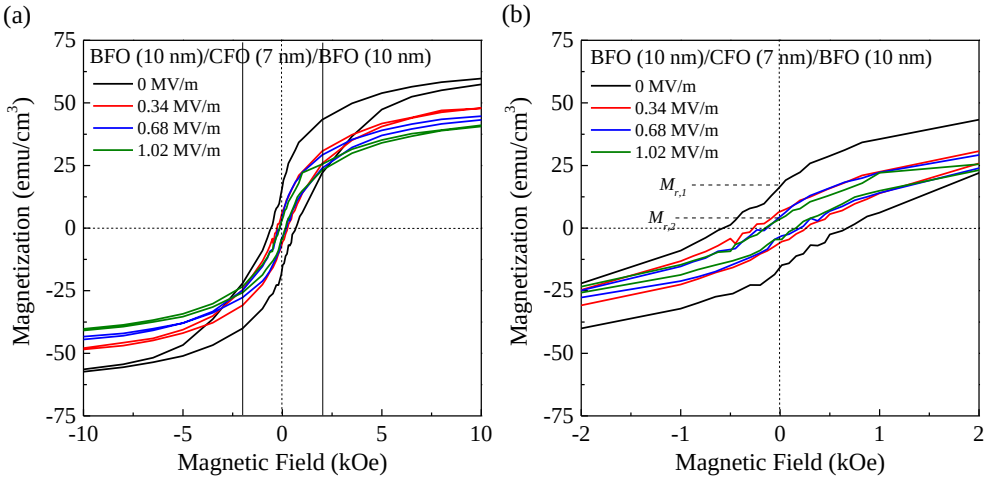

Figure 1.14 (a) Out-of-plane *M-H* hysteresis loops of a $BiFeO_3$ (10 nm)/$CoFe_2O_4$ (7 nm)/ $BiFeO_3$ (10 nm) composite on Nb:$SrTiO_3$ (001) annealed at 550 °C for 60 seconds under oxygen environment as a function of the out-of-plane electric field applied. The change in shape indicates magentoelectric coupling. (b) Zoomed-in view of the same results, $\alpha_{converse}$ can be quantified by considering the change in M_r (M-axis intercept).

1.3.1. Electrical measurements

In systems that involve exchange-bias coupling and ferromagnetic metals, $\alpha_{converse}$ values can be obtained by electrical measurements after integrating the material system into a multiferroic magnetic tunnel junction (MTJ). Via giant magnetoresistance (GMR) effect, the resistivity *R* of the MTJ stack can be plotted as a function of applied voltage. The *R*(*V*) loop can be used to quantify the magnetoelectric coefficient since *R* is directly related to the magnetic state *M* of the magnetic metal. An example is shown in Figure 1.15 (a) and (b), where the measurements were conducted on a multiferroic MTJ based on $BiFeO_3$/CoFe composites (Heron 2014, Heron 2014). The relationship between magnetization and observed GMR resistance is described as the following:

$$\alpha_{converse} = \frac{2\mu_0 M_s t}{R_{AP} - R_P} \frac{dR(V)}{dV} \tag{1.12}$$

where μ_0, M_s, t, R_{AP} and R_P are the magnetic permeability of free space, the in-plane saturation magnetization, the thickness of the antiferromagnetic layer, and the resistance values of the MTJ when the magnetizations (in a single-domain/mono-domain states) of the two layers are antiparallel and parallel, respectively. By implementing the resistances obtained in Figure 1.15 (b) into Equation (1.12), $\alpha_{converse}$ value for the $BiFeO_3$/CoFe system $_e$ is determined to be ~1×10^{-7} s/m, or 100 Oe cm/kV.

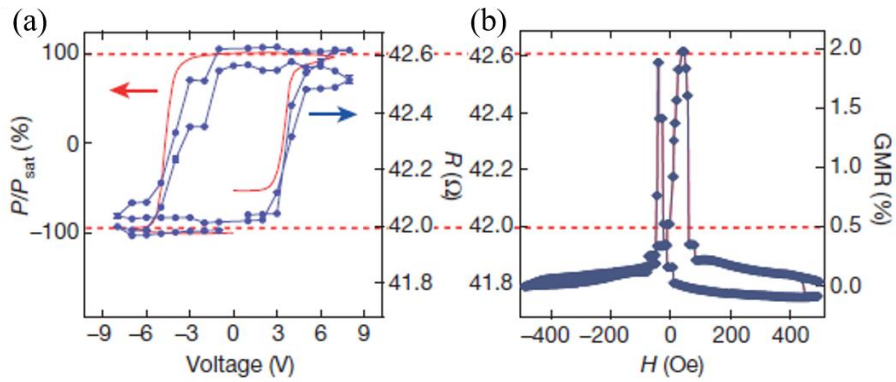

Figure 1.15 (a) $R(V)$ hysteresis loop of a multiferric MTJ based on multiferroic $BiFeO_3$/CoFe composite. (b) MTJ resistivity as a function of the magnetism of the free layer in the MTJ. (Heron 2014)

1.3.2. Scanning probe microscope imaging techniques

Due to the setup complexity of the other methods, attempts in obtaining magnetoelectric coupling effects and $\alpha_{converse}$ were also pursued with scanning probe microscopy (SPM) techniques. For instance, a combination of piezoresponse force microscopy (PFM) and magnetic force microscopy (MFM) is used in order to observe the local domain movement after the application of an external field. With this method, both magnetic domain flipping (Aimon 2015, Sone 2015) and ferroelectric domain flipping (Zavaliche 2005) were successfully observed. Figure 1.16 shows an example for the voltage-induced magnetic domain switching in a bi-layer $CoFe_2O_4$/$BiFeO_3$ composite of ~100 nm in thickness synthesized via a sol-gel method.

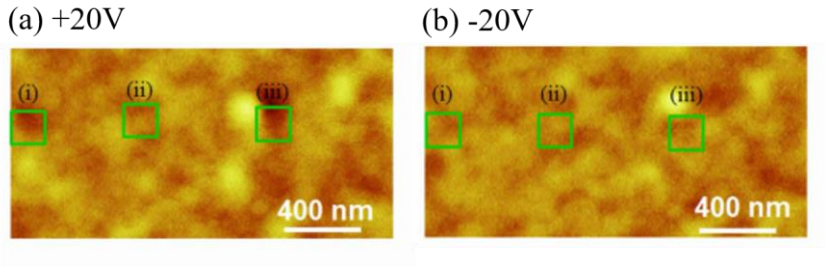

Figure 1.16 Magnetic domain image of a bi-layer $CoFe_2O_4/BiFeO_3$ composite obtained using MFM under (a) +20V and (b) -20V bias. (Sone 2015)

Also, with image processing, the change in local polarization/magnetization can be quantified by calculating the change of area and intensity of different domains/bits (Evans 2013). Inserting those values into Equation (1.8) could yield localized $\alpha_{converse}$ values. Figure 1.17 shows how the change in ferroelectric domains could yield the change in total polarization.

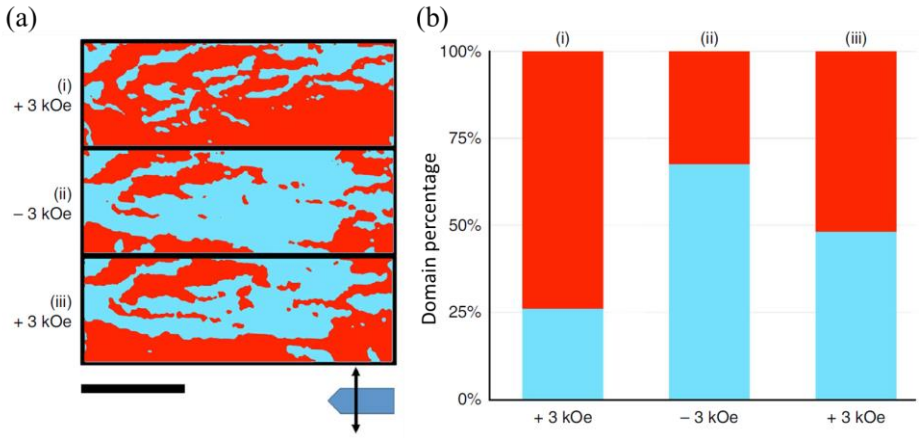

Figure 1.17 Magnetic field induced change of the ferroelectric domains of PZTFT material. Images obtained using PFM after applying magnetic fields from different directions. (a) shows the area histograms of the change domain distribution after applying a magnetic field. (b) shows the change of domain distribution under different fields (Evans 2013).

1.3.3. Magnetic characterizations

Lastly, $\alpha_{converse}$ can also be quantified by monitoring the change in magnetism as a function of applied electric field. After electric field application, the resulted *M-H* hysteresis loops would exhibit a shape change due to due to the interfacial coupling between the constituent phases. Both changes in the magnetic anisotropy as well as magnetization can be

observed. Various methods and equations, namely Equation (1.8), (1.9), and (1.10), may be used to interpret the obtained magnetic response change to derive $\alpha_{converse}$ values. As discussed earlier, it can be obtained by the change in H_c, H_k, M_s or M_r, depending on the coupling scenario, materials system, and applications of interest. $\alpha_{converse}$ values calculated based on H_k or H_c provide insights into the change in magnetic anisotropy. The change in anisotropy energy could be calculated either by the known strain states using density functional theory (DFT) calculations (Fritsch 2012, Aimon 2015), or by numerical calculations based on the *M-H* hysteresis loops since the area of the magnetic hysteresis represents the work applied to switch the magnetism (Spaldin 2003, Cullity 2008).

On the other hand, the use of M_r or M_s provides a more straightforward measure for comparison and device applications. It is noteworthy that $\alpha_{converse}$ values are not specific to the selection of the material only, but also a non-linear function of the field as both the ferroelectric and magnetic phase exhibit hysteresis responses. $\alpha_{converse}$ values under different applied fields can be obtained by performing an *M-E* scan (Thiele 2007). In terms of quantifying $\alpha_{converse}$ values with sample magnetizations, one can simply insert the change in M_r (Zavaliche 2005) or change in M_s (Chien 2016) over the applied field into Equation (1.8). Figure 1.18 is an example of observing magnetoelectric coupling effect via magnetometer measurements and the use of M_s, where the *M-H* hysteresis loops of a 0D-3D PZT/CFO composite were recorded after the application of different *E*-fields, yielding an $\alpha_{converse}$ value of ~100 Oe cm/kV. For the ease of enhancing magnetometer readouts, some reports conducted magnetoelectric coupling measurements when a weak external magnetic field is present (Eerenstein 2007). However, the values obtained by change in M_s do not reflect a "real" voltage-controlled magnetism. This work focuses on the magnetoelectric coupling coefficient $\alpha_{converse}$ obtained with the change in M_r to reveal the magnetoelectric coupling that is closest to the objective of magnetoelectric

device integration. However, $\alpha_{converse}$ calculated from H is discussed also to complete the materials aspect of this work. A summary of the magnetoelectric coupling coefficients obtained using the methods mentioned in this section are provided in Table 1.8.

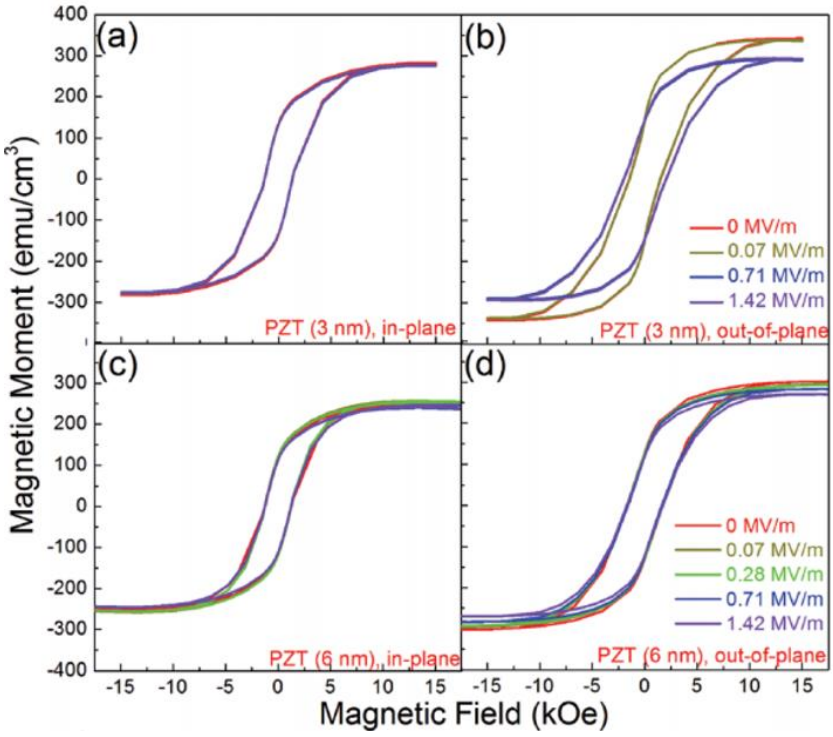

Figure 1.18 Magnetic properties of pirous $CoFe_2O_4$ filled with 3 nm ((a) and (b)) and 6 nm ((c) and (d)) ALD $Pb(Zr,Ti)O_3$, annealed at 700 °C. The samples were *ex situ* poled between 0 and 1.42 MV/m and the magnetic moment was measured with the applied field parallel to the plane of the sample ((a), (c)) or perpendicular to the substrate ((b), (d)) (Chien 2016).

Table 1.8 List of $\alpha_{converse}$ obtained by different methods.

Geometry	Material	$\alpha_{converse}$ (Oe cm/kV)	Method	References
2D-2D	$BiFeO_3$/CoFe	~100	GMR effect	(Heron 2014)
2D-2D	LSMO/BTO	~230	M-V scans	(Eerenstein 2005)
2D-2D	LSMO/PMN-PT	~60	M-V scans	(Thiele 2007)
1D-3D	BFO/CFO	~125	M_r change	(Zavaliche 2005)
1D-3D	BFO/CFO	~45	H_k change	(Aimon 2015)
0D-3D	PZT/CFO	~100	M_r change	(Chien 2016)
Bulk	PZTFT	~100	PFM/MFM	(Evans 2013)

1.4. Atomic Layer Deposition

Properties of functional oxides are greatly influenced by a handful of different factors, including film thickness, chemical stoichiometry, crystal structure, and so on. In order to tailor

the properties of multifunctional materials, the ability of fine controlling the above factors has great importance. Therefore, various material synthesis techniques were developed and taken into the field of research (Martin 2010). At the same time, other factors such as integration difficulty and cost are taken into discussion also for an optimized outcome and efficacy. In general, thin film deposition methods can be divided into two types, physical vapor deposition (PVD) and chemical vapor deposition (CVD). PVD methods grow thin films by the physical adsorption of energetically excited atoms (usually by plasma or laser) onto the substrate surface. CVD methods deposit thin film materials by creating surface chemical bonds thru chemical reactions of the chemical precursors.

Atomic layer deposition (ALD) is a type of CVD technique that allows the synthesis of ultra-thin films in a sub-monolayer manner by sequential self-limiting surface reactions. It is the self-limiting nature that differentiates ALD from ordinary CVD processes, as ALD prevents homogeneous gas phase reactions with a lower substrate temperature. In a typical ALD process, as shown in Figure 1.19, gaseous precursors and oxidants accompanied with respective chemisorption and surface reactions are pulsed into the reaction chamber in an alternating manner while inert gas is purged in between (Leskelä 2002). Since there are only a finite number of active sites on the substrate surface, ALD half-reactions can only deposit a finite number of molecules. Therefore, if at least one of the two surface reactions is self-limiting, the two reactions may proceed in a sequential fashion to deposit binary thin films with an atomic-level precision (George 2010). The self-limiting nature of the surface reactions enables many beneficial properties of ALD, including precise thickness control and conformal coating over large surfaces even with complex geometries. ALD is also highly scalable as it is only limited to the size of the chamber (George 2010). The aforementioned advantages are of great importance for industrial applications, thus ALD has been increasingly utilized in a variety of

fields including microelectronics and energy applications. On the other hand, however, the sequential self-limiting reactions and low deposition temperature also lead to several disadvantages such as low deposition rate. In addition, as-deposited ALD films are often not crystalline since the substrate temperature are lower (George 2010). Although amorphous structures are preferred in dielectric applications, it is not desired in some other applications that highly relies on material crystallinity such as multiferroics and battery electrolytes.

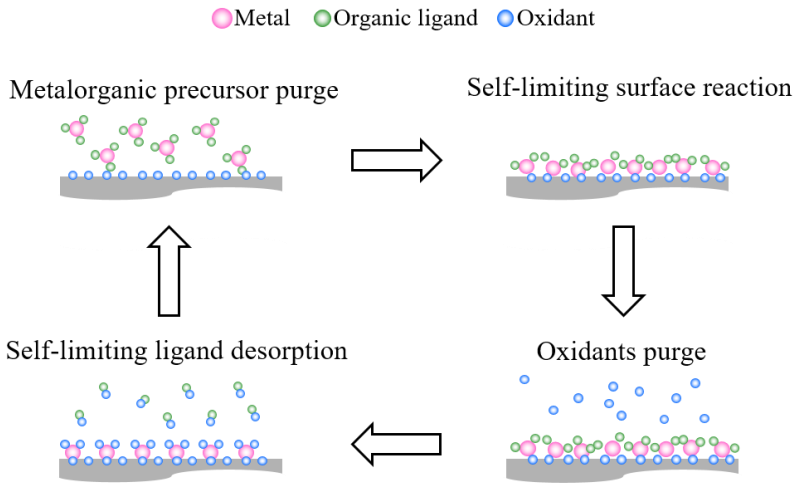

Figure 1.19 Schmatic representation of a typical ALD process of metal oxide with a self-limiting surface chemistry

ALD temperature window is defined as the range of substrate temperatures at which the materials' ALD growth rate is controlled and relatively consistent with given precursor chemistry. A schematic of the ALD window is shown in Figure 1.20. When an ALD process is performed outside of the ALD window, the process is not self-limiting due to the non-ideal reaction behavior including precursor decomposition and incomplete surface reaction. For instance, when the substrate temperature is too high, the precursor may decompose upon arriving to the surface and never form a monolayer. On the other hand, the chemisorption may not be initiated when the surface temperature is too low. Some ALD processes can still display self-limiting growth outside the ALD window, but often with a very high impurity

concentration (George 2010). A thorough understanding of the ALD precursor chemistry is crucial for enabling the ALD growth on substrates that are temperature-sensitive.

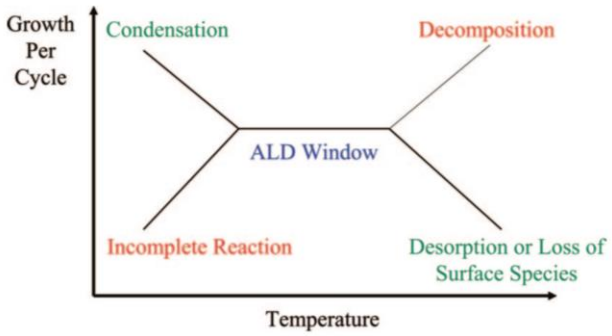

Figure 1.20 Schematic of possibele behavior for the ALD growth per cycle versus temperature showing the ALD window (George 2010).

ALD is suitable for synthesizing a variety of materials including sulfates, nitrides, and metal oxides. This work focuses on the ALD of metal oxides due to the wide spectrum of functionalities it could provide, including ferroelectricity, magnetism, and multiferroicity. When depositing binary metal oxides, metalorganic precursors are pulsed into the chamber and react with the surface active sites, forming a monolayer. Once the monolayer is formed, the surface half-reaction is then terminated. For the following cleaning step, the chamber body is purged or pumped for a certain period of time. A subsequent oxidant pulse removes the organic ligands on the surface and creates a new layer of reactive –OH sites for the following metalorganic precursors to react during the next half-cycle. Repeating the above steps continues the ALD process and allows a layer-by-layer growth of the material of interest.

ALD of complex oxides can be achieved by combining the ALD process of the constituent binary oxides in a sequential manner with a specific cycling ratio. The chemical stoichiometry of the synthesized complex oxide film can be tuned by adjusting the ratio of constituent binary oxide ALD steps. However, the ALD cycle ratio does not necessarily reflect the cation ratio of the complex oxide film. Since the precursor chemisorption greatly depends on the pre-existing surface, the cation composition is often deviated due to either the nucleation

delay or the differences in the available active sites of the dissimilar surfaces (Kim 2010). Since most complex oxides are only functional when crystallized, post-deposition thermal annealing is commonly used to facilitate the crystallization for desired exotic behaviors. It has to be noted that although the annealing processes can be beneficial, excessive amounts of thermal energy can also lead to a decreased surface smoothness and conformality (Kosola 2003, Chang 2017).

Since the ALD temperature windows of the constituent oxides do not necessarily overlap with each other, another challenge in complex oxide ALD is to match the growth windows to avoid large changes of the substrate temperature during the process. This can be mitigated by selecting suitable oxidant chemistry. According to the oxidant used, ALD processes can be generally categorized into two different sub groups, thermal ALD and plasma-enhanced ALD (PE-ALD). Thermal ALD is the most common type of ALD process due to the relatively simple setup. Thermal ALD oxidants include H_2O vapor and O_3, both of which require a higher substrate temperature than PE-ALD processes. Some precursors require elevated temperatures (>400°C) to react through a thermally-activated pathway, where the high temperature can damage the quality of the resulted film (Profijt 2011). Furthermore, some other precursors are not even viable with thermal ALD due to their large and bulky ligand groups that need extra energy to react. In PE-ALD, the surface reaction and activation is facilitated through energetic plasma species, which allow the process to be held at a relatively lower temperature. The higher reactivity of the plasma species allows additional degrees of freedom in both fine-tuning the processing parameters and materials' properties (Profijt 2011). Besides plasma, it was shown that atomic oxygen can also be used as an oxidant for ALD processes (Van 2005, Van 2005, Profijt 2011). The use of oxygen plasmas can result in the crystallization of the ALD film in some cases, which can be beneficial for device integration (Schindler 2016).

In this work, atomic oxygen is used as the oxidant to achieve high quality ALD growth and to facilitate the formation of metastable HfO_2 phases during film growth.

1.4.1. Atomic layer deposition of multifunctional oxide materials

The majority of studies on multiferroic materials are based on physical vapor deposition techniques such as PLD because of the ability to synthesis high-quality prototypical thin films. However, the high cost and incompatibility with large scale manufacturing leads to the need for synthesizing those materials via other methods that are transferrable. ALD, among all the other techniques, possesses great potential in developing multiferroic memory devices due to its uniform and conformal nature over large surfaces with atomic-level precision. The increasing importance of ALD in the semiconductor industry is demonstrated by the development of high-*k* gate dielectric materials (Leskelä 2002, Niinistö 2009, George 2010). Therefore, the ALD synthesis of multifunctional complex oxide materials has its importance in post-CMOS era. Figure 1.21 highlights the elements whose oxides have been synthesized by ALD processing, which forms the building block for complex oxides. Nonetheless, since the ALD thin films are usually amorphous due to low processing temperature, crystallizing the resulted ALD films poses a unique challenge (Kim 2015). It is hoped that the ALD of multiferroic composite heterostructures illustrated in this work can serve as an example for the ALD community.

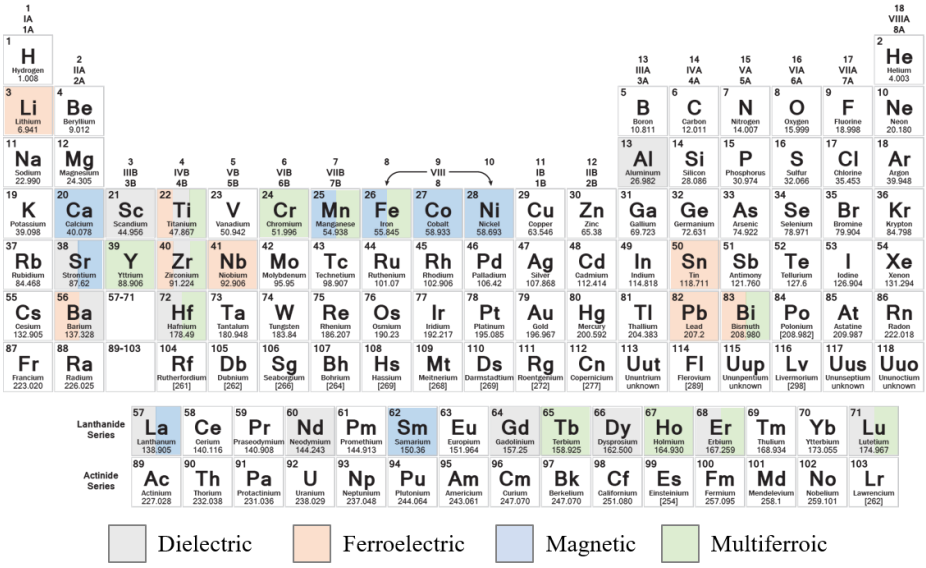

Figure 1.21 Elements that are demonstrated viable for both the thermal and PE-ALD of functional complex oxides. Colors indicate different class of complex oxides (Chang 2017).

For the ALD of multiferroic materials, $YMnO_3$ (Uusi-Esko 2009), $BiFeO_3$ (Zhang 2013, Akbashev 2014, Jalkanen 2014, Liu 2014), and other rare-earth manganate materials (Uusi-Esko 2011) were demonstrated with comparable functional properties. Additionally, epitaxial single-crystalline $BiFeO_3$ thin films were achieved via ALD synthesis with a suitable substrate selection and annealing procedure (Akbashev 2014, Pham 2015). Ferroelectric materials such as $BaTiO_3$ (Leskelä 2002, Matero 2006, Vehkamäki 2007), $PbTiO_3$ (Harjuoja 2006, Weon Hwang 2007) and $Pb(Zr_{0.52}Ti_{0.48})O_3$ (Choi 2013), and magnetic materials such as Fe_3O_4 (Wang 2012), $CoFe_2O_4$ (Chong 2010, Scheffe 2011, Pham 2017) and $NiFe_2O_4$ (Chong 2010) were proven viable with ALD as well.

Most of the aforementioned ALD processes use H_2O vapor and O_3 as the oxidant, which can potentially lead to several obstacles illustrated in the previous sections. Therefore, PE-ALD of multifunctional materials holds its own importance. A summary of functional complex oxides achieved via PE-ALD is shown in

Table 1.9. ALD, with its conformal nature and atomic level precision, offers unique opportunities in the integration of those functional materials and the subsequent

nanostructuring for the composite design, as discussed in Section 1.2.2. The incorporation of energized plasma species to ALD offers improvements in interfacial quality, crystallinity, and material properties. Although demonstration of a fully ALD-enabled multiferroic composite is still lacking thus far, the work on 0–3 PZT/$CoFe_2O_4$ nanocomposites enabled by conformal thermal ALD PZT coating on templated mesoporous $CoFe_2O_4$ matrix serves as the first proof of concept of ALD-enabled complex nanocomposites (Chien 2016). This work aims to further widen the spectrum by demonstrating a fully ALD-enabled multiferroic composite heterostructure that exhibits comparable magnetoelectric behaviors to other systems synthesized via other thin film deposition techniques.

Table 1.9 Summary of complex oxides synthesized PE-ALD

Material	Dep. Temp. (°C)	Precursor 1/ Precursor 2	Growth per cycle	Ferroic properties	Ref.
STO	250	$Sr(METHD)_2$*/ $Ti(O^iPr)_4$	0.78 Å	-	(Kil 2002)
	250-350	$Sr(TMHD)_2$/ $Ti(O^iPr)_4$	0.4 Å	-	(Lee 2002)
	250	$Sr(^iPr_3Cp)_2DME$/ $(CpMe_5)Ti(OMe)_3$	0.7-1.4 Å	-	(Langereis 2011, Longo 2012, Aslam 2014)
	250	$Sr(BuCP)_4$/ $Ti(O^iPr)_4$	0.15 Å	-	(Yim 2011)
SHO**	250	$Sr(^iPrCp)_2$/ $(MeCp)_2Hf(OMe)Me$	~0.4 Å	-	(Black 2011)
BTO	250-300	$Ba(iPr_3Cp^*)_2$/ $Ti(OCH(CH_3)_2)_4$	~2.6 Å	EOT ~4 nm	(Schindler 2016)
CFO	200	$Co(TMHD)_2$/ $Fe(TMHD)_3$	~2.4 Å	M_s ~ 400 emu/cc Poly-growth	(Pham 2017)
BFO	200-210	$Bi(TMHD)_3$/ $Fe(TMHD)_3$	~5.5 Å	M_s ~ 27 emu/cc P_r ~ 10 μC/cm^2 Epi-growth	(Pham 2015)

* METHD = 1-(2-methoxyethoxy)-2,2,6,6,-tetramethyl-3,5-heptanedionate
** SHO = $SrHfO_3$

1.5. Scope and Organization

This work aims to illustrate an alternative path in the synthesis and design of multiferroic composite heterostructures using ALD for energy-efficient magnetoelectric memory applications. This work is divided into two parts: the synthesis and optimization of $BiFeO_3$/$CoFe_2O_4$-based multiferroic composites, and the ferroelectricity in HfO_2 thin films

followed by its integration with $CoFe_2O_4$ into a multiferroic composite. Throughout this work, $CoFe_2O_4$ serves as the magnetic phase of choice due to its high magnetic strength and magnetostriction above other magnetic oxides while providing a stable interface when interfaced with oxide ferroelectrics. To the fact that $BiFeO_3$ itself is a room-temperature multiferroic makes the $CoFe_2O_4/BiFeO_3$ design an intriguing case with the potential of having two interfacial coupling effects taking place simultaneously. However, the biggest limitation of perovskite ferroelectrics lies in its high leakage behavior and poor compatibility with Si. Therefore, the possibility of implementing FE-HfO_2 with $CoFe_2O_4$ into a multiferroic composite is explored subsequently. Its superior electrical properties and great compatibility with CMOS technology make $CoFe_2O_4$/FE-HfO_2 a very promising path for the further development of magnetoelectric memories.

In the first part, the ALD processes of individual $BiFeO_3$ and $CoFe_2O_4$ thin films are illustrated, and are integrated into multiferroic composites with a 2D-2D geometry. ALD-synthesized 2D-2D $CoFe_2O_4/BiFeO_3$ nano-laminates exhibited a retained and tunable functional property with its layering scheme. Magnetoelectric coupling in the 2D-2D composites are observed and quantified using *ex situ* electrical poling SQUID, scanning SQUID with *in situ* poling, and combinatorial SPM setup. The observed magnetoelectric coupling is comparable with other materials systems. Si-integration of the 2D-2D system was demonstrated with the use of $SrTiO_3$-buffered Si substrates.

In the second part, a RE-ALD process of HfO_2 is described, and the crystallinity of HfO_2 thin films are examined as a function of both film thickness and annealing temperature. It is shown that the ferroelectricity in HfO_2 correlates with the degree of film orthorhombicity. Finally, HfO_2 thin films are integrated with $CoFe_2O_4$ to form a multiferroic composite. In the $CoFe_2O_4$/FE-HfO_2 design, $CoFe_2O_4$ serves as not only the structural confinement layer but also

the active magnetic layer that contributes to composite functionality. Composite functionality and $\alpha_{converse}$ values were characterized and demonstrated a comparable magnetoelectric behavior. The results obtained in $CoFe_2O_4$/FE-HfO_2 are compared with $CoFe_2O_4$/$BiFeO_3$ to further highlight the potential of using a non-perovskite ferroelectric with better electrical properties in designing and optimizing magnetoelectric coupling in multiferroic composites for magnetoelectric memory devices.

Chapter 2. Experimental Setup

In order to successfully synthesize and characterize the materials of interest, it is necessary to have an in-depth understanding of available tools and instruments. This chapter covers the radical-enhanced atomic layer deposition (RE-ALD) synthesis system, characterization techniques, and magnetoelectric measurements that were utilized in this work. First, the schematic design of the ultra-high vacuum (UHV) molecular-beam (MB) chamber for the RE-ALD processes, the metalorganic precursors of choice, and the process parameters are presented.

Techniques such as x-ray photoemission spectroscopy (XPS), x-ray diffraction (XRD), and transmission electron microscopy (TEM) were utilized to better understand ALD-growth behavior and to optimize the ALD process. The functional properties were characterized with probe station measurements and superconducting quantum interference device (SQUID) magnetometer measurements. Lastly, the experimental setup for observing and quantifying magnetoelectric coupling effects is illustrated. The subsequent calculations for quantifying converse magnetoelectric coupling coefficients ($\alpha_{converse}$) are also introduced to and compared with other literature reports.

2.1. Molecular-Beam (MB) Chamber

In this study, the materials of interest are synthesized via RE-ALD with the use of the molecular-beam chamber system. The system schematic is shown in Figure 2.1. The system consists of an 8”-diameter stainless steel main chamber and a load lock assembly. The transfer arm that moves across the load lock and the main chamber allows the insertion and removal of samples without venting the entire system. Various components are attached to the main chamber body, including a coaxial microwave cavity radical beam source for the introduction of highly reactive atomic oxygen, an ion gauge for pressure detection, a six-array precursor

doser for flowing metalorganic precursor vapors, and a sample stage that can control the substrate temperature during the ALD process. A CTI 4000 L/s cryogenic pump is attached to the main chamber, an UHV gate valve is installed between to provide isolation between the chamber body and the pump when needed (usually during system maintenance). The top of the chamber is a 10" quartz window that is used to facilitate the beam alignment to the sample surface. The base pressure of the main chamber is around ~2×10^{-6} Torr, and the operating pressure is around ~$1.5\text{-}2\times10^{-5}$ Torr. The base pressure of the load lock assembly is ~5×10^{-5} Torr, maintained by a 56 L/s Pfeiffer-Blazers turbomolecular pump backed by a 6.67 L/s Leybold mechanical pump. Load lock pressure is measured by an MKS Micropirani gauge.

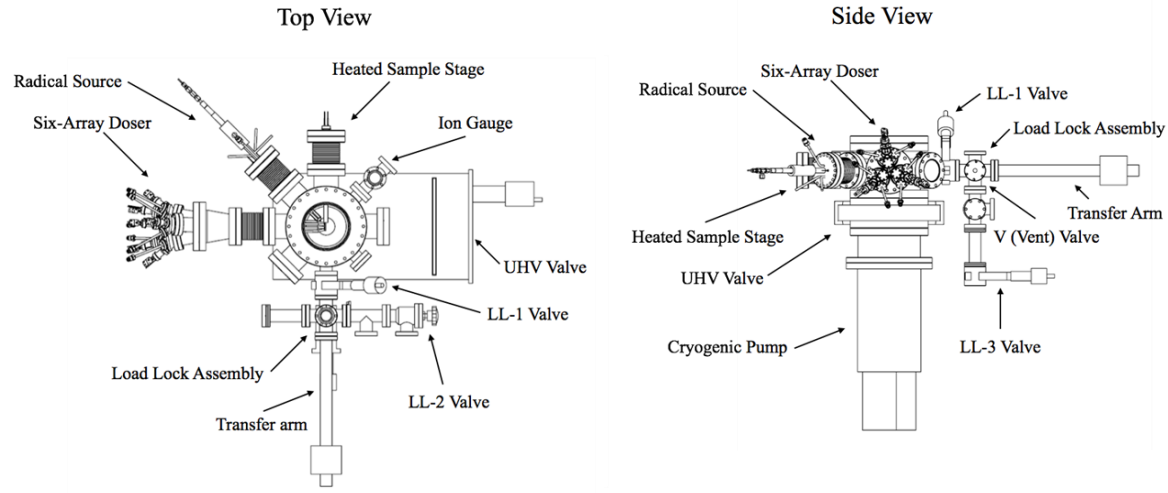

Figure 2.1 Schematics of the multi-beam chamber, showing both top and side views

2.1.1. Metalorganic precursor doser arrays

Precursor doser arrays are attached to the main chamber to deliver metalorganic precursor vapors to the substrate surface. Each precursor doser consists of a precursor housing, a pneumatic valve, an in-vacuum gas line, and several heating units. Each precursor is stored in a separate housing, connected by the corresponding gas line to the main chamber body. The schematic of the precursor array is shown in the Appendices; the parts used are from MDC

Vacuum, Nor Cal products, Swagelok, and Insulator Seal. The six doser array assembly consists of three 5-way 1.33” CF to 2.75” CF multiports (shown in Appendices), which are mounted on a single 3-way 2.75” CF to 6” CF multiport. The 6” CF multiport leads to a 6” CF to 4.625” CF conical reducer. The doser is equipped with a 4.625” CF bellow that leads to the chamber. The bellow allows the manual alignment of the doser beams towards the sample surface.

The precursor housing is a 1.33” OD, 3” long stainless steel nipple with a Conflat flange, with a cap on one end, attached to a SS-HB series Swagelok brand pneumatic valve at the other end using VCR fittings. The pneumatic valve is installed between the feed-through and the housing, controlling the flow of evaporated precursor into the chamber by a 0.25” stainless steel feed-through with an air-side VCR fitting. On the vacuum side, the feed-through is welded to an additional 0.25” stainless steel line that is terminated approximately 2” from the sample surface. Heating wires from McMaster-Carr are wrapped around the air side gas lines, pneumatic valves, and precursor housings to maintain a heated environment that is necessary for an adequate precursor flux. The in-vacuum gas lines are wrapped and heated by flexible Teflon heaters. The temperatures for the gas lines are measured by Omega brand Cr/Al K-type thermocouples and are controlled by several Omega CN1500 series multi-zone ramp and soak controllers which consist of seven independent PID temperature controllers. The pneumatic valves are controlled by LABVIEW software through NI USB-9481 general purpose relay modules for an automated ALD process.

2.1.2. Coaxial microwave cavity radical beam source

A coaxial microwave cavity radical beam source is used to introduce oxygen atoms into the system for the ALD process. Schematics of the radical source are shown in the Appendices. The radical source was originally developed to overcome the disadvantages of high ion/radical

recombination from a traditional remote microwave plasma source setup (Chang 1997). The installation of the radical beam source enables plasma generation close to the substrate surface, reducing the amount of recombination events and maximizing the transport of radicals to the sample surface.

The cavity consists of two coaxial conductors: one hollow 0.25” center conductor and one 0.625” outer conductor, which are fixed in series by a metal clamp that is surrounded by a quartz ampoule at the end. The use of a coaxial cavity allows the radical beam source to have a smaller diameter than the ~10 cm microwave wavelength. The cavity is vacuum-sealed by two Teflon bushings which can seal up to ~10^{-8} Torr; the two Teflon bushings form a small volume that is differentially pumped via a mechanical pump. Gas molecules are fed from the air-side through a vacuum feed-through to the radical beam source and to the quartz ampoule. The plasma is generated inside the quartz ampoule as the microwave power dissociates the feed gas.

Since the plasma generation generates heat, the beam source was designed to utilize water cooling, as heat dissipation is challenging in vacuum environments. Cooling water is fed through both the metal holder for the quartz ampoule and the center conductor. The quartz ampoule holder consists of a piece of stainless steel that is clamped to the ampoule at the top and a hollow block of stainless steel from which cooling water flows through at the bottom. Cooling water is flowed into the inner tube and exits through the annular space between the inner tube and the center conductor.

Microwave power was supplied by a 2.45 GHz, 300 W (maximum) Sairem microwave power supply using an N-type connector which was attached in series to the center conductor. The resonance/striking condition could be achieved by adjusting the cavity length by tuning the air-side tuning slug and the movable collar when the N-type connector was fixed. For the

generation of atomic oxygen, molecular oxygen, at 99.999% purity, is fed to the quartz ampoule at a rate between 0.5 and 0.75 sccm. The flow rate is controlled by an MKS instruments mass flow controller. During operation, the radical beam source was operated at 25 W forward power and 1-3 W reflected power. During normal operation, the radical beam source was controlled remotely by LABVIEW software and a National Instruments (NI) DAQ USB-9481 relay module which controls the microwave power.

2.1.3. Metalorganic precursors

In this study, *β*-diketonate based metalorganic precursors were used for the ALD processing of $BiFeO_3$ and $CoFe_2O_4$. As shown in Figure 2.2 (a), the *β*-diketonate TMHD (2,2,6,6-tetramethyl-3,5-heptanedione) ligands are bounded to the center metal cations. The family of *β*-diketonate metalorganic precursors is a common choice for ALD and CVD processes. During the oxidation half-cycle, the TMHD ligands are replaced by reactive hydroxyl groups upon removal, enabling the subsequent monolayer growth. Highly reactive oxygen atoms are used as oxidants in order to ensure the removal of the bulky TMHD ligands, further enabling high-quality film growth in ALD. $Bi(TMHD)_3$ and $Fe(TMHD)_3$ precursors of 99% purity were purchased from Strem Chemicals, Inc, whereas 99% purity $Co(TMHD)_2$ was provided by Alfa Asear. All the *β*-diketonate precursors used are solid powders under room temperature and pressure.

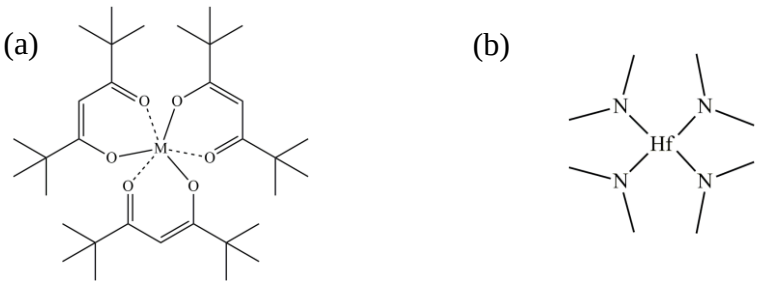

Figure 2.2 Molecular structure of (a) tris(2,2,6,6-tetramethyl-3,6-heptanedionato)M(III) precursors where M = Bi, Fe, Co, and (b) tetrakis(dimethylamino)hafnium(IV)

For the ALD of HfO_2, $Hf(N(CH_3)_2)_4$ (Tetrakis(dimethylamido)hafnium(IV)), TDMAH) was used due to its availability in addition to its well-characterized ALD chemistry. The molecular structure of TDMAH is shown in Figure 2.2 (b). TDMAH is a low melting solid under ambient conditions and is extremely water reactive. Although TDMAH reacts readily with water, atomic oxygen allows the formation of metastable HfO_2 phases due to the lower substrate temperature. TDMAH of 99% purity is provided by Sigma-Aldrich. Table 2.1 lists of the precursors used in this study and their corresponding information.

Table 2.1 Physical properties of the metalorganic precursors used in this study

Precursor	Subl. Temp. (°C)	Form (Room Temp.)	Color	Vapor Pressure	Vendor
$Bi(TMHD)_3$	150-160	Solid powder	White	Subl. 11 Torr	Strem Chemicals
$Fe(TMHD)_3$	120-130	Solid powder	Red	n.a.	
$Co(TMHD)_2$	120	Solid powder	Blue	n.a.	Alfa Asear
$Hf(N(CH_3)_2)_4$*	50-75	Low melting Solid	White	n.a.	Sigma-Aldrich

* $Hf(N(CH_3)_2)_4$ = Tetrakis(dimethylamido)hafnium(IV)), TDMAH

Each precursor is housed in a 1.5”-diameter by 4.93”-long electropolished conflat tube that is connected directly to the precursor doser through a Swagelok manual valve. In all experiments performed, the precursor vapor was delivered to the main chamber body by heating the precursor housing, without the use of a carrier gas. Molecular oxygen gas of 99.999% purity is used as the feed gas for the radical source. A single ALD cycle of the binary oxide growth is comprised of four sequential steps: a metalorganic precursor pulse, a pump down period to prevent gas-phase reactions, an atomic oxygen exposure to regenerate surface reactive sites, and finally another pump down period. By repeating the four steps in a sequential manner, a layer-by-layer growth of the binary oxide can be achieved. The ALD sequence is then repeated until the desired film thickness is reached. Table 2.2 shows the duration of the individual steps for the binary oxides of interest of this work. For the complex oxide $BiFeO_3$ and $CoFe_2O_4$, the ALD growth is enabled by integrating the ALD processes of the constituent

binary oxides into supercycles. A $BiFeO_3$ supercycle consists of 7 Fe_2O_3 cycles and 2 Bi_2O_3 cycles, while a $CoFe_2O_4$ cycle is 5 Fe_2O_3 cycle and 1 CoO cycle.

Table 2.2 Pulsing durations for the binary oxides of interest in this work

Binary Oxide	Precursor (s)	Pump (s)	Atomic Oxygen (s)	Pump (s)
Bi_2O_3	90	5	20	5
Fe_2O_3	90	5	20	5
CoO	90	5	20	5
HfO_2	10	10	20	10

2.2. Materials Characterization

Various characterization techniques were used to identify and investigate the properties of the material synthesized via ALD. In this section, the purpose of the technique, as well as its corresponding physics, will be explained in detail.

2.2.1. X-ray photoemission spectroscopy

X-ray photoemission spectroscopy (XPS) is a characterization technique that can quantify thin film composition. It is a surface sensitive technique that probes the top ~10 nm of the surface and the bonding states of the atoms. During XPS, the sample surface is exposed to x-ray radiation, electrons with corresponding energy are then excited and subsequently emitted from the core of the atom due to photoelectric effect. The binding energy (*BE*) of the electron is quantified using the following equation of energy conservation:

$$KE = h\nu - BE - \Phi \tag{2.1}$$

where *KE* is the kinetic energy of the ejected electron, $h\nu$ is the energy of the incident photon, *BE* is the characteristic binding energy of the electron to its parent atom, and Φ is the work function of the spectrometer. XPS is only sensitive to the surface due to the elastic scattering of the photo-emitted electrons. Since the mean free paths of the emitted electrons are generally around 10 nm, photoelectrons emitted below this range undergo great dissipation and will not be able to be detected (Powell 2000).

Since the binding energies of the photoelectrons are unique to their parental atoms and their chemical environments (bonding states), one can identify not only the atomic species of the measured samples by the presence of different characteristic peaks, but also the chemical bonding state (Watts 2003). During an XPS scan, emitted electrons are collected to construct the spectra, as shown in Figure 2.3 (a), (b), and (c). In order to quantify the atomic composition of the measured sample, one can obtain the concentrations of different atoms through fitting the photoemission spectral peak lineshapes. The governing equation is shown as the following:

$$C_i = \frac{I_i / ASF_i}{\sum_{i=1}^{n} I_i / ASF_i} \tag{2.2}$$

where C_i is the atomic concentration of species i within the sample, I_i is the integrated intensity of the spectral peaks, and ASF_i is the corresponding atomic sensitivity factor for species i. Similar to binding energies, the ASF values are unique to each atom as well. Table 2.3 lists the basic parameters of those elements that are of the interest to this work. To properly fit the XPS peaks, correct constraints are needed. For instance, all the XPS peaks from the same orbital should have the same full width half max (FWHM) values. In addition, depending on the electron shell which the ejected electron is emitted, the ratio between the primary and secondary peaks needs to be set to a proper value corresponding to the spin orbit splitting, as summarized in Table 2.4. Since the functionalities of ferroic materials depend greatly on their atomic composition as well as their impurity level, XPS analysis plays a critical role in this study.

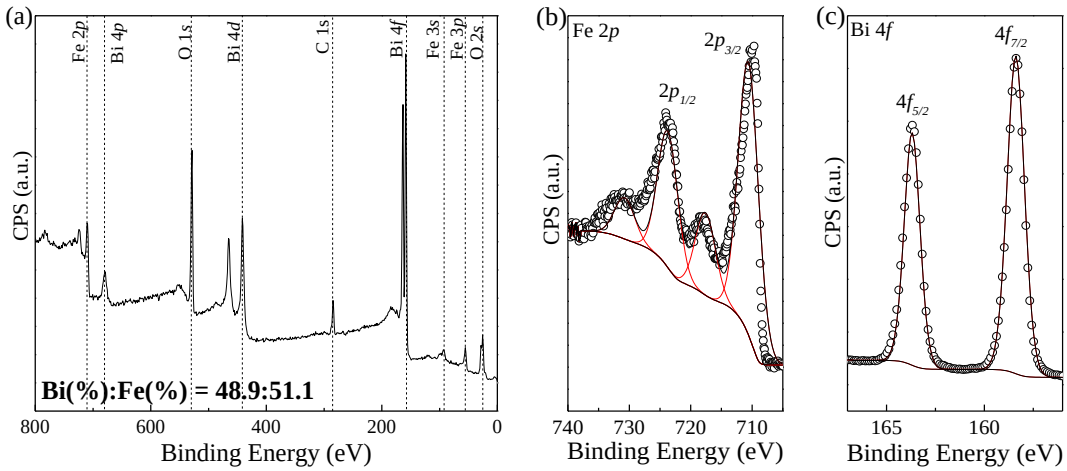

Figure 2.3 (a) XPS survey scan from 800 – 0 eV of a 100 nm stoichiometric $BiFeO_3$ thin film. Detailed and fitted XPS spectra for (b) Fe 2*p* and (c) Bi 4*f* photoelectron peaks. Symbol represents obtained spectra while the lines represent the fitting curves. The film showed a Fe^{3+} to Bi^{3+} ratio of 48.9:51.1. (adapted from (Pham 2015))

Table 2.3 XPS parameters of the elements related to this work

Element	Binding energy (eV)	A.S.F.
Fe 2*p*	706.7	2.95
Bi 4*f*	158.6	9.14
Co 2*p*	780.3	3.59
Hf 4*f*	14.3	2.05
C 1*s*	284.6	1.00
O 1*s*	531.6	2.93

Table 2.4 Peak area ratios of electron shells

Subshell	Area Ratio
s	n.a.
p	1:2
d	2:3
f	3:4

2.2.2. X-ray diffraction spectroscopy

X-ray diffraction spectroscopy (XRD) was used to identify the crystal structure of a given sample. Based on Bragg's law of diffraction, one can determine the crystal structure and lattice parameter based on the diffraction peaks of the sample. The schematic of Bragg diffraction and the corresponding mathematical expression are shown in Figure 2.4 and Equation (2.3), respectively.

$$2d\sin q = nl \tag{2.3}$$

where d is the distance between lattice planes, θ is the Bragg diffraction angle, λ is the incident x-ray wavelength, and n is an integer number order of reflection.

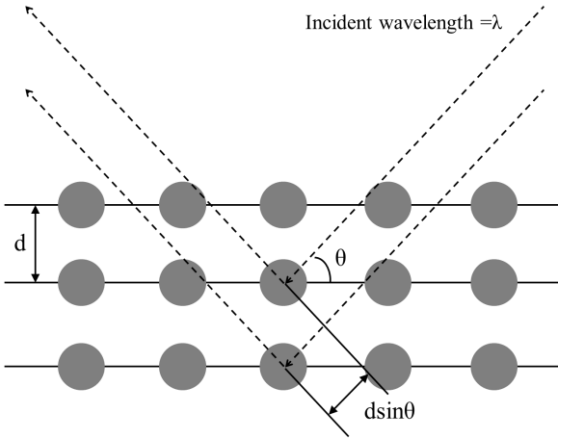

Figure 2.4 Schematic of x-ray photon scattering on lattice planes, constructive interfere will occur when the angle fulfills Bragg's law (adapted from (Blakemore 1985))

During XRD, x-rays with wavelengths shorter than the lattice spacing are cast to the sample, while the incident light angle is altered. When the Bragg diffraction law is fulfilled at an angle θ, constructive interference occurs if the photon path difference is equal to an integral number of wavelengths. The constructive interferences result in the emergence of XRD characteristic peaks; the position of those XRD peaks then provide insight toward the crystal structure of the given sample, and its corresponding lattice parameters. Figure 2.5 is an example XRD scan of $BiFeO_3$ thin film grown on a $SrTiO_3$ (001) substrate. The peaks in the spectra show the existence of $BiFeO_3$ and $SrTiO_3$ crystalline phases, both in 001 orientations. The peaks can be indexed using the Joint Committee on Powder Diffraction Standards (JCPDS) XRD catalog. Table 2.5 lists the related JCPDS codes used in this work. Unlike XPS, XRD can probe the crystal structure of the entire sample including the substrate, thus the detection depth of XRD measurements can be up to 10 mm, unlike XPS.

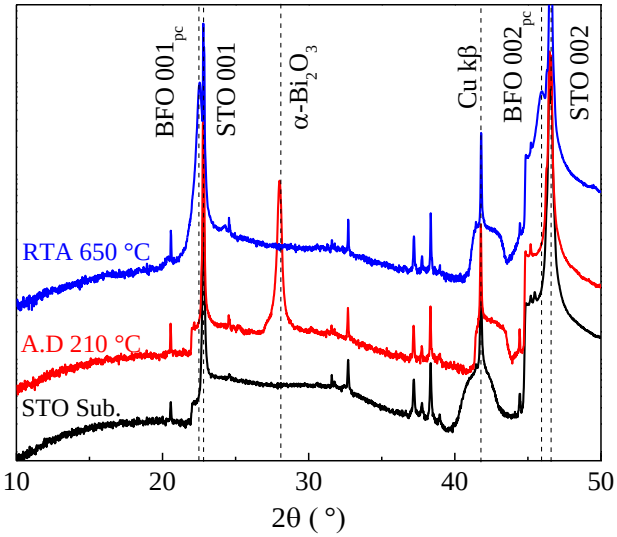

Figure 2.5 XRD scans of a $BiFeO_3$ film deposited on STO substrate, the existence of the $BiFeO_3$ and $SrTiO_3$ peaks implies the presence of $BiFeO_3$ on $SrTiO_3$ after 650 °C RTA step. (adapted from (Pham 2015))

Table 2.5 List of JCPDS codes for materials studied in this work

Materials	JCPDS Ref.	Prominent peaks	
		h k l	*θ* (°)
Si	00-027-1402	4 0 0	69.0
$BiFeO_3$	01-086-1518	0 1 2	22.4
		1 1 0	32.1
		0 2 4	45.8
		2 2 0	30.1
$CoFe_2O_4$	00-025-0090	3 1 1	35.4
		4 0 0	43.1
$SrTiO_3$	01-074-1296	1 0 0	22.8
		2 0 0	46.5
$Bi_2Fe_4O_9$	00-022-1086	0 0 1	14.8
		2 0 0	22.3
		0 0 2	29.8
Bi_2O_3	01-071-2274	2 2 0	30.9
		2 2 2	27.9
Fe_2O_3	00-001-1053	3 1 1	35.5
CoO	00-042-1300	1 1 1	34.2
HfO_2 (m)	01-074-1506	-1 1 1	28.4
		1 1 1	31.6
		0 0 2	34.2
HfO_2 (o)	01-081-0028	2 1 1	30.4
		0 0 2	35.5
SrO	00-001-0886	0 0 2	34.7
TiO_2	00-021-1276	1 0 1	25.3

Additional analysis of XRD diffraction peaks could provide further information regarding the crystallinity of the sample. For instance, by examining the full width half max

(FWHM) of the diffraction peak, one could obtain the averaged grain size of the crystallites using the Scherrer equation. The Scherrer equation is shown as the following:

$$t = \frac{K\lambda}{\beta \cos\theta} \tag{2.4}$$

where τ is the averaged size of the examined crystalline phase, K is the dimensionless shape factor, λ is the wavelength of the incident X-ray, β is the FWHM of the XRD peak of interest, and θ is the peak angle. Figure 2.6 shows a detailed XRD scan of the BFO 001_{pc} reflection, where the FWHM of 0.291° leads to an averaged grain size of ~90 nm using the Scherrer equation.

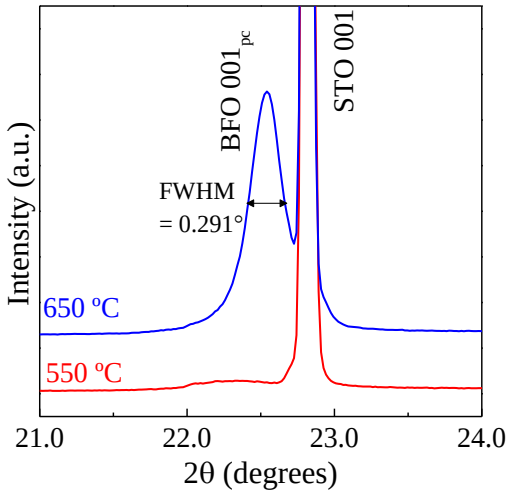

Figure 2.6 Zoomed-in XRD spectra of the $BiFeO_3$ thin films on $SrTiO_3$ (001) substrate after annealing at 550 and 650 °C. (adapted from (Pham 2015))

Since a material's functional properties correlate strongly with its crystalline structure, the structural evolution of the material coupled with other factors, such as film thickness, composition, and annealing temperatures, are of great importance in optimizing the properties of the multiferroic thin film composites.

2.2.3. Spectroscopic ellipsometry

Spectroscopic ellipsometry is used to determine the thickness of the films grown on substrates. A polarized light is directed onto the sample and the change in both amplitude (Ψ) and phase (Δ) of the reflected light is detected. Ψ and Δ are measured as a function of the wavelength of the incident light, which allows the determination of the refractive index (n) and dielectric constant (ε). Through the fitting of the obtained and theoretical values, the thickness of the measured sample can be determined. A schematic of ellipsometry measurement is shown in Figure 2.7.

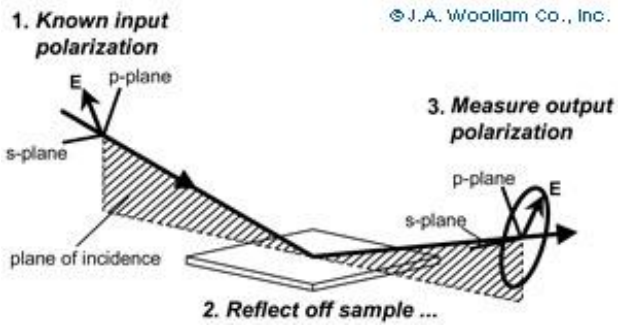

Figure 2.7 Schematic configuration of an ellipsometer, a polarized light is directed onto the film surface and reflection is measured (J. A. Woollam Co, Inc.)

Since n and ε values depend on the quality and structure of the sample, sometimes it is necessarily to develop an optical model for the material of interest in order to accommodate the non-ideal behaviors of as-grown films. For transparent materials, the optical constant can be described using several mathematical oscillator models such as the Lorentz oscillator shown as the following:

$$\tilde{\varepsilon} = \varepsilon_{1,offest} + \frac{AE_c}{E_c - E^2 - iBE} \tag{2.5}$$

where E_C is the center energy of the incident photons, ε_{offset} is the dielectric constant offset in the measurement, E is the energy of the incident photon, and A and B are constants that are unique to the material of interest. In this work, the optical models for the oxide materials were

constructed by cross-referencing the obtained spectra with SEM cross-section images. Table 2.6 lists the related Lorentz parameters for the materials of interest in this work. Figure 2.8 shows the ellipsometry fittings of Fe_2O_3, Bi_2O_3, CoO, and HfO_2 thin films.

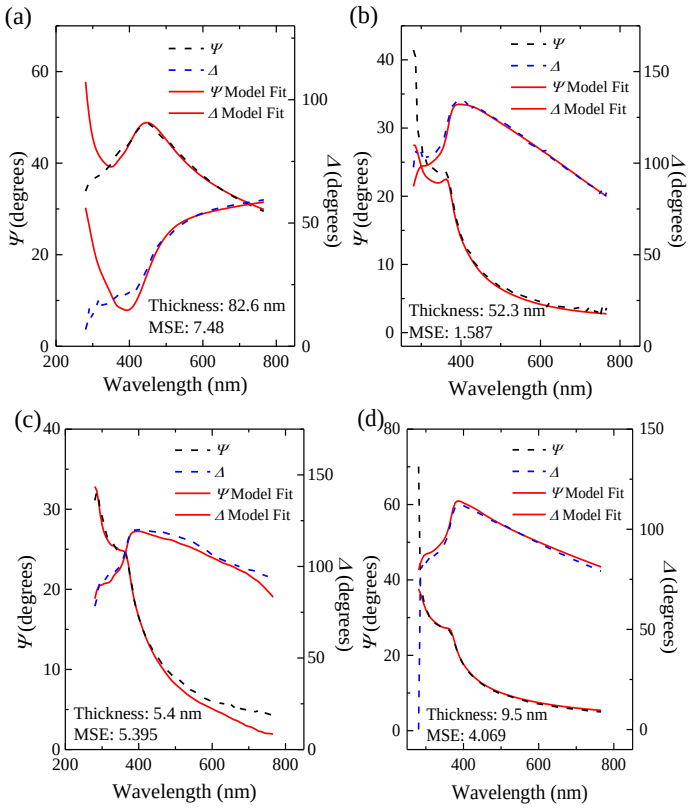

Figure 2.8 Ellipsometric Ψ (polarization) and Δ (intensity) fitting of (a) Fe_2O_3, (b) Bi_2O_3, (c) CoO, and (d) HfO_2 on Si (001) substrates.

Table 2.6 Fitted Lorentz parameters for individual oxide films

Metal Oxide	$\varepsilon_{1,\,offset}$	A	B	E_c
Fe_2O_3	1.76	4.77	1.26	3.49
Bi_2O_3	1.58	107.97	1.07	4.93
CoO	1.04	2.96	0.52	0.51
HfO_2	7.80	195.44	0.20	5.35

2.2.4. Transmission electron microscopy

Transmission electron microscopy (TEM) is an imaging technique that uses accelerated electrons, rather than photons, to obtain images of an object. A schematic TEM system setup is shown in Figure 2.9. TEM allows users to determine the atomic orientation and crystalline structure of the material with ultra-high resolution, in some cases as small as individual atoms.

The sample for TEM analysis has to be thin enough (~100 nm) to provide sufficient electron transmission, while preventing excessive reflection or diffraction. Similar to conventional optical microscopy, an accelerated electron beam is directed onto the object, and the transmitted electrons are detected to construct the microscope image. TEM images are formed based on the interaction between the electrons and object specimens. For example, since atoms with higher atomic numbers will scatter more electrons, heavier atoms are darker in TEM images (Alford 2007). The transmitted electrons are then focused and projected onto a florescent viewing screen, photographic plate, or digital camera.

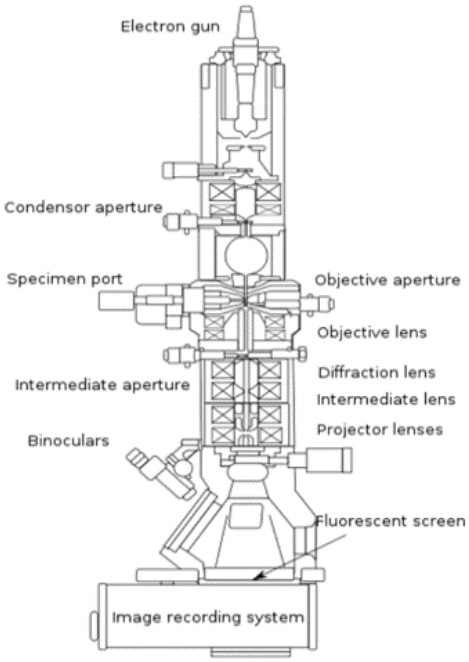

Figure 2.9 Cross-sectional schematic of a TEM system. (Abudayyeh 2012)

The capability of TEM in obtaining ultra-high resolution images is owing to the small de Broglie wavelength of electrons, since the system resolution is proportional to the incident beam wavelength. The wavelength of the incident electron beam can be expressed as the following de Broglie equation:

$$\lambda_e = \frac{h}{\sqrt{2m_0 E(1+\frac{E}{2m_0 c^2})}} \tag{2.6}$$

λ_e is the de Broglie wavelength of the incident electron, h is Planck's constant, m_0 is the rest mass of the electron, c is the speed of light, and E is the energy of the accelerated electron. In TEM systems, an ultra-high vacuum is generally required in order to decrease the noise by reducing the number of particles within the electron beam path. TEM is a powerful technique as it can provide images with ultra-high resolution. With TEM, crystal structures, film growth modes, and defect orientations can be easily identified in order to probe the nature of the deposited films. Figure 2.10 (a) shows a high-resolution TEM (HRTEM) image of a $BiFeO_3$ thin film grown on a $SrTiO_3$ (001) substrate.

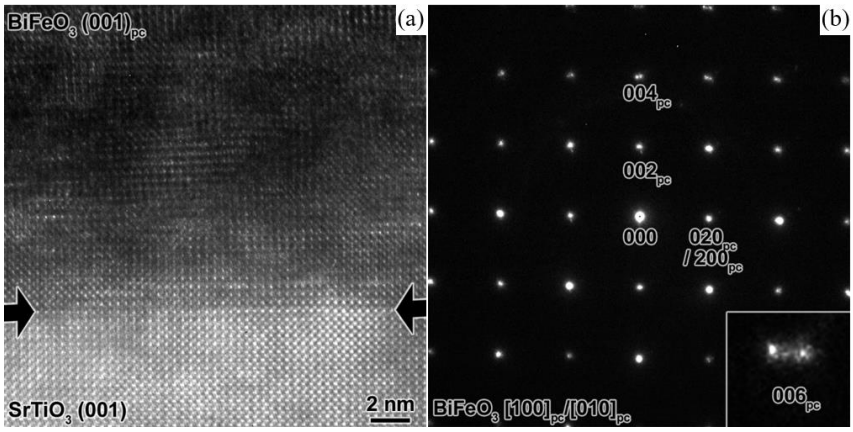

Figure 2.10 (a) High resolution transmission electron microscope (HRTEM) image of a 90-nm thick $BiFeO_3$ thin film grown on a $SrTiO_3$ (001) substrate. (b) Selected area electron diffraction (SAED) pattern of the $BiFeO_3$ thin film and (inset) enlarged 006_{pc} reflection. (adapted from (Pham 2015))

There are a handful of plugin analysis methods that are compatible with TEM systems; selected area electron diffraction (SAED) is one of them. During SAED measurements, instead of focusing the entire image onto the screen, a different set of diffraction lenses are placed to the beam path, allowing the collection of diffraction patterns when Bragg's law (Equation (2.3)) is satisfied. The diffraction pattern from SAED analysis consists of a group of reciprocal

lattice dots. Crystallographic information such as crystal structure and atomic spacing can be obtained by analyzing the obtained diffraction pattern. One advantage of SAED analysis is the ability to obtain regional diffraction patterns based on which part of the sample the election beam is directed towards. Since the patterns are unique to their crystal structure, the crystal structure can be identified and indexed using the JCPDS database. While highly crystalline samples generate highly-ordered diffraction patterns, polycrystalline samples yield ring-like diffraction patterns. Figure 2.10 (b) shows the SAED pattern of a $BiFeO_3$ thin film crystalized at 650 °C on $SrTiO_3$ (001), with the indexed peaks labelled. The lattice spacing of the sample from the patterns can be quantified with the following equation:

$$Rd = / L \tag{2.7}$$

where R is the separation between the diffraction spots on the screen, d is the spacing between the lattice planes, λ is the wavelength of the electrons, which for this work was operated at 300 kV, translating to a wavelength of $\lambda = 4.13 \times 10^{-3}$ nm, and L is the distance from the film to the detector screen known as the Camera Length. When using a known standard sample, such as a single crystal substrate, the specimen can be indexed. For instance, the checkerboard pattern shown in Figure 2.10 (b) indicates a cubic structure, with an estimated lattice spacing of ~3.987 Å. In this work, SAED was one of the main techniques for studying the correlation between the degree of lattice mismatch and the thin film growth modes.

2.2.5. Ferroelectric P-E measurements

In order to verify the ferroelectricity in a material, ferroelectric *P-E* measurements were performed by an electrical probe station connected to a Radiant Precision Multiferroic II ferroelectric tester. SE-SM Tungsten Cat Whisker probe tips were purchased from Singatone Corporation, where the flexible tip could minimize the mechanical damage to the sample upon engaging. Prior to the measurements, Au (100 nm)/Cr (10 nm) electrodes were deposited onto

the material of interest via electron-beam evaporation. The size of the electrodes was determined by the shadow masks used during electron-beam evaporation. The main parameters, namely drive voltage, drive frequency, and sample size, all have a major influence on the output ferroelectric hysteresis. The drive voltage determines the upper limit of the voltage applied during measurements. A drive voltage that is too high essentially leads to the breakdown of the material, while an insufficient drive voltage can lead to a non-saturating *P-E* hysteresis. Since the ferroelectricity of materials often originates from the displacement of cations in the unit cell, the speed of such ferroelectric switching has intrinsic limitations. As the drive frequency correlates to the speed of the electrical sweeping during *P-E* measurements, a suitable frequency is needed to obtain a high-quality *P-E* hysteresis loop. Given the following equation for capacitors:

$$C = e_0 \frac{A}{d} \tag{2.8}$$

C is the capacitance of the material, ε_0 is the permittivity of free space (8.854×10^{-12} F/m), and A and d are the area and the thickness of the measured sample, respectively. It is clear that the output polarization/capacitance is closely related to the size of the sample (d ~250 μm in this work), therefore having a precise understanding of the sample size is crucial for an accurate readout. In the *P-E* curve, the polarization at the highest applied *E*-field represents the maximum polarization that is achievable in the sample, noted as spontaneous polarization (P_s). The electric coercive field (E_c) is determined by dividing the switching voltage (x-axis intercept of the field) by the total thickness of the measured sample, which serves as a measure of the difficulty of switching the polarization direction. The y-axis intercept represents the remnant polarization (P_r) of the sample. A *P-E* hysteresis loop obtained from a 40-nm $BiFeO_3$ thin film on Nb:$SrTiO_3$ (001) and a 10-nm HfO_2 thin film sandwiched by TiN layers on p-Si (111) are shown in Figure 2.11.

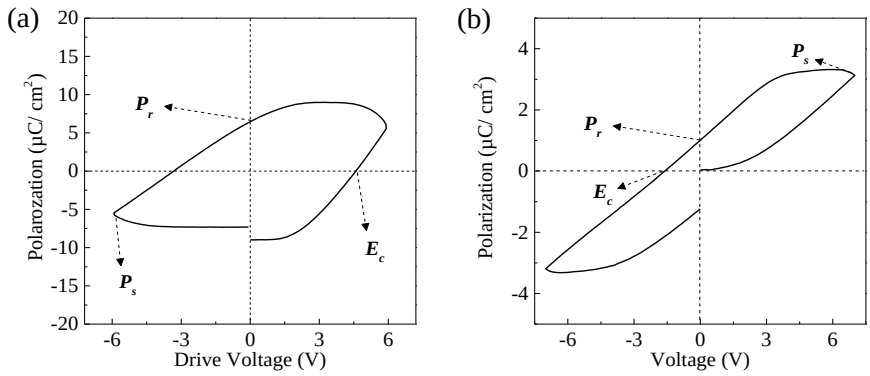

Figure 2.11 *P-E* hysteresis loop of (a) a 40-nm thick $BiFeO_3$ thin film on Nb:$SrTiO_3$ (001) substrate deposited via ALD. To promote crystallization, the sample were annealed at 650 °C for 1 minute under O_2 environment. (b) P-E loop of a 10-nm HfO_2 thin film sandwiched by 10-nm thick TiN layers on p-Si (111). The sample was annealed at 700 °C for 20 seconds under N_2 environment. Related ferroelectric parameters are indicated.

2.2.6. Scanning probe microscope

Scanning probe microscopy (SPM) techniques are important for sample surface characterization. All SPM modes are operating under a similar basis; hence the setups are similar. A typical SPM set up is shown in Figure 2.12. It mainly consists of three parts: a needle-like probe that scans over the sample surface, a laser beam that is reflected by the backside of the probe cantilever, and a photodiode detector that records the deflection of the reflected laser beam. During the measurement, the probe scans across the surface in a line-by-line manner, and the interactions between the sample surface and the SPM probe are recorded by the detector. SPM images are then constructed by merging the line scans together. Under this scheme, deflections within an angstrom can be measured, and images can be constructed with atomic resolution. In terms of tip engagement during measurements, two modes can be used, namely contact mode and tapping mode. In contact mode measurements, the SPM tip is constantly in mechanical contact with the surface, and the deflection is recorded to construct surface morphology. For tapping mode measurements, the SPM tip is oscillated at a certain frequency while tapping along the sample surface. Any deflection of the SPM tip results in a

change of the resonating frequency of the probe, where the deflection can be back-calculated with the help of a lock-in amplifier. In this section, under the SPM family, atomic force microscopy (AFM), piezoresponse force microscopy (PFM), and magnetic force microscopy (MFM), are discussed in detail.

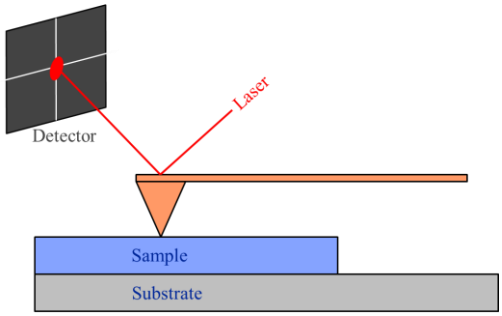

Figure 2.12 Schematic diagram of a SPM instrumental setup

AFM can probe the surface morphologies of a given sample by operating under the same principle mentioned above. During AFM measurements, the surface features lead to the elastic deformation of the tip cantilever during the scan, which changes the deflection path of the laser beam. The surface morphology is constructed by translating the beam deflection into height information. AFM measurements can be conducted either under contact mode or tapping mode; and tapping mode usually provides a better spatial resolution due to the incorporation of a lock-in amplifier. Since the tip is in mechanical contact with the sample surface, it is necessary to select suitable tip materials, such as SiC for hard materials, to prevent tip damage during the scans. However, if the tip itself is too hard, the sample surface may be damaged. Due to their high sensitivity and low operational cost, AFM measurements are widely adopted into different research fields including biological imaging and materials research. Sample AFM scans are shown in Figure 2.13.

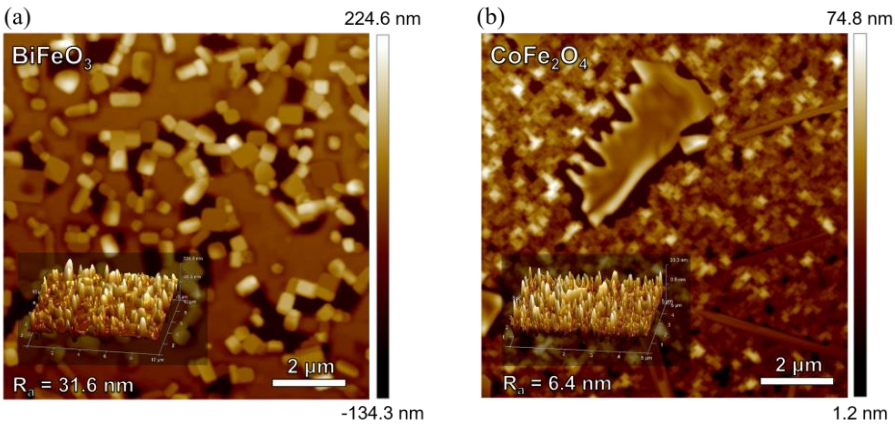

Figure 2.13 Atomic force microscopy (AFM) surface topography of a (a) 150-nm $BiFeO_3$ film and a (b) 15-nm $CoFe_2O_4$ film on $SrTiO_3$ (001) substrate after annealing at 750ºC for 1 minute under O_2 environment. Both scans show surface island formation. Insets are the corresponding isometric 3D mapping images.

Piezoelectric force microscopy (PFM) was used to observe the microscopic ferroelectric switching of the film. The main difference between AFM and PFM measurements is that for PFM measurements, conductive tips are utilized in contact mode and a voltage is applied across the sample surface. The sample film has to be grown onto a conductive substrate in order to provide good electrical contact. Conductive SCM-PIT tips (Veeco Instruments, Inc.) were used for the PFM measurements. The electric field generated by the applied voltage can cause a deformation through the piezoelectric effect in ferroelectric materials. Hence, the ferroelectricity can be identified by observing the remnant piezostrain and state after electrically poling the sample with sufficiently high voltages. Ramp mode measurements are conducted when the tip is held at one location. A voltage sweep can be applied through the PFM tip and can be used to generate a strain-voltage hysteresis loop when the sample is ferroelectric. PFM scans of a 90-nm thick $BiFeO_3$ film on Nb:$SrTiO_3$ (001) (wt% 0.7%) are shown in Figure 2.14.

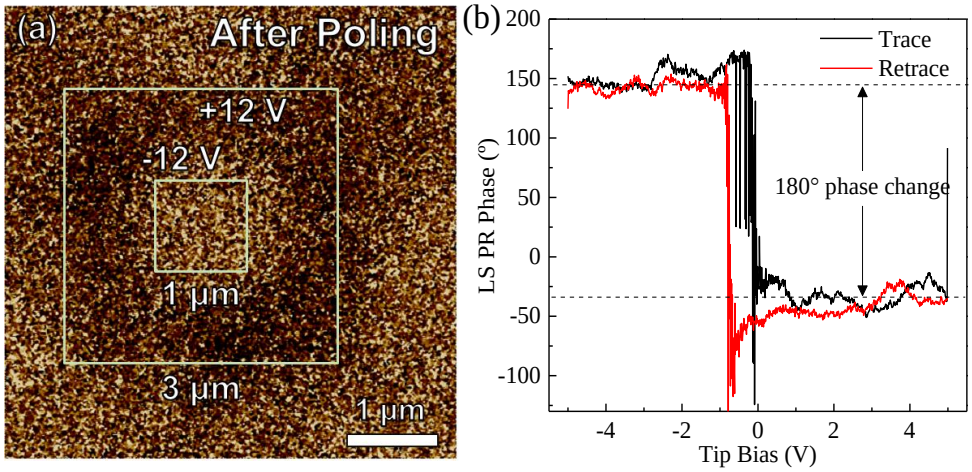

Figure 2.14 (a) PFM image of a 90 nm $BiFeO_3$ film on $SrTiO_3$ (001) substrate poled under +12 V and -12 V (adapted from (Pham 2015)). (b) PFM phase switching of the same $BiFeO_3$ film, showing an 180° switching under voltage sweep.

Magnetic force microscopy (MFM) is another mode of SPM techniques that can be used to observe magnetic domains of a material. MFM tips are coated with magnetic material with known magnetic properties. A MFM line scan consists of two passes: a tapping pass that is similar to AFM measurements, and a lifted tapping pass that is tens of nanometers above the sample surface. During the first pass, the sample surface morphology is recorded, while in the second pass the tip is lifted to a certain height and the morphology recorded in the first pass is mimicked during the scan. The interaction between the tip and the sample surface are then recorded and translated to visualize magnetic domains. The magnetic force, F, induced by the interaction between the sample and the tip can be expressed using the following equation:

$$F = m_0(m \cdot \nabla)H \tag{2.9}$$

where m, H, and μ_0 are the magnetic moment of the tip, stray field from the sample surface, and the magnetic permeability of free space, respectively. A sample MFM measurement of a $CoFe_2O_4$ thin film that captures the magnetic domain distribution is shown in Figure 2.15.

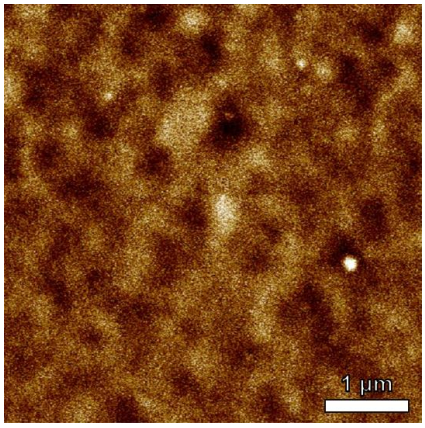

Figure 2.15 (a) MFM phase image of a 90-nm thick $CoFe_2O_4$ thin film on $SrTiO_3$ (001). The contrast in color represents different magnetic domains. The image inducates a grain-like domain structure with size of ~ 200nm. (Pham 2017)

Within the scope of this work, MFM has been used to observe the change in magnetic domains as a function of film thickness. Magnetic MESP tips (Veeco Instruments, Inc.) were used for the MFM measurements. Although MFM provides a straightforward and simple path in recording the magnetic domains, the fact that it relies on the magnetic interaction between the tip and the sample surface adds uncertainties since the sample magnetization may be altered by the MFM tip. In order to circumvent this problem, other magnetic characterization techniques, such as SQUID magnetometry, have been utilized as a complimentary approach for studying magnetic properties.

2.2.7. Superconducting quantum interference device magnetometry

Superconducting quantum interference device (SQUID) magnetometry is used to probe the magnetic properties of a given sample with high sensitivity in measuring magnetic flux. The threshold sensitivity of a SQUID device is up to one magnetic flux quantum, which can

be expressed as $\Phi_0 = h/2e \approx 2.0678\times10^{-15}$ tesla m^2. Φ_0 is the magnetic flux quantum, h is Planck's constant, and e is the charge of electrons.

A SQUID device consists of a pair of electromagnets for magnetizing the sample and several superconducting Josephson junctions in order to provide a quantized measure of the magnetic moments by the Josephson Effect. The Josephson junction has the ability to achieve superconductivity due to the tunneling of the Cooper pair of electrons through the junction without the help of an external electromagnetic field. Change in the superconducting currents is induced by the presence of a magnetic flux, which allows one to quantify the magnetic moment of a given sample. Based on the design, SQUID can be categorized into two types, DC and RF SQUID. Generally, DC SQUID loops have higher sensitivity but require two parallel Josephson junctions, while RF SQUID loops only need one Josephson junction but are less sensitive. A typical DC SQUID loop is comprised of a ring structure featuring two parallel Josephson junctions, which are a pair of superconductors separated by a non-superconducting material (shown in Figure 2.16).

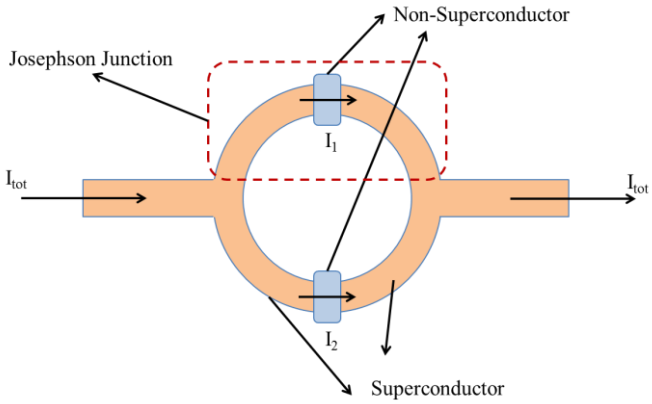

Figure 2.16 Schematic of a DC SQUID loop including two Josephson junctions

During SQUID measurements, a constant biasing current, I_{tot}, is maintained in the SQUID device, and the phase difference between the currents across the junctions, I_1 and I_2, generates a voltage across the SQUID loop that oscillates at a given frequency. When a magnetic flux is present within the SQUID coil, electromagnetic induction takes place,

generating a current flux around the loop itself. The current flux in turn changes the magnitude and phase of I_1 and I_2, and subsequently changes the frequency of the overall voltage. Therefore the change in magnetic flux can be back-calculated from the change in the oscillation of voltage.

In this work, SQUID measurements were performed with a MPMS (Magnetic Property Measurement System) XL tool made by Quantum Design. In the setup, the sample was placed between a pair of electromagnets, and moved up and down in order to generate inductive current for the magnetic flux measurement. The tool can apply an external magnetic field ranging from -5 T to +5 T. *M*-*H* magnetic hysteresis loops were obtained by conducting an *H*-field sweep to the sample while recording the change in magnetic flux. Since this instrument measures the entire moment passing through the SQUID coils, it is necessary to normalize the measured magnetic moment either by its volume, number of atoms, or mass. The saturation magnetization, M_s, illustrates how strong of a magnet the sample is, while the magnetic coercive field, H_c, describes how energetically favorable the magnetization is along a given measurement direction. A higher H_c value indicates a more stable magnetization. For example, by comparing the H_c values along different directions, one can determine in which direction the magnetic easy axis exists. Figure 2.17 shows the *M*-*H* magnetic hysteresis of a $CoFe_2O_4$ thin film, where the response is normalized by the volume of the sample. For extracting the magnetic parameters, M_r is the *y*-intercept of the hysteresis, H_c can be obtained by locating the *x*-intercept of the hysteresis, and M_s is the maximum value of the hysteresis along the *y*-axis where the slope of $dM/dH = 0$.

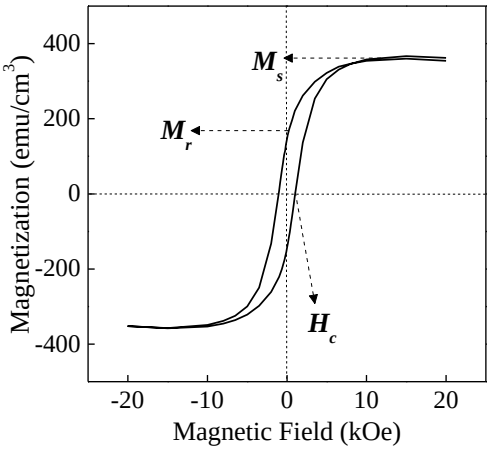

Figure 2.17 In-plane *M-H* magnetic hysteresis loops of a RE-ALD synthesized $CoFe_2O_4$ thin film of thickness ~90 nm. Magnetization values are normalized by the volume of the magnetic film. The measured $CoFe_2O_4$ thin film exhibits a comparable M_s with the values reported from its bulk form (~300-400 emu/cm^3) (Goldman 2006).

After the discovery of Josephson Effect and SQUID, the possibility of probing the local magnetic flux by a scanning SQUID device was soon recognized. However, since SQUIDs are intrinsically sensitive to the magnetic flux passing through the pickup area of the loop, the first two-dimensional scanning SQUID microscope with high enough sensitivity was not realized until 1983 by Rogers and Bermon at IBM Research (Kirtley 2010). The main challenge in achieving scanning SQUID devices is the competition between achieving a signal sensitivity and spatial resolution. A larger SQUID loop can yield a better signal sensitivity, but at the cost of image resolution. Therefore, it is important to design a suitable scanning SQUID structure/strategy for the given application.

Different approaches have been taken to optimize SQUID measurements. The first approach is to use an ultra-small SQUID sensor that can provide enhanced spatial resolution. This method has the advantage of simplicity since only one lithography process is required for the fabrication of the pick-up loops. However, the hysteretic current-voltage (*I-V*) relationship and weak sensitivity are the main drawbacks in actual measurements (Kirtley 2010).

Theoretically SQUID loops can be as small as ~370 nm. The second approach is achieved by using a self-aligned SQUID device, where three aluminum evaporations are made onto a quartz tube that has been pulled into a sharp tip with larger apex diameters. Although the process is more complicated than the first one, the elimination of the *I-V* hysteresis relationship and an improved flux sensitivity make it a superior choice for certain applications. The third approach is to make a more conventional SQUID with well shielded superconducting leads to a small pick-up loop integrated to it (Kirtley 2010). This could provide both acceptable spatial resolution and signal sensitivity due to a reduced interaction between the SQUID loop and the sample. The images of the fabricated devices are shown in Figure 2.18. However, multiple metal deposition/etching processes are required to realize this design which increases fabrication complexity. The shielding layers are implemented in order to reduce the interaction between the coil and its surroundings. A symmetric structure (shown in Figure 2.18 (a)) is needed in order to eliminate the noise coming from the background and to reduce unwanted electromagnetic resonances. With this setup, the scanning SQUID device can achieve a greater sensitivity while retaining acceptable spatial resolution.

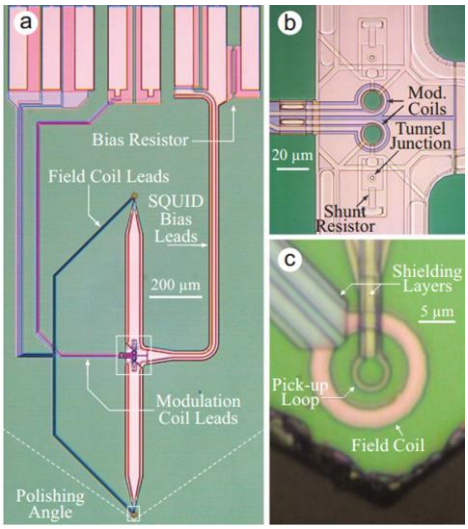

Figure 2.18 Photomicrograph of (a) the full scanning SQUID device with the shileding part attached, (b) the area near the center of the device, and (c) the close up view of the tip. (Huber 2008)

Although MFM could provide higher resolution, one main advantage of SQUID over MFM is the fact that the SQUID does not interact magnetically with the sample and therefore makes SQUID a desirable characterization technique for low coercive field magnets. Since scanning SQUID does not carry magnetization, the recorded magnetic domain structure can be claimed as the "real state". Figure 2.19 shows the scanning SQUID scan of a bi-layer $CoFe_2O_4/BiFeO_3$ composite, where the magnetic domains were mapped out. However, the main drawback for the scanning SQUID is that it is only operative under ultra-low temperatures (~4K), as cooling is needed for the superconducting Josephson Effect. Therefore, MFM and scanning SQUID are used as two complementary measurement techniques in probing microscopic magnetoelectric effects.

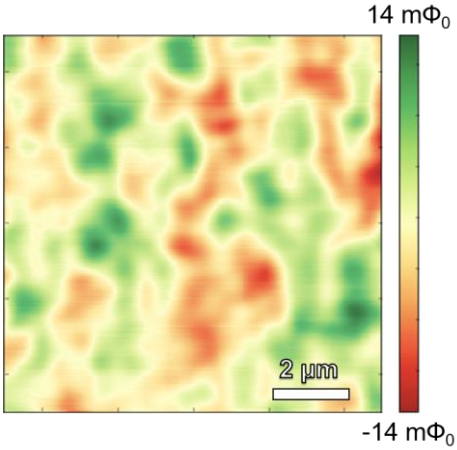

Figure 2.19 Magnetic domain structure of a bi-layer $CoFe_2O_4$ (15 nm)/$BiFeO_3$ (40 nm) composite obtained using scanning SQUID instrument. Constrast indicates different directions in magnetic dipole alignment.

2.3. Magnetoelectric Coupling Measurements and Data Analysis Methods

The magnetoelectric (ME) coupling coefficient $\alpha_{converse}$ provides insights into the strength of the interaction between the magnetic and ferroelectric degrees of freedom. The ME coupling coefficient can be determined by several methods (Zavaliche 2005, Eerenstein 2007, Thiele 2007, Evans 2013, Heron 2014). In this work, $\alpha_{converse}$ is primarily determined by

measuring the change in remnant magnetization (M_r) after electrical poling to provide a better perspective of device applications. Magnetoelectric coupling coefficients are usually expressed in the forms of s/m (SI units) or Oe cm/kV and are calculated using the following equations:

$$\alpha_{converse} = \frac{\Delta M_r}{\Delta E} = \frac{(M_{r,2} - M_{r,1})}{(E_2 - E_1)} \tag{2.10}$$

where $M_{r,2}$ represents the remnant magnetization under the application of electric field E_2, and $M_{r,1}$ corresponds to the remnant magnetization under the application of electric field E_1. Often times, $E_1 = 0$, and $M_{r,1}$ represent the remnant magnetization of an unpoled state.

2.3.1. Observation of ME coupling effects with imaging techniques

In this work, ME coupling was characterized microscopically via two different methods, combinatorial SPM measurements and poled scanning SQUID measurements. For SPM measurements, PFM and MFM are used in a combinatorial fashion to observe the local change of magnetic domains after the application of an electric field. Magnetic and conductive MESP tips (Veeco Instruments, Inc.) were used to minimize the variation in tip location when switching measurement modes. To obtain ME coupling effects, pristine magnetic domains were mapped using MFM within a 5×5 μm^2 area, followed by PFM poling scans. For PFM poling, scans were first conducted under +10 V within a 3×3 μm^2 area and a scan within the 1×1 μm^2 area under –10 V was performed subsequently to create a contrast in the ferroelectric states. The PFM scans are repeated three times for each condition to ensure a good degree of electrical poling. After the electrical poling scans by PFM, surface magnetic domains are recorded again using the MFM mode, and the contrast between different poling regions illustrates the ME coupling. Figure 2.20 shows the magnetic domains of a bi-layer $CoFe_2O_4/BiFeO_3$ nanolaminate on $Nb:SrTiO_3$ (001) substrate before and after PFM electrical poling, where the contrast between regions indicates ME coupling in the sample.

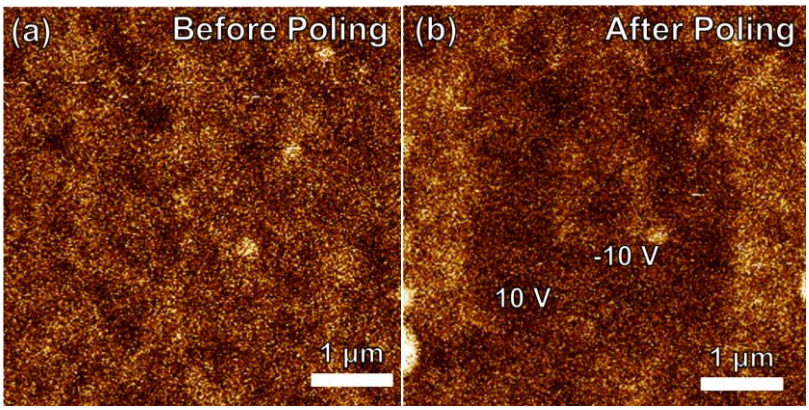

Figure 2.20 MFM magnetic domains (a) before and (b) after electrical PFM poling of a bi-layer $CoFe_2O_4$ (15 nm)/$BiFeO_3$ (40 nm) nanolaminate on Nb:$SrTiO_3$ (001) substrate. The contrast between different poling regions represents ME coupling.

The main drawback of the aforementioned method is the magnetic interaction between the MFM tip and the sample surface. In order to obtain an additional insight into the change of the magnetic behavior and to provide a cross-reference for the observation in MFM/PFM measurements, scanning SQUID magnetometer measurements are used as an alternative method while imaging the magnetic domains under electrical poling. A detailed discussion on scanning SQUID has previously been given in Section 2.2.7. Another advantage of the scanning SQUID technique is that it allows one to simultaneously bias the sample electrically with magnetic imaging; a schematic of the experimental setup is shown in Figure 2.21 (a). Averaged magnetic moments can be obtained by integrating the magnetic flux of all pixels in the obtained scanning SQUID image. Figure 2.21 (b) visualizes the change in averaged magnetism as a function of an applied *E*-field. However, since scanning SQUID measurement can only be conducted under cryogenic conditions (~4K), the reduced ferroelectricity in the measured sample can only result in a subtle change in the magnetic domains compared to MFM/PFM measurements. Therefore, the two measurements serve as complementary techniques in determining the microscopic ME coupling in the multiferroic composites.

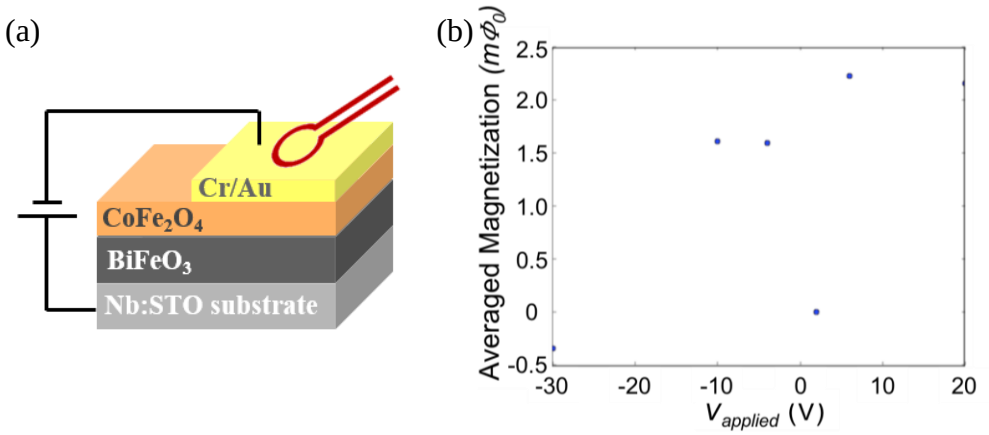

Figure 2.21 (a) Schematic of a scanning SQUID setup with electrical poling, measuring a bi-layer $CoFe_2O_4$ (15 nm)/$BiFeO_3$ (40 nm) sample. (b) Plot of the averaged magnetometry signal as a function of applied voltage, showing a magnetization that is altered by an applied electric field. Each data point represents the magnitude of the averaged magnetization across the whole scanning SQUID image by integrating the magnetic flux of all the pixels in it.

The converse magnetoelectric coupling coefficient, $\alpha_{converse}$, is quantified by monitoring the change in magnetic parameters as a function of an applied electric field and incorporating the observed change into Equation (1.8). After the application of an electrical field, the magnetic hysteresis loops of a magnetoelectric multiferroic are twisted due to the interfacial coupling between the ferroelectric and magnetic phases, therefore changing the magnetic anisotropy as well as overall magnetization. Although some groups observe the magnetization values under a weak external *H*-field for the ease of enhancing magnetometer readouts (Eerenstein 2007), this work uses M_r solely for the quantification of $\alpha_{converse}$ values with magnetization.

In this work, in order to observe the change in M_r after the application of electric fields, an *ex situ* electrical poling setup is utilized for biasing the sample prior to SQUID measurements. A schematic of the poling setup is provided in Figure 2.22 (a). In this setup, the sample of 5×5 mm^2 in areal size is sandwiched by two aluminum electrode rods (d = 1.28 cm), and the top surface is covered by a polymer protective spacer (polyvinylidene chloride, t = 12.7 μm). After insertion, the sample is electrically poled with a DC voltage along the out-of-plane

direction for 10 minutes followed by a subsequent SQUID measurement at room temperature. The SQUID measurement is performed by a Quantum Design MPMS SQUID magnetometer. The aforementioned step is then repeated under different voltages. The result is plotted as Figure 2.22 (b). The change in magnetization values as well as the *M*-*H* loop shape change are expected due to the magnetoelectric nature of the measured samples. The observed change in M_r as well as the corresponding *E*-fields are inserted into Equation (1.8) for quantifying $\alpha_{converse}$ values. In terms of unit conversion, 1×10^{-7} s/m = 100 Oe cm/kV can be used for the ease of comparing $\alpha_{converse}$ values reported in other literature.

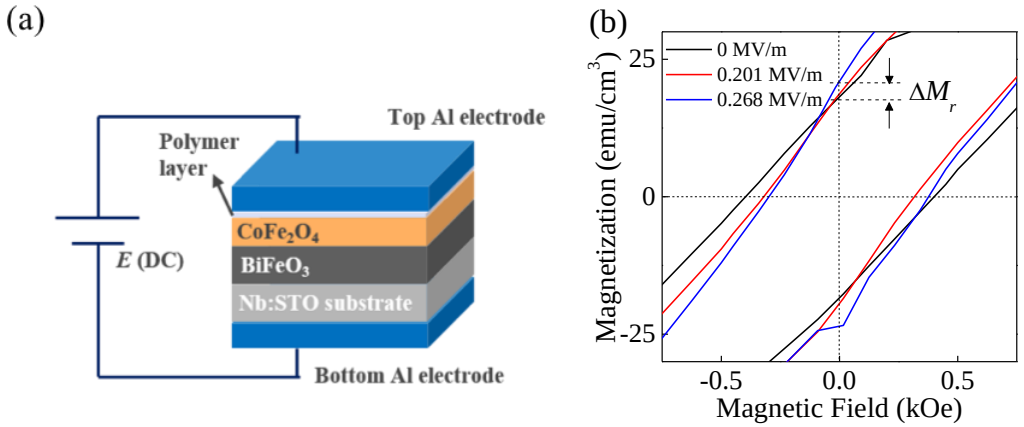

Figure 2.22 (a) Schematic of the *ex situ* electrical poling setup with $CoFe_2O_4$/$BiFeO_3$ nanolaminate. (b) Zoomed-in SQUID hysteresis of a tri-layer $BiFeO_3$ (20 nm)/$CoFe_2O_4$ (15 nm)/$BiFeO_3$ (20 nm) under different applied *E*-fields. The shape change indicates converse magnetoelectric coupling and $\alpha_{converse}$ can be quantified using ΔM_r.

Chapter 3. Synthesis and Characterization of $BiFeO_3$ and $CoFe_2O_4$ by Radical-Enhanced Atomic Layer Deposition

As the building blocks for composite integration, the synthesis by radical-enhanced atomic layer deposition (RE-ALD) and characterization of respective $BiFeO_3$ and $CoFe_2O_4$ were investigated. As the building blocks for the complex oxides, RE-ALD of Fe_2O_3, Bi_2O_3, and CoO were achieved by utilizing metalorganic $Fe(TMHD)_3$, $Bi(TMHD)_3$, and $Co(TMHD)_2$ precursors respectively while atomic oxygen was used as the oxidant. The ALD temperature window and growth rates were confirmed, showing optimized processing temperatures of 200 °C and 210 °C for $CoFe_2O_4$ and $BiFeO_3$ respectively.

RE-ALD of $CoFe_2O_4$ and $BiFeO_3$ were realized by incorporating the RE-ALD processes of the constituent oxides in a sequential manner on $SrTiO_3$ (001) substrates. Specific ALD cycling ratios were optimized to attain a stoichiometric complex oxide film. To achieve film crystallization, a post-deposition thermal annealing step was required to provide the needed energy for atomic rearrangement. A textured-polycrystalline growth was observed for $CoFe_2O_4$ thin films, while $BiFeO_3$ showed a single-crystalline epitaxial growth on $SrTiO_3$ (001). $CoFe_2O_4$ thin films showed tunable magnetic properties with M_s ranging from 260-550 emu/cm^3 and H_c from 0.2-2.2 kOe, both of which are comparable to $CoFe_2O_4$ films synthesized by other deposition techniques and bulk crystal. $BiFeO_3$ thin film exhibits a P_r value of ~7.5 μC/cm^2 with ferroelectric switching confirmed via PFM, and a M_s value of ~20-30 emu/cm^3. The results presented here demonstrated the potential of RE-ALD to synthesize high-quality functional oxides for multiferroic composite integrations.

3.1. RE-ALD of Fe_2O_3, Bi_2O_3, and CoO

Film thicknesses and growth rates are usually the first topics to discuss in ALD processes. RE-ALD of Fe_2O_3, Bi_2O_3, and CoO were conducted on Si (100) substrates using

metalorganic β-diketonate precursors $Fe(TMHD)_3$, $Bi(TMHD)_3$, and $Co(TMHD)_2$ as the cation sources respectively, while atomic oxygen generated by a coaxial microwave cavity beam source serves as the oxidant. The thicknesses of the deposited films were obtained by optical ellipsometry. The ellipsometry data and fitting, as well as the parameters used for the Lorentz oscillator model are listed in Table 2.6. The model fittings agreed well with the obtained Ψ and Δ data, shown in Figure 2.8.

In order to achieve complex oxide ALD process, it is critical to ensure that the ALD temperature windows of the constituent oxides are overlapping to prevent additional temperature adjustments in between local ALD cycles. Figure 3.1 (a) shows the ALD growth rates of the three binary oxides as a function of processing substrate temperature ranging from 190-230 °C. For all the data points, the number of cycles was fixed at 100 and the growth rates were calculated by dividing the measured thicknesses with the number of cycles. For the ALD windows, Bi_2O_3 showed a stable growth regime between 200°C~210°C, while Fe_2O_3 and CoO both showed stable growth over the entire range. Compared to the thermal ALD reports that utilize either O_3 or H_2O as the oxidants, the growth windows for all three oxides all shifted lower due to the higher chemical reactivity of atomic oxygen. A comparison is shown in Table 3.1. This investigation reveals proper temperature windows of 190-230 °C for $CoFe_2O_4$ and 200-210 °C for $BiFeO_3$. As a result, the following RE-ALD for $CoFe_2O_4$ and $BiFeO_3$ were conducted under 200 °C and 210 °C, respectively.

It is also necessary to determine the effect of precursor pulse time upon the growth rate given the self-limiting nature of ALD processing. This investigation helps assess the ability of the developed ALD processes in conformally depositing over nonplanar (three-dimensional (3D) or not in line-of-sight) surfaces. The thicknesses of the three binary oxides on Si (001) after 100 ALD cycles as a function of precursor pulse time are shown in Figure 3.1 (b). Fe_2O_3

and CoO samples were grown at 200 °C, while Bi_2O_3 films were grown at 210 °C. All the samples showed a self-limiting growth profile and the data indicated that a 90 s precursor pulse time is sufficient for all three precursors to reach saturation.

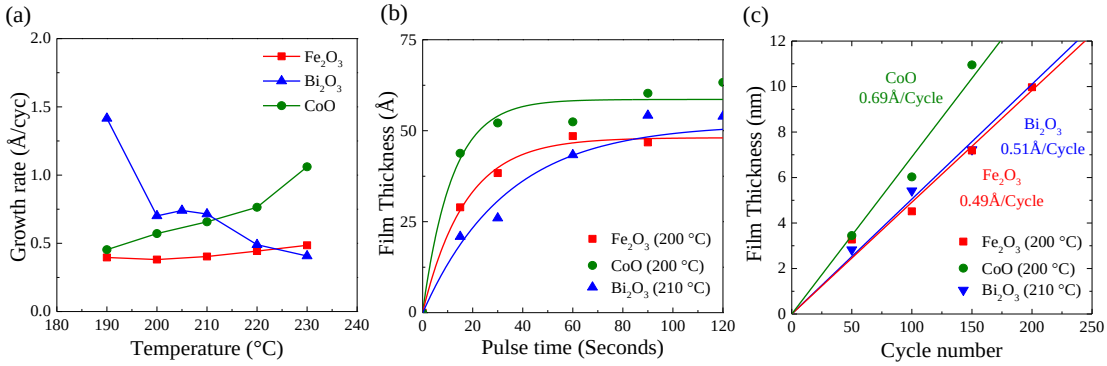

Figure 3.1 ALD growth profiles of Fe_2O_3, Bi_2O_3, and CoO. (a) Growth rate versus substrate temperature, (b) thickness profile as a function of precursor pulse time, and (c) thickness profile as a function of ALD cycle numbers.

Table 3.1 List of different ALD parameters of Fe_2O_3, Bi_2O_3, and CoO

Metal Oxide	Oxidant	ALD window (°C)	Growth Rate (Å/Cycle)	Ref.
Fe_2O_3	O	190-230	0.49	This work
	O_3	160-210	0.124	(Lie 2005)
	H_2O	250	0.04	(Zhang 2013)
Bi_2O_3	O	200-210	0.51	This work
	H_2O	270-300	0.07-0.1	(Shen 2012)
CoO	O	190-230	0.69	This work
	O_3	114-307	0.2	(Klepper 2007)

Figure 3.1 (c) shows the ALD growth curve of all three binary oxides, where the resulted film thickness is plotted as a function of the number of ALD cycles conducted. All the data points were obtained with a precursor pulse time of 90 s. According to the slope of the fitted curves, the growth rates of Fe_2O_3, Bi_2O_3, and CoO are 0.5, 0.5, and 0.7 Å/cycle, respectively, with no apparent incubation period for precursor absorption. In addition, by comparing to other literature values obtained via thermal ALD, the work here demonstrated a substantially higher growth rates, illustrating highly-efficient RE-ALD processes.

3.2. Growth Characterization of $BiFeO_3$ Synthesized by RE-ALD

$BiFeO_3$ films, as the ferroelectric phase of the proposed composite design, were deposited onto $SrTiO_3$ (001) substrates by conducting alternating Fe_2O_3 and Bi_2O_3 ALD depositions at 210 °C. $SrTiO_3$ (001) has a cubic structure (a = 3.9 Å, PDF: 086-0178) that is closely matched to the $BiFeO_3$ in its $(001)_{pc}$ orientation (a_{pc} = 3.96 Å, PDF: 071-2494), which favors the epitaxial stabilization of the ALD-deposited $BiFeO_3$ films after thermal annealing.

In order to achieve a desired Fe:Bi stoichiometry, the RE-ALD of ternary oxide, $BiFeO_3$, is achieved by sequentially pulsing the constituent metalorganic precursors in a supercycle fashion that includes a numbers of cycles $Fe(TMHD)_3$:O and b numbers of cycles of $Co(TMHD)_2$:O. By altering a and b, the overall cation composition in the resulted $BiFeO_3$ thin film can be controlled for optimization of its functional properties. A stoichiometric Fe:Bi ≈ 1:1 ratio is shown to exhibit the best properties (Puttaswamy 2016). XPS analysis was used in determining the atomic ratio between Fe^{3+} and Bi^{3+} ions. Figure 2.3 (a) shows the XPS survey scan of a 100-nm $BiFeO_3$ film with a ALD super sequence of 7[$Fe(TMHD)_3$:O] + 2[$Bi(TMHD)_3$:O], verifying the existence of the constituent atoms. Figure 2.3 (b) and (c) shows the fitted XPS detailed spectra for Fe *2p* and Bi *4f*, where the shape and position of the observed XPS peaks verifies the oxidation states of Fe^{3+} and Bi^{3+}.The Fe^{3+}:Bi^{3+} cation ratio is determined to be very close to 1:1 by integrating the area underneath the XPS characteristic peaks. The carbon content is calculated to be ~15-20%, which is consistent with a prior research publication that used the same experimental setup (Van 2005), highlighting the high-quality of the presented RE-ALD process for $BiFeO_3$. Figure 3.3 shows the resulted film thickness of the stoichiometric $BiFeO_3$ on $SrTiO_3$ (001) substrates as a function of the number of supercycles, exhibiting a linear correlation without apparent incubation period. By extrapolating the slope of the fitted curves, the growth rate of $BiFeO_3$ on $SrTiO_3$ is determined to be ~3.3 Å/supercycle.

The obtained growth rate is seven times higher than the $BiFeO_3$ films synthesized by another thermal ALD processes with the same metalorganic precursors (Zhang 2013), highlighting the increase in process efficacy by incorporating atomic oxygen as oxidants.

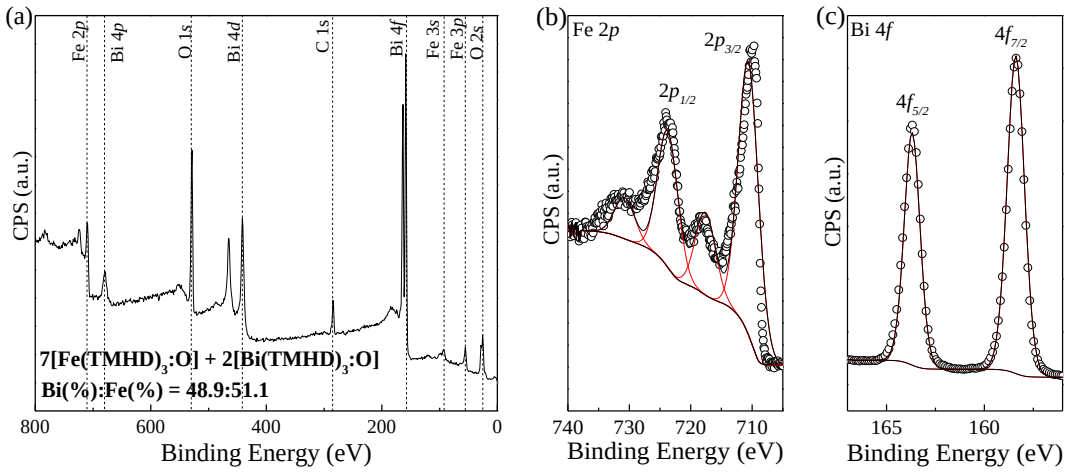

Figure 3.2 (a) XPS survey scan from 800 – 0 eV of a 100 nm stoichiometric $BiFeO_3$ thin film. Detailed and fitted XPS spectra for (b) Fe 2*p* and (c) Bi 4*f* photoelectron peaks. Symbol represents obtained spectra while the lines represent the fitting curves as well as backgrond. The measured film showed a stiochiometric Fe^{3+} to Bi^{3+} ratio very close to 1:1. (Adapted from (Pham 2015))

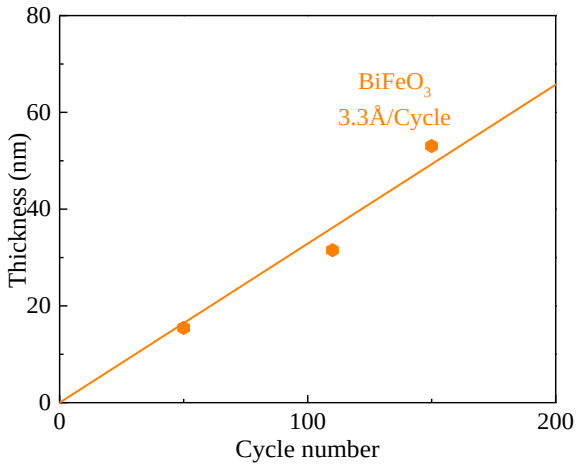

Figure 3.3 Stiochiometric $BiFeO_3$ thickness on $SrTiO_3$ (001) as a function of the sypercycle numbers. $BiFeO_3$ growth rate of 3.3 Å/supercycle was obtained by the slope of a linear regression-fit line.

Since the processing temperature of ALD is relatively low compared to other thin film synthesis techniques, post-deposition thermal annealing is necessary to promote the crystallinity of the as-deposited ALD film. It is worth noting that the annealing condition may

also promote the growth of undesired parasitic phases, damaging film quality or decreasing its functionality. To promote film crystallinity, the as-deposited $BiFeO_3$ thin films were annealed by rapid thermal anneal (RTA) subsequently after growth for 1 minute under an oxygen purge (~5 sccm) over a range of temperatures (450-750 °C). A temperature ramp of 50 °C/sec was used. Oxygen gas was purged into the chamber during the annealing process. Film crystallinity, phase purity, orientation, and texture were then analyzed as a function of the RTA temperature by XRD analysis. Figure 3.4 shows the XRD θ-2θ spectra of the 50-nm $BiFeO_3$ thin films with different annealing temperatures, as well as the bare $SrTiO_3$ (001) substrate. The absence of $BiFeO_3$ reflection peaks from the as-deposited and 450 °C-annealed samples indicates an insufficient thermal energy for $BiFeO_3$ crystallization. However, the presence of α-Bi_2O_3 012 (PDF 71-2274) peak in those two conditions indicates low-temperature crystallization of the constitutional Bi_2O_3 phase, which has also been observed in literature in a separate study (Shen 2012).

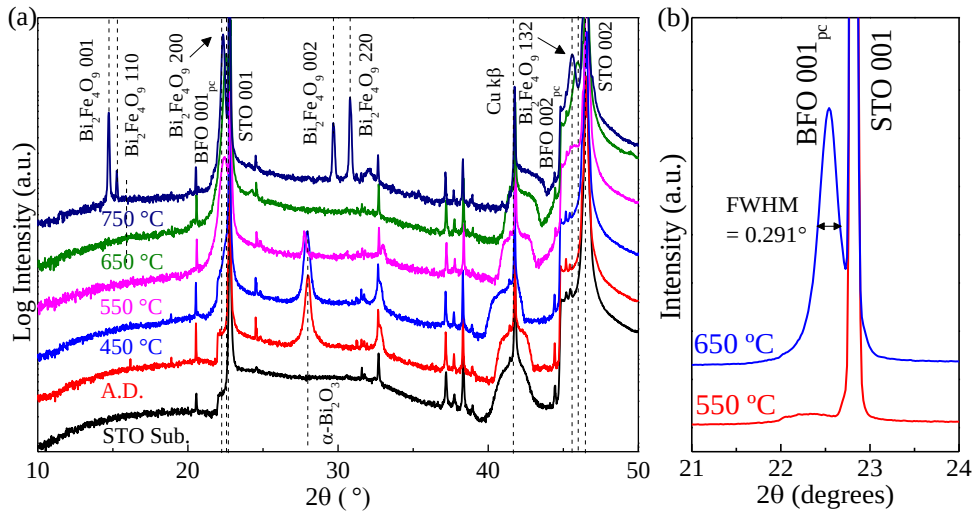

Figure 3.4 (a) XRD spectra of $BiFeO_3$ films on $SrTiO_3$ substrate (001) with varying annealing temperatures (as labeled); film annealed at 550 °C shows onset of $BiFeO_3$ (001) crystallinity while film annealed at 750 °C indicates the formation of parasitic $Bi_2Fe_4O_9$ phases. (b) Zoomed-in XRD spectra of the 550 and 650 °C-annealed samples (Adapted from (Pham 2015)).

At higher RTA temperatures (above 550 °C), the extinction of α-Bi_2O_3 012 peaks and emergence of the family of $BiFeO_3$ 001_{pc} reflections indicates the formation of $BiFeO_3$ $(001)_{pc}$ phase, which is owing to the structural similarity and small lattice mismatch between $SrTiO_3$ (001) and $BiFeO_3$ $(001)_{pc}$. In addition, the BFO reflection became more prominent and narrower with higher temperatures and reached maximum intensity at 650 °C-annealing, indicating the evolution of $BiFeO_3$ crystals with increased annealing temperature. Figure 3.4 (b) shows a zoomed-in comparison between the BFO 001_{pc} peak from the 550 and 650 °C annealed samples. By using the Scherrer equation on the 650 °C-annealed sample, the size of the $BiFeO_3$ crystal grains along the *c*-axis was calculated to be ~30 nm which is similar to the expected film thickness, indicating high-quality $BiFeO_3$ growth after RTA at 650 °C. However, for the 750 °C-annealed sample, the emergence of the family of $Bi_2Fe_4O_9$ (PDF 025-0090) reflections implies a phase transformation that is likely related to bismuth volatilization. Since $Bi_2Fe_4O_9$ can contribute to a greater electrical leakage and impede ferroelectric properties in the sample (Hu 2015), it is critical to prevent its formation during the post-deposition annealing step. The optimized annealing temperature range is between 550 and 650 °C.

AFM measurements were performed to further understand how the structural transitions affect surface topographies. The average deviation R_a of the surface topography height image is used as an indicator for the surface roughness at the nanoscale. To probe the evolution of surface roughness (R_a) with increasing annealing temperature, 5×5 μm^2 AFM scans were conducted on the annealed 50-nm $BiFeO_3$ thin films. Figure 3.5 (a) exhibits extracted R_a values of the acquired AFM scans as a function of sample annealing temperature. The as-deposited $BiFeO_3$ thin film has a R_a of 0.17 nm (denoted by the dashed line in Figure 3.5 (a)), verifying the atomically smooth surface from ALD processing. The R_a value increases to 0.52, 2.34, and 3.40 nm for the samples annealed at 450 °C, 550 °C, and 650 °C, respectively,

and drastically increased to 31.6 nm for the 750 °C-annealed sample. This result suggests a trade-off between $BiFeO_3$ crystallinity and surface smoothness due to the surface island formation during thermal treatments. The drastic increase in R_a from the 750 °C-annealed sample was resulted from the drastic surface island formation, shown in Figure 3.5 (b). By referencing the XRD results presented in Figure 3.4 (a), those islands are likely the $Bi_2Fe_4O_9$ phases that formed after 750 °C-anneal.

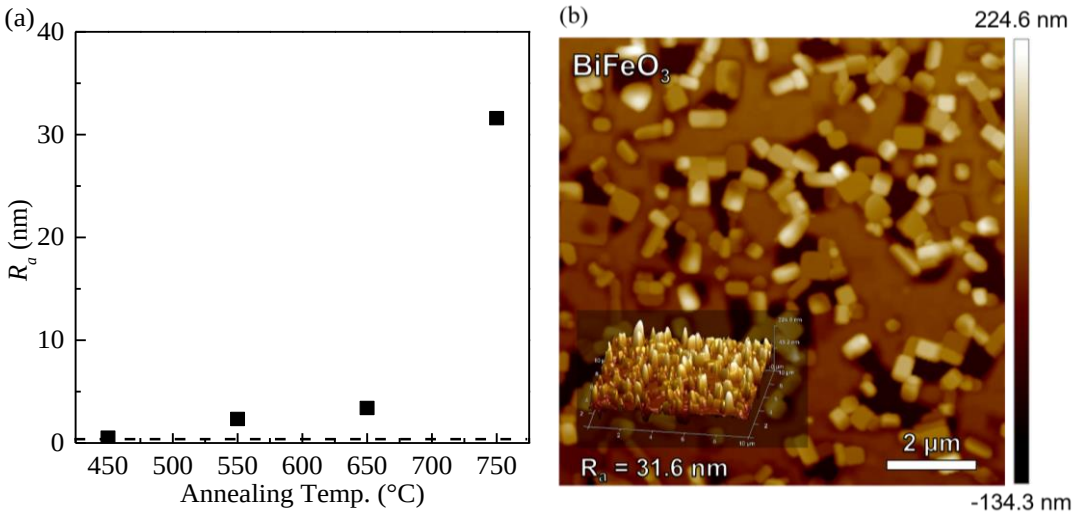

Figure 3.5 (a) Surface R_a values of annealed $BiFeO_3$ thin films of 50 nm thickness on $SrTiO_3$ (001) substrates as a function of annealing temperatures. Ra values are extracted from 5×5 μm^2 AFM topography scans. Dashed line denotes R_a for the as-deposited sample. (b) AFM surface topography image of 750 °C annealed sample, showing an intensified surface island formation. Inset shows an isometric 3D map of the same data.

TEM analysis was used to further characterize the crystal orientation as well as the $BiFeO_3/SrTiO_3$ interface of a 650 °C-annealed $BiFeO_3$ sample of ~90 nm thickness on $SrTiO_3$ (001). Figure 3.6 (a) and (b) showed the zoomed-in and zoomed-out cross-sectional TEM images respectively. Although the lattice mismatch between two phases (3.96 Å and 3.9 Å for $BiFeO_3$ and $SrTiO_3$ respectively) leads to a compressive strain on $BiFeO_3$, no secondary phases were detected by either diffraction or imaging, and it was clear that the examined $BiFeO_3$ thin film is single-crystalline. It is believed that the heteroepitaxial stabilization of $BiFeO_3$ $(001)_{pc}$ is a result of the low mismatch degree (~1.5%) between the two phases. To further compare

with the XRD analysis, SAED analysis was employed. The SARD scans were taken near the $BiFeO_3/SrTiO_3$ interface and the corresponding result is shown in Figure 3.6 (c). $BiFeO_3$ has a *R3c* crystal structure, and peak splitting to the growth-twin domains are clearly visible, shown in the inset of Figure 3.6 (c) for a 006_{pc} reflection. The growth-twin domains are due to the pseudocubic cells of which the corners are displaced relative to a perfect cubic structure ~0.38° along $\langle 110 \rangle_{pc}$ (0.27° along $\langle 100 \rangle_{pc}$ and ~0.27° along $\langle 010 \rangle_{pc}$). By using $SrTiO_3$ pattern as a reference, the out-of-plane $BiFeO_3$ $(001)_{pc}$ lattice parameter was estimated to be 3.987 Å, which is larger than its normal value of 3.96 Å, confirming the in-plane compressive strain caused by the $SrTiO_3$ substrate.

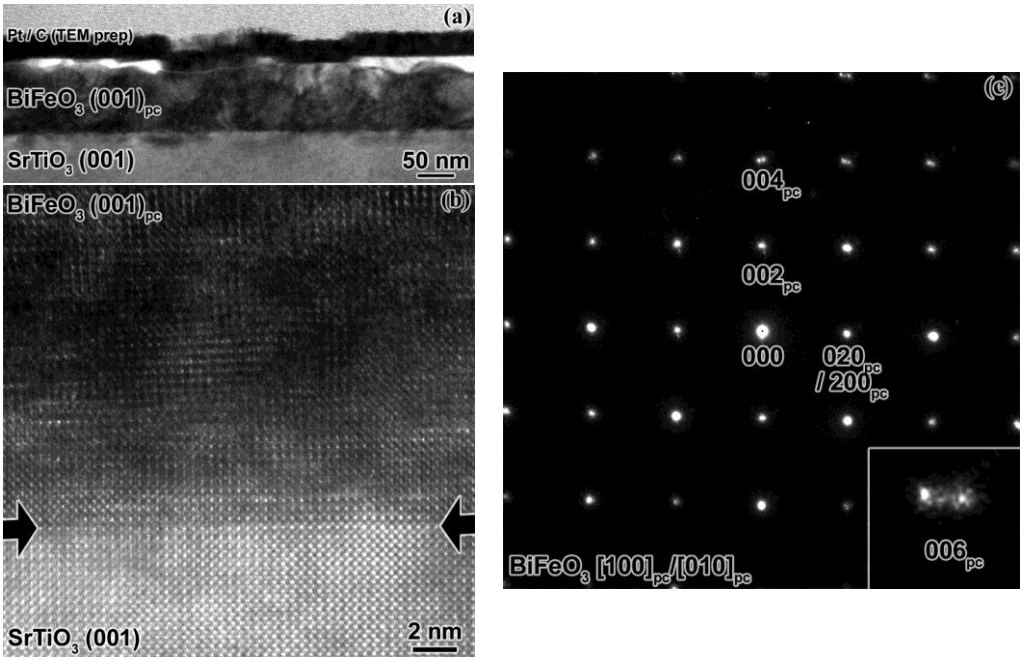

Figure 3.6 (a) Zoomed-in and (b) zoomed-out TEM image of epitaxial $BiFeO_3$ film annealed at 650 °C on $SrTiO_3$ (001) substrate. The arrows indicate the $BiFeO_3/SrTiO_3$ interface. (c) Selective area electron diffraction pattern of the $BiFeO_3$ film, showing a highly-oriented single crystal structure. Inset shows the inlarged 006_{pc} reflection, indicating the growth of twin domains. (Pham 2015)

In summary, single-crystalline epitaxial growth of $BiFeO_3$ thin film on $SrTiO_3$ (001) with a pseudocubic-on-cube orientation was achieved by incorporating RE-ALD processing and a post-deposition RTA step at 650 °C. Since the functional properties depend strongly on

its crystal structure, the synthesis of high-quality single-crystalline $BiFeO_3$ thin films with RE-ALD demonstrates promising prospects for the development of multiferroic complex oxides.

3.3. Multiferroic Properties of $BiFeO_3$ Thin Films

After the high-quality growth of $BiFeO_3$ thin films by RE-ALD is confirmed, it is necessary to characterize its functional properties for comparison and cross-referencing with other works on ALD of $BiFeO_3$ thin films. For electrical measurements, 40-nm thick $BiFeO_3$ thin film was deposited onto conductive Nb:$SrTiO_3$ (001) (0.7 wt%) substrates. The sample was synthesized with the same RE-ALD protocol described in the previous section with a RTA step at 650 °C. To form a capacitor, circular Au (100 nm)/Cr (10 nm) top electrodes (dia. = 250 μm, area ≈ 0.00049 cm^2) were deposited onto the top surface of the $BiFeO_3$ sample via electron-beam (e-beam) evaporation, while the Nb:$SrTiO_3$ (001) substrate served as the bottom electrode. The Au/Cr top electrodes were patterned by incorporating a shadow mask during e-beam evaporation.

P-E ferroelectric hysteresis loop of the 40-nm thick $BiFeO_3$ thin film was obtained using a probe station with a DC voltage (scanning rate = 0.1ms), shown in Figure 3.7 (a). The sample exhibited a P_s value of ~7.5 μC/cm^2 and an E_c of ~650kV/cm^3. Although the polarization values are much lower than the $BiFeO_3$ thin films synthesized via pulsed-laser deposition (~100 μC/cm^2) (Wang 2003), it is higher when compared with other literature reports on $BiFeO_3$ thin films via thermal ALD processing (~0.1-5 μC/cm^2) (Liu 2014, Marchand 2016, Puttaswamy 2016). It is worth noting that the *P-E* hysteresis result here is obtained from a 40-nm thick $BiFeO_3$ while most of the other *P-E* results in the other literature reports are obtained from $BiFeO_3$ thin films that are >100 nm in thickness (Wang 2003, Yang 2005, Lee 2007, Zheng 2008, Puttaswamy 2016). This highlights the high-quality nature of the presented RE-ALD processing for minimizing the leakage current for ultra-thin $BiFeO_3$ films.

To verify the ferroelectric switching, PFM is performed on the bare substrate surface. During the PFM scans, a total area of 5×5 μm^2 was imaged after electrically poling the 3×3 μm^2 area with +12 V and the 1×1 μm^2 area with -12 V in a sequential fashion through the conductive scanning tip. The resulted PFM phase image is presented as the inset of Figure 3.7 (a), while the phase contrast in between different poling regions indicates non-volatile ferroelectric switching behaviors.

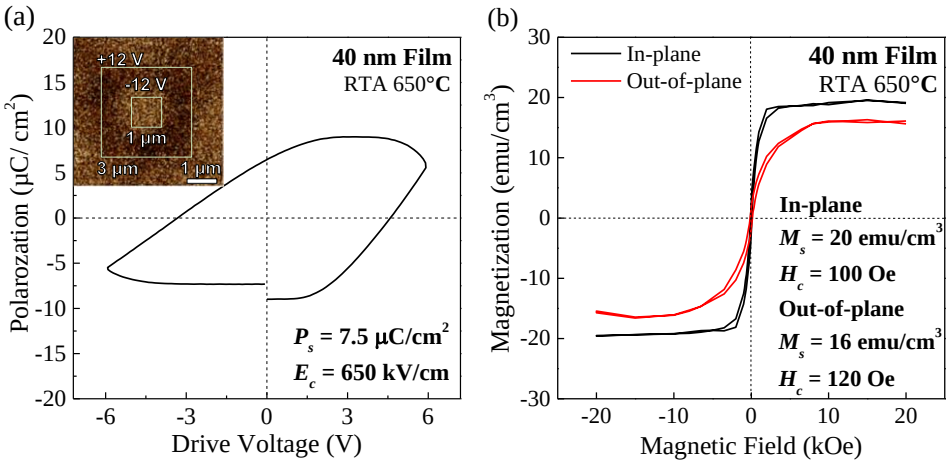

Figure 3.7 (a) P-E hysteresis of a 40-nm thick $BiFeO_3$ thin film after RTA at 650 °C. The inset shows PFM phase image of the $BiFeO_3$ film, different squares within the 5×5 μm^2 scanning area corresponds to different electrical poling regime. (b) *M-H* magnetic hysteresis loop of the same sample under room-temperature, showing weak ferromagnetism rooting from antiferromagntic spin canting. (PFM and *M-H* hysteresis adapted from (Pham 2015)).

Figure 3.7 (b) is the room-temperature *M-H* magnetic hysteresis loop of the same $BiFeO_3$ film obtained by a SQUID magnetometer, showing weak ferromagnetism due to antiferromagnetic spin canting (Dzyaloshinsky 1958, Moriya 1960, Marchand 2016). M_s and H_c values were found to be ~20 emu/cm^3 and ~0.11 kOe respectively, comparable with other literature reports on BFO thin films synthesized via thermal ALD (Jalkanen 2014, Marchand 2016).

In summary, stoichiometric $BiFeO_3$ thin films synthesized via RE-ALD exhibits a high-quality single-crystalline epitaxial growth on $SrTiO_3$ (001) substrates after a post-deposition

thermal annealing step at 550-650 °C in O_2 for 60 s. The use of highly reactive atomic oxygens as the oxidant not only help achieved superior growth rates (~3.3 Å/supercycle), but also yielded a substantially higher functional properties (P_r ~7.5 μC/cm^2, M_s ~20 emu/cm^3) when compared to the $BiFeO_3$ thin films synthesized via thermal ALD processing. However, the weak ferromagnetism in $BiFeO_3$ has limited its applicability in magnetoelectric devices, therefore the next step for composite integration is to develop the magnetic phase, $CoFe_2O_4$.

3.4. Growth Characterization of $CoFe_2O_4$ Thin Films Synthesized by RE-ALD

Ternary ferrimagnetic $CoFe_2O_4$ thin films were synthesized onto $SrTiO_3$ (001) substrate using a RE-ALD process that is similar to the one described for $BiFeO_3$ synthesis. The constituent $Fe(TMHD)_3$ and $Co(TMHD)_2$ precursors were pulsed in a supercycle sequence of a[$Fe(TMHD)_3$:O] + b[$Bi(TMHD)_3$:O], where a and b are the local cycling numbers. By tuning a and b, the Fe^{3+}:Co^{2+} stoichiometry in the deposited thin films can be controlled. Fe^{3+}:Co^{2+} cation ratio have a pronounce influence to the magnetic properties in $Co_xFe_{3-x}O_4$ thin films, and it is shown that a film stoichiometry of Fe^{3+}:Co^{2+} ≈ 2:1 leads to maximized magnetic and magnetostriction behaviors (Bozorth 1955, Chong 2010). If the $CoFe_2O_4$ films were nonstoichiometric, depending on the level of deviation, the overall magnetic strength as well as coercivity would decrease due to the antiferromagnetic nature of the Fe_2O_3 and CoO impurities (Chong 2010).

XPS analysis is utilized in order to identify desirable a and b values for synthesizing stoichiometric $CoFe_2O_4$ thin films by the RE-ALD process. For the XPS compositional analysis, the ternary oxide thin films were deposited onto Si (001) substrates for the ease of sample handling. All the measured ternary oxide films are synthesized with 100 supercycles at a substrate temperature of 200 °C. The cation composition in the film is quantified by integrating and comparing the areas of the fitted Fe *2p* and Co *2p* XPS detailed scan spectra.

Figure 3.8 (a) shows the the ternary film composition as a function of the precursor pulsing ratio, demonstrating the ability to control stoichiometry by ALD. Film stoichiometry of Fe^{3+}:Co^{2+} = 2:1 was achieved at a ALD cycling ratio of *a*:*b* = 5:1. According to the XPS characterization of the synthesized $CoFe_2O_4$ thin films, the averaged stoichiometric number for Fe^{3+} and Co^{2+} is ~1.97 (65.7%) and ~1.03 (34.3%), respectively, with a standard deviation σ of 1.3%, which is at the resolution of the XPS analysis and thus indicates a highly reproducible and well-controlled film composition with RE-ALD. Figure 3.8 (b) and (c) show the fitted XPS detailed spectra of Fe *2p* and Co *2p*, respectively, confirming the oxidation states of the cations. The RE-ALD process was migrated onto $SrTiO_3$ (001) substrates with the process parameters optimized, and the XPS analysis also showed a Fe^{3+}:Co^{2+} = 2:1 stoichiometry. The growth curve of $CoFe_2O_4$ thin films are shown as the inset of Figure 3.8 (a), with a linear growth profile that is specific to ALD processing. The growth rate was determined to be 2.4 Å/supercycle by fitting the slope of the linear regression line. It is worth noting that the growth rate was ~5-6 times higher than the thermal ALD processes of $CoFe_2O_4$ using O_3 as oxidants (~0.4-0.5 Å/supercycle) (Chong 2010, Coll 2014).

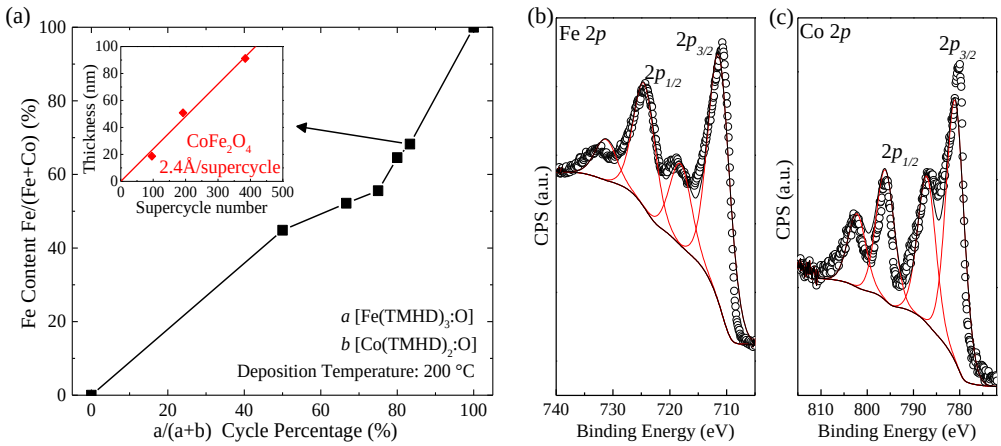

Figure 3.8 (a) Iron cation percentage Fe/(Fe+Co) (%) in $CoFe_2O_4$ films as a function of the ALD dosing ratio between the two metalorganic precursors for the growth on Si (001) substrates. The inset in (a) shows the stoichiometric $CoFe_2O_4$ thicknesses on $SrTiO_3$ (001) as a function of the supercycle numbers. The $CoFe_2O_4$ growth rate was obtained by the slope of a linear regression-fit

line. Fitted detailed XPS spectra for (b) Fe 2*p* and (c) Co 2*p*. (Adapted from (Pham 2017))

Post-deposition thermal annealing were conducted using RTA to promote $CoFe_2O_4$ crystallinity on $SrTiO_3$ (001) substrates. All the annealing processes were conducted under O_2 purge (~5 sccm) with a duration of 60 s and a ramp of 50 °C/sec over a range of temperatures (450-750 °C). Figure 3.9 shows the XRD spectra of a set of 50-nm thick $CoFe_2O_4$ thin films after annealing at different temperatures. The emergence of the intense $CoFe_2O_4$ 004 peak indicates the $CoFe_2O_4$ thin films crystallize with a preferred orientation of [001] surface normal. The 004 reflection got sharper and more intense at higher annealing temperatures, indicating an improved crystallinity as well as an increased *c*-axis crystal grain size from ~23 to ~30 nm (determined by Scherrer equation).

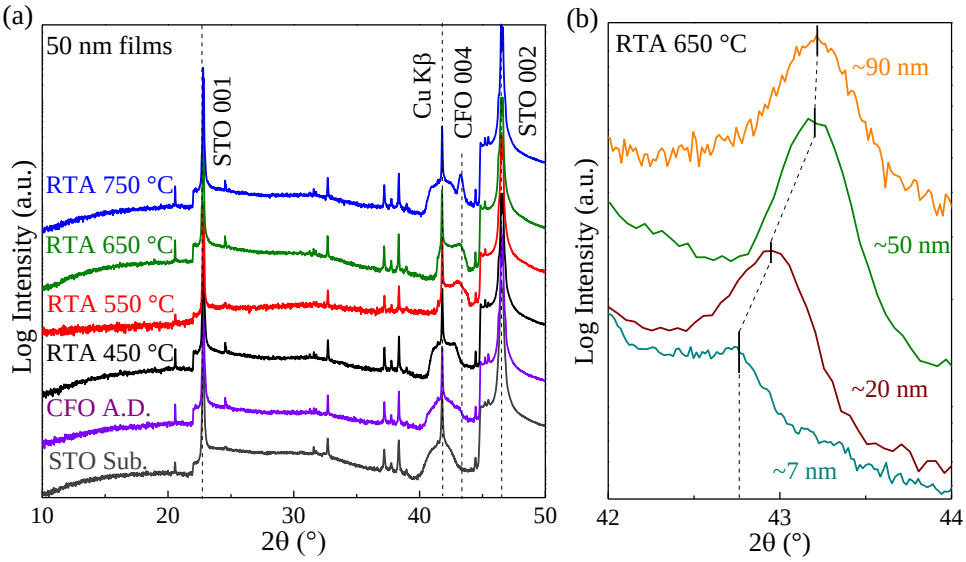

Figure 3.9 X-ray diffraction patterns for (a) $CoFe_2O_4$ films (~50 nm) grown on $SrTiO_3$ (001), as prepared and annealed from 450 °C to 750 °C. The $CoFe_2O_4$ 004 peak dominates in intensity for annealed films. (b) Short-range scans showing $CoFe_2O_4$ 004 reflections for samples of different film thickness. Peak shifts (dotted lines) indicate altered $CoFe_2O_4$ strain states. (PDF: $CoFe_2O_4$ 022-1086, $SrTiO_3$ 086-0178). (Pham 2017)

In order to ensure high-quality interfaces for in $CoFe_2O_4/BiFeO_3$ composites, the $CoFe_2O_4$ surface topography as a function of annealing temperature was investigated using

AFM. AFM analyses with 5×5 μm^2 surface area were conducted on 50-nm thick $CoFe_2O_4$ thin films annealed at different temperatures. The extrapolated R_a values are plotted in Figure 3.10 (a) as a function of annealing temperature. R_a of the as-deposited $CoFe_2O_4$ thin film is 1.82 nm, denoted as the dashed line in Figure 3.10 (a), verifying the atomically smooth surface from ALD processing. The R_a value shows a gradual increase from 2.13 nm at 450 °C and 6.40 nm at 750 °C, exhibiting a positive correlation with the sharpened $CoFe_2O_4$ 004 reflection in XRD. Although 750 °C-annealed samples showed a better crystallinity in Figure 3.9 (a), drastic surface island formation was observed in the corresponding AFM topography scans (Figure 3.10 (b)). The flake-like pattern observed is likely due to the sudden crystallization as well as a relatively large degree of lattice mismatch (~7%) between $CoFe_2O_4$ (a = 8.396 Å, PDF: 022-1086) and $SrTiO_3$ (a = 3.9 Å, PDF: 086-0178). The sizes of the surface islands ranged from ~50 nm to several μms. Similar patterns was also observed in $CoFe_2O_4$ thin films synthesized on $SrTiO_3$ (001) via MBE (Huang 2007) and PLD (Thang 2007) at 700 °C. As a result, the remainder of this section is focused on the annealing condition of 650 °C that yielded a smoother surface in order to ensure atomically smooth interfaces for composite integrations.

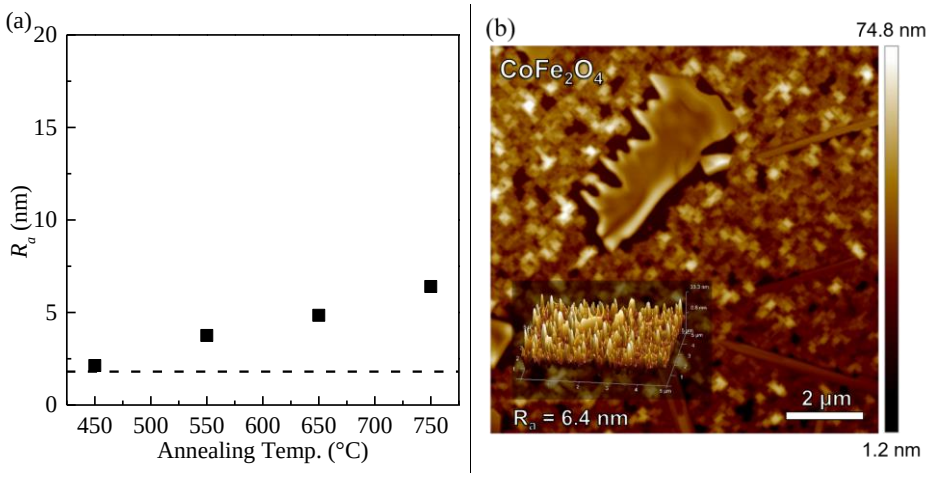

Figure 3.10 (a) Surface R_a values of the annealed 50-nm thick $CoFe_2O_4$ films on $SrTiO_3$ (001) substrates as a function of annealing temperatures. Dashed lines indicate the R_a value of the as-depsoited sample. (b) AFM surface

topography image of 750 °C annealed sample, showing an intensified surface island formation. Inset shows an isometric 3D map of the same data.

For a more detailed view of the local microstructure, a high-resolution TEM imaging was used to characterize 90-nm thick $CoFe_2O_4$ film annealed at 650 °C. The $CoFe_2O_4$ thin film shows a polycrystalline nature at the top, with an epitaxial $CoFe_2O_4$ (001) layer (~5−10 nm) near the substrate, as shown in Figure 3.11 (a) and (b). This effect is believed to be a result of the ~7 % mismatch between the film and the substrate. By comparing the SAED patterns at the $CoFe_2O_4/SrTiO_3$ interface (Figure 3.11(c)) and the bulk (Figure 3.11 (d)), an epitaxial-to-polycrystalline transition was verified by the change from the well-ordered diffraction pattern at the interface to the polycrystalline diffraction rings away from the interface.

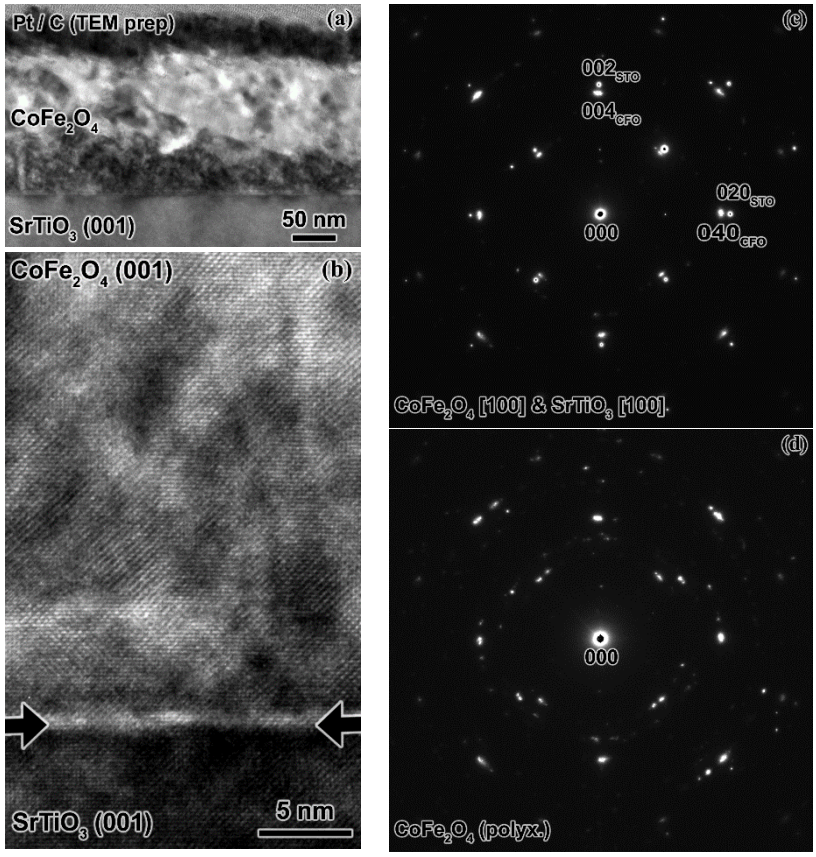

Figure 3.11 (a) Cross-sectional TEM image of $CoFe_2O_4$ film crystallized after 650 °C RTA on $SrTiO_3$ (001) substrate. The substrate is at the bottom in all cross-sectional TEM images. (b) High magnification TEM micrograph of the $CoFe_2O_4$ film, showing oriented polycrystalline growth away from the interface. Arrows indicate the interface. (c) SAED pattern collected from near

the film-substrate interface. Note the sharp film peaks and their alignment with the substrate peaks. (d) SAED pattern collected in the bulk, indicating transition to a polycrystalline film. (Pham 2017)

This effect is further confirmed by $CoFe_2O_4$ 004 XRD peak shift of a set of 650 °C-annealed $CoFe_2O_4$ thin films of different thicknesses (Figure 3.9 (b)), showing that the $CoFe_2O_4$ thin films obtained by RE-ALD are indeed strained, unlike the fully-relaxed $CoFe_2O_4$ thin films obtained by thermal ALD (Coll 2014). Positions of the $CoFe_2O_4$ 004 peaks shifted to a lower value with decreasing thickness, which correlates to an increase in the lattice parameter along the surface-normal *c*-axis. This confirms the strain relaxation process with an increasing $CoFe_2O_4$ film thickness. Because the shift is still observed in the CFO 004 reflection of the 20-nm film (larger than the epitaxial layer thickness from the TEM results), it is believed that the interfacial strain also influences a portion of the polycrystalline region, given that the 50-nm film is fully relaxed. This is possibly due to the grain boundary formation in the polycrystalline region, allowing the strain to further relax at larger thicknesses, which were 50 and 90 nm. It is hypothesized that the observed difference is due to the use of atomic oxygen as oxidants, which enables a denser interfacial bonding with a more effective surface ligand removal. Nonetheless, because $CoFe_2O_4$ is highly magnetostrictive, one can attain desired $CoFe_2O_4$ magnetic behaviors by selecting suitable strain/thickness conditions.

3.5. Magnetic Properties of $CoFe_2O_4$ Thin Films

Since a material's magnetic behaviors are greatly influenced by its crystallinity, structure, strain, and shape anisotropy, magnetic properties of $CoFe_2O_4$ were investigated as a function of both thicknesses and annealing temperatures by a SQUID magnetometer in order to better understand the correlation in between processing parameters.

The magnetic *M-H* hysteresis loops of four 650 °C-annealed $CoFe_2O_4$ thin films are shown in Figure 3.12 (a) and the evolution of the corresponding magnetic parameters along

with annealing temperatures are summarized in Figure 3.12 (b). The investigated thicknesses are ~7, ~20, ~50, and ~90 nm and all the *M-H* loops are obtained under room-temperature. It was observed that the in-plane M_s value increased from 355 to 558 emu/cm^3 with the decreasing thickness while the out-of-plane M_s showed a decreasing trend in general. On the other hand, in-plane H_c slightly increased from 1.4 to 1.6 kOe with decreasing thicknesses, whereas the out-of-plane H_c showed a drastic decrease from 1.8 to 0.3 kOe. Since the difference between the in-plane and the out-of-plane H_c values correlates to the degree of magnetic anisotropy, it was concluded that a thinner film resulted in a stronger magnetic anisotropy for RE-ALD $CoFe_2O_4$.

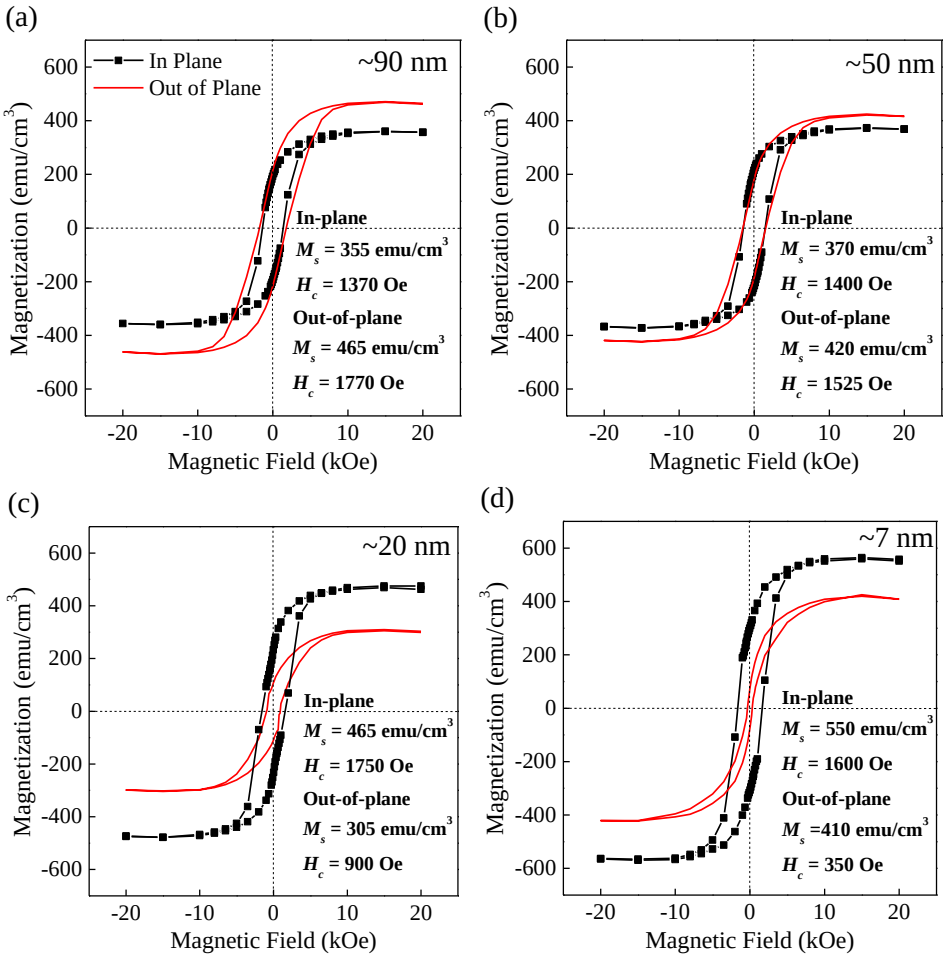

Figure 3.12 In-plane and out-of-plane *M-H* magnetic hysteresis loops of $CoFe_2O_4$ films (annealed at 650 °C for 60 seconds under O_2 gas purge) with

thickness (a) ~ 90 nm, (b) ~ 50 nm, (c) ~ 20 nm, and (d) ~ 7 nm. (Adapted from (Pham 2017))

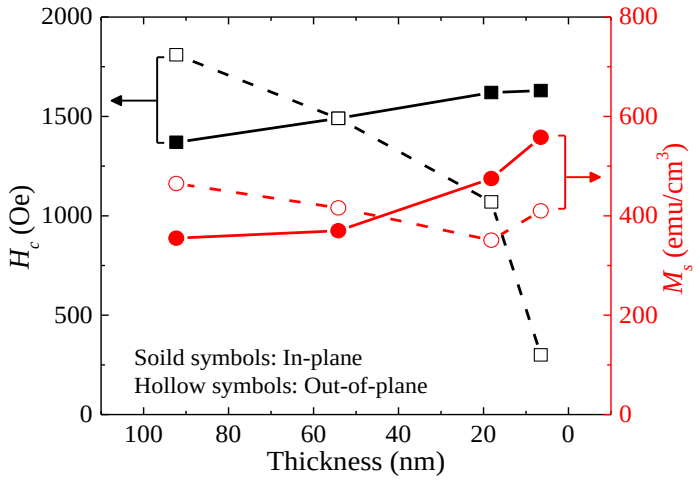

Figure 3.13 Coercivity (black squares) and saturation magnetization (red circles) vs. film thickness for out-of-plane (open symbols) and in-plane orientation (solid symbols) of the applied magnetic field. (Pham 2017)

For the trend observed in M_s, using 400 emu/cm^3 for bulk $CoFe_2O_4$ as a reference (Goldman 2006), the in-plane M_s for the ~7 and ~20-nm thick samples are enhanced while the ~50 and ~90-nm thick samples showed lowered M_s values. This contrast between samples of different thicknesses can be explained by the competition of magnetic contributions from the strain due to substrate-film lattice mismatch versus the top portion of the film that developed away from the interface (Rigato 2009). The surface morphology of epitaxial $CoFe_2O_4$ films grown on $SrTiO_3$ substrates by PLD was reported to consist of microscopic pyramidal features that contributed to the surface roughness. The AFM surface scan of the RE-ALD $CoFe_2O_4$ (see Figure 3.14 (a)) suggested a similar surface morphology. In addition, it was reported that the grain boundaries in $CoFe_2O_4$ thin films has a negative effect on the M_s values due to the decrease in magnetocrystalline anisotropy (Gatel 2013). As a result, 7- and 20-nm thick $CoFe_2O_4$ films exhibited improved M_s values due to the reduced polycrystalline characteristics compared with the 50- and 90-nm films.

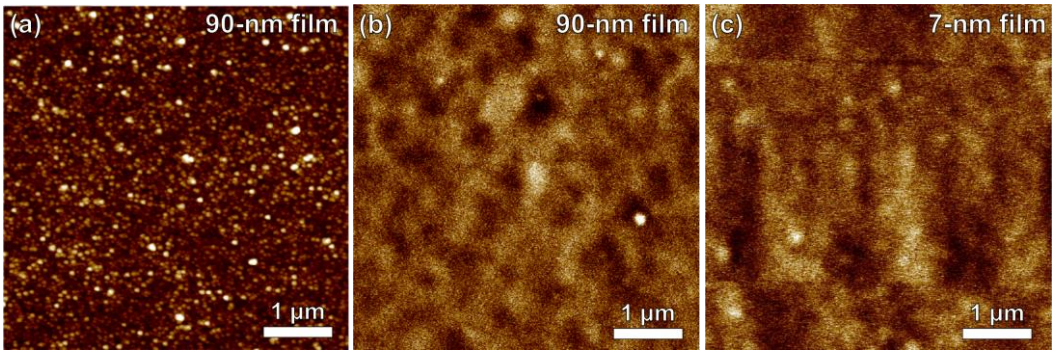

Figure 3.14 (a) AFM surface topography of a 90-nm thick RE-ALD $CoFe_2O_4$ film after 650 °C annealing in oxygen for 1 min, showing a pyramid-like surface topography. The verticle scale is 35 nm. (b) MFM phase image of the same $CoFe_2O_4$ thin film, showing grain-like magnetic domain structures. (c) MFM phase image of a 7 nm $CoFe_2O_4$ film, showing larger magnetic domains relative to the 90-nm film. (Adapted from (Pham 2017))

In terms of the change in H_c, the thinner films have a drastically smaller H_c values along the out-of-plane direction than the in-plane direction, whereas the thicker films exhibit comparable H_c values between the two directions. This indicates that both the magnetic anisotropy and softness were affected by the film-substrate strain state and shape anisotropy, both of which favor in-plane anisotropy at lower thicknesses. In other words, the energy required to flip the magnetic spins along the out-of-plane direction is lower for thinner films. The MFM measurements on the 90- and 7-nm films were conducted to further investigate this effect (Figure 3.14 (b) and (c)), both showing grain-like magnetic domain structures. It is worth noting that the 7- nm film exhibited larger out-of-plane domains, which correlates to a lower domain boundary energy and thus explains the low out-of-plane H_c value. The magnetic response of the thicker films was relatively isotropic, which is considered to be due to a lower influence from the film-substrate interfacial strain by referencing the results in Figure 3.9 (b).

The dependence of $CoFe_2O_4$ magnetic properties on RTA temperatures were investigated as well. All the measured samples were ~20 nm in thickness. The corresponding room-temperature *M-H* hysteresis loops of the 450, 550, 650, and 750 °C- annealed samples are shown in Figure 3.15 (a), (b), (c), and (d), respectively. The evolution of M_s and H_c values

with RTA temperature is summarized in Figure 3.16. Both in-plane and out-of-plane M_s values exhibited increasing trends with annealing temperatures, yet an anomalously high M_s values were found for the 450 °C-annealed sample compared to the other annealing conditions. A possible explanation is that the residual strain from the substrate lattice mismatch relaxes as the polycrystalline domains form with increase in the RTA temperature. In addition, the correlation between the annealing temperature and M_s can be explained by understanding the nature of ALD processing and the crystallization process by RTA. The RE-ALD process used here consists of alternating layers of CoO and Fe_2O_3, which are individually antiferromagnetic and weakly ferromagnetic, respectively. The formation of $CoFe_2O_4$ crystallites with higher RTA temperatures leads to the spin-orbit coupling interactions between Co^{2+} and Fe^{3+} ions that benefit to overall magnetism. The increase in relative intensity and decrease in FWHM of $CoFe_2O_4$ 004 XRD reflections observed in Figure 3.9 (a) confirmed the growth of $CoFe_2O_4$ crystal grains and correlates to an increasing overall magnetism. Similar increase in M_s as a function of processing temperature has also been reported elsewhere for the growth of $CoFe_2O_4$ thin films by PLD (Dorsey 1996). The abnormality at 450 °C could be explained by the residual strain from the substrate lattice mismatch that relaxes as the polycrystalline domains form with increasing RTA temperature.

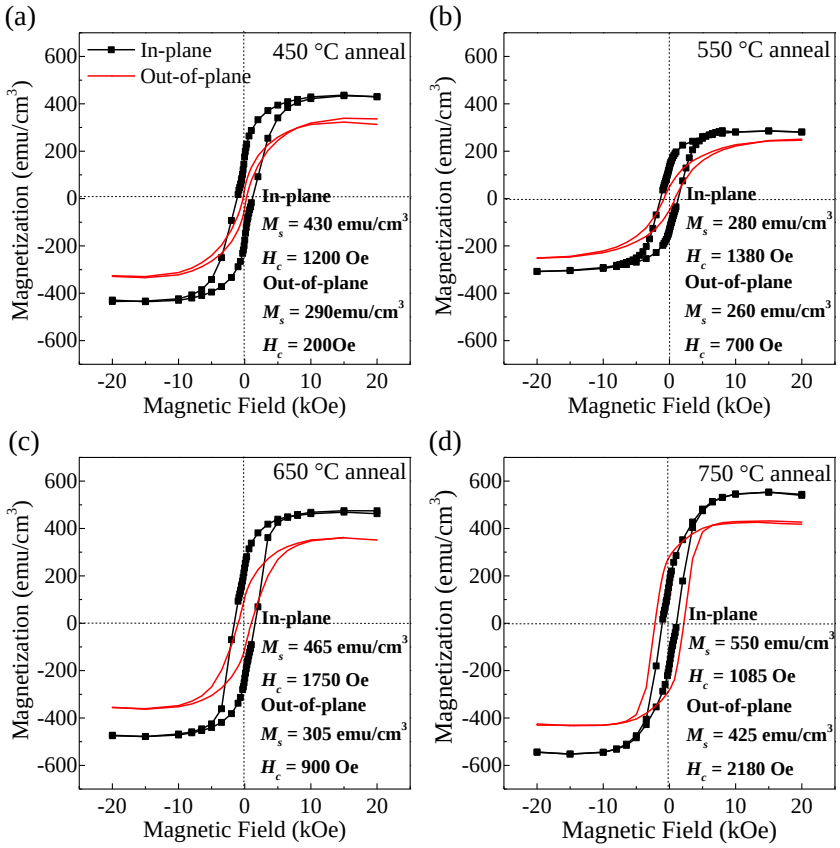

Figure 3.15 Room-temperature *M-H* magnetic hysteresis loops for 20-nm thick $CoFe_2O_4$ thin films annealed at (a) 450 °C, (b) 550 °C, (c) 650 °C, and (d) 750 °C. (Adapted from (Pham 2017))

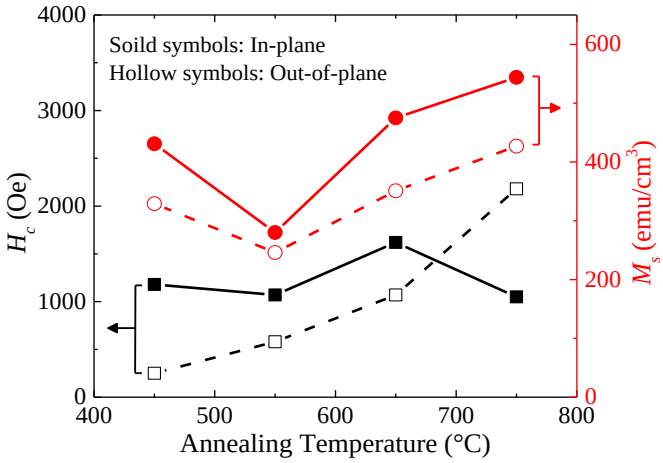

Figure 3.16 Coercivity (black squares) and saturation magnetization (red circles) vs. annealing temperature for out-of-plane (open symbols) and in-plane orientation (solid symbols) of applied magnetic field. (Pham 2017)

Similarly, H_c values exhibit a positive correlation with increasing RTA temperatures. However, the in-plane H_c values reached 1.6 kOe for the 650 °C-annealed sample but decreased

to 1.1 kOe for the 750 °C-annealed sample, while the out-of-plane values continued to increase and reached 2.2 kOe in the 750 °C-annealed sample. In other words, an in-plane magnetic anisotropy is observed in the $CoFe_2O_4$ thin films, and a transition in magnetic easy axis from the in-plane to the out-of-plane is observed when the $CoFe_2O_4$ film is annealed at 750 °C. Since $CoFe_2O_4$ is highly negatively magnetostrictive, the observed in-plane easy axis can be translated as a result of the in-plane compressive strain applied to the $CoFe_2O_4$ from the $SrTiO_3$ substrate. However, when the film is annealed at 750 °C, the strain is possibly released by the formation of surface islands (shown in Figure 3.10 (b)) and thus favors out-of-plane anisotropy.

The magnetic properties of the $CoFe_2O_4$ thin films synthesized by RE-ALD were found to change as a function of both film thickness and annealing temperature given their textured-polycrystalline nature, highlighting the importance of the interfacial epitaxial regime to overall magnetism. Due to the large magnetostrictive behavior in $CoFe_2O_4$, the induced lattice strain from the underlying substrate has a substantial effect on its magnetic properties. It is worth noting that the observed M_s values were anisotropic, despite the fact that an isotropic M_s is generally expected in a material. One possibility for the observed phenomenon is the epitaxial strain arisen from the interfacial lattice mismatch between the $CoFe_2O_4$ film and the $SrTiO_3$ substrate (Horng 2004, Huang 2006, Dhakal 2010). Furthermore, a suitable substrate selection with minimal lattice mismatch is expected to eliminate the formation of the polycrystalline top layer and help achieve ALD-grown epitaxial $CoFe_2O_4$ thin films. Table 3.2 shows that RE-ALD grown $CoFe_2O_4$ thin films have comparable magnetic properties relative to other reported literature values from bulk and thin films, which are synthesized by other non-chemical thin film deposition techniques.

Table 3.2 Comparison of $CoFe_2O_4$ synthesized by different methods

	Bulk	MBE	PLD	Sputtering	RE-ALD
H_c (Oe)	~0.3	0.5-12	0.5-5.2	~0.5-3.4	~0.2-2.2
M_s (emu/cm^3)	~400	140-500	~420-490	~50-523	~260-550
t (nm)	-	~80-120	~200-500	~100-1000	~7-90
Crystal quality	-	Epitaxial		Polycrystalline or epitaxial	Textured polycrystalline
Ref.	(Goldman 2006)	(Huang 2006)	(Dorsey 1996)	(Matsushita 1992)	This work

To summarize, RE-ALD is a synthesis technique that can produce films with desirable magnetic properties, as we demonstrate here with $CoFe_2O_4$ thin films with thicknesses as low as 7 nm, illustrating a path for the large-scale synthesis of high-quality and ultrathin $CoFe_2O_4$ films for important technological applications.

Chapter 4. Synthesis and Characterization of Ferroelectric HfO_2 Thin Films by Radical-Enhanced Atomic Layer Deposition

Ferroelectric hafnia (FE-HfO_2) thin film is a critical topic in recent semiconductor electronics research, owing to its superior compatibility with CMOS technology and desirable electrical properties for device fabrication (Park 2015, Kwon 2017). All those advantages make FE-HfO_2 an ideal ferroelectric phase of choice for enabling multiferroic composites as well. In this work, undoped FE-HfO_2 thin were synthesized via RE-ALD and studied as the model system due to processing simplicity. Tetrakis(dimethylamido)hafnium(IV) (TDMAH) and atomic oxygen were utilized as the metalorganic precursor and oxidizing agent, respectively. ALD temperature window and growth curves were investigated in order to obtain an optimized condition HfO_2 growth. The growth rate of the HfO_2 thin films were determined to be ~1.4 Å/cycle at a substrate temperature of 190 °C.

Ferroelectric and structural characterizations were conducted by measuring TiN (10 nm)/HfO_2/TiN (10 nm) structures on p-Si (111) substrates with various HfO_2 thicknesses and annealing temperatures. The incorporation of top and bottom TiN layers provides needed thermal-mechanical constraints during post-deposition thermal processing, which stabilizes the metastable orthorhombic FE-HfO_2 phase. High-resolution XRD measurements were used to differentiate the HfO_2 phases. Both higher annealing temperature and lower HfO_2 thickness contribute to an increased HfO_2 orthorhombic phase and ferroelectricity. The resulted FE-HfO_2 thin films exhibit a remnant polarization (P_r) value up to ~1.00 μC/cm^2 and an electrical coercive field (E_c) value ranging from 150-1800 kV/cm. The correlation between film ferroelectricity and processing parameters illustrates a way to achieve optimized FE-HfO_2 thin films.

4.1. Synthesis of HfO_2 Thin Films by Radical-Enhanced Atomic Layer Deposition

For FE-HfO_2, it is necessary to first optimize the RE-ALD process for HfO_2 thin films. For the deposition process, metalorganic TDMAH precursors were used as the cation source, while atomic oxygen generated from the microwave cavity serves as the oxidant for the growth of HfO_2. RE-ALD HfO_2 thin films were first synthesized on Si (111) substrates at temperatures ranging from 160-200 °C, where the film thicknesses were determined via optical ellipsometry. Figure 4.1 (a) shows the growth rate per RE-ALD cycle as a function of substrate temperatures. For all the data points, the samples were synthesized with 100 ALD cycles. The growth rates were obtained by dividing the film thickness by the total number of ALD cycles conducted. RE-ALD synthesized HfO_2 films showed a relatively constant growth rate of ~1.4 Å/cycle from 170 to 190 °C and increased drastically to ~1.9 Å/cycle at 200 °C, indicating an ALD temperature window for HfO_2 of 170-190 °C. For the remaining part of this study, a substrate temperature of 190 °C is used for the RE-ALD growth of HfO_2. Figure 4.1 (b) shows the film thickness as a function of the number of ALD cycles conducted, the inset shows the corresponding pulsing sequence and the substrate temperature. The linear relationship between the two parameters verifies the ALD layer-by-layer growth of the HfO_2 film. The slope of the linear regression-fit line between the two variables indicated a HfO_2 growth rate of ~1.4 Å/cycle without any apparent incubation period for precursor absorption. All the growth characterizations suggest an ideal RE-ALD process for HfO_2 thin film growth.

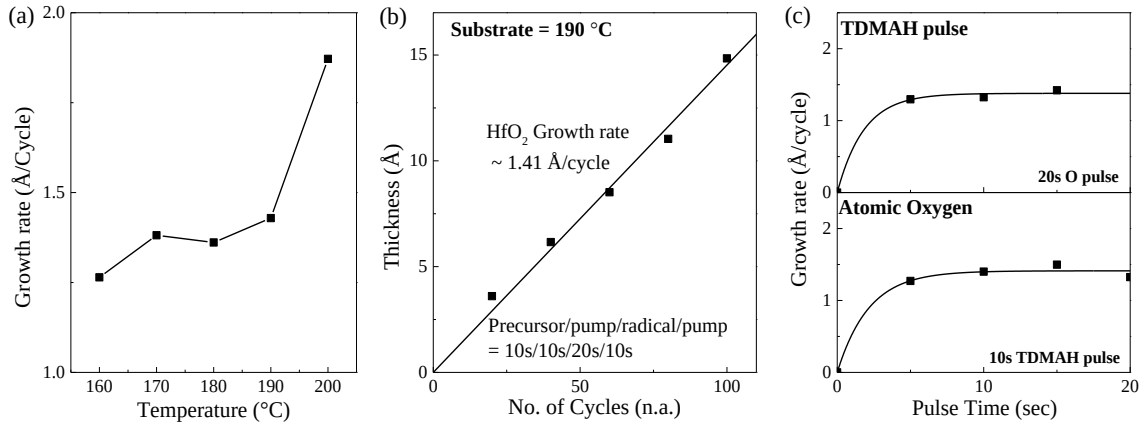

Figure 4.1 ALD growth profiles of HfO_2 thin films with TDMAH and atomic oxygen on Si (001). (a) ALD growth rate as a function of substrate temperature, showing an ideal ALD temperature window of ~170-190 °C. (b) HfO_2 film thicknesses plotted as a function of the number of RE-ALD cycles, exhibiting a linear growth profile with a growth rate of ~1.4 Å/cycle. The pusing sequence duration is shown as inset. The growth rate was determined by the slope of linear regression-fit lines. (c) Thickness profile of the HfO_2 thin films deposited via RE-ALD as a function of TDMAH precursor pulse time (upper panel) and atomic oxygen pulse time (lower panel), both showing self-limiting behaviors.

ALD pulsing durations are critical parameter as well for an effective ALD process due to its self-limiting nature. The RE-ALD growth rate for HfO_2 thin films as a function of TDMAH and atomic oxygen pulse are shown as the top and bottom panel in Figure 4.1 (c), respectively. Similarly, all the data points were measured with films deposited with 100 RE-ALD cycles and a substrate temperature of 190 °C. The growth rate vs. pulse time curves for both TDMAH and atomic oxygen show self-limiting profiles that are specific to ALD processing. The saturating time for both TDMAH and atomic oxygen pulses were ~10-20s, therefore a 10s TDMAH pulse and a 20s atomic oxygen pulse were used in the remainder of this work.

XPS analysis was used to characterize the composition of the RE-ALD HfO_2 films. Figure 4.2 (a) shows the XPS survey of a ~15-nm thick HfO_2 thin film synthesized at 190 °C, verifying the growth of HfO_2 with no impurity peaks. Atomic composition of the film was estimated by calculating and comparing the areas of the elemental XPS peaks. The carbon

content was calculated to be ~28.8%, which is higher than the ambient carbon content (~15-20%) of the sample synthesized using the same RE-ALD system (Van 2005, Pham 2015). However, the detailed Hf *4f* XPS spectrum of the same film (Figure 4.2 (b)) confirms the complete and clean oxidation of Hf^{4+} cations. Therefore it is suggested that although the synthesized HfO_2 films were completely oxidized, impartial removal of the reacted ligand residues lead to carbon impurities in the film. Further optimization in the precursor chemistry and chamber wall temperature can likely resolve the issue but it was shown that the carbon impurities at the same time promote the stabilization of HfO_2 ferroelectric orthorhombic phase and therefore enhances film ferroelectricity as well (Kim 2016).

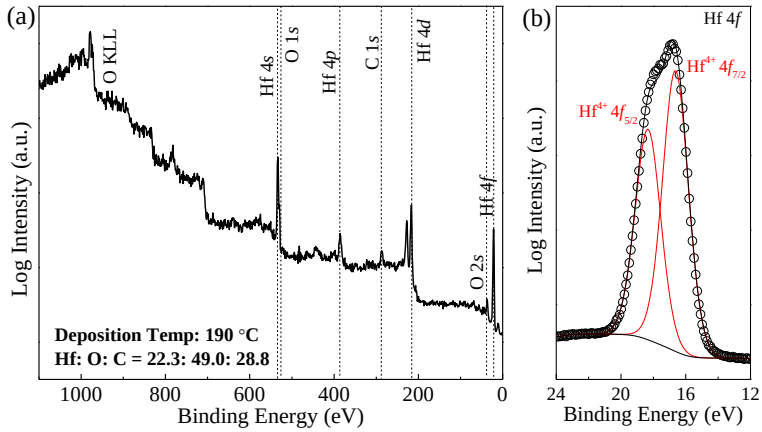

Figure 4.2 (a) XPS survey scan from 1100 – 0 eV of a HfO_2 thin film (100 cycles, ~15 nm in thickenss) grown at a substrate temperature of 190 °C, confirming the RE-ALD growth of HfO_2. (b) Detailed XPS spectra of the Hf *4f* peak, symbols represent the obtained spectra while the lines represent the fitting curves as well as the background.

4.2. Ferroelectricity in HfO_2 Thin Films with TiN as the Confinement Layer

Ferroelectricity in HfO_2 thin films arises from its metastable non-centrosymmetric orthorhombic phase, while the dielectric centrosymmetric monoclinic phase is the most energetically favorable under ambient conditions. As a result, the use of structural confinement layers and post-deposition thermal annealing steps were incorporated into the fabrication process in order to stabilize the metastable orthorhombic FE-HfO_2 phase. The mismatch in

thermal expansion between the interfacing layer and HfO_2 during the annealing step would favor HfO_2 crystallization into its orthorhombic phase. In this section, TiN is used as the confinement layer for baseline characterizations since it is the most-utilized confinement layer of choice in the field of FE-HfO_2 research (Lomenzo 2014, Lin 2018).

For this study, HfO_2 thin films of different thicknesses were integrated with 10-nm thick TiN bottom and top layers to form TiN (10 nm)/HfO_2/TiN (10 nm) structure on p-Si (111) substrates. This section aims to investigate the correlation of the induced HfO_2 ferroelectricity with different HfO_2 thicknesses and annealing temperatures, which is not widely studied on undoped pure HfO_2 systems (Park 2015, Polakowski 2015, Kim 2016, Nishimura 2016).

The corresponding fabrication process flow is shown in Figure 4.3 (a). The TiN layers were deposited via RF magnetron sputtering deposition and the sandwiched HfO_2 layer was grown via RE-ALD. Following the TiN layer deposition, the samples were then rapid thermal annealed (RTA) for 20 seconds at different temperatures to promote film crystallization. The RTA step was conducted under N_2 purge and a temperature ramp rate of 50 °C/sec was used to reach the targeted temperature. Circular Au (100 nm)/Cr (10 nm) electrodes pads with diameters of ~250 μm were deposited after the annealing step by e-beam evaporation. The circular shape was obtained by using a shadow mask of that size and shape. The metal electrodes then served as the hard masks for the subsequent wet solution etch to form isolated capacitors devices. The solution etch was conducted by dipping the sample into SC1 solution (H_2O/H_2O_2 (30% wt.)/NH_3OH (70% wt.) = 70:15:15) for 10 minutes at 50 °C to remove the exposed TiN confinement layer. Figure 4.2 (b) shows a schematic of the final device structure after the all the fabrication steps illustrated above. Three HfO_2 thicknesses (20, 10, 6 nm) and 4 annealing temperatures (500, 600, 700, and 800 °C) were investigated.

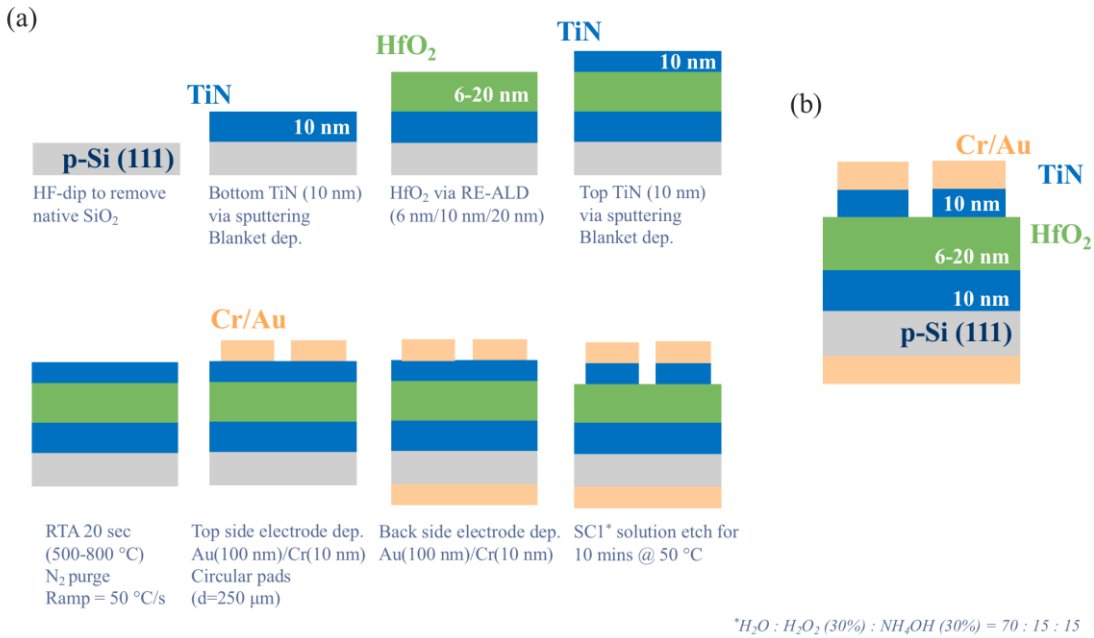

Figure 4.3 (a) Process flow for the TiN (10 nm)/HfO_2/TiN (10 nm) metal-insulator-metal (MIM) capacitor structures on p-Si (111) substrates in this work. (b) Schematic of the final structure.

Starting from the 20-nm thick HfO_2 films, sample crystallinity was characterized by grazing incidence wide angle X-ray scattering (GIWAXS) obtained at Stanford Synchrotron Radiation Laboratory (SSRL) using beamline 11-3 with a wavelength of λ = 0.9744 Å. The GIWAXS spectra are shown in Figure 4.4 (a) and the corresponding the *P-E* measurements after different annealing conditions are shown in Figure 4.4 (b). The *P-E* measurements were conducted using a probe station equipped with Signatone SE-SM tungsten "cat whisker" probes in conjunction with a Radiant Multiferroic II Ferroelectric Test System. Although the orthorhombic phase reflection is noticeable from all the annealing conditions, the fact that the monoclinic crystallites are present impedes film ferroelectricity and therefore a linear *P-E* relationship is observed.

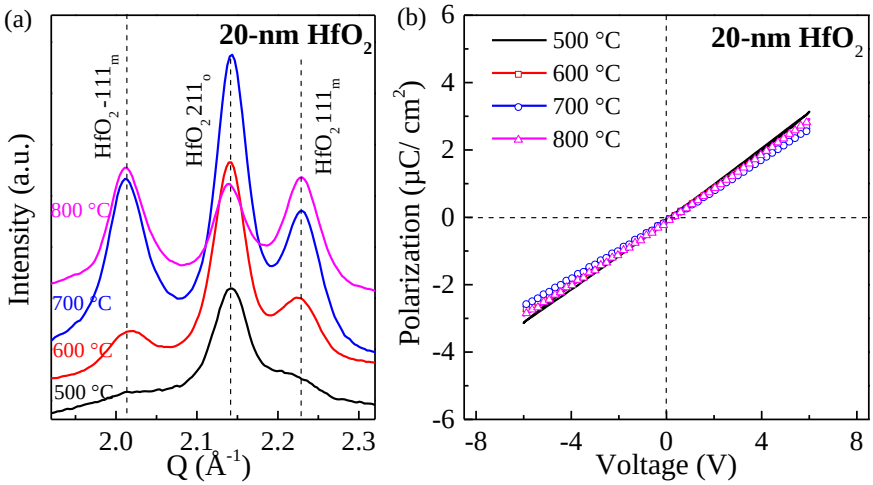

Figure 4.4 (a) GIWAXS spectra of the TiN (10 nm)/HfO_2/TiN (10 nm) structure with 20-nm thick HfO_2 on p-Si (111) substrates annealed at 500-800 °C. The annealing steps were carried for 20 seconds under N_2 purge. The co-exitence between the orthorhombic (denoted by *o*) and mononiclic (denoted by *m*) indicates a mix phase HfO_2. (b) *P-E* hysteresis loops of the corresponding somples investigated via GIXAS. The straight lines suggest dielectric behaviors.

It is worth noting that the sample is very slightly ferroelectric (as seen in Figure 4.4 (b)) for 500 °C annealing, which correlates to the fact that the film shows majorly orthorhombic reflection (HfO_2 211_o). The reason for the weak ferroelectricity is possibly due to the low crystallinity of the 500 °C sample, meaning that the HfO_2 layer could remain mostly amorphous but contains small ferroelectric orthorhombic crystallites. Another interesting effect is the decrease in the intensity of the orthorhombic phase reflection when annealed at 800 °C, monoclinic phase outweighs the orthorhombic phase and dominates the HfO_2 layer. Since the confinement effect from the top TiN layer and the subsequent HfO_2 crystallization are inhomogeneous given the polycrystalline nature of HfO_2, a possible explanation is that the energy landscape for HfO_2 crystallization does not correlate linearly with annealing temperatures and thus the monoclinic phases re-emerged at 800 °C. The dielectric behavior observed here with 20-nm thick HfO_2 is consistent with previous reports on thicker undoped HfO_2 thin films, where higher HfO_2 thicknesses led to a greater dissipation of the confinement layer influence into the HfO_2 phase (Polakowski 2015).

Similar investigations were conducted with 10-nm thick HfO_2 films. The GIWAXS results for different annealing temperatures are shown in Figure 4.5 (a). The corresponding *P-E* hysteresis loops are shown in Figure 4.5 (b) and summarized in Figure 4.5 (c). Although 500 °C-annealed sample showed a dominating orthorhombic phase reflection, the *P-E* measurement did not show ferroelectricity. This is likely due to the partial crystallization with low annealing temperature, which yields a mostly amorphous HfO_2 film with small orthorhombic crystallites embedded within.

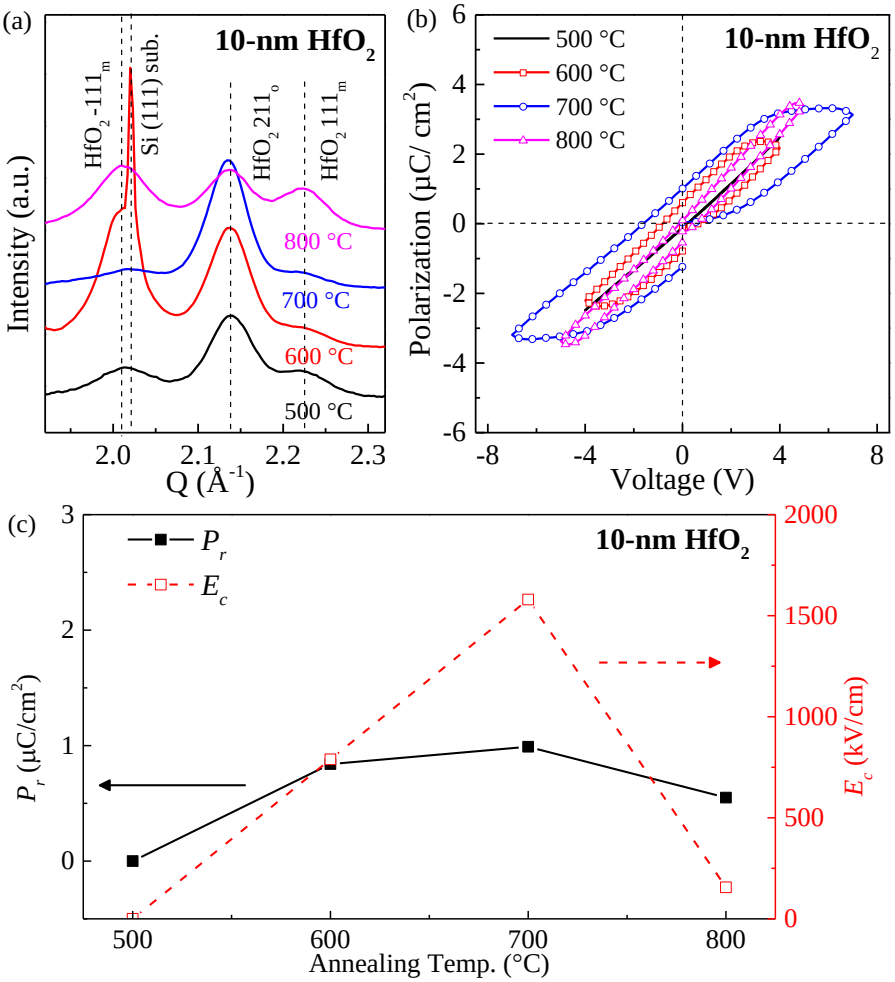

Figure 4.5 (a) GIWAXS spectra of 10-nm thick HfO_2 layers sandwiched by 10-nm thick TiN layers and annealed at 500-800 °C. Greater intensities for the *o*-phase peaks are observed compared to the 20-nm thick HfO_2 case. (b) *P-E* hysteresis loops of the corresponding samples. The emergence of ferroelectricty correlates with the increasing intensity of *o*-phase reflections and annealing

temperatures. (c) P_r and E_c of the 10-nm thick FE-HfO_2 as a function of annealing temperature.

All the measured samples are mixed phase besides the 700 °C-annealed sample, which correlates to the greatest ferroelectric behavior in Figure 4.5 (c) with a P_r ~1.00 μC/cm^2 and an E_c ~1580 kV/cm. The large E_c correlates to the dominance of the orthorhombic phase in HfO_2, which is potentially because the orthorhombic crystallites are larger in size compared to the mixed phase HfO_2 films annealed at other temperatures. Interestingly, after 800 °C anneal, the monoclinic phase re-emerged and therefore a decrease in E_c down to ~156 kV/cm was observed. This highlights the importance of understanding the correlation between HfO_2 crystallization and annealing condition for an optimized ferroelectric behavior.

Lastly, the GIWAXS scans of the thinnest 6-nm thick HfO_2 are shown in Figure 4.6 (a) and the *P*-*E* measurements are shown in Figure 4.6 (b). Figure 4.6 (c) summarizes the evolution of ferroelectric behaviors as a function of annealing temperature. Unlike the 10-nm and 20-nm thick HfO_2 films, 6-nm thick HfO_2 films exhibits only orthorhombic phase reflections from all annealing conditions, suggesting that the ferroelectric phase is more energetically favored at lower HfO_2 thicknesses. Similar effects were also observed in many other FE-HfO_2 studies (Park 2014, Polakowski 2015, Chernikova 2016), it is believed that the interfacial confinement effect is more prominent when HfO_2 is thinner due a decreased energy dissipation.

The 500 °C-annealed sample was mostly amorphous and therefore showed a non-ferroelectric behavior from the corresponding *P*-*E* measurement (Figure 4.6 (b)), likely due to a greater required thermal energy when crystalizing thinner films. Studies on ALD-deposited $SrHfO_3$ (McDaniel 2015) and HfO_2 thin films (Polakowski 2015) have observed similar phenomena for ultra-thin films that are thinner than 6 nm. HfO_2 crystallization at low temperatures can be achieved by dopant incorporations (Karbasian 2017), longer annealing durations, and thicker confinement layers (Kim 2017). Besides the 500 °C sample, samples

annealed at 600 °C and above all revealed prominent orthorhombic peaks with distinct ferroelectricity. Furthermore, it is worth noting that the stabilization of orthorhombic phase persists even with 800 °C annealing for the 6-nm thick HfO_2 film, resulting in a further increased P_s and E_c values.

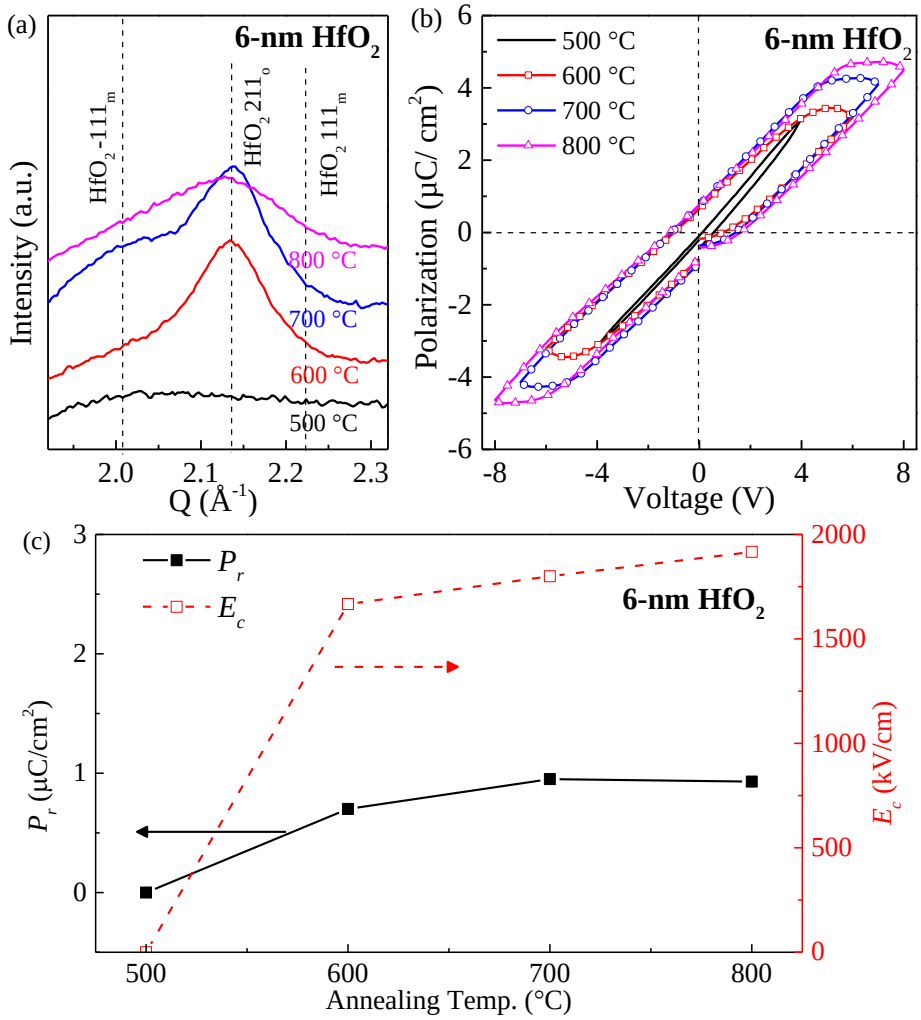

Figure 4.6 (a) GIWAXS spectra of the the 6-nm thick HfO_2 films sandwiched by 10-nm thick TiN layers and annealed at 500-800 °C. The samples exhibited mainly *o*-phase reflections. (b) *P-E* hysteresis loops of the corresponding samples annealed at different temperatures. The elimition of the *m*-phase leads to further promoted ferroelectric behaviors compared to the case of 10-nm and 20-nm thick HfO_2 films. (c) P_r and E_c of the 6-nm thick FE-HfO_2 as a function of annealing temperature.

Table 4.1 is a summary of the three investigated HfO_2 thicknesses, and it is shown that HfO_2 ferroelectricity emerges and increases with a decreasing thickness. 20-nm thick HfO_2 is

incapable to reveal any sort of ferroelectricity, while 10-nm and 6-nm thick HfO_2 thin films are ferroelectric under suitable annealing conditions. The metastable HfO_2 orthorhombic phases is further stabilized with lower HfO_2 thicknesses due to a stronger confinement effect arising from the interfaces as well as an altered thermodynamic landscape for film crystallization (Park 2014, Hoffmann 2015, Park 2015, Polakowski 2015). On the other hand, the ferroelectric samples that did not show prominent monoclinic phase reflections exhibit much greater E_c values that is comparable with the other reports on FE-HfO_2 systems (E_c ~1000-2000 kV/cm) (Park 2015), verifying the successful stabilization of ferroelectric orthorhombic phase with minimum monoclinic phase incorporation. Although the P_r values obtained (up to ~1 $\mu C/cm^2$) here are somewhat lower than the other reports on undoped HfO_2 thin films (up to ~5-10 $\mu C/cm^2$) (Polakowski 2015, Kim 2016, Nishimura 2016), they are nonetheless on the same order of magnitude. Therefore, instead of perfecting the ferroelectric behavior, the main focus of the following sections are to integrate FE-HfO_2 with ferrimagnetic $CoFe_2O_4$ into multiferroic composites.

Table 4.1 Summary of the ferroelectricity observed in the MIM capacitors with HfO_2 thin films of different thickness and annealing conditions

t_{HfO2} (nm)	RTA Temp. (°C)	P_r ($\mu C/cm^2$)	E_c (kV/cm)
20	500	n.a.	n.a.
	600	n.a.	n.a.
	700	n.a.	n.a.
	800	n.a.	n.a.
10	500	n.a.	n.a.
	600	~0.07	~789
	700	~0.65	~1580
	800	~1.00	~156
6	500	n.a.	n.a.
	600	~0.7	~1667
	700	~0.95	~1800
	800	~0.93	~1917

4.3. Summary

In this chapter, FE-HfO_2 thin films were synthesized on p-Si (111) substrates via RE-ALD and demonstrated great prospects. The RE-ALD growth of HfO_2 thin films were achieved by using metalorganic TDMAH precursor and atomic oxygens as the oxidant. An ALD temperature window of 170-190 °C and a superior growth rate of ~1.4 Å/cycle compared to H_2O chemistry were obtained. After growth characterizations, HfO_2 thin films were integrated into TiN (10 nm)/HfO_2/TiN (10 nm) structures to induce ferroelectricity via post-deposition thermal annealing. In this work, HfO_2 structure and ferroelectricity were studied with a range of film thicknesses (6-20 nm) and annealing temperatures (500-800 ºC). It was demonstrated that the ferroelectric orthorhombic phase is further stabilized when HfO_2 thicknesses are lower, owing a better structural confinement effect from the interface. Annealing temperature is shown to be an important factor for an optimized ferroelectricity as well. The FE-HfO_2 here showed P_r values ranging from ~0.07-1 μC/cm^2 and E_c values from ~156-1900 kV/cm, on the same orders of magnitude with reports on FE-HfO_2 thin films (P_r ~5-10 μC/cm^2 and E_c ~1000-2000 kV/cm).

Chapter 5. Magnetoelectric 2D-2D $CoFe_2O_4/BiFeO_3$ Nano-laminates

The first part of this chapter focuses on describing the integration of ferrimagnetic $CoFe_2O_4$ and multiferroic $BiFeO_3$ via the RE-ALD processes illustrated in the previous chapter. $CoFe_2O_4$ (~15 nm) and $BiFeO_3$ (~40 nm) are integrated into nano-laminates with 2D-2D geometry onto $SrTiO_3$ (001) and Si (001) substrates. The ferroic properties are characterized and showed further enhanced behavior. Furthermore, a nanolayering technique was employed to further optimize the ferroic properties, while the total thickness and ratio of the respective $CoFe_2O_4$ and $BiFeO_3$ phases are held at a constant. The tri-layer structure shows the optimal trade-off between ferroelectricity and magnetism. For the Si-integration of the tri-layer structure on MBE-grown $SrTiO_3$ (001)-buffered Si (001) substrates, it exhibits a retained magnetism while ferroelectric imprint is observed. The imprint effect highlights the importance of the quality of the $SrTiO_3$/Si interface for an applicable ferroelectric behavior.

The second part of this chapter details the subsequent magnetoelectric coupling characterizations of the optimized tri-layer $BiFeO_3/CoFe_2O_4/BiFeO_3$ structure. Both microscopic and macroscopic magnetoelectric coupling were observed. By considering the change in remnant magnetization (M_r) upon electrical poling, the converse magnetoelectric coupling coefficient $\alpha_{converse}$ is determined to be ~22 Oe cm/kV, which is within the range of reported values in literatures (10-100 Oe cm/kV). In order to reveal the importance of interfaces to overall ME coupling in the composite design, the sample was then scaled into thinner thicknesses, where the 16-nm thick sample exhibits a much higher $\alpha_{converse}$ value of ~64 Oe cm/kV.

5.1. Synthesis and characterization of 2D-2D $CoFe_2O_4/BiFeO_3$ Nano-laminates on $SrTiO_3$ (001) Substrates

ALD-grown $CoFe_2O_4/BiFeO_3$ multiferroic nano-laminates with 2D-2D geometry were synthesized by integrating the respective ALD process for $CoFe_2O_4$ and $BiFeO_3$ with a multi-beam ALD system described in the previous chapter. $CoFe_2O_4$ and $BiFeO_3$ were used as the building blocks for the composite design due to their robust room-temperature functionalities (magnetic $T_{c,CFO}$ ~ 870K, ferroelectric $T_{c,\,BFO}$ ~ 1100K, and antiferromagnetic $T_{N,\,BFO}$ ~ 643K), which in turn leads to a room-temperature ME coupling. The multiferroic behavior in $BiFeO_3$, as well as the highly magnetostrictive nature of $CoFe_2O_4$ make the composite system an intriguing one for utilizing multiple interfacial coupling simultaneously, namely magnetic exchange coupling (Sone 2015) and strain-mediated coupling (Aimon 2015). In the composite design, $BiFeO_3$ and $CoFe_2O_4$ serve as the ferroelectric and the magnetic phase respectively, where the $CoFe_2O_4$ magnetism is altered by both the manipulation of the $BiFeO_3$ antiferromagnetic moments as well as its strain state.

Starting with the simplest structure the bi-layer 2D-2D $CoFe_2O_4$ (15 nm)/ $BiFeO_3$ (40 nm) nanolaminate was grown on conductive Nb:$SrTiO_3$ (0.7 wt. %) (001) substrates. As illustrated previously, the respective growth rates for $CoFe_2O_4$ and $BiFeO_3$ are ~2.4 and 3.3 Å/supercycle. The ALD supercycles were then repeated until the resulted film reaches targeted thicknesses. A post-deposition rapid thermal annealing (RTA) treatment was conducted immediately after growth for 1 minute under an O_2 environment at 550 °C to promote film crystallization. Nb:$SrTiO_3$ (001) (cubic, space group: $Pm\bar{3}m$, a = 3.9 Å, PDF: 086-0178) substrates allow the stabilization of $BiFeO_3$ (rhombohedral distorted perovskite, space group: *R3c*, a = 5.63 Å, α = 59.4°, PDF 071-2494, ~0.7 % mismatch in (012) = $(001)_{pc}$) and $CoFe_2O_4$ (cubic inverse spinel, space group: *Fd3m*, a = 8.396 Å, PDF: 022-1086, ~ 7% mismatch) in

their desirable crystal phases. Figure 5.1 (a) shows the XRD θ-2θ spectra of the bi-layer composite as well as the respective single-phase $CoFe_2O_4$ (~15 nm) and $BiFeO_3$ (~40 nm) on Nb:$SrTiO_3$ (001) substrates after the aforementioned RTA step. The bi-layer sample showed $BiFeO_3$ 001_{pc} reflection that is coherent with the single-phase $BiFeO_3$ film of the same thickness, indicating a high-quality and comparable $BiFeO_3/SrTiO_3$ interface. However, the absence of the $CoFe_2O_4$ 004 reflection suggests that the $CoFe_2O_4$ layer is mostly polycrystalline, which is likely due to the interfacial atomic diffusion during the RTA step as well as the lattice mismatch between $CoFe_2O_4$ and $BiFeO_3$. Similar observations were reported in the bi-layer $CoFe_2O_4/BiFeO_3$composites synthesized via a solution-based synthesis method, where the $CoFe_2O_4$ reflections were characterized by a GI-XRD setup (Sone 2015). The AFM height image of the annealed bi-layer 2D-2D $CoFe_2O_4/BiFeO_3$ sample is shown in Figure 5.1 (b), indicating a very low surface roughness R_a value of ~1.78 nm with minimal surface island formation after annealing, confirming the high-quality and conformal nature of ALD.

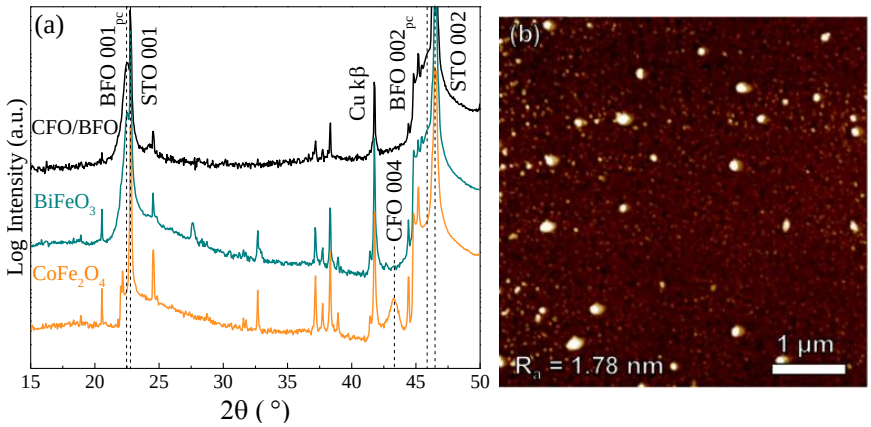

Figure 5.1 (a) XRD spectra of the single-phase $CoFe_2O_4$ (15 nm), $BiFeO_3$ (40 nm), and bi-layer $CoFe_2O_4$ (15nm)/$BiFeO_3$ (40 nm) multiferroic nanolaminate on single crystal $SrTiO_3$ (001) substrate after rapid thermal annealing (RTA) at 550 °C for 60 s under O_2 environment. (b) Atomic force microscopy (AFM) surface topography of the annealed nanolaminate sample, showing a smooth surface with a R_a of 1.78 nm. The vertical scale is ~25 nm.

The *P-E* ferroelectric and *M-H* magnetic hysteresis loops of the bi-layer sample are shown in Figure 5.2 (a) and (b) respectively, confirming the coexistence of ferroelectricity and magnetism in the nanolaminate design. For the *P-E* loop, the bi-layer sample exhibited an increased remnant polarization (P_r) value from ~7.5 to ~12 μC/cm^2 (~60% improvement). In addition, a lower ferroelectric coercivity (E_c) was observed, indicating that it is more energetically efficient to switch the polarization in the bi-layer nanolaminate than in single-phase $BiFeO_3$. The abovementioned improvements in ferroelectricity are likely due to a reduced leakage current from the incorporation of the insulating $CoFe_2O_4$ layer (Fritsch 2012). A similar effect has also been observed in the $BiFeO_3$ thin film with an $SrTiO_3$ insertion layer ($BiFeO_3/SrTiO_3/BiFeO_3$ structure), where both the ferroelectric and piezoelectric behaviors were improved after the incorporation of the insulating $SrTiO_3$ layer (Lee 2015). Although the $CoFe_2O_4$ 004 reflection is absent in the XRD θ-2θ scan, the *M-H* magnetic hysteresis showed a saturation magnetization (M_s) value of ~105 emu/cm^3 (normalized over the entire composite thickness while only $CoFe_2O_4$ contributes to the magnetism), which is comparable with the single-phase $CoFe_2O_4$ that is of a similar thickness and thus suggests that the atomic diffusion is confined within a limited range from the interface and is not deteriorating the overall functionality. It is worth noting that the magnetic coercive field (H_c) is lower than the case of single-phase $CoFe_2O_4$ thin films deposited via ALD (Pham 2017), which is likely due to a decreased magnetocrystalline anisotropy as well as the interfacial magnetic exchange coupling with the $BiFeO_3$ phase.

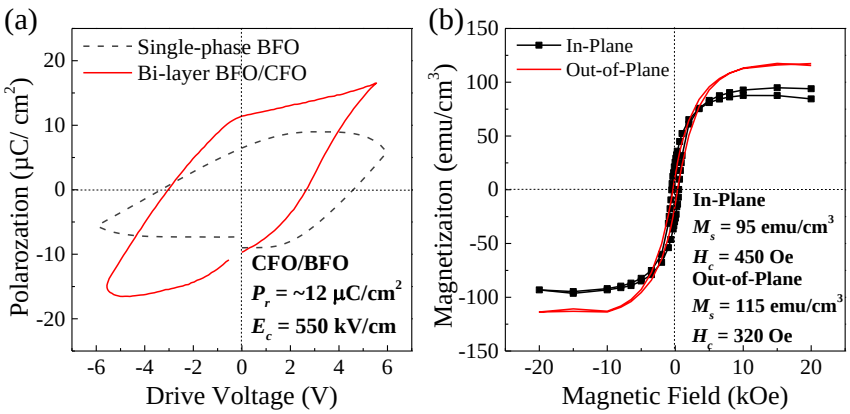

Figure 5.2 (a) Room temperature *P-E* hysteresis loops of the single-phase $BiFeO_3$ (40 nm) and the bi-layer $CoFe_2O_4/BiFeO_3$ nanolaminate. (b) In-plane and out-of-plane *M-H* hysteresis loops of the bi-layer sample under room temperature condition.

To further characterize the functional behavior microscopically, piezoresponse force microscopy (PFM) and magnetic force microscopy (MFM) were utilized. For the PFM measurements, it was first conducted under a –10 V tip bias within the 3×3 μm^2 area, and a subsequent scan within the 1×1 μm^2 area region with +10 V bias was performed to create a contrast in the ferroelectric states. As shown in the PFM phase image (Figure 5.3 (a)), the contrast in between the square patterns with different poling biases confirms the ferroelectric switching arising from the $BiFeO_3$ phase in the $CoFe_2O_4/BiFeO_3$ bi-layer. On the other hand, Figure 5.3 (b) shows the MFM phase image of the bi-layer sample, where a grain-like magnetic domain structure that is specific to $CoFe_2O_4$ thin films is observed. The domains are about ~150-300 nm in size, consistent with the observations from other reports (Huang 2007, Sone 2015, Pham 2017).

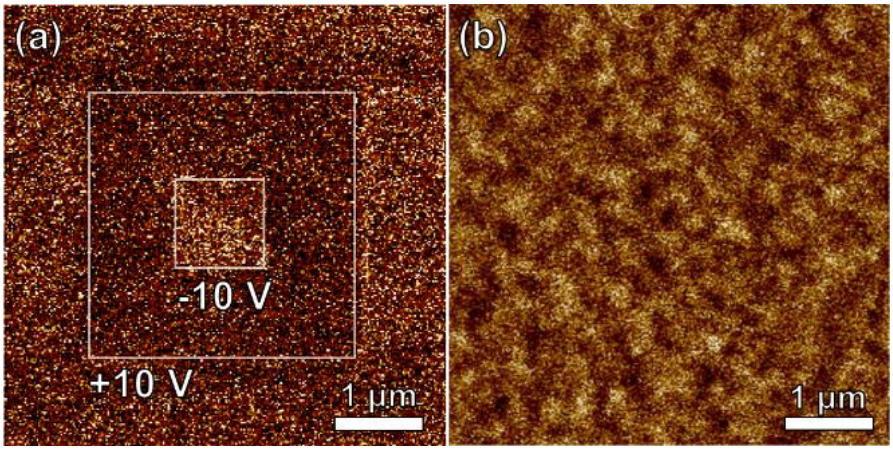

Figure 5.3 (a) Piezoresponse force microscopy (PFM) phase image of the bi-layer $CoFe_2O_4/BiFeO_3$ nanolaminate on Nb:$SrTiO_3$ (001) substrate after biased under ±10 V with the PFM tip, squares indicate different poling regions. (b) Magnetic force microscopy (MFM) phase image of the same sample, showing a grain-like magnetic domain pattern that is specific to $CoFe_2O_4$.

It is also important to verify the nature of interfacial coupling given the multiferroic nature of the $BiFeO_3$ phase. To examine the possible interfacial magnetic exchange coupling of the adjacent magnetic moments at the interface, the evolution of H_c values were recorded as a function of the top $CoFe_2O_4$ layer thickness under the bi-layer scheme, shown in Figure 5.5 (a). The $CoFe_2O_4$ thicknesses ranged from ~7-~30 nm while the $BiFeO_3$ thickness is fixed at ~40 nm. Single-phase $CoFe_2O_4$ samples that are directly grown on $SrTiO_3$ substrates are shown as well for comparison. There is an obvious discrepancy in the trends when the $CoFe_2O_4$ layer is interfaced with $BiFeO_3$ even when its thickness is similar, indicating an additional influence to magnetic anisotropy while the shape anisotropy is controlled. In the bi-layer design, H_c values decrease along with the thickness of the top $CoFe_2O_4$ layer. The composite H_c value eventually approaches the value of single-phase $BiFeO_3$ (denoted $H_{c,BFO}$) when the $CoFe_2O_4$ thickness is around the exchange length between $BiFeO_3$ and $CoFe_2O_4$ (I_{ex} ~ 6~7 nm). The exchange length I_{ex} was calculated using $I_{ex} = \sqrt{2A/\mu_0 {M_s}^2}$ (Nogués 2005), where A is the exchange stiffness constant of $BiFeO_3$ (3.22×10^{-12} J/m at room temperature) and μ_0 is the magnetic permeability of free space. However, it is worth noting that the intensity of such

interfacial magnetic coupling is a function of temperature, and is more intense under lower temperatures. As a result, the length of the exchange coupling might differ at higher temperatures and the magnetic domain structure of the composite is not necessarily stripe-like under room-temperature (Sone 2015). Because the bi-layer $CoFe_2O_4/BiFeO_3$ with a $CoFe_2O_4$ thickness ~15 nm has the best trade-off in terms of the contrast between the magnetic states (represented by H_c), the following functionality optimization is based on this thickness condition/ratio ($CoFe_2O_4/BiFeO_3$ = 15 nm/40 nm). Figure 5.4 (b) shows the PFM ramp mode measurements of the bi-layer ($CoFe_2O_4/BiFeO_3$ = 15 nm/40 nm) sample. During the measurement, a DC bias was applied through a nano-sized scanning microscope tip, and the ferroelectric domains were locally excited via converse-piezoelectric effect. The piezoresponse phase scan exhibits a hysteresis profile with 180° switching, while the corresponding deflection measurement calculated by the piezoresponse amplitude change shows a signature butterfly-like loop, both indicate the existence of a non-volatile strain interaction resulted from ferroelectric switching. This type of non-volatile behavior would then lead to a non-volatile magnetoelectric coupling in the composite design, and the simultaneous action of the antiferromagnetic switching would enhance the coupling effect. By taking the slope of the butterfly loop, the piezoelectric coefficient d_{33} is determined to be ~10 pm/V for the bi-layer sample, consistent with the literature values with a similar thickness (Zhao 2012).

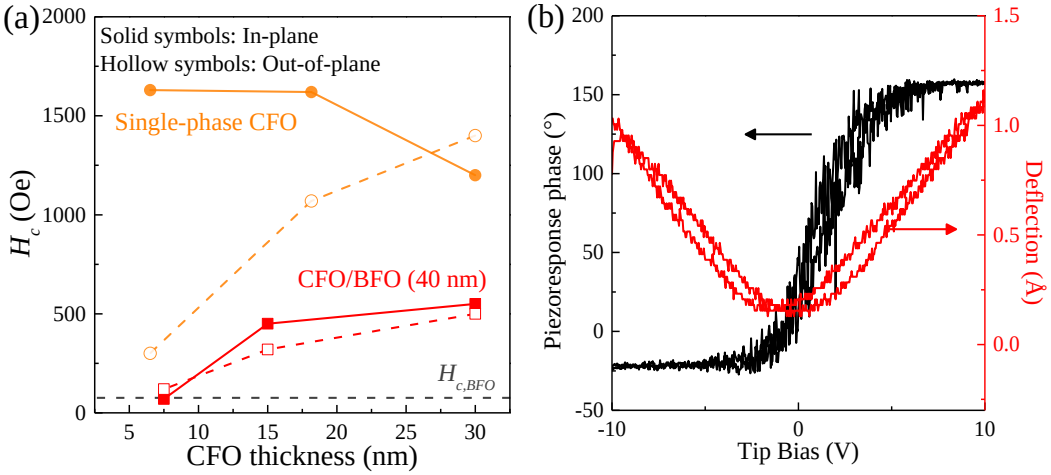

Figure 5.4 (a) Comparison of the magnetic coercive fields (H_c) of the bi-layer $CoFe_2O_4$ (~7-~30 nm) /$BiFeO_3$ (fixed at 40 nm) composite and single-phase $CoFe_2O_4$ thin film as a function of $CoFe_2O_4$ thickness along the in-plane and out-of-plane direction. Bi-layer $CoFe_2O_4$/$BiFeO_3$ composites showed much lower H_c values. Grey dashed lines represent the H_c value of single-phase $BiFeO_3$ at 40 nm. (b) Piezoresponse force microscopy (PFM) ramp mode measurements of a bi-layer $CoFe_2O_4$ (15 nm)/$BiFeO_3$ (40 nm) nanolaminate. Switching of the piezoresponse phase (black) and deflection (red) indicates piezoelectric strain coupling.

After the multiferroicity is confirmed in the ALD-synthesized $CoFe_2O_4$/$BiFeO_3$ bi-layer nanolaminate, it is necessary to utilize the advantages that ALD could offer to further optimize the functional properties. Here, a nanolayering strategy was employed by leveraging the atomic precision that ALD provides during material growth under the nanolaminate scheme. In this set of experiments, the total ratio between $CoFe_2O_4$ and $BiFeO_3$ were fixed at 15 nm and 40 nm respectively, while the total numbers of layers were altered from two to five.

Figure 5.5 (a) shows the evolution of the P_r and M_s as a function of the total number of layers within the nanolaminate. The P_r and M_s values were extracted from the *M-H* and *P-E* loops respectively, and serves as the indicators for the strengths of the samples' functional properties. In terms of ferroelectricity, the overall polarization of the $CoFe_2O_4$/$BiFeO_3$ composite increases from ~12 μC/cm^2 to ~17 μC/cm^2 at the tri-layer structure and dropped back to ~7 μC/cm^2 for the four and five-layer structures. Although it is known that the number of heterointerfaces in the nanolaminate would improve the overall ferroelectricity by reducing

the leakage behavior (Liu 2008, Barman 2015, Lee 2015), a decrease in the polarization values is observed when further layering the nano-laminates to more than four layers. Figure 5.5 (b) shows the XRD θ-2θ scans of the $CoFe_2O_4$/$BiFeO_3$ nano-laminates, showing the $BiFeO_3$ 001_{pc} and $SrTiO_3$ 001 reflection under different layering schemes. The definition of the $BiFeO_3$ 001_{pc} peak decreases for the four and five-layer structures, correlating to the decrease in polarization. The observation in XRD is likely due to the decreased phase stability under nanoscale as well as the decreased $BiFeO_3$ crystallinity when grown on polycrystalline $CoFe_2O_4$ surface, both of which lead to the decrease in ferroelectricity. The decreased phase stability under nanoscale is due to the increase in surface energies when the amount of interfacial area per volume ratio increases (Bajaj 2015). Such decrease in phase stability is also likely the cause for the M_s decrease from ~125 emu/cm^3 in the tri-layer structure to ~30 emu/cm^3 in the four-layer and five-layer structures. $CoFe_2O_4$ is a ferrimagnetic complex oxide in which the magnetic dipoles originate from the adjacent Co^{2+} and Fe^{3+} cations align in an antiparallel fashion, and the intensified intermixing between $BiFeO_3$ and $CoFe_2O_4$ would break the alignment and deteriorate overall magnetism intensity. In brief, it is shown that the nanolayering approach could simultaneously improve and impede the functional properties at nanoscale, and the trade-off between the aforementioned factors has to be considered for an optimized nanostructure.

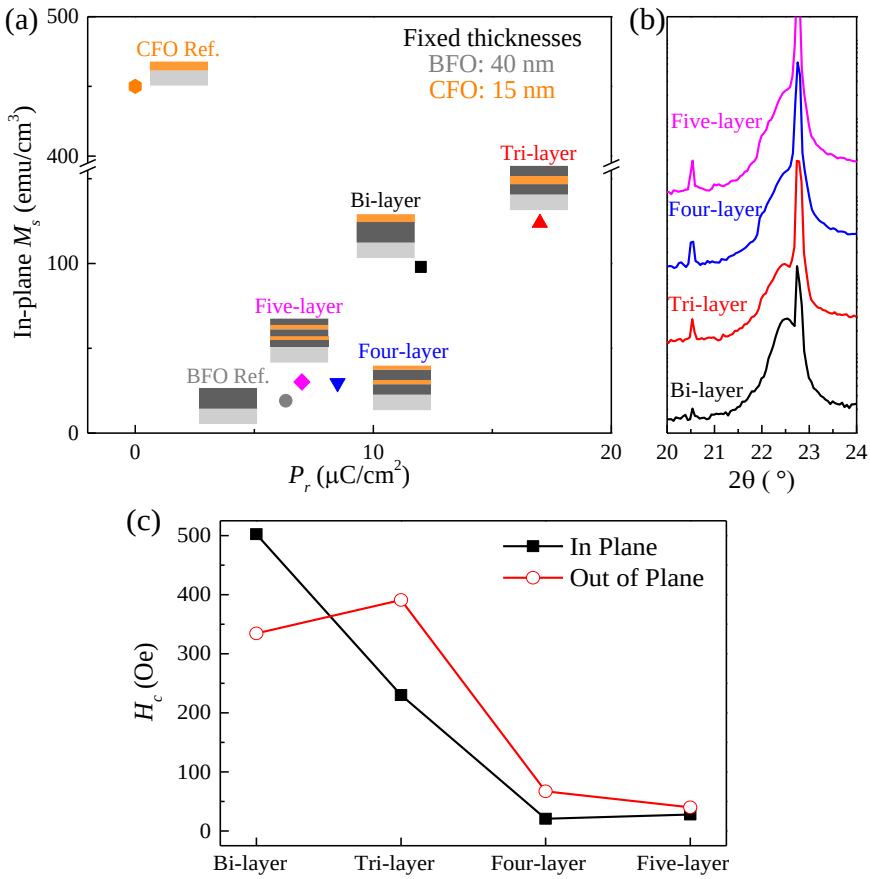

Figure 5.5 (a) Remnant polarization (P_r) and in-plane saturation magnetization (M_s) as a function of total layer numbers in the $CoFe_2O_4/BiFeO_3$ nano-laminates. The total volume of the composite and the ratio between $CoFe_2O_4/BiFeO_3$ were kept at a constant. Results of single-phase $CoFe_2O_4$ and $BiFeO_3$ are shown as references. The tri-layer structure showed an optimized functionality. (b) XRD spectra of the $CoFe_2O_4/BeiFeO_3$ nano-laminates under different layering schemes. $BiFeO_3$ 001 reflection became less defined with increasing number of total layers. (c) Evolutation of magnetic coercivity (H_c) values as a function of layering schemes.

Figure 5.5 (c) shows the evolution of H_c values as a function of the number of layers. An in-plane to out-of-plane anisotropy change was observed, showing a competition between strain and shape anisotropy that can be leveraged in the terms of designing magnetoanisotropy. Here, the tri-layer $BiFeO_3$ (20 nm)/$CoFe_2O_4$ (15 nm)/$BiFeO_3$ (20 nm) structure shows an optimal functionality with P_r and M_s values of ~17 μC/cm^2 and ~125 emu/cm^3 respectively as well as an out-of-plane anisotropy. In addition, it must be noted that the nano-laminates presented here exhibit applicable properties when it is only tens of nanometers, while the

multiferroic composite systems achieved in other reports are often ≥100 nm (Eerenstein 2007, Heron 2014, Aimon 2015), differentiating ALD from other synthesis techniques for enabling multiferroic composites at the nanoscale. It is also believed that the aforementioned problems regarding interfacial diffusion and film crystallinity may be mitigated by optimizing the annealing parameters carefully.

In summary, this section demonstrated the very first ALD synthesis of high-quality $CoFe_2O_4/BiFeO_3$ multiferroic nano-laminates on STO (001) substrates and showed great promise for the development of magnetoelectric devices. Both ferroelectricity and magnetism were confirmed macroscopically and microscopically. The nano-laminates exhibited attainable functional properties with a total thickness of ~55 nm, lower than other multiferroic composite systems reported and is very attractive for nanoscale integrations. Moreover, a nanolayering strategy was employed to obtain an optimal tri-layer $BiFeO_3$ (20 nm)/$CoFe_2O_4$ (15 nm)/$BiFeO_3$ (20 nm) scheme with the precise and self-limiting nature of ALD processing. The optimized tri-layer structure showed a much higher P_r of ~17 μC/cm^2, corresponding to a ~42% increase when compared to the bi-layer structure. The magnetization of the tri-layer structure is retained, showing an M_s value of ~125 emu/cm^3.

5.2. Si-Integration of Tri-Layer $BiFeO_3/CoFe_2O_4/BiFeO_3$

Another main advantage of ALD processing is industrial CMOS compatibility, and the possibility of integrating the optimized tri-layer layer $BiFeO_3$ (20 nm)/$CoFe_2O_4$ (15 nm)/$BiFeO_3$ (20 nm) nanolaminate onto Si-substrates was therefore explored. The tri-layer sample was grown onto $SrTiO_3$ (001)-buffered p-Si (001) substrates by ALD with the same processing parameters. An 8-nm (20 unit cells) thick $SrTiO_3$ buffer layer was synthesized by molecular beam epitaxy (MBE) on Si (001). The use of the $SrTiO_3$ buffer layer for Si-integration is a widely adopted strategy for the epitaxial integration of functional complex

oxides on Si, owing to the well-studied epitaxial growth of $SrTiO_3$ on Si (001) surface (McKee 1998, McDaniel 2013, Kim 2014, Ngo 2014).

Similar post-deposition RTA steps were conducted to promote film crystallinity, but with two different time durations. Figure 5.6 (a) shows the XRD spectra of the tri-layer sample on $SrTiO_3$/Si substrates with an annealing step of 60 and 30 seconds. The emergence of TiO_2 101 and SrO 002 peaks in the 60-second annealed sample indicates the phase separation of the $SrTiO_3$ buffer into TiO_2 and SrO, while the 30-second annealing limits such effect. Figure 5.6 (b) and (c) shows the AFM surface topography images of the sample annealed for 60 and 30 seconds, respectively. The sample that undergoes a 60-second anneal shows an intensified surface island formation (R_a = 2.76 nm) while the 30-second annealed sample exhibits a smooth surface (R_a = 1.47 nm), highlighting the importance of RTA duration for minimizing the separation and intermixing of phases in $CoFe_2O_4/BiFeO_3$ nano-laminates on $SrTiO_3$ (001)-buffered Si (001) substrates.

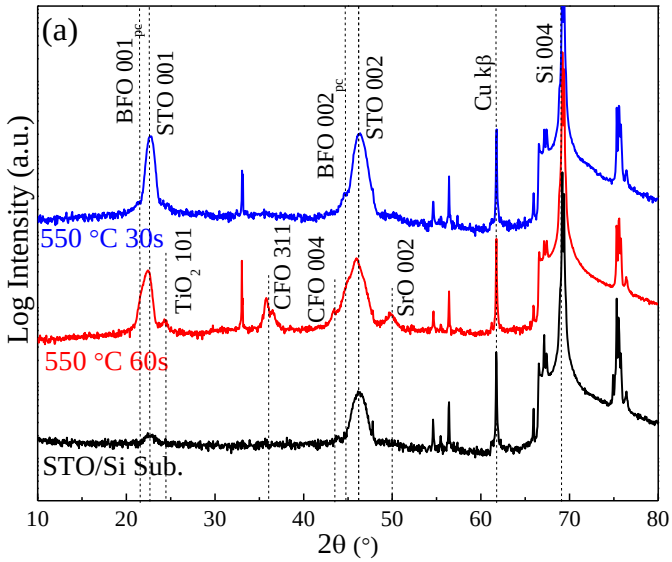

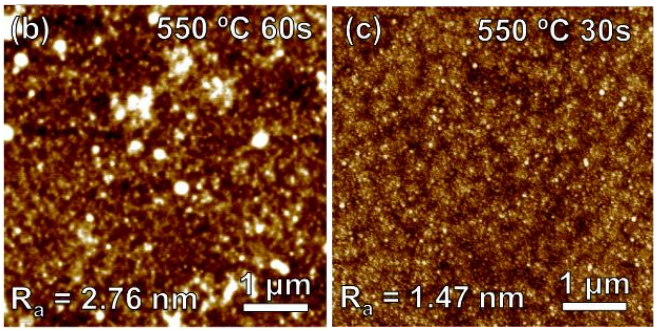

Figure 5.6 (a) XRD spectra of the tri-layer $BiFeO_3$ (20 nm)/$CoFe_2O_4$ (15 nm)/$BiFeO_3$ (20 nm) nano-laminates on $SrTiO_3$ (8 nm)/Si (001)substrates under different annealing conditions. Sample with a shorter annealing period shows less impurity phases. AFM surface topography images of tri-layer sample with annealing durations of (b) 60 seconds and (c) 30 seconds. Sample with 30s annealing period shows a smoother surface.

Functional properties of the tri-layer nanolaminate on STO-buffered Si (001) substrates were characterized after obtaining an optimal annealing condition. Figure 5.7 (a) shows the *M*-*H* hysteresis loop of the tri-layer sample. Retained M_s and H_c values when compared to the sample of the same structure on $SrTiO_3$ (001) substrate verified the high-quality ALD growth on $SrTiO_3$/Si substrates. On the other hand, while sample ferroelectricity was confirmed via *P*-*E* measurements, as shown in Figure 5.7 (b), it exhibited a lowered polarization value (P_s ~4 µC/cm^2, no P_r observed), as well as an imprint behavior that shifted the hysteresis loop to the positive direction. For the ferroelectric measurements, the voltage was driven from the bottom of the nanolaminate stack and returned from the patterned top electrode, indicating to a polarization that is favored toward the substrate (inset of Figure 5.7 (b) shows a schematic). Such imprint effect is resulted by the incorporation of the $SrTiO_3$ buffer layer. Since the MBE growth of epitaxial $SrTiO_3$ (001) on Si (001) by MBE requires a minimal SiO_2 formation at the $SrTiO_3$/Si interface during the first couple monolayers (McKee 1998), the oxygen partial pressure has to be low enough initially and thus leads to the formation of oxygen vacancies. The interfacial oxygen vacancies then create a build-in *E*-field in the $SrTiO_3$ buffer, leading to a downward polarization in the adjacent tri-layer nanolaminate. Mitigating ferroelectric imprint

effects is an ongoing field of study, with a variety of proposed mechanisms and possible solutions. For instance, the insertion of a non-switchable polar layer (Ghosh 2016) and a symmetric contact condition across the ferroelectric capacitor (Liu 2016) is shown to be effective in achieving a tunable imprint behavior. Although the imprint effect must be resolved to enable an effective magnetism switching of the nanolaminate, the data presented here demonstrated the potential of ALD in integrating high-quality magnetoelectric multiferroic composites onto Si substrates.

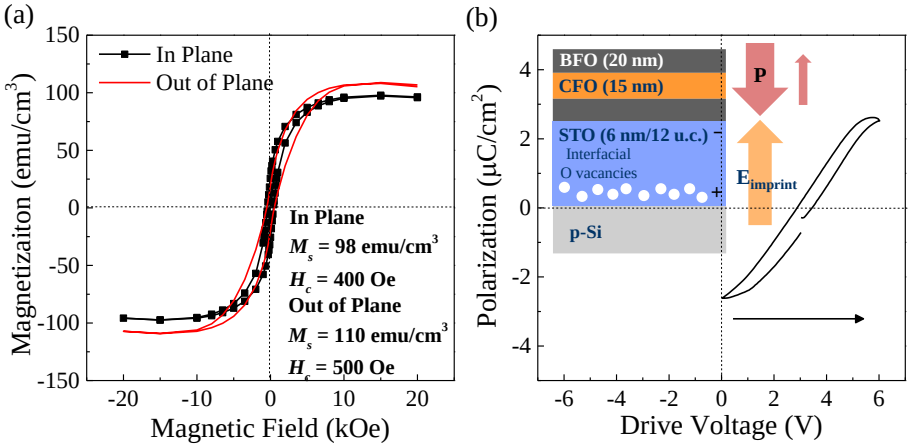

Figure 5.7 (a) In-plane and out-of-plane *M-H* hysteresis loops of the tri-layer nanolaminate, showing a retained magnetic behavior when compared to the sample grown on $SrTiO_3$ (001) substrate (see Figure 5.6 (b) and Figure 5.5 (a)). (b) *P-E* hysteresis loop of the same sample on $SrTiO_3$-buffered Si (001) substrate, confirming the ferroelectricity. The shift of the *P-E* hysteresis along the *x*-axis indicates a ferroelectric imprint effect that is preferred towards the substrate. Inset shows a schematic for the imprint effect.

In summary, the optimized tri-layer structure obtained in Section 5.1 was integrated on Si (001) substrates with the help of a MBE-deposited $SrTiO_3$ (001) layer that is ~8 nm in thickness. Additional fine-tuning in RTA conditions limits the phase separation of the $SrTiO_3$ buffer layer, leading to a retained magnetism of M_s ~100 emu/cm^3. Although the sample showed ferroelectric imprint that could impede its magnetoelectric coupling performance, it demonstrates the capability of using ALD to integrate multiferroic composites into actual industrial processes as well as magnetoelectric nanoelectronics.

5.3. Magnetoelectric Coupling in Tri-Layer $BiFeO_3/CoFe_2O_4/BiFeO_3$

In this section, magnetoelectric coupling was then characterized and quantified to benchmark the outcomes obtained in this work with other literature reports. In this section, the magnetoelectric coupling measurements was conducted on the tri-layer layering scheme since it is the structure with the best trade-off between ferroelectricity and magnetism, which leads to a maximized magnetoelectric coupling. In addition, the nature of interfacial coupling in the presented $BiFeO_3$ and $CoFe_2O_4$ is characterized as well. Magnetoelectric coupling is characterized microscopically first to confirm voltage-controlled magnetism via PFM/MFM and a poled scanning SUQID method, and then quantified using a bulk SQUID MPMS setup with after the sample is electrically biased with a poling station.

In order to confirm the coupling effect that was observed in the bi-layer design, both PFM measurements and scanning-SQUID measurements were utilized to observe the strain and magnetic interactions in the tri-layer sample. Figure 5.8 (a) shows the PFM ramp mode measurements. Similar to the bi-layer case, the 180° switching and the characteristic butterfly-shaped loop confirms a retained piezoelectric behavior. The piezoelectric coefficient d_{33} is calculated to be ~10 pm/V, similar to the bi-layer scheme as well as other reports on ALD-synthesized $BiFeO_3$ (Coll 2015, Deepak 2015). The coercive voltages observed from Figure 5.8 (a) are consistent with each other but are slightly asymmetric, which might be related to the clamping effect from the neighboring grains (Plokhikh 2017) as well as tip wear and tear during the measurements.

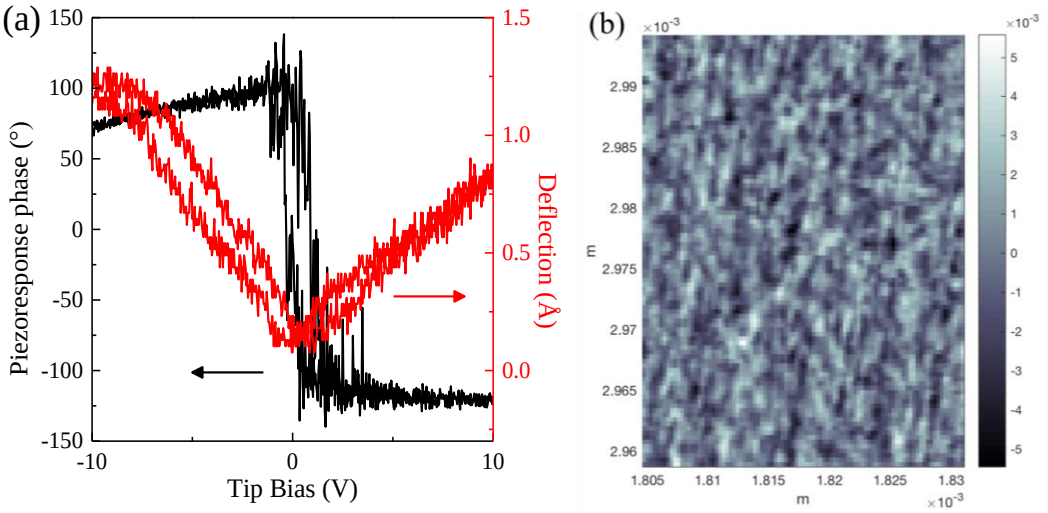

Figure 5.8 (a) Piezoresponse force microscopy (PFM) ramp mode measurements of a tri-layer $BiFeO_3$ (40 nm)/$CoFe_2O_4$ (15 nm)/$BiFeO_3$ (20 nm) nanolaminate. Switching of the piezoresponse phase (black) and deflection (red) indicates piezoelectric strain coupling. (b) Surface magnetic domain image of the tri-layer sample obtained at 4K via scanning SQUID, showing a stripe-like structure that is specific to $BiFeO_3$ thin films.

Figure 5.8 (b) shows the surface magnetic domain image obtained with the scanning SQUID setup at 4K. It is clear that the measured tri-layer sample exhibited a stripe-like texture that is specific to $BiFeO_3$ antiferromagnetic (ferroelectric) domains (Zhao 2006) instead of the grain-like $CoFe_2O_4$ structure (Pham 2017), indicating that the magnetic exchange interaction is indeed taking place at $BiFeO_3$/$CoFe_2O_4$ interface. Such magnetic interaction could alter the magnetic anisotropy (Sone 2015), as well as induce a synergic effect with the strain interaction for a more pronounced magnetoelectric coupling effect (Wang 2014). However, it is worth noting that the intensity of such interfacial magnetic coupling is a function of temperature and is more intense at low temperatures. As a result, the effective length of the exchange coupling might differ at higher temperatures and the magnetic domain structure of the nanolaminate is not necessarily stripe-like under room-temperature, as observed in the MFM scans (Figure 5.9 (a)).

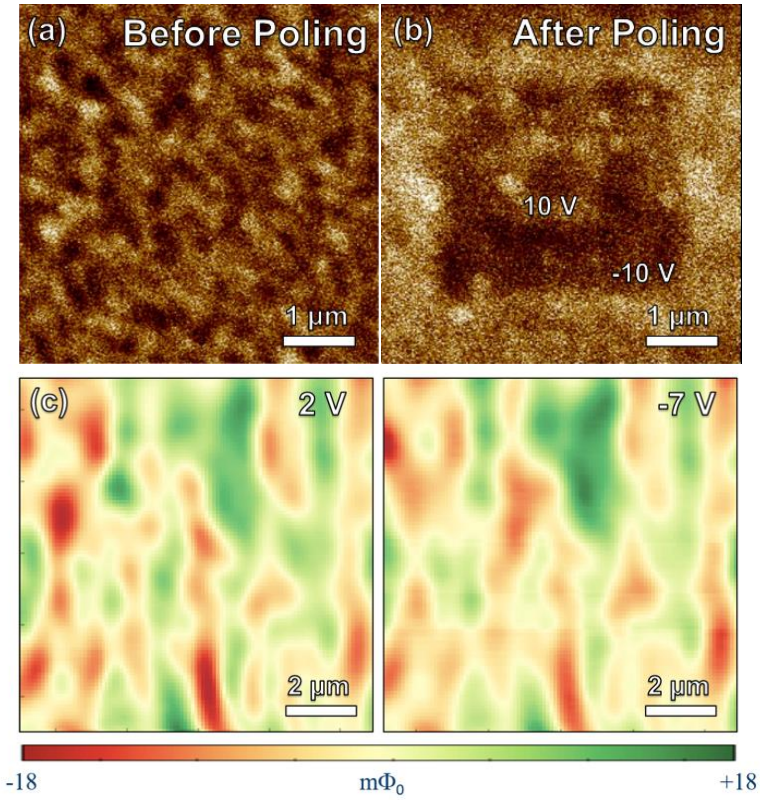

Figure 5.9 Room-temperature magnetic force microscopy (MFM) phase images of the tri-layer $BiFeO_3$ (20 nm)/$CoFe_2O_4$ (15 nm)/$BiFeO_3$ (20 nm) composite (a) before and (b) after surface electrical poling. The contrast between the poling areas indicates magnetoelectric coupling. (c) Surface magnetic domains measured at 4 K via scanning SQUID under 2 V and -7 V applied voltage. Magnetic domain wall movements verify magnetoelectric coupling.

To further characterize magnetoelectric coupling, MFM and PFM were used in a combinatorial fashion to observe the change of magnetic domains with an applied bias. Both PFM and MFM images were acquired by MESP probes by a Bruker Dimension Icon Atomic Force Microscope with ScanAsyst. Figure 5.9 (a) and (b) showed the surface MFM phase image of the magnetic domains before and after PFM electrical poling respectively. The grain-like MFM domain structure in Figure 5.9 (a) is coherent with previous reports on $CoFe_2O_4$ magnetic domains (Abes 2016, Pham 2017). The observed domain sizes were ~200 nm. For the PFM poling scans, an 3×3 μm^2 area scan was first conducted under –10 V, followed by an 1×1 μm^2 area scan under +10 V to generate a contrast in surface ferroelectric states between different poling regions. A 5×5 μm^2 MFM surface scan was then conducted to observe the

change in magnetic domains due to induced ferroelectric switching. The contrast in magnetic domains between different poling regions in Figure 5.9 (b) indicates a robust room-temperature magnetoelectric coupling.

Since the probe used in the MFM/PFM measurements was magnetic, it is necessary to verify the magnetoelectric coupling via other characterization techniques. *In situ* electrical poling scanning-SQUID measurements were conducted as a cross-reference for the observed magnetoelectric coupling in MFM/PFM measurements. To bias the sample *in situ*, patterned Au (100 nm) electrodes with a Cr (10 nm) adhesive layer were deposited onto the top surface of the tri-layer samples via e-beam evaporation to allow the application of a gate voltage during scanning SQUID measurements. The measurements were conducted under 4K for an optimal signal to noise ratio. The diameter of the circular electrodes was 400 μm. Figure 5.9 (c) shows the scanning SQUID image of a 10×10 μm^2 area under +2 V and –7 V. Unlike the domain patterns observed via MFM, the magnetic domain observed in scanning SQUID exhibited a domain structure that combined stripe-like and grain-like pattern, which is likely due the enhanced interfacial exchange coupling at low temperatures. The domains observed are ~500 nm-1 μm in size and the size discrepancy is due to the lower spatial resolution of the scanning SQUID setup. The diameter of the SQUID pick-up loop used was ~100 nm, which corresponds to an effective spatial resolution of ~ 500 nm. Meanwhile, the resolution of the MFM/PFM measurements could be down to a couple nanometers. By comparing to the two images in Figure 5.9 (c), the change in the domain microstructures under different poling voltages verifies magnetoelectric coupling in the sample. The changes are less pronounced compared to Figure 5.9 (a) and (b), which is most likely due the fact that the measurements were conducted under 4K, where the ferroelectric coercivity (E_c) would increase.

To further characterize and quantify the converse magnetoelectric coupling coefficient $\alpha_{converse}$ in the tri-layer design, the sample was then poled *ex situ* with an applied electric field that is perpendicular to the sample surface, followed by SQUID *M-H* hysteresis measurements. The sample is poled for 10 minutes prior to the individual SQUID measurements, and the effective electric field (E_{eff}) was calculated accordingly by dividing the voltage drop across the overall thickness of the sample (Chien 2016). Since the SQUID *M-H* hysteresis measurements were conducted without the existence of the electric field simultaneously, it is fair to assume that the overall polarization of the composite is at its ferroelectric remnant state, hence the change observed in magnetism is non-volatile.

In this setup, the applied electric field results in the change of ferroelectric states in $BiFeO_3$, which in turn changes the strain and magnetic state given its multiferroic nature. The changes are then transferred to the $CoFe_2O_4$ state via interfacial coupling, leading to a magnetoelectric effect. Shown in Figure 5.10 (a) and (b) and summarized in Figure 5.11 (a) are the *ex situ* poling SQUID results of the 55-nm thick tri-layer nanolaminate as a function of applied electric fields. The change in shape of the *M-H* hysteresis indicates room-temperature magnetoelectric couplings. Along with the increasing applied *E*-field, M_r tends to increase due to the change in magnetic anisotropy. The change in magnetic anisotropy is also verified by the decrease in the difference between in-plane and out-of-plane H_c values. A larger change in M_r is observed in the out-of-plane direction due to the substrate-clamping effect that impedes strain transfer along the in-plane direction. Such clamping effect is minimized along the out-of-plane direction due to the less dominance of mechanical constraints and thus the following discussions on extracting magnetoelectric coupling coefficients are based on the out-of-plane results. To extrapolate the converse magnetoelectric coupling coefficient $\alpha_{converse}$, here we consider the change M_r while using $\alpha_{converse} = {\Delta M_r}/{\Delta E}$ as M_r represents the sample's

magnetic strength without the presence of an external magnetic field. The M_r values have a ~15.6% difference after electrical poling, and the corresponding $\alpha_{converse}$ is ~22 Oe cm/kV.

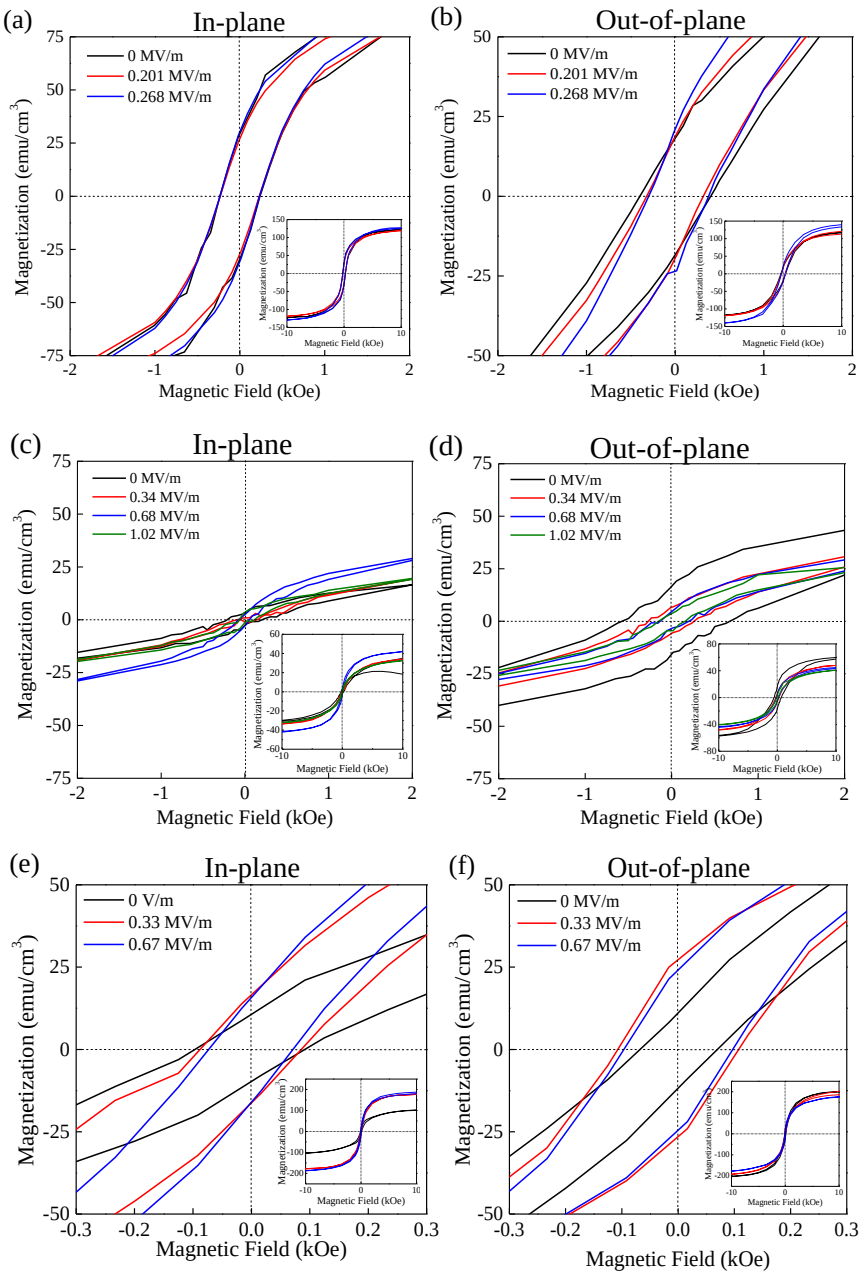

Figure 5.10 In-plane zoomed-in magnetic hysteresis loops of the (a) 55-nm, (c) 27-nm, and (e) 16-nm thick tri-layer $BiFeO_3/CoFe_2O_4/BiFeO_3$ composite as a function of applied voltage. Out-of-plane zoomed-in magnetic hysteresis loops of the (b) 55-nm, (d) 27-nm, and (f) 16-nm samples as a function of applied voltage. The shape change of the hysteresis loops and the change in remnant magnetization (M_r) indicates non-volatile magnetoelectric coupling. All measurements were conducted under room-temperature.

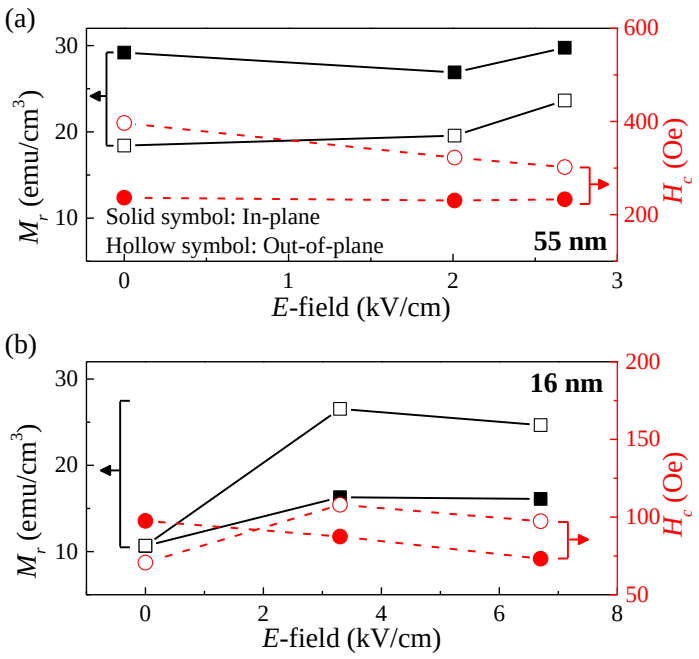

Figure 5.11 Remnant magnetization (M_r) and coercive field (H_c) of the tri-layer $BiFeO_3/CoFe_2O_4/BiFeO_3$ sample as a function of applied electric field with (a) 55 nm and (b) 16 nm in thickness. The 16-nm thick sample shows a switch in magnetic easy axis as well as a larger change in M_r. All the measurements were conducted under room-temperature.

To further investigate the importance of interfacial area per volume to overall magnetoelectric coupling, the sample was then scaled down to smaller thicknesses with the exact structure and ratio between $CoFe_2O_4$ and $BiFeO_3$. The synthesis of these thinner samples was achieved by leveraging the highly controllable and precise nature of ALD during materials growth. Two other thicknesses, 27 and 16 nm were investigated with similar characterizations. The *ex situ* poling SQUID results for the two samples are shown in Figure 5.10 (b)-(f) and summarized in Figure 5.11 (b). Similarly, the out-of-plane scans showed a larger change when comparing to the in-plane scans due to the absence of substrate clamping. It is clear that the change in M_r upon electrical poling in the 16-nm thick sample is much higher than the 55-nm thick sample. Furthermore, an in-plane to out-of-plane easy axis transition is observed upon electrical poling in the 16-nm thick sample, highlighting the competition between strain shape anisotropy in sample magnetism. Unlike the thicker samples, however, the change in M_r in the

16-nm thick sample is much larger (~60.2% difference) and corresponds to a ~3× higher converse magnetoelectric coefficient $\alpha_{converse}$ of ~64 Oe cm/kV. It is noteworthy that the obtained magnetoelectric coupling is not only comparable to many works on other materials systems, which mostly ranged from 10-100 Oe cm/kV (Thiele 2007, Heron 2014), but also one of the rare report on room-temperature magnetoelectric coupling in a 2D-2D geometry.

To unveil the nature of the enhancement for magnetoelectric coupling with sample scaling, we examined the correlation between functional properties and the resulted magnetoelectric coupling of each thickness conditions. A comparison between all three thicknesses is summarized in Figure 5.12. It is shown that both ferroelectricity and magnetism are reduced with decreasing thicknesses. The ferroelectric polarization exhibits a decreasing trend while E_c increased with lowering thicknesses (Figure 5.12 (a)), both resulted from a reduced amount of ferroelectric material within a capacitor (Liu 2014) and ferroelectric size effects (Chu 2007) at lower thicknesses. On the other hand, out-of-plane M_r and H_c exhibited in Figure 5.12 (b) a decreasing trend and reached ~12 emu/cm^3 and ~70 Oe respectively. Larger H_c values were expected with increased magnetic shape and strain anisotropy at lower thicknesses(Pham 2017) and this can be explained by the existence of the magnetic coupling at $CoFe_2O_4$/$BiFeO_3$ interface, where magnetically isotropic $BiFeO_3$ (Pham 2015) decreases $CoFe_2O_4$ anisotropy lead to a decrease in overall H_c. Interestingly, the magnetoelectric coupling shown in Figure 5.12 (c) is enhanced at lower thicknesses despite the drastic decrease in film functionalities, suggesting the enhancement in magnetoelectric coupling by an increased interfacial area per volume dominates the system and thus outweighs the weakened functionality at lower thicknesses.

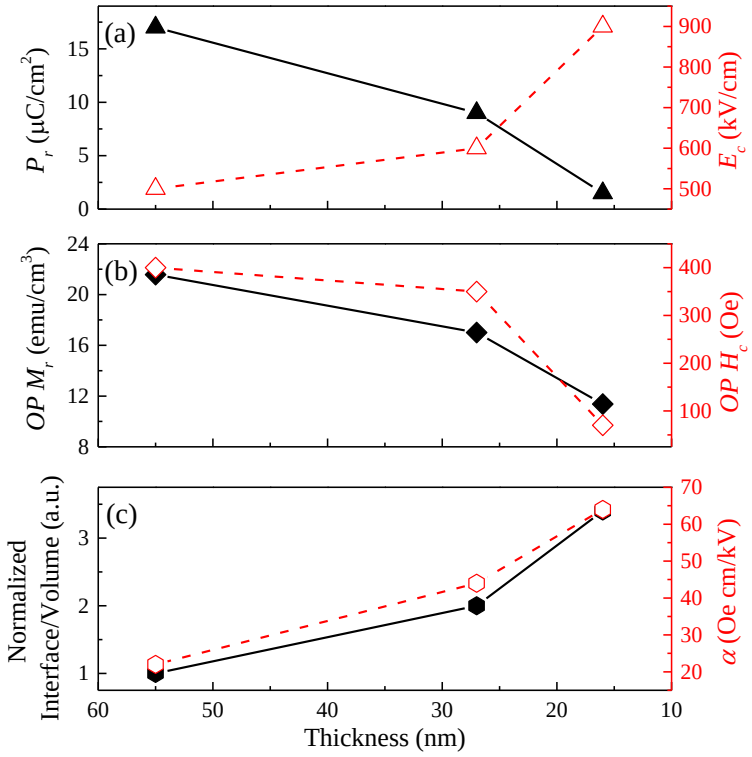

Figure 5.12 Magnetoelectric behavior of tri-layer $BiFeO_3/CoFe_2O_4/BiFeO_3$ nano-laminates as a function of total nanolaminate thicknesses. (a), (b), and (c) shows sample ferroelectricity (remnant polarization P_r and electrical coercivity H_c), magnetism (remnant magnetization M_r and magnetic coercivity H_c), and magnetoelectric coupling coefficient α as a function of total thickness respectively.

In summary, both microscopic and macroscopic magnetoelectric effects were obtained in a tri-layer $BiFeO_3/CoFe_2O_4/BiFeO_3$ 2D-2D nanolaminate design using scanning probe microscopy (SPM), *in situ* electrical poling scanning SQUID magnetometer, and *ex situ* electrical poling SQUID magnetometer setup. Although multiferroic composites that are comprised of $BiFeO_3$ and $CoFe_2O_4$ were reported previously based on exchange-bias (Sone 2015) and strain-mediated coupling (Aimon 2015) respectively, the presented work the first report that considers both coupling effects simultaneously. PFM and scanning SQUID conducted on the 55-nm thick tri-layer $BiFeO_3$ (20 nm)/$CoFe_2O_4$ (15 nm)/$BiFeO_3$ (20 nm) verified both the strain and magnetic interactions at the interface. A converse magnetoelectric

coupling coefficient $\alpha_{converse}$ of ~22 Oe cm/kV is achieved, whereas the scaling of the sample from 55 to 16 nm resulted in a ~3× increase in $\alpha_{converse}$ to ~64 Oe cm/kV. Such increase is believed to be contributed from an increase in interfacial area per volume within the nanolaminate.

5.4. Summary

Ferrimagnetic $CoFe_2O_4$ (15 nm) and multiferroic $BiFeO_3$ (40 nm) were integrated into nano-laminates with 2D-2D connectivity onto SrTiO3 (001) and $SrTiO_3$-buffered Si (001) substrates using the RE-ALD processes developed in the previous section. The bi-layer design shows a retained magnetism (~100 emu/cm^3, normalized by the overall thickness) as well as an enhanced ferroelectric polarization (~12 μC/cm^3), confirmed by both macroscopic hysteresis measurements and scanning probe measurements. Both magnetic and strain coupling at the interface is observed. By leveraging the precise nature of ALD synthesis, a nanolayering strategy is demonstrated effective in tailoring and optimizing the respective functional properties. The optimal tri-layer $BiFeO_3$ (20 nm)/ $CoFe_2O_4$ (15 nm)/ $BiFeO_3$ (20 nm) structure exhibited a ~42% increase in the polarization is obtained (~17 μC/cm^3), and a ~25% increase in magnetism to ~125 emu/cm^3. It is noteworthy that the nano-laminates exhibited comparable functional properties with a total thickness of ~55 nm, much thinner than other multiferroic composite systems reported and is very attractive for nanoscale integrations. Moreover, despite the ferroelectric imprint effect, the integration of the tri-layer structure onto buffered Si (001) substrates highlights the potential of utilizing ALD processing in current industrial CMOS technologies.

Lastly, magnetoelectric characterizations were carried out on the tri-layer structure on $SrTiO_3$ (001). Microscopic characterization such as PFM/MFM and *in situ* poling scanning SQUID suggested a voltage-controlled magnetism in the samples, while macroscopic SQUID

hysteresis scans after electrical poling suggested a comparable and non-volatile room-temperature converse magnetoelectric coupling with $\alpha_{converse}$ of ~22 Oe cm/kV. The scaling of the sample from 55 nm to 16 nm in total thickness leads to a ~3× increase in magnetoelectric coupling with $\alpha_{converse}$ up to ~64 Oe cm/kV. The importance of interfacial area per volume is unveiled by considering the respective functional properties as well as magnetoelectric coupling as a function of total nanolaminate thickness. This work could serve as a guideline for achieving an enhanced magnetoelectric behavior in multiferroic composite nano-laminates synthesized via ALD.

Chapter 6. Multiferroic Integration of Undoped FE-HfO_2 and $CoFe_2O_4$

The multiferroic integration of ferroelectric HfO_2 (FE-HfO_2) is another main emphasis of this thesis. FE-HfO_2 thin film exhibits desirable electrical properties and superior compatibility with CMOS technology compared to conventional perovskite ferroelectrics, both of which are critical for the development of multiferroic composite research. In this work, the first multiferroic composite integration with undoped FE-HfO_2 and ferrimagnetic $CoFe_2O_4$ on Si substrates via radical-enhanced atomic layer deposition (RE-ALD) is demonstrated. In the composite design, $CoFe_2O_4$ simultaneously serves as the confinement layer and an active magnetic layer.

Composite ferroelectricity was studied as a function of FE-HfO_2 film thickness (6 and 10 nm) as well as post-deposition annealing temperatures (500-800 °C). Film crystallinity was investigated as well through the use of a synchrotron beam source to understand the structural evolution. 700 °C annealed $CoFe_2O_4$ (10 nm)/FE-HfO_2 (6 nm) composites on TiN (10 nm)/p-Si (111) exhibited a remnant polarization (P_r) ~5.5 μC/cm^2 and an electrical coercivity (E_c) ~2000 kV/cm as well as an out-of-plane magnetic anisotropy with a saturation magnetization (M_s) of ~155 emu/cm^3 and a magnetic coercivity (H_c) ranging from ~1000-3400 Oe. Lastly, magnetoelectric coupling effect was observed both microscopically and macroscopically with a magnetoelectric coupling coefficient (α) of ~5.5-16.8×10^{-8} s/m (~55-168 Oe cm/kV). With the desirable ferroelectric property and superior Si-compatibility that FE-HfO_2 can offer, this work not only highlights the potential of FE-HfO_2 based multiferroic composites in realizing magnetoelectric devices, but also unveils the possibility of utilizing functional structural confinement layers for achieving multifunctional composite heterostructures.

6.1. Ferroelectric HfO_2 Thin Films with $CoFe_2O_4$ Confinement Layers

After confirming the formation of FE-HfO_2 thin films, the next step forward is to probe the possibility of integrating FE-HfO_2 thin films with the magnetic phase of choice in this thesis, $CoFe_2O_4$. It is shown that the incorporation of structural confinement layers is necessary for stabilizing the ferroelectric orthorhombic phase in undoped HfO_2 thin films (Polakowski 2015). For this purpose, TiN is the most widely used structural confinement layer of choice in the field of FE-HfO_2 research with a thermal expansion coefficient $\alpha_{TiN} = 9.35\times10^{-6}$/K (Lomenzo 2014, Karbasian 2017, Lin 2018). Interestingly, $CoFe_2O_4$ has a similar thermal expansion coefficient $\alpha_{CFO} = 10\times10^{-6}$/K (Zhou 2012) and thus is a good candidate for stabilizing FE-HfO_2. Therefore, $CoFe_2O_4$ thin films were directly integrated onto HfO_2 thin films and the possibility of inducing ferroelectricity was explored. Since only 10-nm and 6-nm thick HfO_2 thin films exhibited ferroelectric behavior in Chapter 4, only these two HfO_2 thicknesses were studied in this section. For the fabrication process, the top 10-nm thick TiN confinement layer is replaced by RE-ALD synthesized $CoFe_2O_4$ (see Chapter 3) thin films of a similar thickness, and the remaining structure are identical between the two scenarios. Similarly, the crystal structure and the corresponding the ferroelectric behaviors were characterized after annealed at four different temperatures ranging from 500-800 °C.

Starting with 10-nm thick HfO_2 with 10-nm thick $CoFe_2O_4$, Figure 6.1 (a) shows the GAWAXS spectra of the $CoFe_2O_4$ (10 nm)/HfO_2 (10 nm) on TiN (10 nm)/p-Si (111) substrates with different annealing temperatures. The orthorhombic HfO_2 211_o reflection is observed in all measured samples, with an intensifying HfO_2 -111_m reflection with increased annealing temperature. This phenomenon suggests that although the ferroelectric orthorhombic phase was be stabilized at all temperatures, that higher annealing temperature would shift the crystal phase mixture more toward the monoclinic phase. Furthermore, the existence $CoFe_2O_4$ 311

peaks confirms the formation of ferrimagnetic $CoFe_2O_4$ phase, indicating a successful integration and the coexistence of the two phases.

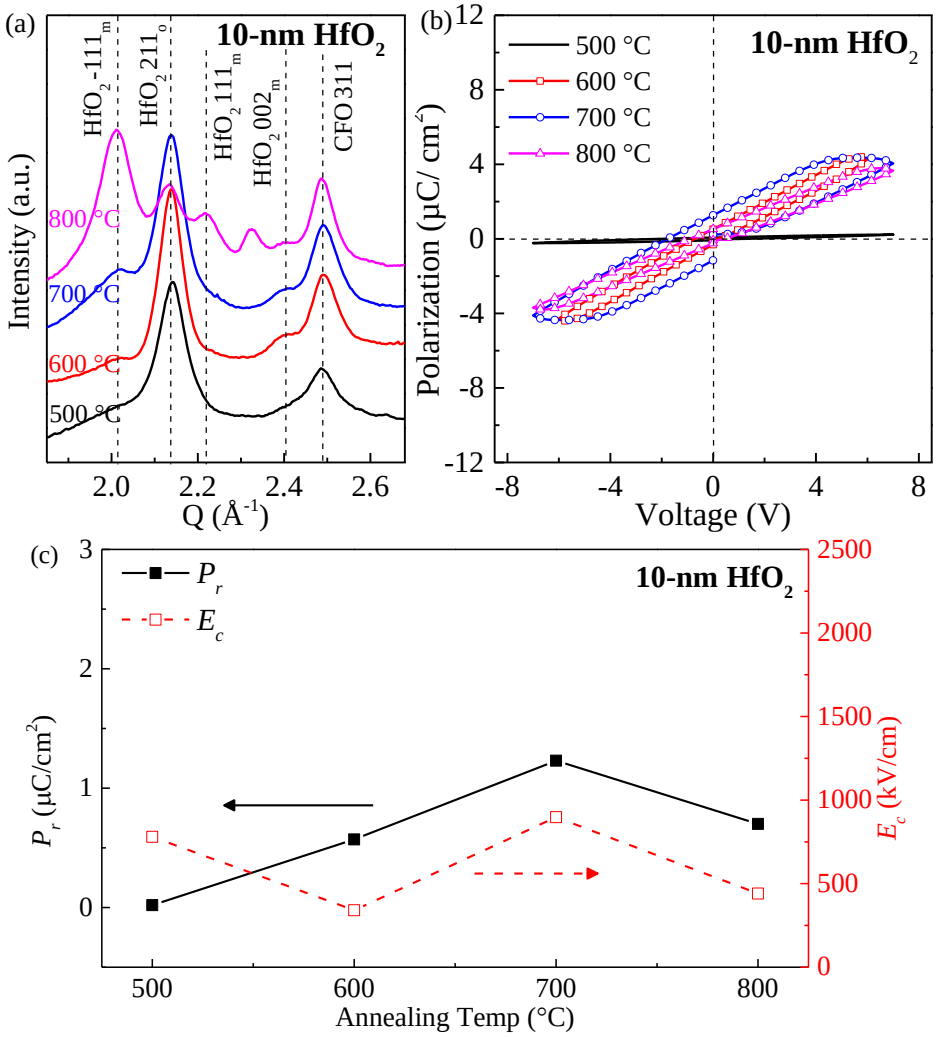

Figure 6.1 (a) GIWAXS spectra of the $CoFe_2O_4$ (10 nm)/FE-HfO_2 (10 nm) stack on TiN (10 nm)/p-Si(111) substrates annealed at 500-800 °C. The samples exhibited majorly *o*-phase HfO_2 reflections. $CoFe_2O_4$-related reflections verifies the coexistence of the two constuient phases. (b) *P-E* hysteresis loops of the corresponding samples annealed at different temperatures. The emergence of the *m*-phase HfO_2 reflections after 800 °C annealing corresponds to a decreased ferroelectricity. (c) Summary of P_r and E_c values as functions of annealing temperature.

The corresponding *P-E* hysteresis loops are shown in Figure 6.1 (b), all showing ferroelectric behavior. A summary is provided in Figure 6.1 (c). By referencing the GIWAXS spectra and the *P-E* measurement obtained from the 500 °C-annealed sample, it is speculated that the film remained largely amorphous given the shape of the *P-E* response (Figure 6.1(b)),

despite the strong orthorhombic HfO_2 211_o reflection detected. For the other samples, an optimal ferroelectric behavior with P_r ~1.23 μC/cm^2 and E_c ~898 kV/cm was obtained from the 700 °C-annealed sample, as the corresponding GIWAXS scan showed the most distinct HfO_2 211_o peak. Further increasing the annealing temperature to 800 °C resulted in the dominance of monoclinic HfO_2 phase and thus decreased P_r and E_c down to ~0.7 μC/cm^2 and E_c ~441 kV/cm, respectively. It is noteworthy that the orthorhombic reflection obtained with $CoFe_2O_4$ are more intense compared to than the ones obtained with TiN (see Figure 4.5 (a)).

Multiferroic $CoFe_2O_4$/FE-HfO_2 composites with 6-nm thick HfO_2 on TiN/p-Si (111) were subsequently investigated. Figure 6.2 (a) shows the GIWAXS spectra at different annealing temperatures, and both HfO_2-related as well as $CoFe_2O_4$-related peaks were observed. Similar to the case of TiN, all the samples exhibit orthorhombic reflections with no apparent monoclinic phase reflections beside the 500 °C-annealed sample. Moreover, the orthorhombic reflections obtained in this set of samples are also more intense and distinct than the case with TiN (see Figure 4.6 (a)) 500 °C annealing yielded an HfO_2 film that is mostly monoclinic, which can be verified by the weak ferroelectric behavior in Figure 6.2 (b). By comparing the other *P*-*E* hysteresis loops, it is shown that the P_r value reached a maximum value of ~5.43 μC/cm^2 at 700 °C annealing, corresponding to the sharpest HfO_2 211_o reflection in the GIWAXS scan. Similar to the case with 10-nm thick FE-HfO_2 layers, the ferroelectricity behavior as well as the sharpness of the orthorhombic phase reflection decreased after annealed under 800 °C.

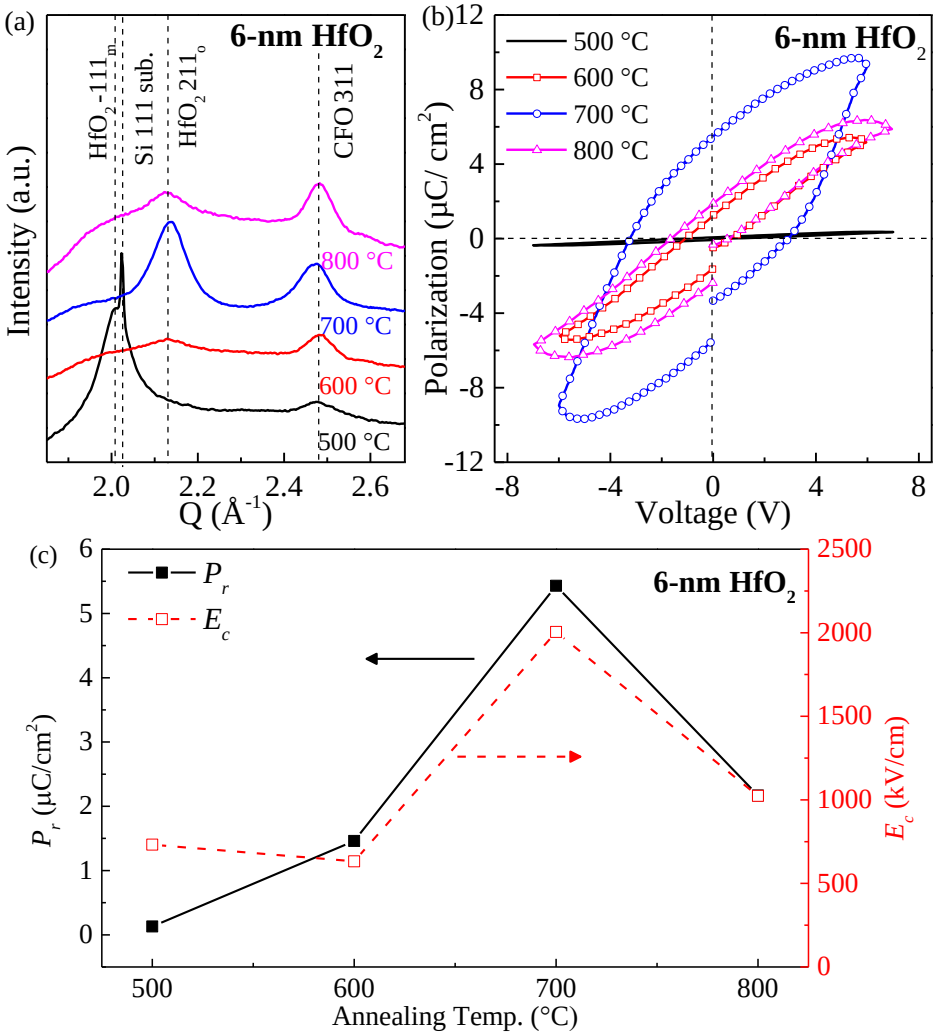

Figure 6.2 (a) GIWAXS spectra of the $CoFe_2O_4$ (10 nm)/FE-HfO_2 (6 nm) stacks on TiN (10 nm)/p-Si (111) annealed at 500-800 °C. The samples annealed at 600 °C and above exhibited only *o*-phase HfO_2 reflections. Family of $CoFe_2O_4$ reflections verifies the existence and crystallizaiton of the $CoFe_2O_4$. (b) *P-E* hysteresis loops of the corresponding stacks annealed at different temperatures. (c) Summary of P_r and E_c values as functions of annealing temperature.

A summary of the 10-nm and 6-nm thick HfO_2 thin films with 10-nm thick $CoFe_2O_4$ confinement layers is listed in Table 6.1. Two obvious trends can be observed. Firstly, the ferroelectricity is greater in the 6-nm HfO_2 samples, similar to the observation in the case with TiN. Secondly, the ferroelectric parameters in both cases reached their peak value with 700 °C annealing. The orthorhombic stabilization effect from $CoFe_2O_4$ confinement layers arises from the fact that it has a similar lattice constant and thermal expansion coefficient (a_{CFO} = 8.396 Å, α_{CFO} ~10×10^{-6} K^{-1} (Zhou 2012)) with TiN (a_{TiN} = 4.208 Å, α_{TiN} ~9.35×10^{-6} K^{-1} (Lomenzo

2014)). In addition, it is noteworthy that the ferroelectric behavior obtained here are much greater than the results obtained with TiN (see Table 4.1), where the higher thermal expansion coefficient from $CoFe_2O_4$ could be the major factor contributing to the enhancement. Due to the greatest ferroelectricity observed in the $CoFe_2O_4$ (10 nm)/HfO_2 (6 nm) with 700 °C annealing, the following magnetic and magnetoelectric characterizations were conducted under this condition.

Table 6.1 Summary of the ferroelectrcitiy induced in HfO_2 thin films with 10-nm thick $CoFe_2O_4$ confinement layers

t_{HfO2} (nm)	RTA Temp. (°C)	P_r (μC/cm^2)	E_c (kV/cm)
10	500	~0.02	~780
	600	~0.57	~341
	700	~1.23	~898
	800	~0.7	~441
6	500	~0.13	~732
	600	~1.46	~632
	700	~5.43	~2000
	800	~2.167	~1024

6.2. Magnetic and Magnetoelectric Properties of $CoFe_2O_4$ (10 nm)/FE-HfO_2 (6 nm) on TiN (10 nm)/p-Si (111) Substrates

After confirming the possibility of inducing FE-HfO_2 via $CoFe_2O_4$, it is necessary to confirm the magnetism in the composite design to claim multiferroicity of the system. Since the sample with 6-nm thick HfO_2 and 700 °C anneal exhibits the greatest ferroelectric behavior, its magnetic properties were further examined at first using a SQUID magnetometer for a potentially greatest magnetoelectric coupling.

Figure 6.3 (a) shows both the in-plane and out-of-plane *M-H* hysteresis loops obtained under room-temperature, confirming that the composite design is indeed a multiferroic with magnetism arising from the $CoFe_2O_4$ component. The saturation magnetization M_s of the composite design is ~155 emu/cm^3, lower than the ~200-300 emu/cm^3 value of a reference RE-ALD $CoFe_2O_4$ of a similar thickness on $SrTiO_3$ (001) (see Figure 6.3 (b)). The lower M_s is

primarily due to the difference in film crystallinity. In the case of $CoFe_2O_4$ grown on low-mismatch single-crystalline perovskite surfaces such as $SrTiO_3$ (001), an epitaxial relationship could be achieved at the interface and in turn resulted in textured-polycrystalline $CoFe_2O_4$ films (Coll 2014, Pham 2017). On the other hand, the presented case of growing $CoFe_2O_4$ on polycrystalline HfO_2 surface yields purely polycrystalline $CoFe_2O_4$ films as observed by the GIWAXS results (see Figure 6.1 (a) and Figure 6.2 (a)). Since it is shown that the amount of grain boundaries has a negative effect to the $CoFe_2O_4$ magnetism (Gatel 2013), the $CoFe_2O_4$ films grown on HfO_2 surfaces therefore exhibit a weaker overall magnetism. Nonetheless, the M_s values along the in-plane and out-of-plane directions are isotropic, indicating the absence of epitaxial grains and strains in the film, whereas the reference exhibited a difference between in-plane and out-of-plane M_s values.

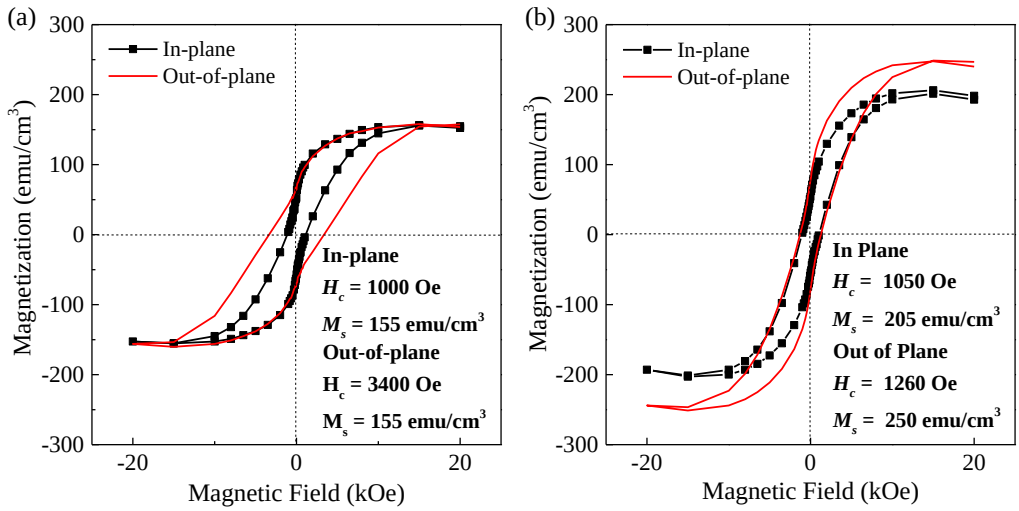

Figure 6.3 (a) Room-temperature in-plane (black solid line with symbols) and out-of-plane (red solid line) *M-H* hysteresis loops of the $CoFe_2O_4$ (10 nm) /FE-HfO_2 (6 nm) on TiN (10 nm)/p-Si (001) substrates with 700 °C RTA, comfirming the multiferroic behavior of the composite design. The composite showed an out-of-plane easy axis. (b) Room-temperature in-plane and out-of-plane *M-H* hysteresis loops of a reference 10-nm thick $CoFe_2O_4$ on $SrTiO_3$ (001) substrate, exhibiting slightly higher magnetizaiotn behaviors that are more isotropic.

In terms of the magnetic coercivity H_c, the composite design showed an out-of-plane easy axis with an H_c ~3400 Oe. This implies that an in-plane tensile strain is present in the

$CoFe_2O_4$ phase due to its negative magnetostrictive nature. On the other hand, the reference $CoFe_2O_4$ film on $SrTiO_3$ (001) is mostly isotropic with H_c ~1050-1206 Oe. Such difference is likely due to the strain induced at the $CoFe_2O_4/HfO_2$ interface during RTA. HfO_2 has an anisotropic thermal expansion behavior that is largely in-plane along the *a*-axis (Haggerty 2014), which would lead to a primarily in-plane deformation during RTA cooling. With the intimately coupled interfaces that ALD could provide, such strain is then transferred to the $CoFe_2O_4$ phase and resulted in the observed out-of-plane anisotropy.

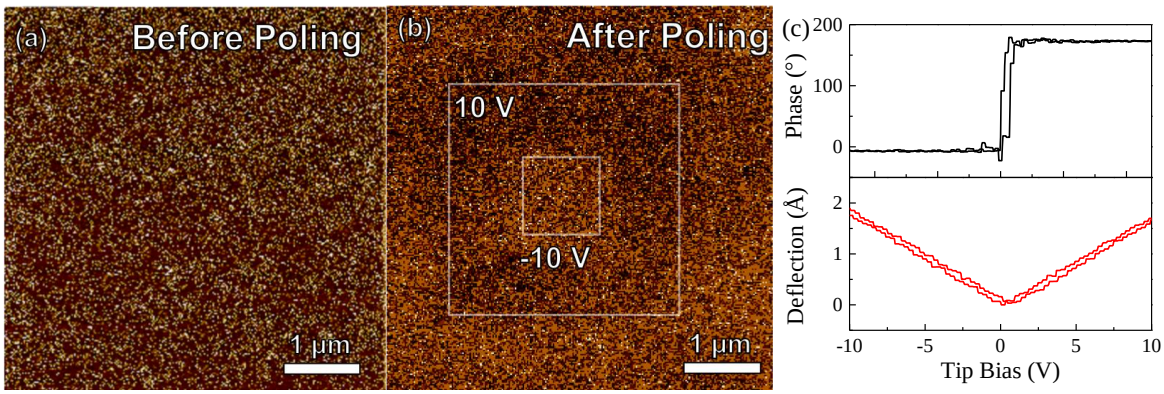

Figure 6.4 Piezoresponse force microscopy (PFM) phase image of the $CoFe_2O_4$ (10 nm)/FE-HfO_2 (6 nm) composite on TiN (10 nm)/p-Si (111) substrate after 700 °C annealing in N_2 for 20 secs (a) before and (b) after electrical poling at ±10V with the PFM tip in square patterns. The constrast between different polign regions indicates ferroelectrci switching. (c) PFM ramp mode measurements of the same sample, the switcing of piezoresponse phase (top) and deflection (bottom) indicates the strain interaction in the composite.

Microscopic multiferroic behavior was characterized by scanning probe microscopy (SPM) techniques. The ferroelectric switching behavior of the 700 ºC annealed $CoFe_2O_4$ (10 nm)/FE-HfO_2 (6 nm) on TiN (10 nm)/p-Si (111) substrates was explored using piezoresponse force microscopy (PFM). For PFM measurements, conductive SCM-PIT tips were used to provide the needed biasing. Figure 6.4 (a) shows the PFM phase image of a 5×5 μm^2 area before applying electrical bias. For the poling step, electrical bias was applied through the conductive tip. Electrical poling first conducted under a +10 V tip bias within the 3×3 μm^2 area, and a subsequent scan within the 1×1 μm^2 area region with –10 V bias was performed to create

a contrast in the ferroelectric states. As shown in Figure 6.4 (b), the color contrast between the square patterns under different biasing voltages indicates ferroelectric switching in the composite design, arising from the FE-HfO_2 phase. PFM ramp mode measurements are shown in Figure 6.4 (c), where a DC bias was applied through the PFM tip and the ferroelectric domains is locally excited via the converse-piezoelectric effect. The PFM phase (top panel) exhibits a 180º change with sweeping tip voltages, again confirms the ferroelectric switching incident. On the other hand, the corresponding deflection measurement (bottom panel) exhibits a butterfly-like loop, indicating the existence of the non-volatile strain interaction resulted from ferroelectric switching. Such non-volatile behavior would then lead to a non-volatile magnetoelectric coupling in the composite design.

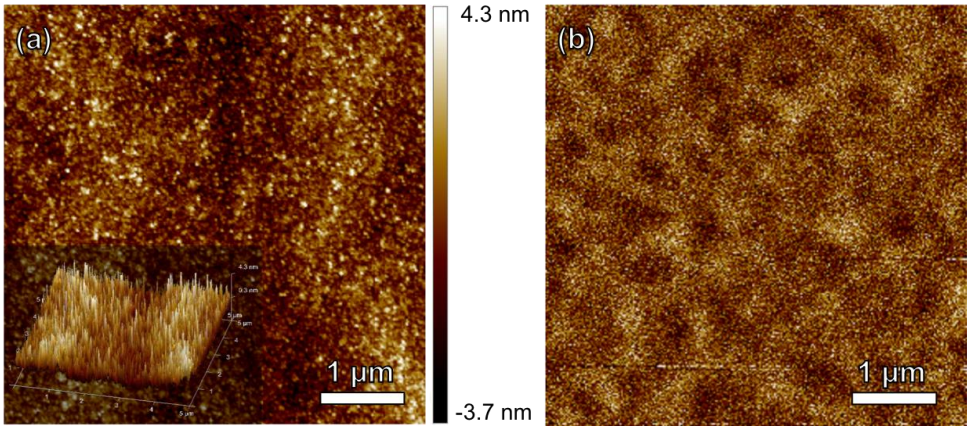

Figure 6.5 (a) Atomic force microscopy (AFM) surface topography of an ALD $CoFe_2O_4$ (10 nm)/FE-HfO_2 (6 nm) composite on TiN (10 nm)/p-Si (111) substrate after 700 °C annealing in N_2 for 20 secs, showing an atomically smooth surface with an RMS of 0.89 nm. Inset shows an isometric 3D map of the same data. (b) Magnetic force microscopy (MFM) phase image of the same sample, revealing a grain-like magnetic domain structure that is specific to $CoFe_2O_4$ (Pham 2017).

For microscopic magnetism characterizations, magnetic force microscopy (MFM) was utilized to visualize the surface magnetic domains. To observe magnetism, magnetic MESP tips were used. MFM scans were conducted using a “lift height” method, which is comprised of two scanning passes for a horizontal scan in the image. Surface topography is recorded just like atomic force microscope (AFM) during the first pass, while the second pass is “lifted” to

a certain height (50 nm in the presented data) and the path of the scan mimics the first pass. The deviation in scanning path resulted by the magnetic interaction between the surface and the tip is then used to construct the magnetic domain structure of the material. Figure 6.5 (a) shows the AFM surface topography image of the 700 °C-annealed $CoFe_2O$ (10 nm)/FE-HfO_2 (6 nm) on TiN (10 nm)/p-Si (111) substrates. The scan revealed an atomically smooth surface with a very low RMS value of 0.89 nm, which is believed to be attributed form the conformal and high-quality nature ALD processing. Figure 6.5 (b) shows the MFM phase image of the same surface area. The composite exhibited a grain-like domain structure that is specific to $CoFe_2O_4$ thin films with sizes ranging from 200-500 nm (Pham 2017).

After confirming the functionalities both macroscopically and microscopically, magnetoelectric behaviors of the 700°C annealed multiferroic $CoFe_2O_4$ (10 nm)/FE-HfO_2 (6 nm) on TiN (10 nm)/p-Si (111) were then investigated by a combinatorial MFM/PFM technique described in Section 5.3. For the measurements, the surface magnetic domains were imaged first via MFM surface scans (shown in Figure 6.6 (a)), while surface PFM poling scans were conducted subsequently. For the PFM scans, a 3×3 μm^2 area scan was first poled under –10 V, followed by a 1×1 μm^2 area scan under +10 V to generate a contrast in surface ferroelectric states between different poling regions. Finally, a 5×5 μm^2 MFM surface scan was then conducted again to observe the change in magnetic domains. The contrast in magnetic domains between different poling regions in Figure 6.6 (b) indicates a robust room-temperature magnetoelectric coupling. In order to ensure the magnetoelectric coupling observed, another set of experiments with the same procedure was conducted on a 6-nm thick FE-HfO_2 thin film annealed at the same temperature, as shown in Figure 6.6 (c) and (d). A very subtle contrast is observed in the MFM phase image after electrical poling (Figure 6.6 (d)). The contrast might correlate to a minor electrostatic interaction between the MFM tip and the poled surface,

suggesting a potential interfacial charge coupling taking part simultaneously with the proposed strain-mediated coupling scheme. Further verifications is needed to unveil the nature of the observed magnetoelectric coupling.

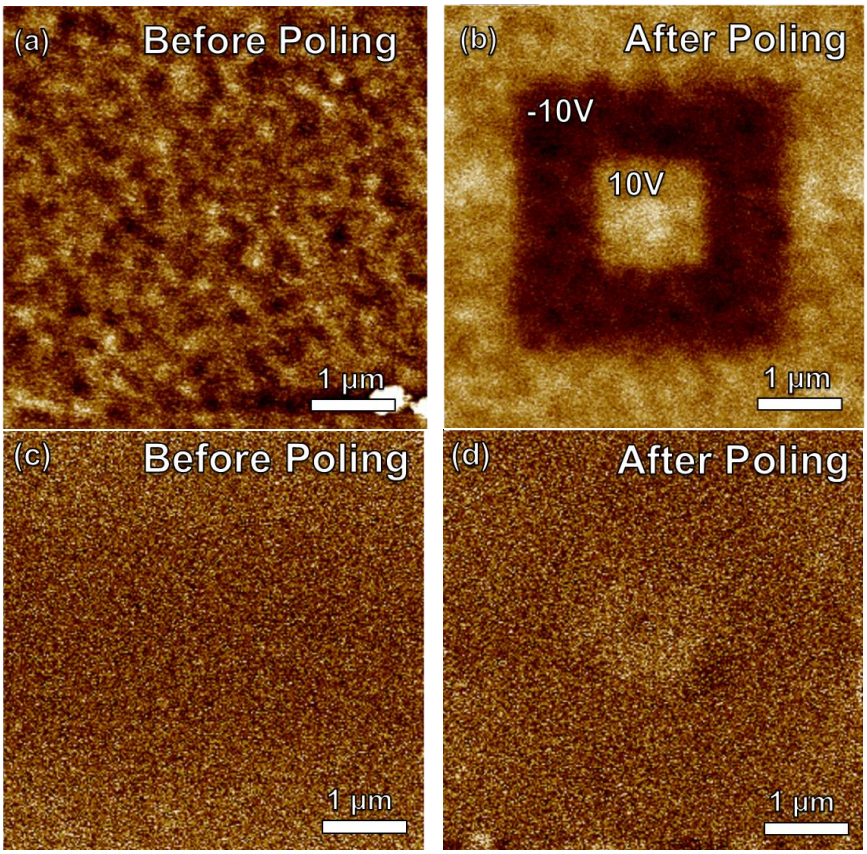

Figure 6.6 Room temperature MFM phase image of the $CoFe_2O_4$ (10 nm)/FE-HfO_2 (6 nm) composite on TiN (10 nm)/p-Si(111) substrates (a) before and (b) after PFM poling. The phase constrast between different poling regions indicate magnetoelectric coupling. (c) and (d) shows the results obtained from a single phase FE-HfO_2 thin film with the same processing parameters.

The converse magnetoelectric coupling coefficient $\alpha_{converse}$ was then quantified using an *ex situ* poling SQUID magnetometer setup. During the measurement, the ferroelectric state of the composite stack was altered by an electrical bias for 10 minutes inside a poling station, and subsequent SQUID scans were conducted along both the in-plane and out-of-plane direction to monitor the change in magnetic hysteresis. The in-plane and out-of-plane results are shown in Figure 6.7 (a) and (b), respectively, and the shape change of hysteresis loops as a

function of electric field implies magnetoelectric coupling. With increasing electric field, in-plane magnetization showed a decreasing trend, while the out-of-plane date showed the opposite. In addition, the M_s values are no longer isotropic after electrical poling, likely due to the structural transition during the "wake-up" period that is often seen from FE-HfO_2 thin films (Park 2015, Polakowski 2015, Park 2016, Pešić 2016). The structural transition changes the state of the $CoFe_2O_4$/FE-HfO_2 interface in turn changes the microstructure of the interfacial $CoFe_2O_4$ as well as the magnetization along different axes.

On the other hand, the in-plane H_c increased drastically from ~1000 Oe to ~2800 Oe while the out-of-plane shows a slight decrease from ~3400 Oe to ~3200 Oe, indicating a decreased magnetic anisotropy. This effect can be explained by the structural transition during the "wake-up" period as well. From an energy standpoint, the microstructure evolution depends on the minimization of magnetoelastic energy of the composite system that leads to magnetoelastic anisotropy reduction. Often times, post-RTA electrical cycling with ~10^3-10^5 cycles can help achieve a fully "waken-up" FE-HfO_2 and minimize the drastic microstructure transformation (Pešić 2016).

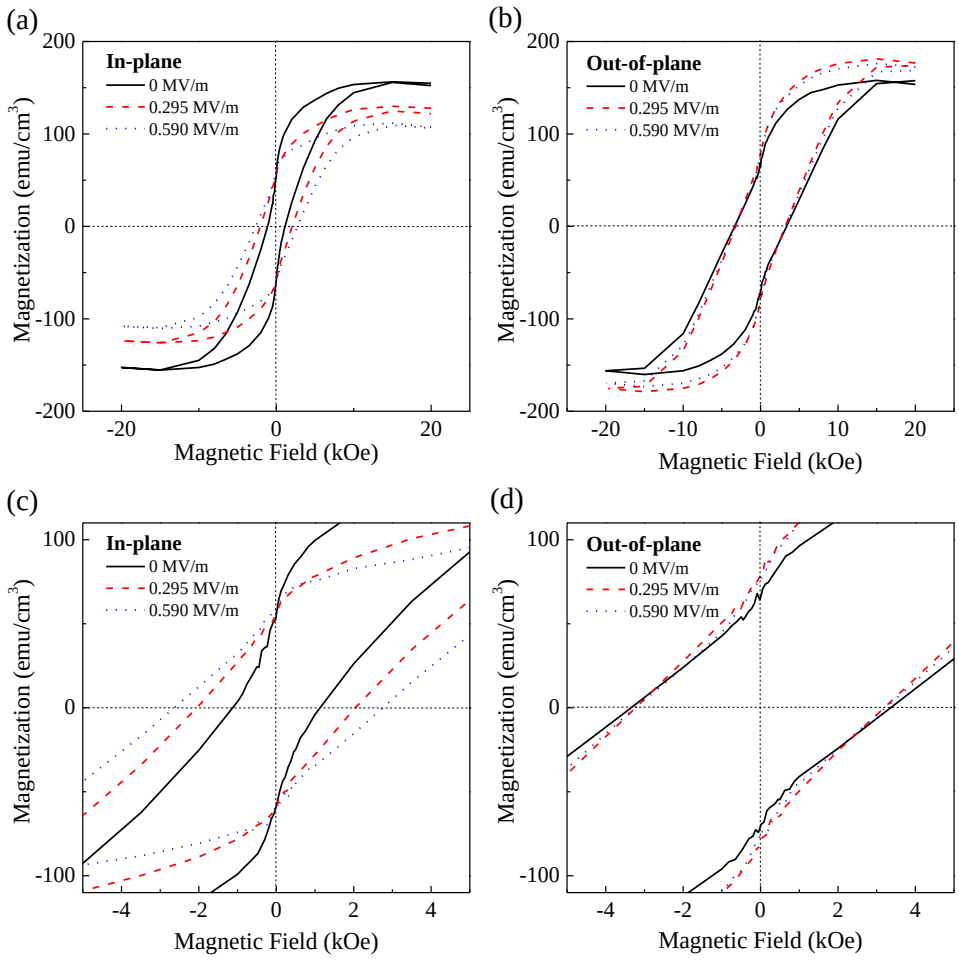

Figure 6.7 (a) In-plane and (b) out-of-plane *M-H* hysteresis loops of the 700 ºC annealed $CoFe_2O_4$ (10 nm)/FE-HfO_2 (6 nm) on TiN (10 nm)/p-Si (111) substrate measured at room-temperature as a function of applied *E*-fields. In-plane measurements exhibited a larger change in H_c, while out-of-plane scans showed a larger change in M_r values.

In order to assess the magnetoelectric coupling in the 700 °C annealed $CoFe_2O_4$ (10 nm)/FE-HfO_2 (6 nm) composite on TiN (10 nm)/p-Si (111) substrate, it is necessary to extrapolate the magnetoelectric coupling coefficient $\alpha_{converse}$. $\alpha_{converse}$ was calculated with $\alpha_{converse} = \frac{\Delta M_r}{\Delta E}$, while the use of M_r in the calculation represents the magnetoelectric coupling of the material without the presence of an external magnetic field. This method is more relevant to an application aspect. Zoomed-in in-plane and out-of-plane *M-H* hysteresis loops are shown in Figure 6.7 (c) and (d) respectively. The results are summarized in Figure 6.8 (a), showing the extracted M_r values as a function of the applied electric field. The change in M_r in both

directions seems to be saturated after an applied electric field of 0.295 MV/m. By comparing the two sets of data, the change in remnant magnetization (M_r) is significantly greater in the out-of-plane direction (18.7-23.2%) compared to in-plane (0.6-2.8%), which is likely due to the presence of substrate clamping along the in-plane direction. $\alpha_{converse}$ was calculated to be ~55 Oe cm/kV at the point of saturation (E-field = 0.295 MV/m).

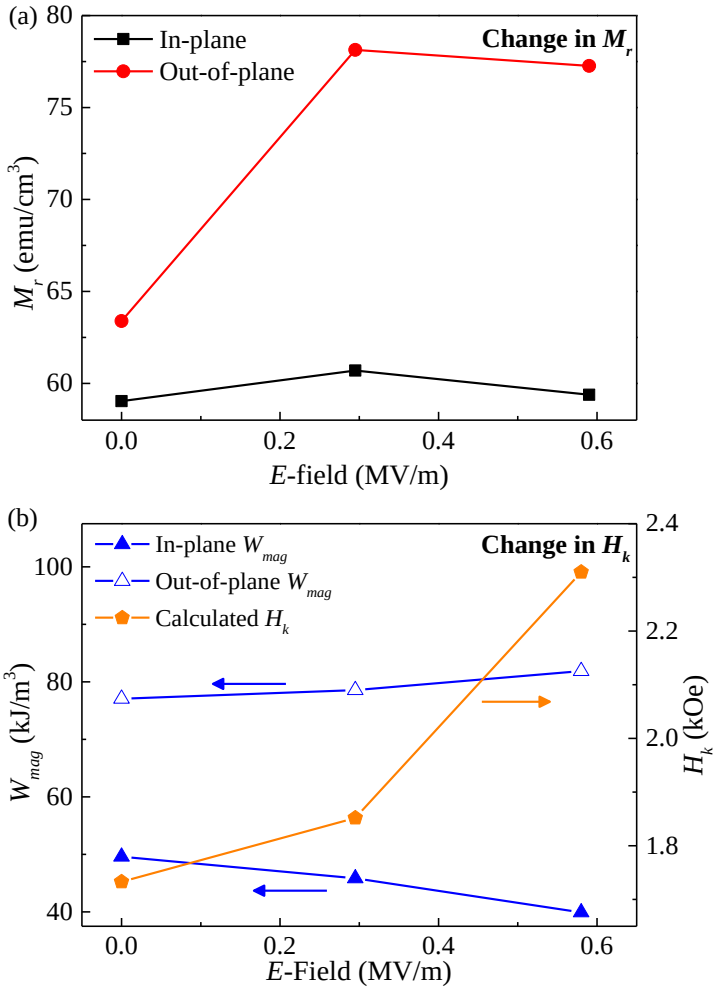

Figure 6.8 (a) In-plane and out-of-plane remnant magnetizaiton of the 700 °C annealed $CoFe_2O_4$ (10 nm)/HfO_2 (6 nm) composite on TiN (10 nm)/p-Si (111) substrate as a function of applied electric field. The change along the out-of-plane direction is more prominent than the in-plane change. (b) In-plane and out-of-plane E_{mag} required to change the magnetization, as well as the calculated anisotropy field H_k of the composite as a function of applied electric field. The trend observed suggests the changed magnetic anisotropy due to electrical poling, confirming the magnetoelectric coupling in the $CoFe_2O_4$ /FE-HfO_2 composite. (removed the alpha values)

In addition to the quantification mentioned above, $\alpha_{converse}$ was also extracted by considering the change in anisotropy field H_k with $\alpha_{converse} = \frac{\Delta H_k}{\Delta E}$. This method provides insight into how the magnetic anisotropy is changed in the composite upon electrical poling and is more beneficial from a materials standpoint. H_k values were extrapolated by considering the anisotropy energy K and with the relationship below:

$$H_k = \frac{K}{\mu_0 M_s} \tag{6.1}$$

where μ_0 is the magnetic permeability of vacuum and M_s is the saturation magnetization of the analyzed *M-H* hysteresis. Anisotropy energy K can be estimated by considering the difference of the magnetization work ($W_{mag} = \int H \, dM$) needed zero field to saturation (first quadrant of the *M-H* loop) along in-plane and out-of-plane directions. The calculation can be summarized as the following (Wu 2016):

$$\begin{aligned} K &= W_{mag,\,\text{in-plane}} - W_{mag,\,\text{out-of-plane}} \\ &= \left(\int H\,dM\right)_{\text{in-plane}} - \left(\int H\,dM\right)_{\text{out-of-plane}} \end{aligned} \tag{6.2}$$

Figure 6.8 (b) exhibits the W_{mag} required to magnetize the composite along the in-plane and out-of-plane direction, as well as the calculated anisotropy field H_k, as a function of applied electric field. It is shown that W_{mag} required to magnetize the sample exhibit opposite trends along the in-plane and out-of-plane directions, confirming the magnetic anisotropy change under a strain-mediated scheme since $CoFe_2O_4$ is highly magnetostrictive. Therefore, an increasing H_k was then extrapolated and corresponds to an $\alpha_{converse}$ ~168 Oe cm/kV. It is noteworthy that the difference in the two $\alpha_{converse}$ values is arisen from the nature of the two calculations: $\alpha_{converse}$ obtained by considering M_r change implies the absence a magnetic field input, while the influence of the external magnetic field is included when calculating $\alpha_{converse}$ from H_k. Both $\alpha_{converse}$ quantification methods were reported in the field of multiferroics

research, and this report aims to provide a fuller picture for the magnetoelectric nature of the $CoFe_2O_4$/FE-HfO_2 composite.

Furthermore, the transfer efficiency of the magnetoelastic energy to the magnetic anisotropy energy can be calculated. For the magnetoelastic energy stored in the $CoFe_2O_4$ phase via FE-HfO_2 piezostrain, it can be estimated with the following equation (Cullity 2008):

$$E_{me} = -\frac{3}{2}\lambda\sigma\cos^2\theta \tag{6.3}$$

where λ is the magnetoelastic coefficient for the magnetic phase ($CoFe_2O_4$ = -110 ppm), σ is the stress applied to the material (piezostress from the FE-HfO_2 phase in this case), and $cos\theta$ is the directional cosine that defines the angle between the magnetization and the strain. Since the biasing and the magnetism measuring directions are both along the out-of-plane direction, $\theta = 0°$ and $cos\theta = 1$. The equation can be further simplified with Young's modulus Y into the following form:

$$E_{me} = -\frac{3}{2}\lambda Y\varepsilon \tag{6.4}$$

where Y is ~150 GPa for $CoFe_2O_4$ (Kim 2015), ε is the strain induced in $CoFe_2O_4$ by FE-HfO_2 piezostrain. ε can be estimated by the d_{33} value obtained from the PFM ramp mode measurements (Figure 6.4 (c)) multiplied by the voltage applied and divide by the total composite thickness of ~16 nm. The estimation of the displacement induced in the highest case scenario (largest voltage range in Figure 6.4 (c)) is 10 pm/V × 10V = 100 pm. As a result, ε is determined to be ~0.0063 (highest strain generated). On the other hand, the lower bound for the strain induced can be obtained by considering the coercive voltage (~3.3 V) obtained in the *P-E* hysteresis loop for ε, resulting a lower bound value of ~0.0021. Lastly, by inserting all the corresponding numbers into Equation (6.4), E_{me} is calculated to be ~54.14-154.69 kJ/m^3.

The anisotropy energy K can be determined by Equation (6.2) and Figure 6.8 (b), yielding a value ~14.52 kJ/m^3. Therefore, the efficiency of energy transfer can be estimated to be 14.52/154.14 ≈ 9.4% to 14.52/54.14 ≈ 28.4%. This indicates that although a charge-mediated coupling effect could be taking place as well, the strain component is indeed an important factor that cannot be overlooked for the magnetoelectric coupling effects observed experimentally. It is worth noting that for characterizing the charge-mediated magnetoelectric coupling, techniques such as (X-ray magnetic circular dichroism) XMCD would be necessary for fully revealing the nature of the interfacial interactions.

Although different in nature, both $\alpha_{converse}$ values form are nonetheless comparable with many other reported multiferroic systems reported (Thiele 2007, Heron 2014, Chien 2016). In addition, the values obtained from the presented $CoFe_2O_4$ (10 nm)/FE-HfO_2 (6 nm) system on TiN (10 nm)/p-Si (111) are also comparable with the value that was extracted from the $BiFeO_3$ (6 nm)/$CoFe_2O_4$ (4 nm)/$BiFeO_3$ (6 nm) system on Nb:$SrTiO_3$ (001) under a similar total thickness with the same characterization method (~64 Oe cm/kV). Although $BiFeO_3$ itself enables two magnetoelectric coupling schemes simultaneously, FE-HfO_2 allows much better electrical properties and Si-compatibility, makes itself a promising ferroelectric phase of choice for multiferroic composites. With the possibility to further enhance the ferroelectricity and magnetoelectric coupling via dopant incorporation to the FE-HfO_2 phase, it is believed that the comparable $\alpha_{converse}$ values achieved from the $CoFe_2O_4$/FE-HfO_2 system have demonstrated its potential for future magnetoelectric devices.

6.3. Summary

In this chapter, FE-HfO_2 thin films was integrated with $CoFe_2O_4$ confinement layers to form a multiferroic composite on p-Si (111) substrates via RE-ALD and demonstrated great prospects. In the design, $CoFe_2O_4$ not only serves as a confinement layer but also an active

layer that provides magnetism to the overall multiferroic composite. 10-nm thick $CoFe_2O_4$ were interfaced with FE-HfO_2 on TiN (10 nm)/p-Si (111) substrate and the composite ferroelectricity were studied as a function of annealing temperature and HfO_2 film thickness. It is shown that the orthorhombic phase stabilization as well as composite ferroelectricity were further promoted with $CoFe_2O_4$ confinement layer compared to TiN. An optimal ferroelectricity is achieved in $CoFe_2O_4$ (10 nm)/FE-HfO_2 (6 nm) composite on TiN (10 nm)/p-Si (111) substrates with 700 °C RTA, demonstrating a P_r of ~5.43 μC/cm^2 and an E_c of ~1083 kV/cm. The ferroelectric behavior observed is comparable with literature reports with TiN top layers and a similar FE-HfO_2 thickness (Polakowski 2015, Kim 2016, Nishimura 2016). Subsequent magnetic measurements verified the magnetism arising from the $CoFe_2O_4$ phase, while the strain interaction was verified via PFM, both of which verifies the multiferroic nature of the composite design. Magnetoelectric characterization revealed promising converse magnetoelectric coupling coefficient $\alpha_{converse}$ ~55-168 Oe cm/kV, which comparable with other literature reports on multiferroic heterostructures. With the ideal electrical stability and superior Si-compatibility compared to conventional perovskite ferroelectrics, it is believed that the FE-HfO_2 based multiferroic composite demonstrated here opens many new avenues for realizing magnetoelectric devices.

Chapter 7. Summary

This thesis demonstrated the RE-ALD synthesis of two different multiferroic composite systems with the aim of enabling energy-efficient future memory devices. The use of RE-ALD processing allows intimately coupled materials interfaces with precise growth control over large surface areas, all of which are advantageous for industrial applicability. In this work, ferrimagnetic $CoFe_2O_4$ serves as the magnetic phase of choice while multiferroic $BiFeO_3$ and ferroelectric HfO_2 (FE-HfO_2) were utilized as the ferroelectric phase respectively for the composite design.

For the integration of multiferroic $CoFe_2O_4$/$BiFeO_3$ composites, the RE-ALD processes of the respective $BiFeO_3$ and $CoFe_2O_4$ phases were developed and described firstly. Crystalline $BiFeO_3$ and $CoFe_2O_4$ on $SrTiO_3$ (001) substrates was achieved by alternating the constituent binary oxide RE-ALD cycles at 200 °C and a post-deposition thermal annealing step at 450-750 °C. Stoichiometric $BiFeO_3$ and $CoFe_2O_4$ thin films were obtained by adjusting the ALD cycling ratios. RE-ALD synthesized $BiFeO_3$ thin films exhibit a single-crystalline epitaxial growth after 650 °C annealing, whereas $CoFe_2O_4$ thin films show a textured-polycrystalline nature. The observed difference arises from the difference in lattice mismatch between the films and the substrate. Ferroelectric switching and *P-E* hysteresis loops confirms the ferroelectricity in $BiFeO_3$. In addition, weak magnetism was observed due to antiferromagnetic spin canting. On the other hand, RE-ALD $CoFe_2O_4$ thin films exhibit magnetic properties that are comparable to both bulk crystal and films grown by other deposition methods, with a thickness as low as ~7 nm, demonstrating the potential of RE-ALD for the synthesis of high-quality magnetic oxides with large-scale processing compatibility.

Magnetoelectric $CoFe_2O_4$/$BiFeO_3$ nano-laminates were synthesized on both $SrTiO_3$ (001) and Si (001) substrates by integrating the RE-ALD processes for $CoFe_2O_4$ and $BiFeO_3$.

For the case on $SrTiO_3$ (001), the multiferroicity of composite is verified with a polarization up to ~17 μC/cm^2 and a magnetism of ~125 emu/cm^3. The functional properties can be further improved by a nanolayering approach while the total composite thickness and $CoFe_2O_4$-to-$BiFeO_3$ ration is fixed at a constant. The tri-layer $BiFeO_3$/$CoFe_2O_4$/$BiFeO_3$ structure exhibits optimized functional properties with P_r ~17 μC/cm^2. Si-integration onto Si (001) substrates is achieved with the use of a MBE-deposited $SrTiO_3$ (001) buffer layer, highlighting the potential of utilizing ALD for processing future magnetoelectric devices. Magnetoelectric coupling of the tri-layer nanolaminate on $SrTiO_3$ (001) was characterized via several methods including MFM/PFM, scanning SQUID magnetometer, and *ex situ* poling SUQID magnetometer measurements. The converse magnetoelectric coupling coefficient $\alpha_{converse}$ is determined to be ~22 Oe cm/kV and can be further improved to ~64 Oe cm/kV when the stack is scaled to 16 nm in thickness. The work here not only serves as the first multiferroic composite design grown fully by ALD, but also highlights the importance of interfacial area per volume to overall composite magnetoelectric coupling.

Lastly, FE-HfO_2 and its multiferroic integration with $CoFe_2O_4$ was demonstrated. An ideal RE-ALD process for HfO_2 with metalorganic TDMAH precursor was described. The resulted growth rate is ~1.4 Å/cycle at a substrate temperature of 190 °C. The stabilization of metastable orthorhombic FE-HfO_2 was first investigated by TiN confinement layers and post-deposition thermal annealing steps. FE-HfO_2 ferroelectric behavior was investigated as a function of film thickness (6-20 nm) and annealing temperatures (500-800 ºC). It is shown that the metastable orthorhombic phase is favored the most at 6 nm HfO_2 thickness and 700-800 °C annealing, correlating to a P_r up to ~1 μC/cm^2 and a E_c ~1900 kV/cm. The top TiN layer is replaced by $CoFe_2O_4$ in the subsequent integration of FE-HfO_2 into a multiferroic composite on TiN (10 nm)/p-Si(111). The $CoFe_2O_4$ phase serves as both a structural confinement layer

and an active functional in this novel composite design. The incorporation of $CoFe_2O_4$ leads to a further improved FE-HfO_2 ferroelectricity with a P_r of ~5.43 μC/cm^2 and an E_c of ~1000 kV/cm^2. The improvement is likely due to the greater thermal expansion behavior of $CoFe_2O_4$. The multiferroicity in $CoFe_2O_4$ (10 nm)/FE-HfO_2 (6 nm) on TiN (10 nm)/p-Si (111) is confirmed by magnetic and magnetoelectric characterizations. The composite design exhibits promising converse magnetoelectric coupling coefficient $\alpha_{converse}$ of ~55-168 Oe cm/kV, which is comparable with the $CoFe_2O_4$/$BiFeO_3$ system and other literature reports. It is believed that the FE-HfO_2 based multiferroic composite demonstrated in this work opens up many new avenues for realizing next-generation magnetoelectric devices.

This work provided a proof of concept for obtaining desirable magnetoelectric coupling behaviors with ALD-synthesized thin film composite nanostructures. Besides the $CoFe_2O_4$/$BiFeO_3$ and $CoFe_2O_4$/FE-HfO_2 systems described in this work, ALD's the high-quality nature can benefit the synthesis and optimization of many other multifunctional composite systems. Next steps for this work include unveiling the coupling mechanism at the $CoFe_2O_4$/FE-HfO_2 interface and the integration of both FE-HfO_2 into magnetic memory devices such as magnetic tunnel junctions (MTJs). To further study the observed ME coupling effect, X-ray magnetic circular dichroism (XMCD) and SSRL high-resolution XRD can be used to probe the change in the electronic and structural environment at the interface respectively. For device integrations, ultra-thin FE-HfO_2 can be implemented as the tunneling barrier to maximize the voltage-controlled magnetic anisotropy (VCMA) effect, which is critical for the switching efficiency of MTJ devices.

Appendices

Appendix A. Schematics of the Ultra-high Vacuum Multi-bean Chamber Design

A.1. Main Chamber

REACTOR

Main Chamber

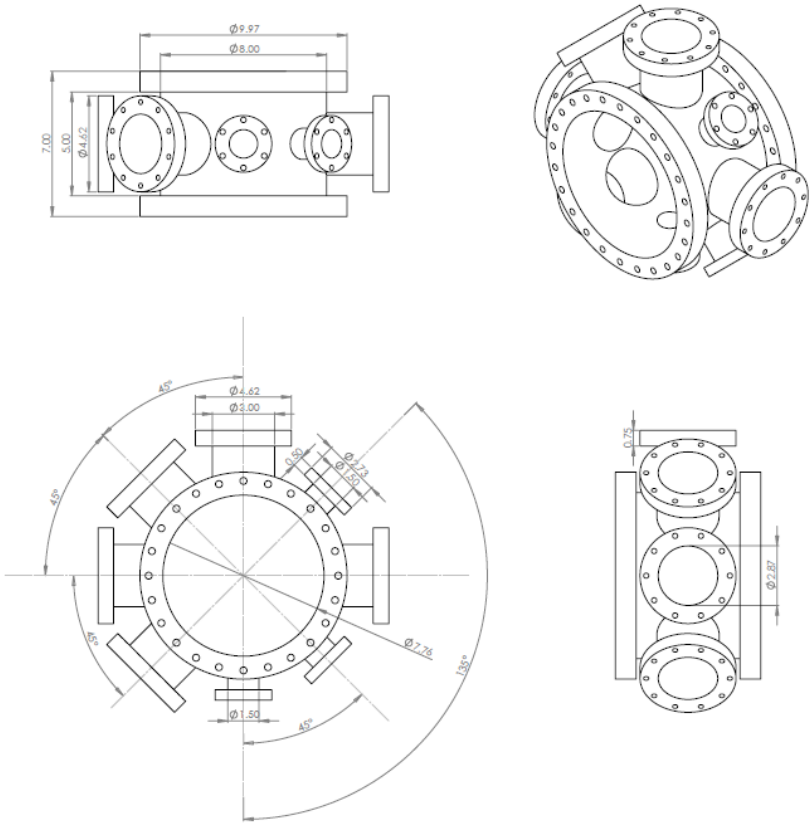

University of California, Los Angeles, Department of Chemical and Biomolecular Engineering							
Part	Main Chamber	Material	Stainless steel (316)				
Filename	MB Chamber.pdf	Scale	No	Units	inch	Quantity	1
Designer	Angstron Systems	Date					
Revised by	Jeffrey Chang	Date	5/20/2014				
Contractor		Date					
Comments	Adapted from Angstron Systems		Tolerance	+/- .0001			

A.2. Radical Source

RADICAL SOURCE

Full Assembly

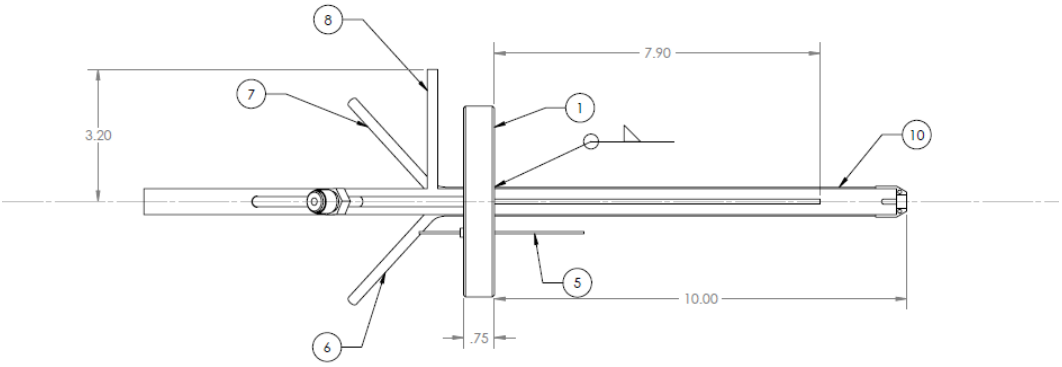

(Side View 1)

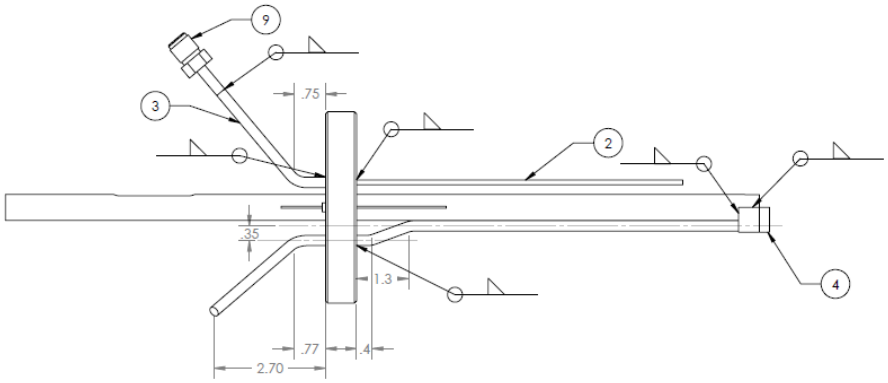

(Side View 2)

ITEM NUMBER	DESCRIPTION.
1	FLANGE, 4-5/8" CF BLANK, MOD'ED
2	GAS LINE, INNER, 3mm DIA O.D. TUBING
3	GAS LINE, OUTER, 0.25in DIA O.D. TUBING
4	AMPOULE HOUSING
5	POWER FEEDTHROUGH, ISI P/N 9411018
6	COOLANT LINE, RHS, 0.25in DIA O.D. TUBING
7	COOLANT LINE, LHS, 0.25in DIA O.D. TUBING
8	PUMP SPOUT, 0.25in DIA O.D. TUBING
9	1/4" VCR MALE FITTING
10	MAIN TUBE

University of California, Los Angeles, Department of Chemical and Biomolecular Engineering							
Part	Radical source	Material	Mixed (stainless steel, teflon)				
Filename	Radical source.pdf	Scale	No	Units	inch	Quantity	1
Designer	Angstron Systems	Date					
Revised by	Jeffrey Chang	Date	05/20/2014				
Contractor		Date					
Comments	Adapted from Angstron Systems		Tolerance	+/- .0001			

RADICAL SOURCE (Continued)

Full Assembly

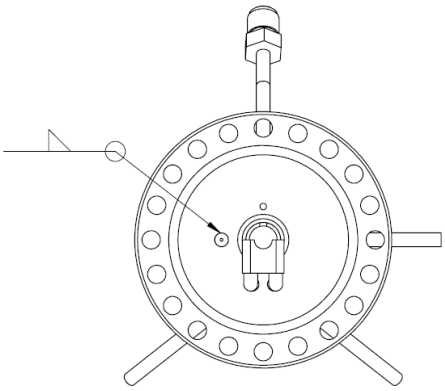

View from vacuum side

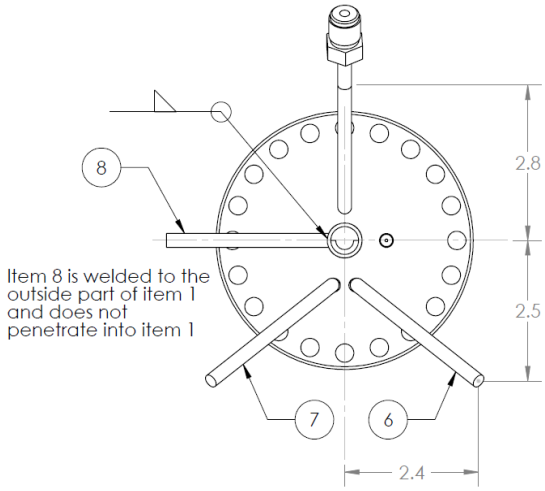

View from ambient side

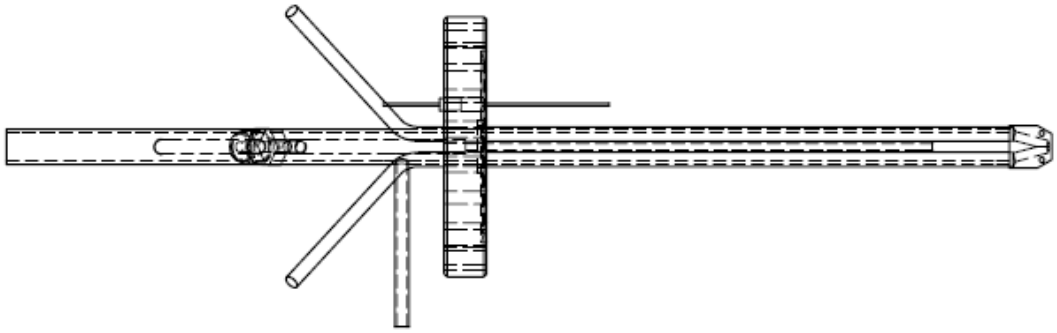

Full view

University of California, Los Angeles, Department of Chemical and Biomolecular Engineering								
Part	Radical source	Material	Aluminum Alloy (6082)					
Filename		Scale	No	Units	inch	Quantity	1	
Designer	Angstron Systems	Date						
Revised by		Date						
Contractor		Date						
Comments	Adapted from Angstron Systems		Tolerance	+/- .0001				

RADICAL SOURCE (Continued)

Coaxial Waveguide

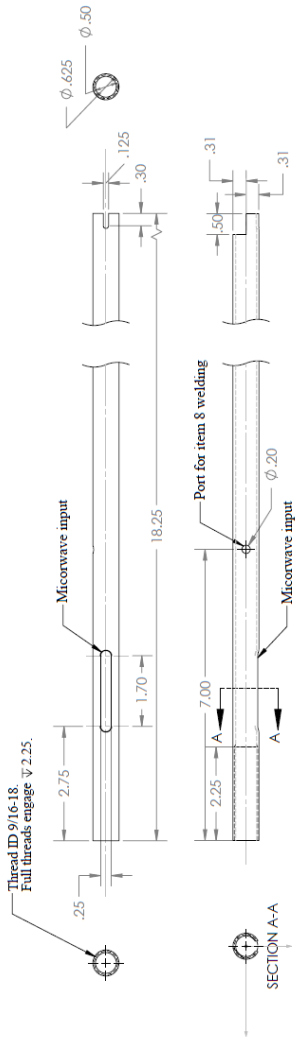

University of California, Los Angeles, Department of Chemical and Biomolecular Engineering								
Part	Radical source	Material	Stainless steel, OD 0.625, Wall 0.0625					
Filename	Radical source.pdf	Scale	No	Units	inch	Quantity	1	
Designer	Angstron Systems	Date						
Revised by	Jeffrey Chang	Date	5/21/2014					
Contractor		Date						
Comments	Adapted from Angstron Systems		Tolerance	+/- .0001				

RADICAL SOURCE (Continued)

Top Clamp for Quartz Ampoule

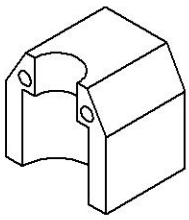

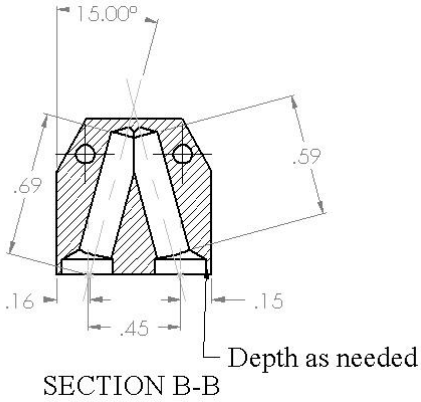

SECTION B-B

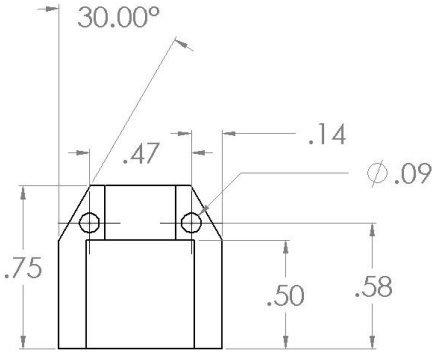

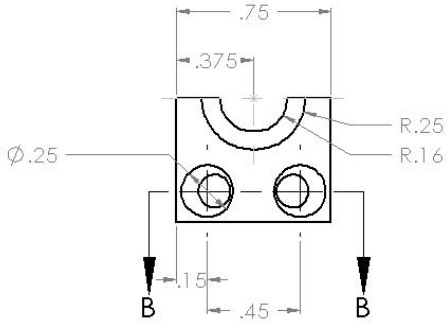

University of California, Los Angeles, Department of Chemical and Biomolecular Engineering							
Part	Radical source	Material	Stainless steel (316)				
Filename		Scale	No	Units	inch	Quantity	1
Designer	Angstron Systems	Date					
Revised by	Jeffrey Chang	Date	5/21/2014				
Contractor		Date					
Comments	Adapted from Angstron Systems		Tolerance	+/- .0001			

RADICAL SOURCE (Continued)

Bottom Clamp for Quartz Ampoule

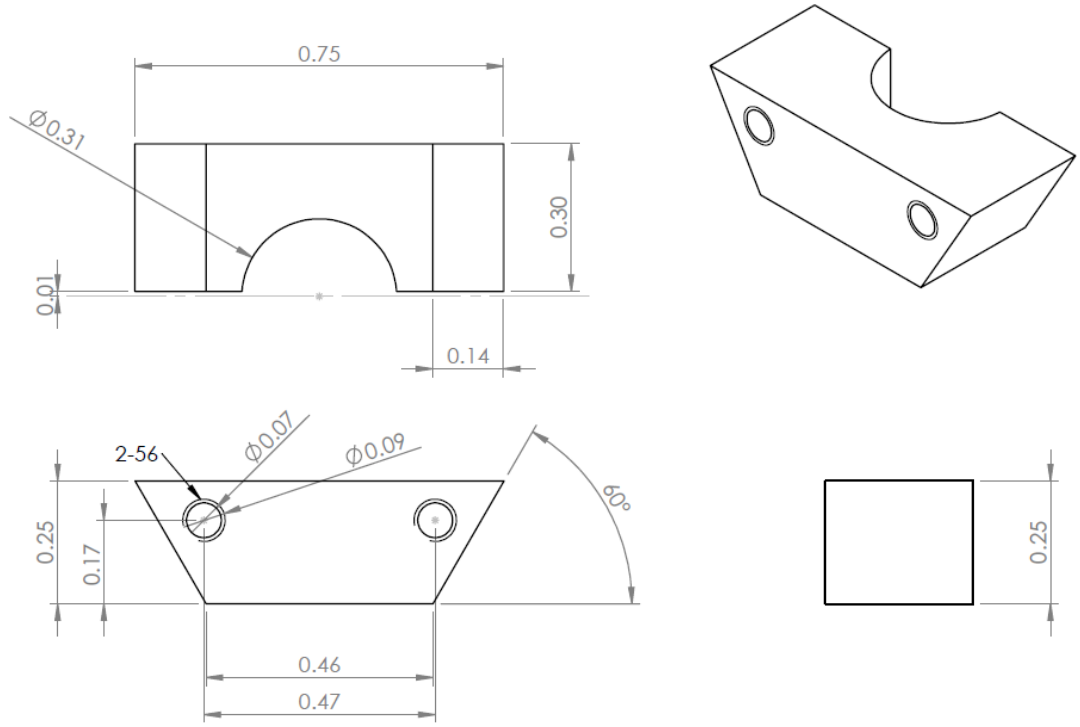

University of California, Los Angeles, Department of Chemical and Biomolecular Engineering								
Part	Radical source	Material	Stainless steel (516)					
Filename	quartz bottom	Scale	No	Units	inc	Quantity	1	
Designer	Angstron Systems	Date						
Revised by	Jeffrey Chang	Date	05/21/2014					
Contractor		Date						
Comments	Adapted from Angstron Systems		Tolerance	+/- .0001				

RADICAL SOURCE (Continued)

Modified 4-5/8” Conflat Flange

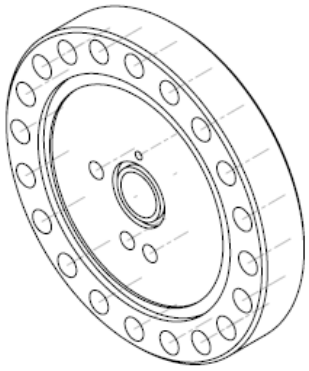

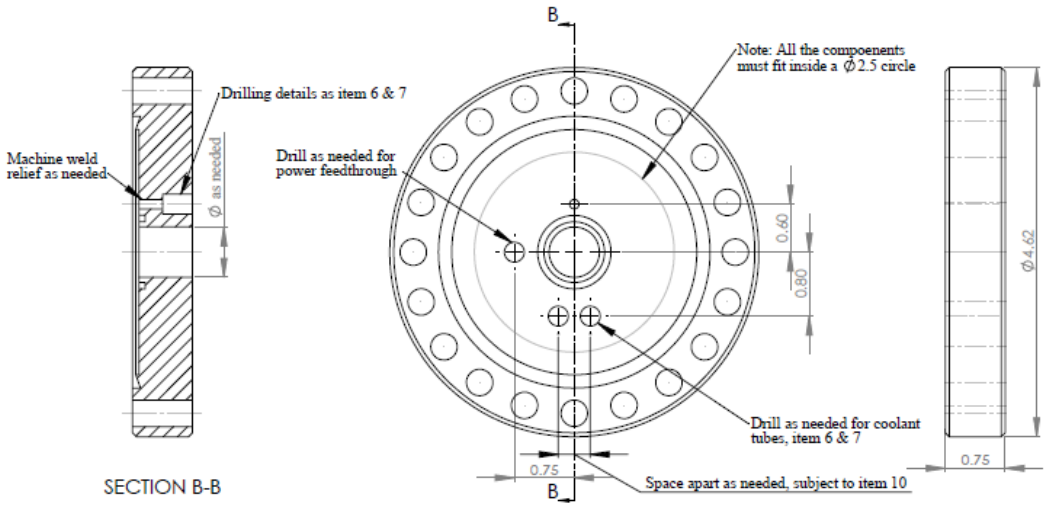

University of California, Los Angeles, Department of Chemical and Biomolecular Engineering								
Part	Radical source	Material	4-5/8” Conflat flange (stainless steel)					
Filename		Scale	No	Units	inch	Quantity	1	
Designer	Angstron Systems	Date						
Revised by		Date						
Contractor		Date						
Comments	Adapted from Angstron Systems		Tolerance	+/- .0001				

RADICAL SOURCE (Continued)

Tuning Slug

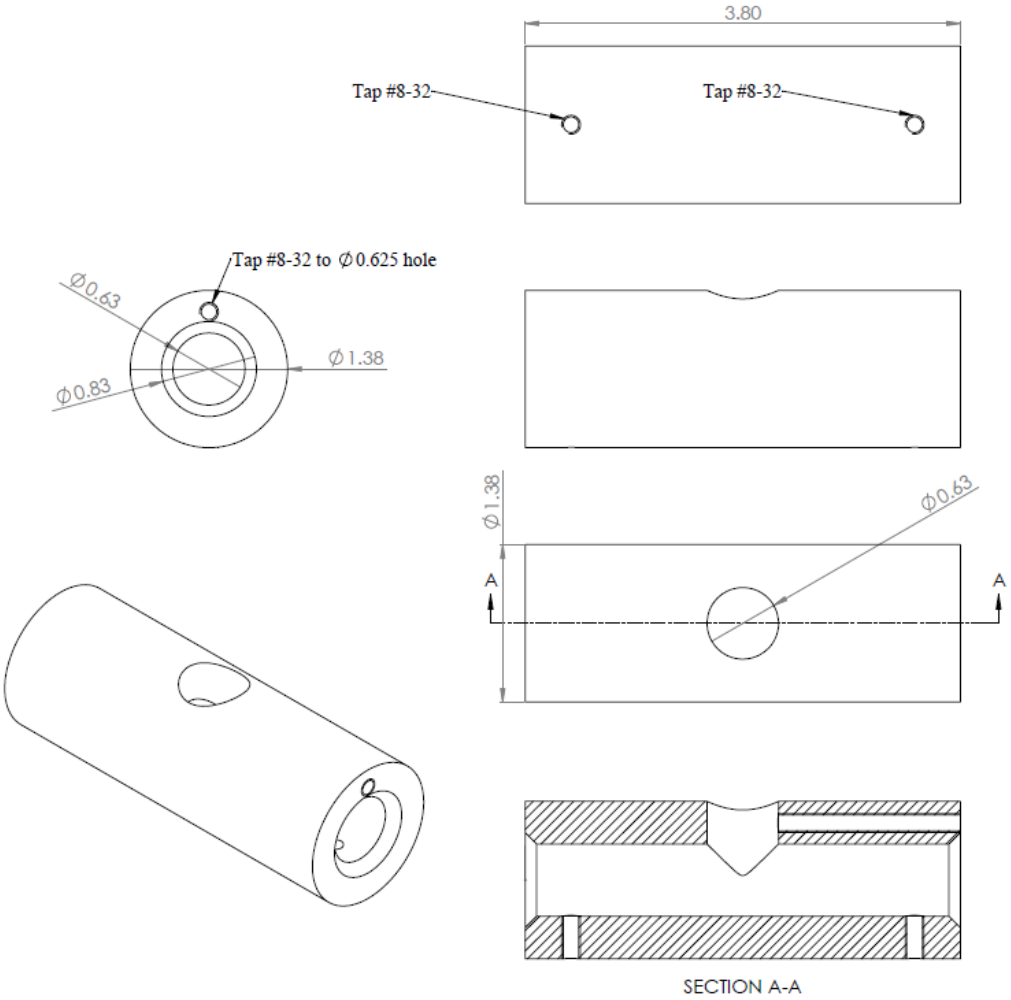

University of California, Los Angeles, Department of Chemical and Biomolecular Engineering								
Part	Radical source	Material	Stainless steel (516)					
Filename	TuningSlug.pdf	Scale	No	Units	inch	Quantity	1	
Designer	Angstron Systems	Date						
Revised by	Jeffrey Chang	Date	5/22/2014					
Contractor		Date						
Comments	Adapted from Angstron Systems		Tolerance	+/- .0001				

RADICAL SOURCE (Continued)

Teflon Bushing

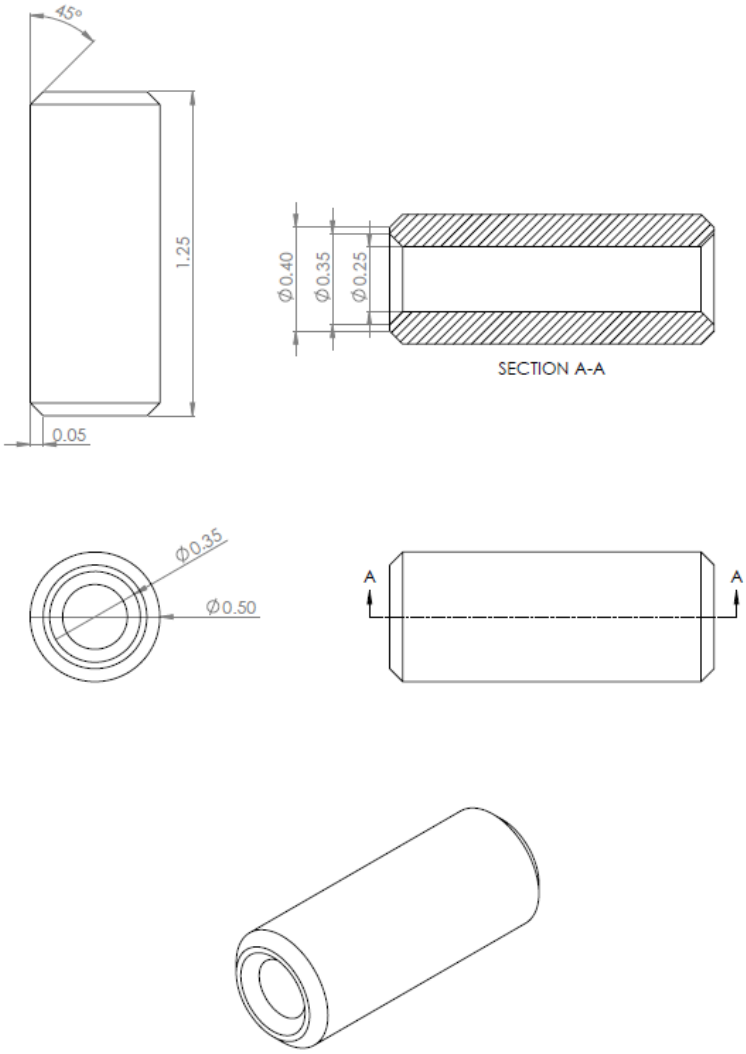

University of California, Los Angeles, Department of Chemical and Biomolecular Engineering								
Part	Radical source	Material	Teflon					
Filename	Teflon.pdf	Scale	No	Units	inch	Quantity	1	
Designer	Angstron Systems	Date						
Revised by	Jeffrey Chang	Date	05/22/2014					
Contractor		Date						
Comments	Adapted from Angstron Systems		Tolerance	+/- .0001				

RADICAL SOURCE (Continued)

Central Conductor

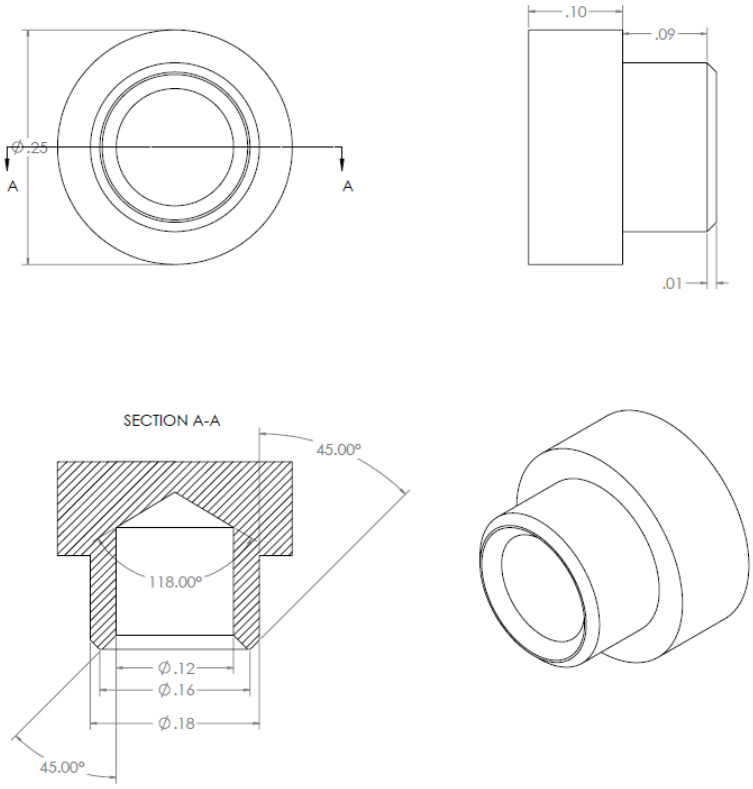

(Tip and Tube)

University of California, Los Angeles, Department of Chemical and Biomolecular Engineering								
Part	Radical source	Material	Stainless steel					
Filename	Central conductor.pdf	Scale	No	Units	inch	Quantity	1	
Designer	Angstron Systems	Date						
Revised by	Jeffrey Chang	Date	05/22/2014					
Contractor		Date						
Comments	Adapted from Angstron Systems		Tolerance	+/- .0001				

RADICAL SOURCE (Continued)

Quartz Ampoule

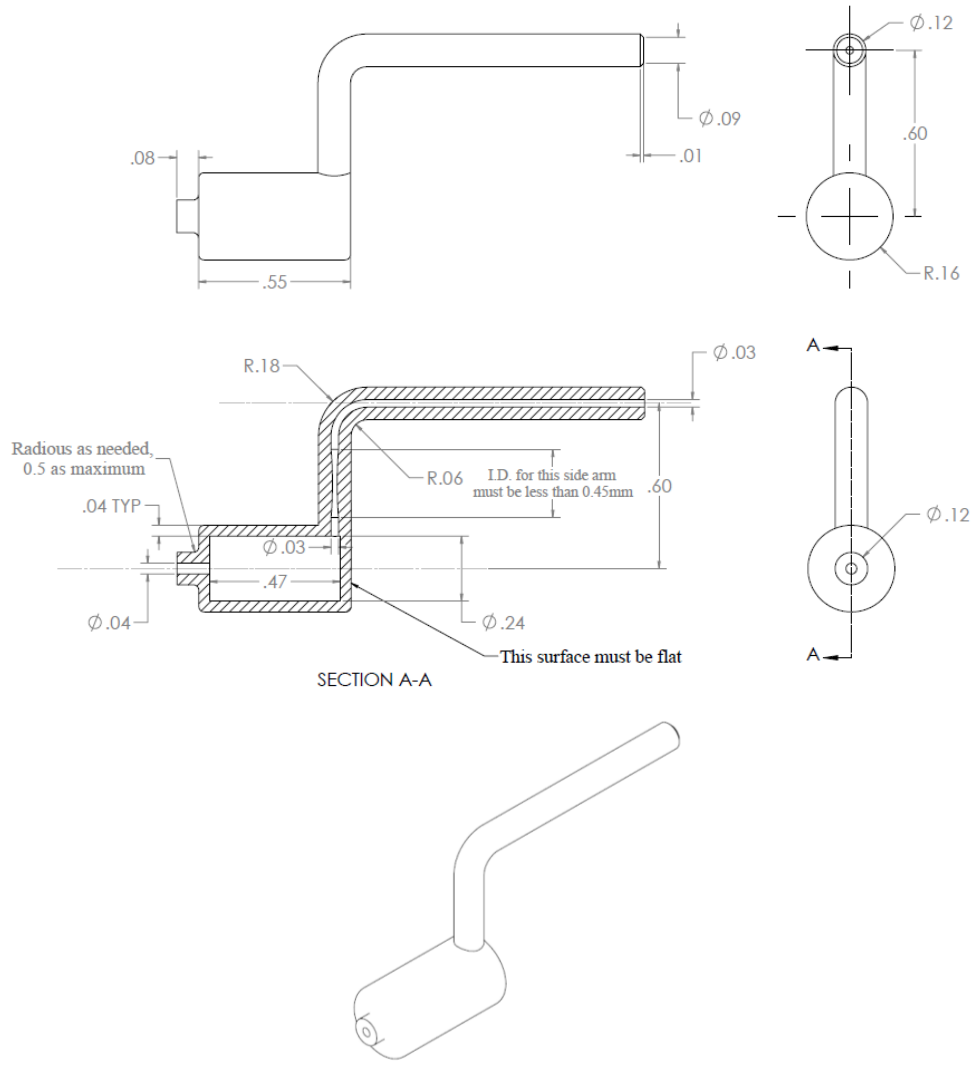

University of California, Los Angeles, Department of Chemical and Biomolecular Engineering								
Part	Radical source	Material	Quartz					
Filename	Quartz Ampoule	Scale	No	Units	inch	Quantity	1	
Designer	Angstron Systems	Date						
Revised by	Jeffrey Chang	Date	05/22/2014					
Contractor		Date						
Comments	Adapted from Angstron Systems		Tolerance	+/- .0001				

A.3. Six-Array Precursor Doser

SIX-ARRAY DOSER

Full Assembly

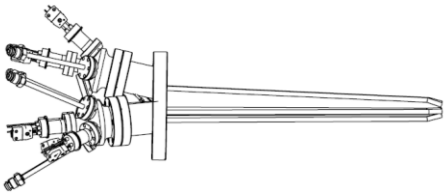

Side View

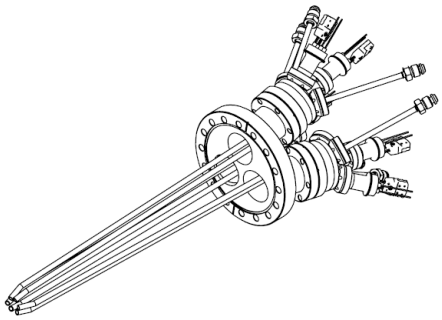

Trimetric View

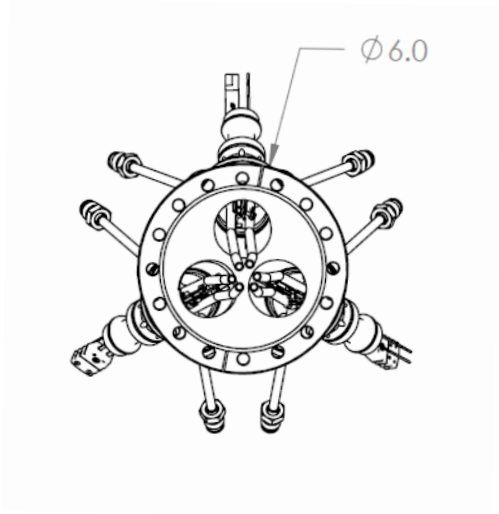

Front View (from vacuum)

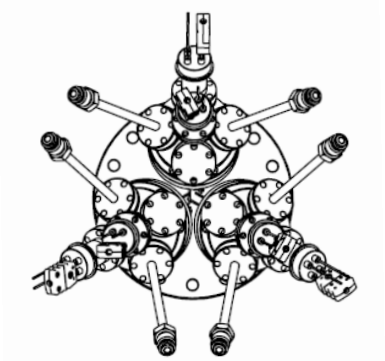

Back View (from ambient)

University of California, Los Angeles, Department of Chemical and Biomolecular Engineering								
Part	Six Array Doser	Material	Stainless steel					
Filename		Scale	No	Units		Quantity		1
Designer	John Hoang	Date						
Revised by		Date						
Contractor		Date						
Comments	Three 2-array dosers on 3-way multi-flange		Tolerance	+/- .0001				

SIX-ARRAY DOSER (Continued)

Two-Array Precursor Doser Assembly

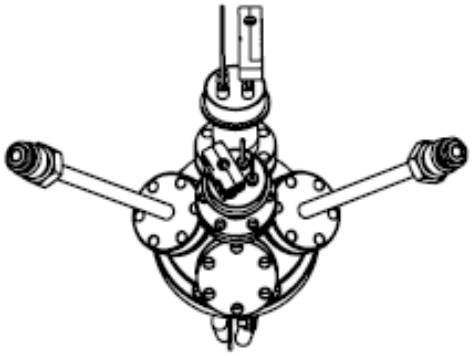

Back view (From ambient)

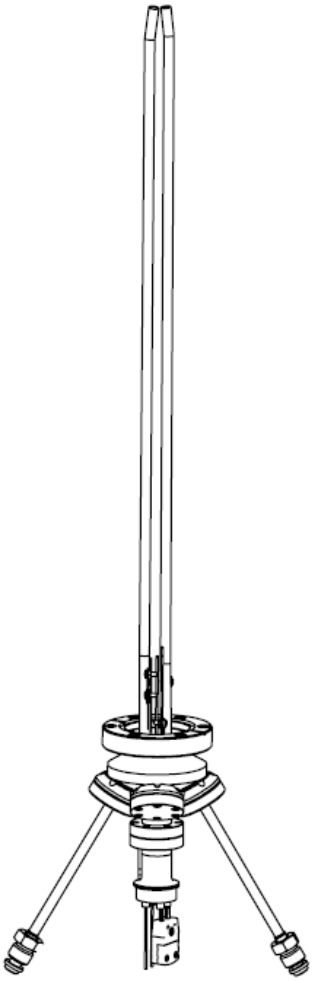

Side view

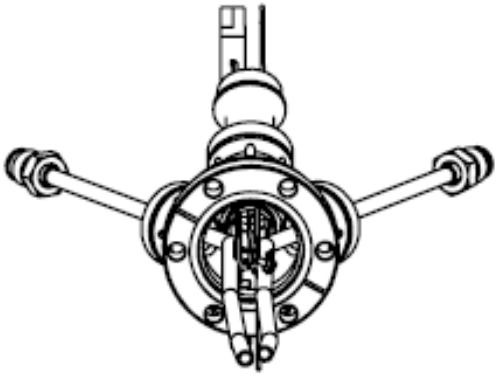

Front view (From vacuum)

University of California, Los Angeles, Department of Chemical and Biomolecular Engineering								
Part	2 Array Doser	Material	Stainless steel					
Filename	2_array_doser.pdf	Scale	No	Units		Quantity	3	
Designer	John Hoang	Date						
Revised by	Jeffrey Chang	Date	05/28/2014					
Contractor		Date						
Comments	5-way multiport connects to 2-3/4” Conflat		Tolerance	+/- .0001				

SIX-ARRAY DOSER (Continued)

5-Way Multicomponent Conflat Flange, 2.74”CF to 1.33” CF Mini

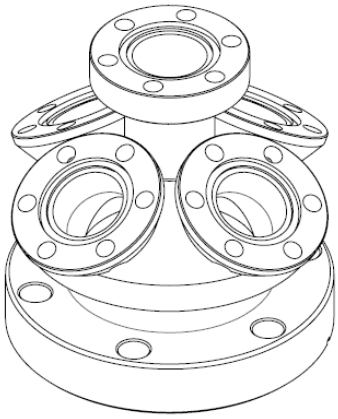

Trimetric view

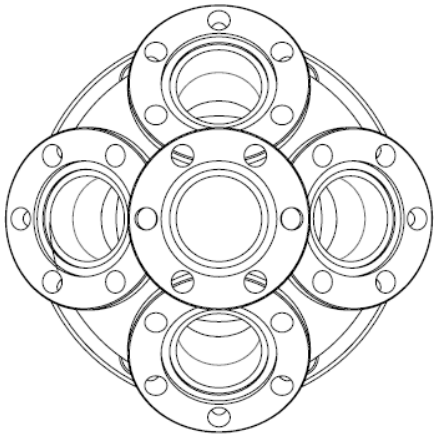

Top view

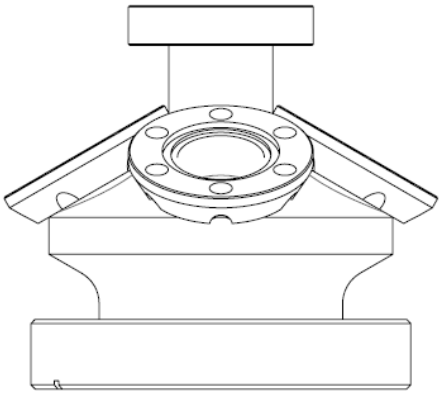

Side view

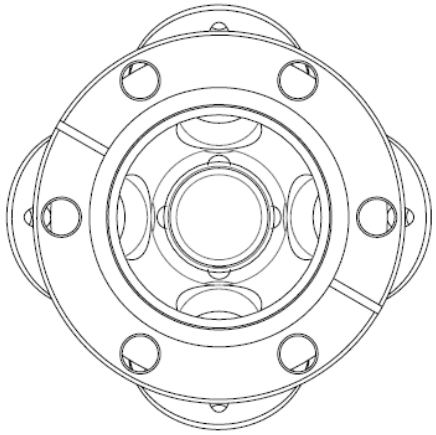

Bottom view

University of California, Los Angeles, Department of Chemical and Biomolecular Engineering								
Part	5-way Multiport 2.75"x5-1.33"Mini	Material	Stainless steel					
Filename	5way.pdf	Scale	No	Units		Quantity		3
Designer	MDC Vacuum	Date						
Revised by	Jeffrey Chang	Date	05/28/2014					
Contractor		Date						
Comments			Tolerance	+/- .0001				

SIX-ARRAY DOSER (Continued)

Thermocouple/ Power Feedthrough, 1.33” CF Mini

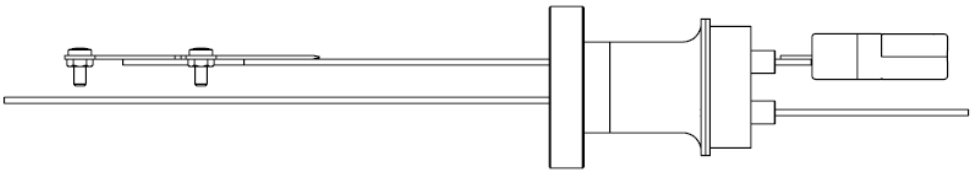

Top view

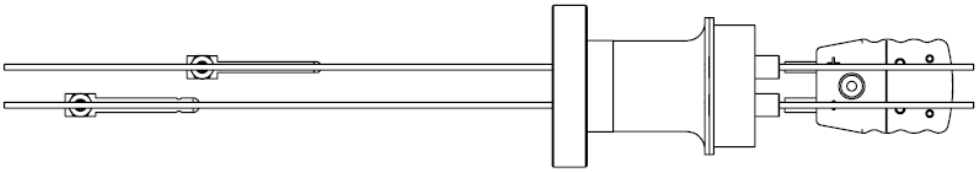

Side view

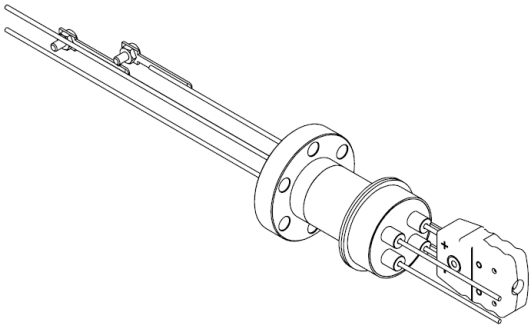

Trimetric view

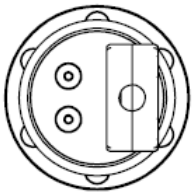

Front view (from ambient)

University of California, Los Angeles, Department of Chemical and Biomolecular Engineering								
Part	Thermocouple/Power Feedthrough	Material	Stainless steel					
Filename	TC.pdf	Scale	No	Units		Quantity		6
Designer	Insulator Seal	Date						
Revised by	Jeffrey Chang	Date	05/28/2014					
Contractor		Date						
Comments			Tolerance	+/- .0001				

Appendix B. MB Chamber Operating Procedures

For this part of appendix, please refer to Figure B.1, Figure B.4, and Figure B.5 for valve locations

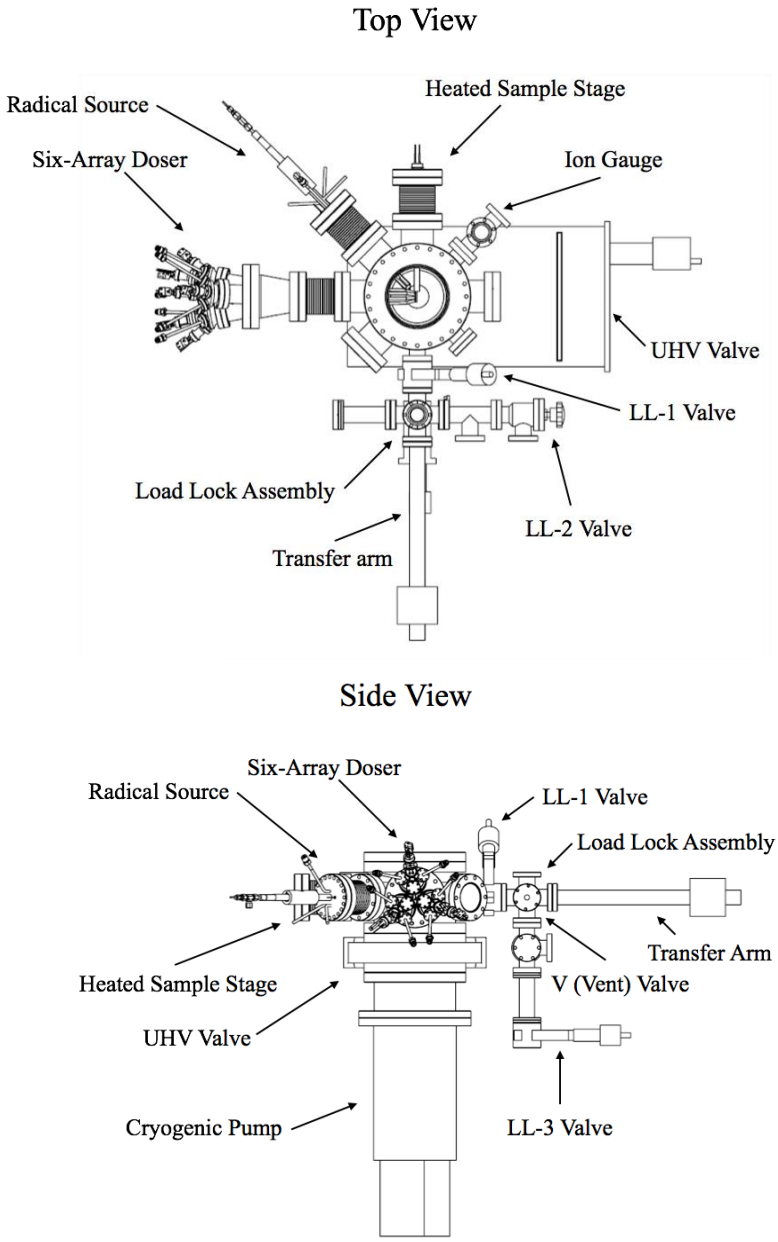

Figure B.1 Schematic of the main chamber (top and side views)

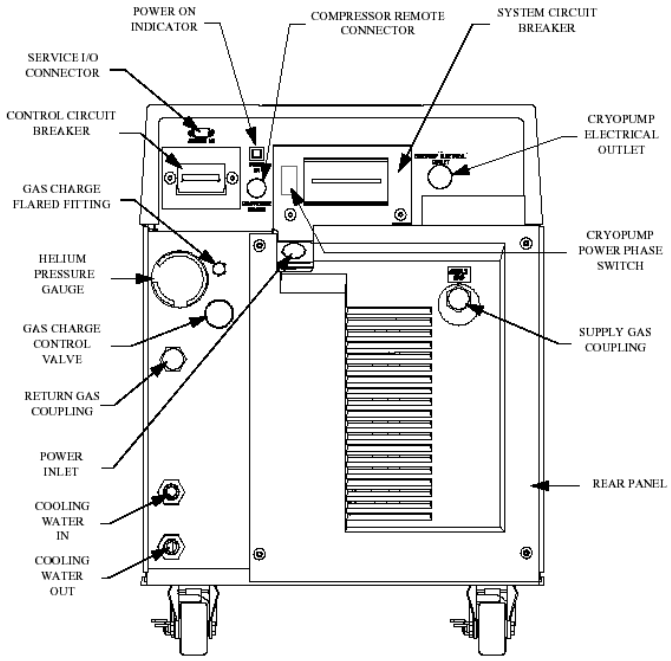

Figure B.2 Cryogenic pump compressor

B.1. Loadlock Chamber

B.1.1. Venting the Loadlock Chamber:

1. Close LL-1 gate valve first to isolate the main MB chamber from the loadlock chamber (this valve should normally be closed)
2. The LL-2 valve should be closed, isolating the loadlock chamber from the mechanical pump (this valve is normally closed as the loadlock is pumped by the turbomolecular pump)
3. Close LL-3 gate valve to isolate the loadlock chamber from the turbomolecular pump
4. Half-open the vent valve V to slowly vent the chamber while observing the Pirani gauge to allow for controlled venting
5. The readings on the Pirani gauge should be ~5-6×10^2 Torr when the loadlock chamber is completely vented
6. After the loadlock is completely vented, a sample can now be removed from/loaded into the load lock chamber

B.1.2. Pumping down the Loadlock Chamber

1. Close the V valve
2. Close the 5-U (back-up pumping of the turbomolecular pump from the mechanical pump) pneumatic valve (green light) to isolate the turbomolecular pump from the mechanical pump, this prevents a sudden pressure spike on the backside of the turbomolecular pump while rough pumping the loadlock chamber by the mechanical pump

3. Close the 5-L (differential pumping atom source) pneumatic valve (red) for the differential pumping of the radical source to prevent the pressure spike in the main chamber while rough pumping loadlock chamber with the mechanical pump
4. Slowly open the LL-2 valve (loadlock to mechanical pump) completely, then open the 5-L pneumatic valve, watch and wait until the TC gauge reaches the base pressure (60-100 mTorr). The Pirani gauge should read ~2.5×10^{-2} Torr
5. Open the 5-U pneumatic valve, once the loadlock chamber reaches base pressure
6. Slowly close the LL-2 valve. Open the LL-3 gate valve, pump down loadlock chamber with turbomolecular pump until the base pressure < 9×10^{-5} Torr is shown on the Pirani gauge (*note*: this usually takes 20-25 minutes)
7. The chamber is ready for sample transfer once the base pressure is reached

B.2. MB Radical Source

B.2.1. Turning on the Plasma Radical Source

1. If using H_2 gas, notify the lab and post the sign first
2. Ensure the cooling water is on; cooling water temperature should be ~18-20 °C
3. Turn on the microwave power supply unit (*note*: let the electronics warm up for at least 20 minutes before engaging microwave power) (This should be normally on)
4. Check the pressures of the gas cylinder and the gas line; if H_2 is used, open the H_2 gas cylinder and the gas line (*note*: all three valves on the regulator should be open and the pressure of the gas line should be ~20-30 psi)
5. Ensure the corresponding gas MFC flow rate is at 0%
6. Open the valve before MFC controller:
    a. 1-U if O_2 is used or
    b. 2-U if Ar is used
7. Open the valve after the MFC controller:
    a. 1-L if O_2 is used or
    b. 2-L if Ar is used
8. Close the 5-L pneumatic valve (closing the differential pumping line for radical system)
9. Close the 5-U pneumatic valve (closing the back-pumping line for the turbomolecular pump)
10. Evacuate the gas line through the mechanical pump by opening valve A-2 while monitoring the pressure on the TC vacuum gauge
11. Wait until the pressure on the TC returns to the base pressure of ~60-100 mTorr (the pressure should not fluctuate much)
12. Close the purging valve A-2 when the base pressure of ~60-100 mTorr is reached on the TC gauge
13. Open the 5-U pneumatic valve (opening the differential pumping line for radical system)
14. Open the 5-L pneumatic valve (opening the back-pumping line for the turbomolecular pump)
15. Open the injection valve A-1
16. Set the desired gas flow rate (~3%) on the MFC to achieve an operating pressure ~2×10^{-5} Torr (*note: the main chamber pressure should not exceed $3x10^{-5}$ Torr)*
17. Press “ON” (green button) on the microwave power supply unit

18. Increase the power to 25 watts
19. If necessary, to attain the minimized reflected power to 0-2 watts, tune the tuning slug between the outer and inner conductor of the radical source

B.2.2. Turning off the Plasma Radical Source

1. Press "ON" (green button) on the microwave power supply unit
2. Decrease the microwave forward power to zero
3. Press "OFF" (red button) on the microwave power supply unit
4. Close the valve before the MFC
    a. 1-U if O_2 is used or
    b. 2-U if Ar is used
5. Decrease the MFC gas flow rate to 0%
6. Close the valve after the MFC
    a. 1-U if O_2 is used or
    b. 2-U if Ar is used
7. Close the injection valve A-1
8. If H_2 is used, close the gas cylinder and the gas regulator
9. If H_2 is used, fill in the log sheet for H_2 run time
10. Turn off the microwave power supply unit (not required)

B.3. Precursor Doser

B.3.1. Flowing the Precursors

1. When idle, make sure that all the valves are open to prevent the gas lines from clogging
2. Make sure that all the temperature controllers are turned on, except during system maintenance
3. Each precursor doser has three different heaters corresponding to different doser location. The corresponding heater switch numbers of the temperature controller for different precursors are listed as the following:

Precursor	Temperature controller			Pneumatic valve
	Housing	Gas line/valve	In-vacuum	
TDMAH	Controller 1, channel 4	Controller 1, channel 5	Controller 1, channel 6	#2
$Fe(TMHD)_3$	Controller 3, channel 1	Controller 3, channel 2	Controller 3, channel 3	#5
$Bi(TMHD)_3$	Controller 3, channel 5	Controller 3, channel 6	Controller 3, channel 7	#6
$Co(TMHD)_2$	Controller 1, channel 1	Controller 1, channel 2	Controller 1, channel 3	#7

4. Heat the precursors to operating temperatures by temperature controllers. The operating temperature of different precursors are listed below, the heat up period is ~40 minutes (*note: the operation temperatures should not exceed individual precursor's decompose temperature*):

Precursor	Operating temperature (°C)		
	Housing	Gas line/valve	In-vacuum
TDMAH	50	120	110
$Fe(TMHD)_3$	120-130	190	185
$Bi(TMHD)_3$	150-160	200	185
$Co(TMHD)_2$	120	190	185

B.3.2. Stopping the precursor Flow after deposition

1. Idle pneumatic valves should be open at all times (prevent doser system clogging)
2. Remove the sample back to the loadlock chamber, Turn off the heaters that was turned on during deposition, and open the pneumatic valves to reconnect the hosing with the main chamber
3. Check the MB chamber pressure by IG while the heaters are cooling down, make sure that the pressure goes down to its base value (ion gauge reading ~2×10^{-6} Torr)

B.4. MB Chamber Compressor & Cryogenic Pump

B.4.1. Starting the cryogenic pump

1. Close UHV and CM valve to isolate the cryogenic pump from both the main chamber and mechanical pump (*note: CM valve is only open during pump regeneration*)
2. If regeneration is needed, ensure the pressure of cryogenic pump is high enough (higher than the base pressure of mechanical pump, reading should exceed 80 K) before pumping down the cryogenic pump. If the cryogenic pump was recently turned off, condensation is a good sign
3. If regeneration is needed, open the CM valve slowly to pump down the cryogenic pump by mechanical pump
4. If regeneration is needed, wait until mechanical pump base pressure is reached (~60-100 mTorr), close the CM valve
5. When the pump is regenerated, quickly set the system circuit breaker to the ON (up) position (see Figure B.2), and then set the Control Circuit Breaker to the ON (up) position.
6. Air molecule condensation will occur once the cryogenic pump is turned on
7. Wait until the temperature of the cryogenic pump reaches its operational value (~4K on the thermometer attached)
8. Open the UHV valve to connect the main chamber and the cryogenic pump

B.4.2. Turning off the Cryogenic Pump (usually for Maintenance and Regenerating Purpose)

1. Isolate the cryogenic pump by closing UHV valve
2. Set the System Circuit Breaker to the OFF (down) position
3. Set the Control Circuit Breaker to the OFF (down) position

4. Temperature will start to increase and the absorbed gas molecule will start to release from the pump body

B.5. Main Chamber

B.5.1. Venting main chamber (usually for maintenance and cleansing purposes)

1. Make sure the 5-L (PV-9) valve is closed to end the differential pumping for radical source
2. The A-1 valve should be closed to stop gas injection to radical source
3. Turn off the ion gauge by selecting the controller (Multi-gauge channel 1) and pressing "Emis" *(note: the ion gauge will can be seriously damaged if it remains on while venting)*
4. If the loadlock chamber pressure is higher than its base, pump it with the turbomolecular pump first until it reaches the base pressure of ~5-9×10^{-5} Torr (*note: for the pump down process of the load lock chamber, please see section B.1.2*)
5. Close valve LL-3 and open valve LL-1 to connect the loadlock chamber and main chamber, pumping them both with the cryogenic pump
6. Close the UHV gate valve to isolate the cryogenic pump, wait for the pressure to increase slowly to ~ 5×10^{-4} Torr due to chamber outgassing
7. Slowly open venting valve V, observe the pressure increase on Pirani gauge (*note: the Thermocouple gauge should stay at base pressure since mechanical pump is isolated*)
8. Eventually, the Pirani gauge should be displaying ~5-6×10^{2} Torr, depending on the ambient condition

B.5.2. Pumping down the Main Chamber

1. Make sure that the load lock chamber is connected to the main chamber and both of them are completely vented (Pirani gauge displaying ~5-6×10^{2} Torr)
2. Close the V venting valve and the load lock door
3. Close the 5-U pneumatic valve (green) for the turbomolecular pump and close the 5-L pneumatic valve (red) for the radical source differential pumping to isolate them from the mechanical pump *(note: prevent back flow)*
4. Open LL-2 roughing valve to pump down the system by mechanical pump, the Pirani gauge readings should decrease while the Thermocouple gauge will first have a drastic increase but decrease to its base pressure afterwards. (*note: the base pressures for Pirani gauge and Thermocouple gauge are low < 9×10^{-5} Torr and ~60-100 mTorr, respectively*)
5. Remember not to isolate the Turbomolecular pump too long otherwise the Turbomolecular pump can suffer from serious damage. Therefore, it is normally recommended to turn off the turbomolecular pump if it remains isolated longer than 10 minutes. However, when turning off the turbomolecular pump is not feasible, the turbomolecular pump should be back-up pumped by mechanical pump every 10-15 minutes. This can be done by closing the LL-2 valve and then open the 5-U valve for a few minutes. Close 5-U valve and open LL-2 valve to pump down the system again after the base pressure is reached on the Thermocouple gauge (~60-100 mTorr).

6. Once the base pressure of the mechanical pump is reached, start pumping down the system with Turbomolecular pump by first open the 5-U valve (*note: to connect the Turbomolecular pump with the mechanical pump*), then close the LL-2 valve (*note: to isolate the mechanical pump*), and subsequently open the LL-3 valve. The Pirani gauge reading should be < 3×10^{-4} Torr *(note: this is the base pressure when using turbomolecular pump to pump the loadlock and main chamber*)
7. When the base pressure is reached, close LL-1 gate valve to isolate the load lock chamber from the main chamber
8. Open the UHV gate valve to pump down the main chamber by the cryogenic pump. Turn the ion gauge by selecting Multi-gauge channel 1 and pressing "Emis". The base pressure should be lower than ~2-3×10^{-6} Torr

B.6. Deposition Procedures

1. Load the sample into loadlock chamber after venting, pump down the chamber following the instructions provided in section B.1.2 to base pressure (*note: it takes 25 minutes to pump down the load lock chamber from ambient to its base pressure, <9×10^{-5}Torr*)
2. Make sure that the system is at its base pressure, and the pneumatic valves are open so that the gas lines will not clog during operation
3. Open LL-1 gate valve, half close the UHV gate valve (*note: to prevent the sample from falling into the cryogenic pump*). Attach the sample onto sample heater using the magnetic transfer arm.
4. Pull the magnetic transfer arm back to the loadlock chamber, close LL-1 gate valve and reopen the UHV gate valve completely. Start pumping down the main chamber again.
5. Turn on the heaters to its operating temperature (*note: it takes 45 minutes to for the system to be pumped down and heated up to the operating condition*)
    a. Make sure to close the pneumatic precursors valves you aren't using
    b. If you have a specially volatile precursor, close its valve as well to prevent CVD
6. Leave the chamber for ~40-45 minutes for the heater set point to be reached
7. Check and make sure that the pressure and temperatures are at the correct set point
8. Close the pneumatic valves of the heated dosers in order to prevent gas phase reaction when the radical source is on
9. Close the 5-U and 5-L pneumatic valve
10. Pump down the radical course gas supply lines by opening A-2 manual valve, and open the lower and upper pneumatic valves depending intended gas (1-U and 1-L for O_2, 2-U and 2-L for Ar) for several seconds, refer to section B.2.1 for details
11. Close the A-2 manual valve; reopen the 5-U and 5-L pneumatic valve. Double-check the pressure gauge for leaking. If no, open the A-1 manual valve, then open the MFC for intended gas to 3.0%
    a. Close the valve for the precursor you will be heating before flowing gas source
12. Turn on the radical source following guidelines in section B.2.1, with microwave power supply unit running under 25 watts, reflected power 0-1 watts
13. Check if the plasma strikes by seeing the white-colored glow in the quartz ampule. If no, go to radical source maintenance, section C.2.2
14. Leave it striking for several seconds to regenerate the substrate surface active sites with radical atoms

15. Meanwhile, setup the desired LabView ALD recipe
16. Turn off radical source power supply before clicking run on LabView
    a. Please see section F for details of automation
17. To manually end the deposition, stop the LabView ALD recipe immediately after the last plasma step. Regain manual control of the microwave generator in the LabView ALD program if needed. Dial down the microwave power to 0 and turn off the microwave power source.
18. Close the lower pneumatic MFC valve; turn the MFC flow to 0%; close the upper pneumatic MFC valve; close the A-1 manual valve.
19. Turn off the substrate heater; transfer the sample to the loadlock
    a. Isolate the loadlock before removing the sample by closing the LL-1 and LL-2 gate valves.
20. Turn off the precursor heaters and open the pneumatic valves.

B.7. Emergency Shutdown Procedure

1. Turn off the ion gauge for the main chamber. Press the Varian Multi-Gauge display On CHAN to switch to the chamber pressure, then press EMIS to turn off.
2. Close the UHV and LL-1 gate valves, both are manual valves (see Figure B.1)
3. Turn off the Control Circuit Breaker on the compressor (see Figure B.2)
4. Turn off the System Circuit Breaker on the compressor (see Figure B.2)
5. Turn off the TMP by pressing the power button on the controller.
6. Open LL-2 to pump the MB system using mechanical pump

B.8. Utilities for MB System

B.8.1. Schematics for Electrical, Water, and Gases Systems

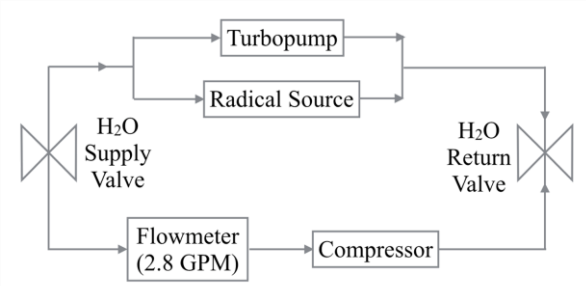

Figure B.3 Schematic of the cooling water system

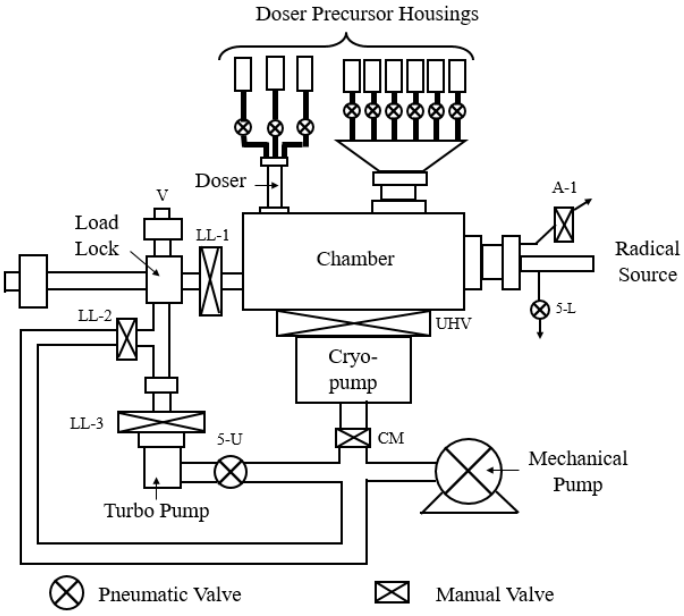

Figure B.4 Schematic of valves and gas lines for MB system

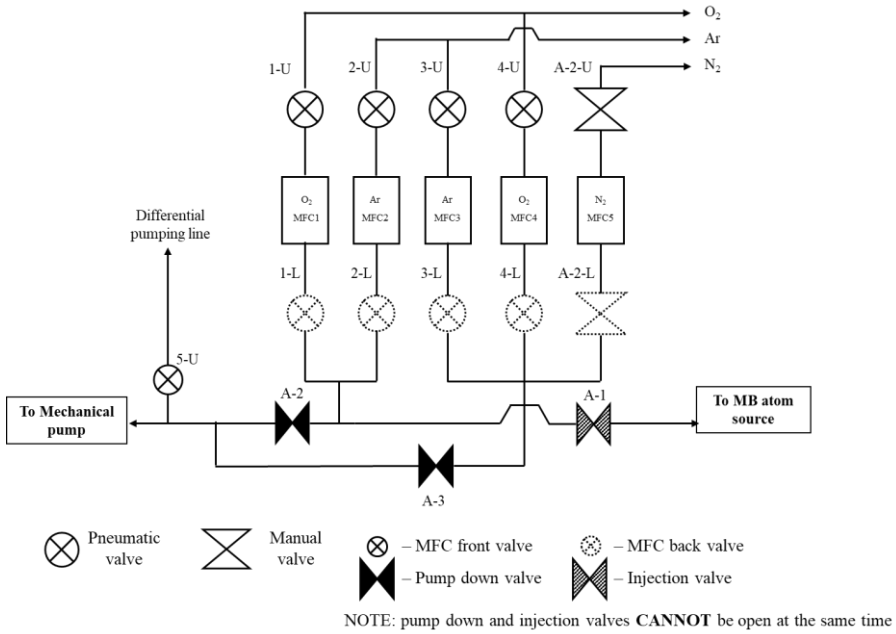

Figure B.5 Schematic of valves and gas lines for MB system

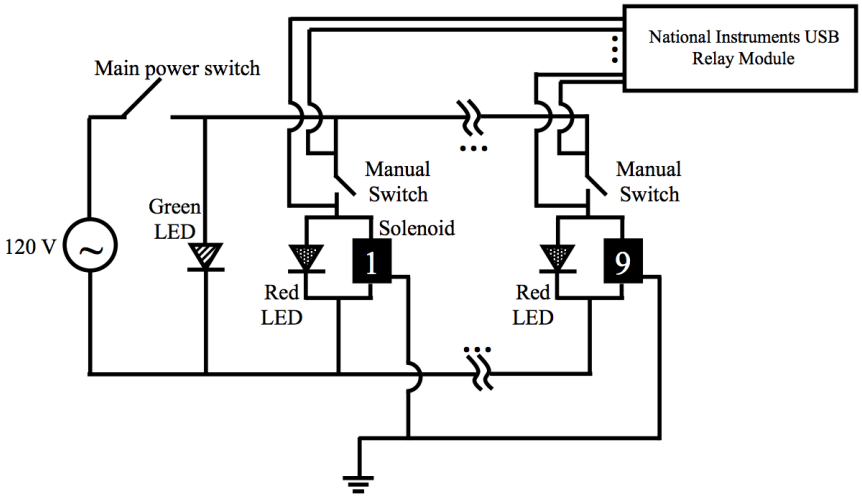

Figure B.6 Schematic of electrical wiring for pneumatic valve control

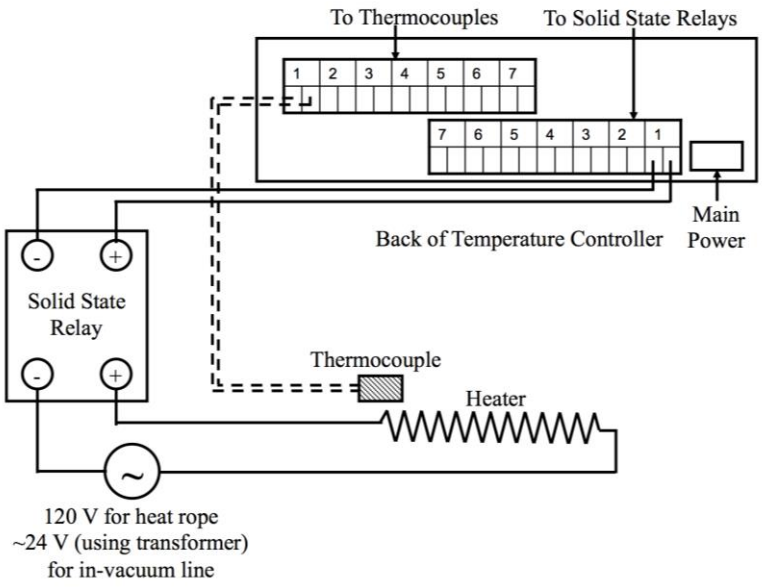

Figure B.7 Schematic of electrical wiring for controlled heaters

B.9. List of Equipment Used in Electrical, Water, and Gas Systems

B.9.1. List of Electrical Equipment Parameters

Electrical equipment	Parameters
Mechanical pump	115 VAC, single phase
Cryogenic pump compressor	208 VAC, 3 phase, 30 A min
Turbomolecular pump	115 VAC, single phase
Microwave radical source power supply	110 VAC, single phase
Ion source power supply	115 VAC, single phase
Temperature controller	120 VAC, single phase
Sample heater	Variable 0-30 VAC using transformer
Radical source mass flow controller	120 VAC, single phase
Multi-gauge controller	115 VAC, single phase
Heating wires	120 VAC
Kapton heaters	120 VAC

B.9.2. List of Water and Gas Equipment Parameters

Equipment	Parameters
Water compressor	Flow rate = 2.8 GPM
H_2 Cylinder to MFC5 to Radical Source	Flowing H_2
O_2 Cylinder to MFC4 to Radical Source	Flowing O_2
N_2 Cylinder to MFC3 to Radical Source	Flowing N_2
Ar Cylinder to MFC2 to Ion Source	Flowing Ar
Ar Cylinder to MFC1	Flowing Ar

B.9.3. List of the Equipment/Parts Used for MB System Setup

Vendor	Catalog No.	Description
Alfa Aesar	11386	Indium foil, 0.1mm (0.004in) thick Puratronic, 99.9975%, 100mm x 100mm
Alfa Aesar	41359	Bis(2,2,6,6-tetramethyl-3,5-heptanedionato)Cobalt (II) 99.9%-Co
Bid Service	40144	Ion Beam Drive, Commonwealth Scientific ID-2500-C
C.W. Swift	23N-50-0-30	Microwave connector, N type, article number 22642835
Cerac Inc.	1314-36-9	Yttrium Oxide, 99.9999 (REO basis)
Controlled Motion Solutions	PSFTN0N10NP	10 Station manifold
Controlled Motion Solutions	PS2982B53P	120/60 Coil Sol Kit
Duniway	FIL-7A	Replacement Filament for T-NUDE-F Ion Gauge
G. Finkenbeiner, Inc.		Quartz ampoule (custom-made)
Momentive Performance Materials	HTR1001	Boralectric™ heater on PBN plate substrate
Helix	7021002P001	Charging Line, 10' (For Compressor)
Helix	8140000K001	Installation Tool Kit (For Compressor)
Helix	8031403	Two Stage Regulator (For Compressor)
Helix	8080250K003	Maintenance Manifold (For Compressor)
ISI	9392000	1 TC pair/1 Power Pair / with TC connectors, C type

ISI	5TC-GG-K-30-36	Glass Insulated Thermocouples
ISI	9412008	Power feedthrough, 8 pins, 10 Amps, 500 V, 1-1/3" flange, conductor material Moly
ISI	9924001	Power-Push-On, 150 deg. C Air, 400 deg C Vacuum Service, Gold Plated
Kaptontape	KPTD-1/2	Double-sided Kapton tape
Kaptontape	KPT5-1/2	Single-sided Kapton tape
Long beach valves & fitting	SS-4-UT-6-400	Ultra-torr Swagelok Tube Fitting Union
Maxtek	BSH-151	Bakeable QCM sensorhead/feedthrough (vacuum)
Maxtek	103200-3	QCM Sensor Crystal, 6 MHz, SCV-14A-6N-Sil-S-B (Si over Au solid side)
MDC	409007	Cluster Flange 6"x3-2.75"
MDC	402039	Conical Reducer 6"x4.58"
MDC	110000	Flange, 1.33", Blank
MDC	409004	MultiPort Flange 2.75"x5-1.33" Mini, T
MDC	402000	Nipple, 1.33"
MDC	41010	O-ring, Viton 2-010
National Instruments	779453-01	USB-9481 4-ch SPST Relay Module
Nor-Cal	133-1/4-MVCR	1 1/3" CF to Male VCR
Nor-Cal	LFT-075-1-025	Single Liquid Feedthroughs
Omega	5TC-GG-K-30-36	316 SS VCR Face Seal Fitting, 1/4 in. Unplated Gasket, Non-Retained Style
Omega	CN1507TC	7 Channel Controller
Omega	NI80-012-200	80%Ni/20%Cr, 200' pool of 28 gauge bare resistance heating wire, diameter 0.0126"
Omega	CO1-K-72 INCH	Cement on T/C
Omega	SSR330DC25	Solid State Relay DC 25 Amp
Omega	TT-K-20-SLE-100	Special Limits of Error wire
Pfeiffer Vacuum	PM041264X	Power cable for TPC 121 (PMC01475A M-02095)
Strem	93-3943	Yttrium foil, 99.9% REO, 25x25 mm, 0.127mm thick
Strem Chemicals	83-1000	Tris(2,2,6,6-tetramethyl-3,5-heptanedionato)Bismuth (III) 99.9%-Bi
Strem Chemicals	26-3610	Tris(2,2,6,6-tetramethyl-3,5-heptanedionato)Iron (III) 99.9%-Fe
Swagelok	SS-4-VCR-1	VCR Fitting, 1/4 in. Female Nut
Swagelok	SS-4MG-VCR-MH	SS Metering valve, 1/4 in. Male Swagelok VCR Metal Gasket Face Seal Fitting, Vernier Handle
Swagelok	SS-HBVV51-C	Stainless Steel High-Pressure Bellows-Sealed Valve, 1/4 in. Female Swagelok VCR Face Seal Fitting, NC Actuator, Polyimide Stem Tip
Swagelok	SS-4-VCR-4	VCR Fitting, 1/4 in. Male Nut
Swagelok	316L-4-VCR-3AS	VCR Fitting, Short Automatic Tube Butt Weld Gland, 1/4 in. VCR
Transfer Engineering		Custom-made sample transfer, sample station, and heating system
Varian	L8321301	UHV Board (pressure controller)
Varian	L64403010	UHV Cable (pressure controller)

Appendix C. Maintenance

C.1. Heated Sample Stage

C.1.1. Removing the heated sample stage

1. Vent the chamber (see Section B.5.1)
2. Remove the heated sample holder from the main chamber carefully, and be cautious not to damage the radical source and doser (*note: avoid contacting the chamber wall while removing the sample stage*)
3. After reattaching the sample stage, double check the alignment with transfer arm and adjust bellow as necessary

C.2. Radical Source

C.2.1. Replacing the quartz ampoule (a custom made part)

1. Vent the main chamber and then remove all fittings and connections (Section B.5.1), remove the radical source as well (*note: be careful and do not bump the radical source assembly to the inner wall of the chamber*)
2. Remove the top clamp to reveal the quartz ampoule
3. Remove Teflon heat-shrink tubing extending from gas-line feedthrough that is attached to the quartz ampoule
4. When installing a new quartz ampoule, Indium foil must be wrapped around the cylindrical section to ensure enough heat conduction. Failure to do so might result in unstable plasma due to overheating and poor heat removal
5. Replace Teflon heat-shrink tubing to connect the gas line to quartz ampoule
6. Place quartz ampoule in the housing again to make sure that a proper thermal contact is achieved.
7. Make sure that the end of the quartz ampoule is contacting the microwave waveguide
8. Secure the quartz ampoule to radical source by screwing down the top clamp
9. Wrap wire extending from electrical feed through to allow tesla coil induced plasma generation if necessary

C.2.2. Tuning the radical source

1. The distance from the attached N-1 cable to the end of the waveguide must be tuned since the plasma generation highly depends on the waveguide resonance condition
2. Turn off the microwave power supply first, then remove the N-1 cable and move the tuning slug to desired location
3. For large adjustments, the set screws can be loosened allowing more free movement, otherwise, the corkscrew section of the tuning slug can be rotated to allow for fine adjustments

4. Adjust the tuning until the reflected power is at its minimum value (usually ~0-0.1 watt), make sure that the plasma can strike spontaneously upon the application of microwave power
5. Sometimes the oxidation of the N-1 cable contact tip can lead to contact problems to the coaxial waveguide, remove the N-1 cable and clean the oxide on the tip using a sandpaper. Replace the contact tip if necessary.

C.3. Precursor Doser Arrays

C.3.1. Replacing precursor in housing

1. Do not vent the main chamber. Isolate the cryopump from the main chamber, using only the turbomolecular pump to pump the main chamber
    a. This protects the cryopump from any unintended sudden flow from the precursor housings
2. Place a blank sample in the main chamber
3. Remove the aluminum foil wrapping from the precursor housing
4. Unravel heating coil
5. Turn off power switch for heaters and thermocouples
    a. Start with transformer and go up the line
6. Disconnect the power cord to the precursor heater you are replacing in the back
    a. The top outlet row is for housing; middle outlet row is for valves (labeled as for vacuum lines); bottom row is for in-vac heaters
7. Disconnect heating and thermocouple line (they are color coded)
8. Turn on power switches in the same order
    a. Start with transformer
9. Close precursor housing with VCR gasket and fitting while the housing is removed
10. Disconnect/remove precursor housing
    a. Use 3/4” and 5/8” wrenches
11. Triple rinse precursor housing
    a. First disassemble and dispose of leftover precursor
    b. Then sonicate in acetone/IPA/water (15 min each)
    c. Bake for 60 min at 120 C
12. Once the precursor housing is reconnected, make sure that all valves are closed again
13. You will need to vent the main chamber after reconnecting precursor housing before opening any of the valves
    a. Ensure the cryopump is isolated and isolate the Turbopump. Close the differential pumping valve.
    b. Vent main chamber as if you are venting loadlock. After vented, open valve to precursor you replaced only.
    c. Pump down main chamber as if pumping down loadlock. Open the rest of the precursor housing valves before connecting the turbopump to pump down the main chamber (you will notice the pressure spiked).
14. Reconnect all the heating coil and thermocouple lines as before
15. Cover the housing with aluminum
16. Bake the precursor housing (at 100 C) with the turbopump on only at first for 2 hours, then the cryopump overnight.

C.3.2. Replacing in-vacuum heaters

1. Do not vent the chamber. Remove the precursor doser carefully.
2. Remove the Teflon gape, then the old Kapton heater (two, each in 12” × 1”) from doser gas lines
3. Prepare a new Kapton heater, in the size of 12” × 1”, which is sufficient for covering the entire in-vac gas line
4. Wrap the gas lines with the Kapton heater spirally *(note: the heater should be evenly spaced with no overlapping to give a uniform heating throughout the entire gas line)*
5. Tightly wrap the Kapton heater with the Teflon tape to fix the heater onto the gas lines
6. Make sure that the heaters are attached onto the gas lines properly, and remember to secure the corresponding thermocouple to the gas line *(note: if the thermocouples are not well attached, the heater might be heated up uncontrollably and burn out)*
7. Attach the heaters to the corresponding power feed-through and thermocouple
8. Heat up the in-vacuum gas lines for several hours to test and remove the moisture before using it

C.3.3. Replacing the air-side vacuum heaters for gas lines and precursor housing

1. For air-side vacuum gas lines and precursor housing heaters, spirally wrap the parts with heating wires and make sure it is wrapped with even spacing, proper contact, and no overlapping
2. Secure the corresponding thermocouple to the gas line or precursor housing (*note: if the thermocouples are not well attached, the heater might be heated up uncontrollably and burn out*)
3. MAKE SURE TO TURN OFF THE POWER STRIP BEFORE PLUGGING IN HEAT ROPE. In order to prevent clogging, wrap the heating wire more closely and tighter at the cold spots (valves and connections such as VCR and Swagelok connections). Setting a higher temperature can also prevent clogging

C.3.4. Unclogging gas lines and valves

1. Remove the clogging precursor by using acetone and by plugging another gas line with a smaller diameter into the clogged gas line
2. After removing precursors, rinse the gas line with copious amount of acetone in order to remove all the remaining chemicals on the gas line wall
3. Dry out all the chemical solvents before placing the parts back onto the chamber
4. Dispose the chemical waste with proper procedures

C.3.5. Replace valve bellows assembly

1. Remove the pneumatic valve. May be necessary to vent the chamber.

2. MUST actuate the valve with compressed air before disassembling the valve bellow assembly *(note: make sure that the valve is operating normally)*
3. Unscrew the top of the valve while its actuated to the OPEN position, be careful not to damage the gas line fittings (note: unscrewing while the valve is in CLOSE position will damage the valve)
4. Unscrew the bellows assembly from the valve and replace gaskets as needed

C.4. Cryogenic Pump and Compressor

Note: for complete documentation, refer to HELIX 9600 Compressor operation manual

C.4.1. Regenerating the cryogenic pump

1. Isolate the cryogenic pump by closing the UHV gate valve, and then close the LL-1 valve to isolate the main chamber. LL-2 should also be closed so that the mechanical pump serves to back the turbo pump only at this point
2. Turn off the compressor:
    a. Set the System Circuit Breaker on the compressor to the "OFF" position
    b. Set the Control Circuit Breaker on the compressor to the "OFF" position
3. Wait around 30 minutes for the manifold inside the cryogenic pump to approach room temperature
4. Close the 5-U pneumatic valve and the 5-L pneumatic valve, isolating the turbomolecular pump and the differential pumping from the mechanical pump. Connect the mechanical pump to the cryogenic pump by opening the CM valve.
5. Heat up the cryogenic pump with heating sleeves to ~100°C (100% when using a transformer). At this point we are waiting for the cryogenic pump to reach base pressure (~30m Torr) by the mechanical pump. This can take several hours.
6. Occasionally (*note: each 20-30 mins*) pump down the turbomolecular pump by mechanical pump by closing CM valve and opening the 5-U pneumatic valve in order to prevent it from winding down
7. After the base pressure of the cryogenic pump is reached, close CM valve and then pump down the turbomolecular pump by the mechanical pump (*note: if the whole chamber is vented, follow the pump down procedure in section B.1.5*)
8. Turn on the compressor:
    a. Set the System Circuit Breaker on the compressor to the "ON" position
    b. Set the Control Circuit Breaker on the compressor to the "ON" position
9. Initiate the compressor and wait ~2 hours for the cryogenic pump to cool down to the temperature of liquid He (~17K on the cryogenic pump temperature reader)
10. When the loadlock and main chamber are pumped down to turbomolecular pump base pressure, open the UHV valve and close the LL-1 gate valve to start pumping down the main chamber by cryogenic pump (*note: for details, please see Section B.5*)

C.4.2. Helium recharge

1. Obtain UHP (99.9999%) He gas cylinder and secure the regulator to its top (*note: the regulator should be only used for He cylinder to prevent contamination*)
2. Open the LL-1 gate valve to unify the pressure between loadlock chamber and the main chamber (*note: to prevent potential pressure back shoot that could damage the turbomolecular pump*)
3. Isolate the cryogenic pump by closing UHV gate valve
4. Turn off the compressor:
    a. Set the System Circuit Breaker on the compressor to the "OFF" position
    b. Set the Control Circuit Breaker on the compressor to the "OFF" position
5. Open the valves on the regulator (*note: to purge the gas in the regulator gas line by He flow*)
6. Open the brass cap labeled as "Helium Gas Charge"
7. Attach the regulator gas line to the "Helium Gas Charge" port but do not tighten it completely (*note: continuing the purge process*)
8. Purge the gas line continue for ~1 minute
9. Fully tighten the gas line onto the "Helium Gas Charge" connection and adjust the regulator valve to proper extent
10. Crack open the gas charge control valve (black) under the "Helium Gas Charge" to recharge Helium into the compressor until the pressure gauge reaches "SYSTEM PRESSURE OFF POSITION" (the white region)
11. Immediately close the gas charge control valve (black) on the compressor
12. Remove the gas line and close the regulator valve
13. If the pressure gauge is reading higher than the "SYSTEM PRESSURE OFF POSITION" crack open the gas charge control valve (black) when there is nothing attached on the "Helium Gas Charge" to release the pressure inside compressor until the acceptable region is reached
14. Return the cap to "Helium Gas Charge" port
15. Turn on the compressor
    a. Set the System Circuit Breaker on the compressor to the "ON" position
    b. Set the Control Circuit Breaker on the compressor to the "ON" position
16. Initiate the compressor and wait ~2 hours to cool down the cryogenic pump to the temperature of liquid He (~17K on the cryogenic pump temperature reader)
17. When the loadlock and main chamber are at the turbomolecular pump base pressure, open the UHV valve and close LL-1 gate valve to start pumping down the main chamber by cryogenic pump (*note: for details, please see Section B.5*)

C.4.3. Discharging the helium

1. Open the LL-1 gate valve to unify the pressure between loadlock chamber and main chamber (*note: to prevent potential pressure back shoot that could damage Turbomolecular pump*)

2. Simultaneously, isolate the cryogenic pump by closing UHV gate valve
3. Remove the flare cap from “Helium Gas Charge” fitting
4. Open the gas charge control valve (black) very slowly to allow a slight amount of He to escape
5. Leave the valve open until the He pressure gauge is within the range of “SYSTEM PRESSURE OFF POSITION” and then immediately close the gas charge control valve (black)
6. Turn On the compressor
    a. Set the System Circuit Breaker on the compressor to the “ON” position
    b. Set the Control Circuit Breaker on the compressor to the “ON” position
7. Initiate the compressor and wait ~2 hours to cooling down the cryogenic pump to the temperature of liquid He (~17K on the cryogenic pump temperature reader)
8. When the loadlock and main chamber are at the turbomolecular pump base pressure, open the UHV valve and close LL-1 gate valve to start pumping down the main chamber by cryogenic pump (*note: for details, please see Section B.5*)

C.4.4. Replacing the absorber

1. Open the LL-1 gate valve to unify the pressure between the loadlock chamber and the main chamber (*note: to prevent potential pressure back shoot that could damage Turbomolecular pump*)
2. Simultaneously, isolate the cryogenic pump by closing the UHV gate valve
3. Turn off the compressor:
    a. Set the System Circuit Breaker on the compressor to the “OFF” position
    b. Set the Control Circuit Breaker on the compressor to the “OFF” position
4. Remove the 4 screws which secure the rear panel and remove the rear panel
5. Use wrenches included with system (1-3/16” and 1-1/8”) and disconnect the Helium connectors quickly to reduce leakage
6. Using a 7/16” wrench, remove the absorber mounting bolt
7. Move the absorber from under the mounting tabs in the base and remove the absorber from the compressor
8. Install the replacement absorber under the mounting tabs and secure it into place with the bolt removed during step 6
9. Using the two wrenches as in step 5, connect the two self-sealing Helium couplings quickly to minimize Helium leakage
10. Install the compressor rear panel

Appendix D. Troubleshooting

D.1. Heated Sample Stage

Problem: The temperature controller does not register an increase in sample heater temperature after being turned on

Solutions:

- It might be because of the heaters:
    - Check the power connections of the heater, the power strip and transformers, make sure that the heaters are being fed with power
    - Check the electrical connections of the heater, whether if it has a correct resistance and electrical continuity *(note: the heater resistance should be ranging between 9Ω to 13Ω)*. If the resistance is not in the range of 9Ω to 13Ω, remove the sample stage as Section C.1.1 and troubleshoot it

Problem: The sample holder arms are wobbling or not secure enough

Solutions:

- Vent the chamber, and remove the sample holder according to Section C.1.1
- Remove the sample holder and the heater assembly to remove the bellow
- Remove the bellow
- Check the tightness of the screws securing the arm to the flange, according to the screw condition, either tighten the screw or replace it
- Reassemble the sample holder unit (sample holder, heater, bellow, etc.) and reattach the entire unit back to the chamber

D.2. Radical source

Problem: Plasma cannot be generated during operation

Solutions: There are several factors that can lead to the situation

- Oxygen flow
    - To check the oxygen flow, make sure that main chamber base pressure is somewhat elevated (~2×10^{-5} as of Dec. 2017) from its original base pressure
    - If the pressure is not elevated, check the Oxygen connections and gas lines to see whether there is a leakage or not (for example, check the compressed air gas lines to see any possible leakage that prevent pneumatic valve to work normally, the mass flow controller flow reading, low pressure in Oxygen gas cylinder, etc.)
- Cooling water flow
    - Make sure that the cooling water is working normally, the center conductor should be around 10-15°C (feeling cool by touching)
    - The cooling water line might be clogged with algae
    - If the quartz ampoule is not properly contacted to cooling block by Indium foil, the temperature of the ampoule could be too high *(note: this problem is not likely to happen if the quartz ampoule is not being removed recently as of Dec. 2017)*
- Electrical connection

- Tesla coil could be used to test the radical source; when the plasma gas is glowing and when microwave power source is on and set to intended input power, contact the tip of the Tesla coil to the electrical feed through and quickly turn on and off Tesla coil **(*note: take extreme caution when using tesla coil, it generates a voltage ~10,000-50,000V, make sure the tip is contacted to electrical feedthrough*)** This is not a permanent solution as the Tesla oil cannot be automated
- It maybe also because of the bad contact between the N-1 cable and the inner conductor, check whether if there is greenish-blue oxidation of the inner conductor, which might influence the electric conduction. It can be fixed by using sand paper to scrub the inner conductor surface and by tuning the location of contact

Problem: Plasma is unstable or with high reflected power
Solutions:

- Make sure the 5-L differential pumping valve is open for the radical source tube
- Check the tip of Huber N-type microwave cable and the surface if the inner conductor, if greenish-blue oxidation has grown, remove it by sanding the surface to give proper contact between the N-1 cable and inner conductor
- Clean the inner conductor with isopropyl alcohol and with can of compressed air, metal fragments could potential provide grounding and shortage to the conductors
- Adjust the contact angle of needed *(by rotating the inner coaxial waveguide)*

D.3. Precursor Doser Arrays

Problem: Temperature controller channel does not register an increase in temperature for in-vacuum heater, has line heater, or housing heater after being turned on
Solutions:

- Make sure that all the power strips and connections for the heaters are well connected and functioning
- Check the system with the thermometer probe to see if the heaters are actually heated up, in order to find out the problem is because of the heaters or the thermocouples (note: this may not be possible for the in-vacuum heaters)
- If the heaters are heated up, it means that the thermocouple is not functioning, check whether if the thermocouple is properly attached to temperature controller and the heaters
- Replace the thermocouples if the readings of thermocouples are not correct even with correct connection (sometimes the thermocouple would degrade and cause an open circuit)
- If the heaters does not heat, check the resistance of the heater by a multi-meter, see whether the resistance is normal or the heaters are grounded to gas lines *(note: a resistance in the MΩ scale indicates that the heater is broken)*
- Replace the heater if needed

Problem: Low precursor flux to substrate sample surface
Solutions:

- Alignment

    - Double check the alignment of the precursor doser to the sample surface, tune it of necessary
- Precursor
    - Precursor may not be sufficiently heated to give enough air flux, further heat up the parts to a higher temperature if necessary (*note: check the precursor MSDS in obtain the information of sublimation and decomposition temperature*)
    - Check precursor housing to see whether there is sufficient amount of precursor remaining (this requires refilling the precursor)
- Clogging
    - Clogging may happen inside the valves, precursor gas will frequently adsorb on gas lines and valves if they're not clean enough and or existing local cold spots
    - Detach the precursor gas line, clean it with acetone and then sonicate it to clean up the precursor clogging
    - Precursor gas lines must be baked (to remove the moisture) properly before being installed to the chamber (***note: acetone is extremely flammable, therefore make sure acetone has been totally removed before baking***)

D.4. Cryogenic pump and Compressor

Problem: Chamber is not pumping down to base pressure or pumping speed is reduced
Solutions:

- Pressure
    - Check and make sure that the compressor has enough He pressure by seeing the He pressure gauge
    - If the pressure is out of operational range, either recharge or discharge He gas (see Section D.4)
- Temperature
    - Make sure that the cryogenic pump is working under proper temperature (~24K)
    - If the temperature is not under operating range, regenerate the cryogenic pump if necessary (see section D.4)

Appendix E. LabVIEW and Automated Deposition

E.1. Programming an Automated Deposition

E.1.1. To program a full deposition sequence

We can express the deposition process into a pseudo-code format that consists several nested "For" loops and sequences as following:

```
for [number of overall deposition sequences, for analysis purposes](normally set to 1)
        wait [10 seconds]
                begin [remote microwave power interface]
        for [number of global cycles]
                for [number of local sequences for precursor]
                        while [time for precursor exposure]
                        Actuate channel to switch ON pneumatic valve
                end

                while [time for pump down]
                        Actuate channel to switch OFF pneumatic valve
                end

                while [time for radical exposure]
                        Actuate channel to switch ON radical source
                end

                while [time for pump down]
                        Actuate channel to switch OFF radical source
                end

        end
        ...(repeat for each precursor )
        stop [remote microwave power interface]
end
```

E.1.2. Programming one single local deposition cycle

1. Inside the global cycle loop, create a "For" loop and insert a flat sequence
2. Connect a constant to the for loop, right click it, and left click on "change to control"
3. Create four blank frames in the flat sequence
4. In order to set a create waiting timer, create one control constant by creating a new constant and right clicking it, then left clock on "change to control". Create another constant and set it to 1000 (*note: the unit of time in the program is millisecond*).
5. Create a multiplication operation and connect the control constant and the "1000" constant into the input (left) side.
6. Create a "wait (ms)" and connect it to the output (right) side of the multiplication output.
7. Each frame is used to actuate the following process respectively:

    a. Frame 1: Turn ON the pneumatic valve for a specific precursor, start precursor pulse
    b. Frame 2: Turn OFF the pneumatic valve for a specific precursor, starting pump down process
    c. Frame 3: Turn ON the microwave supply to start radical pulse
    d. Frame 4: Turn OFF the microwave supply to start another pump down step
8. Depends on the process and precursor used, construct different local cycle loops if needed

E.2. Programming for Data Acquisition Tool

E.2.1. Inserting data acquisition module to block diagram code for NI-USB 9481 relay module

1. Inside the desired block inside block diagram, right click on empty space and click Express -> Output -> DAQ Assistant
2. Double clock the DAQ Assistant block, expend General Signals -> Digital Signals -> Line Output to setup which switch are the assistant is going to control
3. Find the corresponding device and add the first output, the device are named as following
    a. MicrowavePower (USB-9481): Radical source
    b. PC1Thru4 (USB-9481): Pneumatic valves number 1-4
    c. PC5Thru8 (USB-9481): Pneumatic valves number 5-8
    d. PneumaticControl (USB-9481): Pneumatic control panel
4. After choosing the desired control panel, click the first controller and press finish button
5. In the configuration tab, press the blue + button and add the rest of the controllers in (*note: the controllers will not follow its original sequence so please pay attention which corresponds to which*)
6. Click x to finish setting up DAQ Assistant

E.2.2. Actuating relay within block diagram code

1. Create a new numbered array by creating Array Constant
2. Create a new Boolean T/F module inside the Array Constant
3. Drag the connector from the numbered array in 1. To a data acquisition module in the block diagram code
4. For the desired channel, set T for turning it ON, or set F for turning it off. (*note: make sure to set the undesired channel F*)

E.3. Running automated deposition

E.3.1. Stating automated deposition

1. After the instructions in B.6, input the desired experimental parameters onto the LabVIEW automation control center. For example, number of total global cycles, number of local precursor cycles, exposure time for precursor or radical pulse, and pump down time (all in seconds).
2. Press the start button (black triangle)

E.3.2. Stopping an automated deposition

1. If a deposition is still going on and has not reached the total number of global cycles, click the STOP button following the radical exposure step
2. Click on the top bar, Tools -> Measurement & Automation Explorer
3. Expend the Devices and Interfaces tab under My System
4. Find the NI-USB 9481 “Microwave Power” tab and right click -> left click on Test Panels
5. Click START and make sure all the switches are at the LOW configuration
6. Press STOP to resume the switches to its initial state
7. Close the Test Panels and close the Measurement & Automation Explorer
8. Press ON button of the microwave power source switch and ramp the power down to zero
9. Press OFF button of the microwave power source
10. Turn off the flow of oxygen gas by closing the upper valve, setting the mass-flow controller to zero, and then close the lower valve
11. Close A-1 manual valve to isolate the oxygen source and thus pump down the main chamber
12. Remove the sample from the main chamber to the loadlock chamber
13. Turn the pneumatic valves for all the precursors to the ON position in order prevent clogging of the precursor housing
14. Turn off all the temperature controllers

Bibliography

Abes, M., C. T. Koops, S. B. Hrkac, J. McCord, N. O. Urs, N. Wolff, L. Kienle, W. J. Ren, L. Bouchenoire, B. M. Murphy and O. M. Magnussen (2016). "Domain structure and reorientation inCoFe2O4." *Physical Review B* **93**(19).

Abudayyeh, H. (2012). *Synthesis and Analysis of ZnO Nanowires*.

Aimon, N. M., H. K. Choi, X. Y. Sun, D. H. Kim and C. A. Ross (2014). "Templated self-assembly of functional oxide nanocomposites." *Adv Mater* **26**(19): 3063-3067.

Aimon, N. M., D. H. Kim, X. Sun and C. A. Ross (2015). "Multiferroic behavior of templated BiFeO3-CoFe2O4 self-assembled nanocomposites." *ACS Appl Mater Interfaces*.

Aimon, N. M., J. Liao and C. A. Ross (2012). "Simulation of inhomogeneous magnetoelastic anisotropy in ferroelectric/ferromagnetic nanocomposites." *Applied Physics Letters* **101**(23): 232901.

Akbashev, A. R., G. Chen and J. E. Spanier (2014). "A facile route for producing single-crystalline epitaxial perovskite oxide thin films." *Nano Lett* **14**(1): 44-49.

Alford, T. L., L. C. Feldman and J. W. Mayer (2007). *Foundamentals of Nanoscale Thin Film Analysis*.

Amiri, P. K. and K. L. Wang (2015). "The Computer Chip That Never Forgets." *IEEE Spectrum*.

Aslam, N., V. Longo, W. Keuning, F. Roozeboom, W. M. M. Kessels, R. Waser and S. Hoffmann-Eifert (2014). "Influence of stoichiometry on the performance of MIM capacitors from plasma-assisted ALD SrxTiyOzfilms." *physica status solidi (a)* **211**(2): 389-396.

Auciello, O., J. F. Scott and R. Ramesh (1998). "The physics of ferroelectric memories." *Physics today* **51**(7): 22-27.

Bajaj, S., M. G. Haverty, R. Arroyave, W. A. Goddard Iii Frsc and S. Shankar (2015). "Phase stability in nanoscale material systems: extension from bulk phase diagrams." *Nanoscale* **7**(21): 9868-9877.

Bang-Hung, T., S. Heidger and J. A. Weimer (2000). *Sputtered barium titanate and barium strontium titanate films for capacitor applications*. ISAF 2000. Proceedings of the 2000 12th IEEE International Symposium on Applications of Ferroelectrics (IEEE Cat. No.00CH37076).

Barman, R. and D. Kaur (2015). "Leakage current behavior of BiFeO3/BiMnO3 multilayer fabricated by pulsed laser deposition." *Journal of Alloys and Compounds* **644**(Supplement C): 506-512.

Benedek, N. A. and C. J. Fennie (2013). "Why Are There So Few Perovskite Ferroelectrics?" *The Journal of Physical Chemistry C* **117**(26): 13339-13349.

Bibes, M. and A. Barthelemy (2008). "Multiferroics: Towards a magnetoelectric memory." *Nat Mater* **7**(6): 425-426.

Bichurin, M. I., V. M. Petrov and G. Srinivasan (2003). "Theory of low-frequency magnetoelectric coupling in magnetostrictive-piezoelectric bilayers." *Physical Review B* **68**(5): 054402.

Black, K., M. Werner, R. Rowlands–Jones, P. R. Chalker and M. J. Rosseinsky (2011). "SrHfO3Films Grown on Si(100) by Plasma-Assisted Atomic Layer Deposition." *Chemistry of Materials* **23**(10): 2518-2520.

Blakemore, J. S. (1985). *Solid state physics*.

Bozorth, R. M., E. F. Tilden and A. J. Williams (1955). "Anisotropy and Magnetostriction of Some Ferrites." *Physical Review* **99**(6): 1788-1798.

Cao, H., V. H. Schmidt, R. Zhang, W. Cao and H. Luo (2004). "Elastic, piezoelectric, and dielectric properties of 0.58Pb(Mg[sub 1/3]Nb[sub 2/3])O[sub 3]-0.42PbTiO[sub 3] single crystal." *Journal of Applied Physics* **96**(1): 549.

Caruntu, G., A. Yourdkhani, M. Vopsaroiu and G. Srinivasan (2012). "Probing the local strain-mediated magnetoelectric coupling in multiferroic nanocomposites by magnetic field-assisted piezoresponse force microscopy." *Nanoscale* **4**(10): 3218-3227.

Cazayous, M., Y. Gallais, A. Sacuto, R. de Sousa, D. Lebeugle and D. Colson (2008). "Possible Observation of Cycloidal Electromagnons in BiFeO3." *Physical Review Letters* **101**(3).

Chang, J. and J. P. Chang (2017). "Achieving atomistic control in materials processing by plasma–surface interactions." *Journal of Physics D: Applied Physics* **50**(25): 253001.

Chang, J. P., J. C. Arnold, G. C. H. Zau, H.-S. Shin and H. H. Sawin (1997). "Kinetic Study of Low Energy Argon Ion-Enhanced Plasma Etching of Polysilicon with Atomic/Molecular Chlorine." *Journal of Vacuum Science & Technology A* **15**(4): 1853-1863.

Chatterjee, K., S. Kim, G. Karbasian, A. J. Tan, A. K. Yadav, A. I. Khan, C. Hu and S. Salahuddin (2017). "Self-aligned, Gate Last, FDSOI, Ferroelectric Gate Memory Device with 5.5 nm Hf0.8Zr0.2O2, High Endurance and Breakdown Recovery." *IEEE Electron Device Letters*: 1-1.

Cheong, S.-W. and M. Mostovoy (2007). "Multiferroics: a magnetic twist for ferroelectricity." *Nat Mater* **6**(1): 13-20.

Chernikova, A., M. Kozodaev, A. Markeev, D. Negrov, M. Spiridonov, S. Zarubin, O. Bak, P. Buragohain, H. Lu, E. Suvorova, A. Gruverman and A. Zenkevich (2016). "Ultrathin Hf0.5Zr0.5O2 Ferroelectric Films on Si." *ACS Appl Mater Interfaces*.

Chien, D., A. N. Buditama, L. T. Schelhas, H. Y. Kang, S. Robbennolt, J. P. Chang and S. H. Tolbert (2016). "Tuning magnetoelectric coupling using porosity in multiferroic nanocomposites of ALD-grown Pb(Zr,Ti)O3 and templated mesoporous CoFe2O4." *Applied Physics Letters* **109**(11): 112904.

Choi, J. H., F. Zhang, Y.-C. Perng and J. P. Chang (2013). "Tailoring the composition of lead zirconate titanate by atomic layer deposition." *Journal of Vacuum Science & Technology B* **31**(1): 012207.

Chong, Y. T., E. M. Y. Yau, K. Nielsch and J. Bachmann (2010). "Direct Atomic Layer Deposition of Ternary Ferrites with Various Magnetic Properties." *Chemistry of Materials* **22**(24): 6506-6508.

Chu, Y. H., L. W. Martin, M. B. Holcomb, M. Gajek, S. J. Han, Q. He, N. Balke, C. H. Yang, D. Lee, W. Hu, Q. Zhan, P. L. Yang, A. Fraile-Rodriguez, A. Scholl, S. X. Wang and R. Ramesh (2008). "Electric-field control of local ferromagnetism using a magnetoelectric multiferroic." *Nat Mater* **7**(6): 478-482.

Chu, Y. H., Q. Zhan, L. W. Martin, M. P. Cruz, P. L. Yang, G. W. Pabst, F. Zavaliche, S. Y. Yang, J. X. Zhang, L. Q. Chen, D. G. Schlom, I. N. Lin, T. B. Wu and R. Ramesh (2006). "Nanoscale Domain Control in Multiferroic BiFeO3 Thin Films." *Advanced Materials* **18**(17): 2307-2311.

Chu, Y. H., T. Zhao, M. P. Cruz, Q. Zhan, P. L. Yang, L. W. Martin, M. Huijben, C. H. Yang, F. Zavaliche, H. Zheng and R. Ramesh (2007). "Ferroelectric size effects in multiferroic BiFeO[sub 3] thin films." *Applied Physics Letters* **90**(25): 252906.

Cibert, C., J. Zhu, G. Poullain, R. Bouregba, J. More-Chevalier and A. Pautrat (2013). "Magnetoelectric coupling in Tb0.3Dy0.7Fe2/Pt/PbZr0.56Ti0.44O3 thin films deposited on Pt/TiO2/SiO2/Si substrate." *Applied Physics Letters* **102**(2): 022906.

Clarkson, J. D., I. Fina, Z. Q. Liu, Y. Lee, J. Kim, C. Frontera, K. Cordero, S. Wisotzki, F. Sanchez, J. Sort, S. L. Hsu, C. Ko, L. Aballe, M. Foerster, J. Wu, H. M. Christen, J. T. Heron, D. G. Schlom, S. Salahuddin, N. Kioussis, J. Fontcuberta, X. Marti and R. Ramesh (2017). "Hidden Magnetic States Emergent Under Electric Field, In A Room Temperature Composite Magnetoelectric Multiferroic." *Sci Rep* **7**(1): 15460.

Coll, M., J. Gazquez, I. Fina, Z. Khayat, A. Quindeau, M. Alexe, M. Varela, S. Trolier-McKinstry, X. Obradors and T. Puig (2015). "Nanocrystalline Ferroelectric BiFeO3 Thin Films by Low Temperature Atomic Layer Deposition." *Chemistry of Materials*: 150820072430004.

Coll, M., J. M. Montero Moreno, J. Gazquez, K. Nielsch, X. Obradors and T. Puig (2014). "Low Temperature Stabilization of Nanoscale Epitaxial Spinel Ferrite Thin Films by Atomic Layer Deposition." *Advanced Functional Materials* **24**(34): 5368-5374.

Cullity, B. D. and C. D. Graham (2008). *Introduction to Magnetic Materials*, Wiley-IEEE Press.

Deepak, N., P. Carolan, L. Keeney, P. F. Zhang, M. E. Pemble and R. W. Whatmore (2015). "Bismuth Self-Limiting Growth of ultra-thin BiFeO3Films." *Chemistry of Materials*: 150911090809003.

Dhakal, T., D. Mukherjee, R. Hyde, P. Mukherjee, M. H. Phan, H. Srikanth and S. Witanachchi (2010). "Magnetic anisotropy and field switching in cobalt ferrite thin films deposited by pulsed laser ablation." *Journal of Applied Physics* **107**(5): 053914.

Dorsey, P. C., P. Lubitz, D. B. Chrisey and J. S. Horwitz (1996). "CoFe2O4 thin films grown on (100) MgO substrates using pulsed laser deposition." *Journal of Applied Physics* **79**(8): 6338-6340.

Dzyaloshinsky, I. (1958). "A Thermodynamic Theory of Weak Ferromagnetism of Antiferromagnetics." *Journal of Physics and Chemistry of Solids* **4**(4): 241-255.

Ederer, C. and N. Spaldin (2005). "Weak ferromagnetism and magnetoelectric coupling in bismuth ferrite." *Physical Review B* **71**(6).

Eerenstein, W., N. D. Mathur and J. F. Scott (2006). "Multiferroic and magnetoelectric materials." *Nature* **442**(7104): 759-765.

Eerenstein, W., F. D. Morrison, J. Dho, M. G. Blamire, J. F. Scott and N. D. Mathur (2005). "Comment on "Epitaxial BiFeO3 multiferroic thin film heterostructures"." *Science* **307**(5713): 1203; author reply 1203.

Eerenstein, W., M. Wiora, J. L. Prieto, J. F. Scott and N. D. Mathur (2007). "Giant sharp and persistent converse magnetoelectric effects in multiferroic epitaxial heterostructures." *Nat Mater* **6**(5): 348-351.

Evans, D. M., A. Schilling, A. Kumar, D. Sanchez, N. Ortega, M. Arredondo, R. S. Katiyar, J. M. Gregg and J. F. Scott (2013). "Magnetic switching of ferroelectric domains at room temperature in multiferroic PZTFT." *Nat Commun* **4**: 1534.

Fiebig, M. (2005). "Revival of the magnetoelectric effect." *Journal of Physics D: Applied Physics* **38**(8): R123-R152.

Flink, M. (2014). "The End of a Necessary Evil: Collapsing the Memory Hierarchy." *Hewlett Packard Enterprice Newsroom*.

Florent, K., S. Lavizzari, L. D. Piazza, M. Popovici, J. Duan, G. Groeseneken and J. V. Houdt (2017). "Reliability Study of Ferroelectric Al:HfO2 Thin Films for DRAM and NAND Applications." *IEEE Transactions on Electron Devices* **PP**(99): 1-8.

Fritsch, D. and C. Ederer (2012). "First-principles calculation of magnetoelastic coefficients and magnetostriction in the spinel ferrites CoFe2O4 and NiFe2O4." *Physical Review B* **86**(1).

Gao, T., X. Zhang, W. Ratcliff, 2nd, S. Maruyama, M. Murakami, A. Varatharajan, Z. Yamani, P. Chen, K. Wang, H. Zhang, R. Shull, L. A. Bendersky, J. Unguris, R. Ramesh and I. Takeuchi

(2017). "Electric-Field Induced Reversible Switching of the Magnetic Easy Axis in Co/BiFeO3 on SrTiO3." *Nano Lett*.

Gao, X. S., D. H. Bao, B. Birajdar, T. Habisreuther, R. Mattheis, M. A. Schubert, M. Alexe and D. Hesse (2009). "Switching of magnetic anisotropy in epitaxial CoFe2O4thin films induced by SrRuO3buffer layer." *Journal of Physics D: Applied Physics* **42**(17): 175006.

Gatel, C., B. Warot-Fonrose, S. Matzen and J. B. Moussy (2013). "Magnetism of CoFe2O4 Ultrathin Films on MgAl2O4 Driven by Epitaxial Strain." *Applied Physics Letters* **103**(9): 092405.

George, S. M. (2010). "Atomic Layer Deposition: An Overview." *Chem. Rev.* **110**: 111-131.

Ghosh, A., G. Koster and G. Rijnders (2016). "Tunable and stable in time ferroelectric imprint through polarization coupling." *APL Materials* **4**(6): 066103.

Goldman, A. (2006). *Modern Ferrite Technology*, Springer.

Haggerty, R. P., P. Sarin, Z. D. Apostolov, P. E. Driemeyer, W. M. Kriven and L. Gauckler (2014). "Thermal Expansion of HfO2 and ZrO2." *Journal of the American Ceramic Society* **97**(7): 2213-2222.

Harjuoja, J., A. Kosola, M. Putkonen and L. Niinistö (2006). "Atomic layer deposition and post-deposition annealing of PbTiO3 thin films." *Thin Solid Films* **496**(2): 346-352.

Heron, J. T., J. L. Bosse, Q. He, Y. Gao, M. Trassin, L. Ye, J. D. Clarkson, C. Wang, J. Liu, S. Salahuddin, D. C. Ralph, D. G. Schlom, J. Iniguez, B. D. Huey and R. Ramesh (2014). "Deterministic switching of ferromagnetism at room temperature using an electric field." *Nature* **516**(7531): 370-373.

Heron, J. T., D. G. Schlom and R. Ramesh (2014). "Electric field control of magnetism using BiFeO3-based heterostructures." *Applied Physics Reviews* **1**(2): 021303.

Hill, N. A. (2000). "Why Are There so Few Magnetic Ferroelectrics?" *The Journal of Physical Chemistry B* **104**(29): 6694-6709.

Hoffmann, M., U. Schroeder, T. Schenk, T. Shimizu, H. Funakubo, O. Sakata, D. Pohl, M. Drescher, C. Adelmann, R. Materlik, A. Kersch and T. Mikolajick (2015). "Stabilizing the ferroelectric phase in doped hafnium oxide." *Journal of Applied Physics* **118**(7): 072006.

Horng, L., G. Chern, M. C. Chen, P. C. Kang and D. S. Lee (2004). "Magnetic anisotropic properties in Fe3O4 and CoFe2O4 ferrite epitaxy thin films." *Journal of Magnetism and Magnetic Materials* **270**(3): 389-396.

Hu, B., J.-F. Wang, J. Zhang, Z.-B. Gu and S.-T. Zhang (2015). "Synthesis, structures and properties of single phase BiFeO3 and Bi2Fe4O9 powders by hydrothermal method." *Journal of Materials Science: Materials in Electronics* **26**(9): 6887-6891.

Hu, J. M., L. Q. Chen and C. W. Nan (2015). "Multiferroic Heterostructures Integrating Ferroelectric and Magnetic Materials." *Adv Mater*.

Huang, W., L. X. Zhou, H. Z. Zeng, X. H. Wei, J. Zhu, Y. Zhang and Y. R. Li (2007). "Epitaxial growth of the CoFe2O4 film on SrTiO3 and its characterization." *Journal of Crystal Growth* **300**(2): 426-430.

Huang, W., J. Zhu, H. Z. Zeng, X. H. Wei, Y. Zhang and Y. R. Li (2006). "Strain Induced Magnetic Anisotropy in Highly Epitaxial CoFe2O4 Thin Films." *Applied Physics Letters* **89**(26): 262506.

Huber, M. E., N. C. Koshnick, H. Bluhm, L. J. Archuleta, T. Azua, P. G. Bjornsson, B. W. Gardner, S. T. Halloran, E. A. Lucero and K. A. Moler (2008). "Gradiometric micro-SQUID susceptometer for scanning measurements of mesoscopic samples." *The Review of scientific instruments* **79**(5): 053704.

ITRS (2011). "Emerging Research Devices (ERD)." *International Technology Roadmap for Semiconductors*.

Jalkanen, P., V. Tuboltsev, B. Marchand, A. Savin, M. Puttaswamy, M. Vehkamäki, K. Mizohata, M. Kemell, T. Hatanpää, V. Rogozin, J. Räisänen, M. Ritala and M. Leskelä (2014). "Magnetic Properties of Polycrystalline Bismuth Ferrite Thin Films Grown by Atomic Layer Deposition." *The Journal of Physical Chemistry Letters* **5**(24): 4319-4323.

Kadomtseva, A. M., Y. F. Popov, A. P. Pyatakov, G. P. Vorob'ev, A. K. Zvezdin and D. Viehland (2006). "Phase transitions in multiferroic BiFeO3 crystals, thin-layers, and ceramics: enduring potential for a single phase, room-temperature magnetoelectric 'holy grail'." *Phase Transitions* **79**(12): 1019-1042.

Karbasian, G., R. dos Reis, A. K. Yadav, A. J. Tan, C. Hu and S. Salahuddin (2017). "Stabilization of ferroelectric phase in tungsten capped Hf0.8Zr0.2O2." *Applied Physics Letters* **111**(2): 022907.

Karbasian, G., A. Tan, A. Yadav, E. M. H. Sorensen, C. R. Serrao, A. I. Khan, K. Chatterjee, K. Sangwan, H. Chenming and S. Salahuddin (2017). *Ferroelectricity in HfO<inf>2</inf> thin films as a function of Zr doping*. 2017 International Symposium on VLSI Technology, Systems and Application (VLSI-TSA).

Khomskii, D. I. (2006). "Multiferroics: Different ways to combine magnetism and ferroelectricity." *Journal of Magnetism and Magnetic Materials* **306**(1): 1-8.

Kil, D. S., J. M. Lee and J. S. Roh (2002). "Low-Temperature ALD Growth of SrTiO3 Thin Films from Sr β-Diketonates and Ti Alkoxide Precursors Using Oxygen Remote Plasma as an Oxidation Source." *Chemical Vapor Deposition* **8**(5): 195-197.

Kim, D. H., N. M. Aimon, X. Y. Sun, L. Kornblum, F. J. Walker, C. H. Ahn and C. A. Ross (2014). "Integration of Self-Assembled Epitaxial BiFeO3-CoFe2O4Multiferroic Nanocomposites on Silicon Substrates." *Advanced Functional Materials* **24**(37): 5889-5896.

Kim, K. D., M. H. Park, H. J. Kim, Y. J. Kim, T. Moon, Y. H. Lee, S. D. Hyun, T. Gwon and C. S. Hwang (2016). "Ferroelectricity in undoped-HfO2thin films induced by deposition temperature control during atomic layer deposition." *J. Mater. Chem. C* **4**(28): 6864-6872.

Kim, S. J., D. Narayan, J.-G. Lee, J. Mohan, J. S. Lee, J. Lee, H. S. Kim, Y.-C. Byun, A. T. Lucero, C. D. Young, S. R. Summerfelt, T. San, L. Colombo and J. Kim (2017). "Large ferroelectric polarization of TiN/Hf0.5Zr0.5O2/TiN capacitors due to stress-induced crystallization at low thermal budget." *Applied Physics Letters* **111**(24): 242901.

Kim, S. K., S. W. Lee, J. H. Han, B. Lee, S. Han and C. S. Hwang (2010). "Capacitors with an Equivalent Oxide Thickness of <0.5 nm for Nanoscale Electronic Semiconductor Memory." *Advanced Functional Materials* **20**(18): 2989-3003.

Kim, Y., C. Pham and J. P. Chang (2015). "Potentials and challenges of integration for complex metal oxides in CMOS devices and beyond." *Journal of Physics D: Applied Physics* **48**(6): 063001.

Kirtley, J. R. (2010). "Fundamental studies of superconductors using scanning magnetic imaging." *Reports on Progress in Physics* **73**(12): 126501.

Klepper, K. B., O. Nilsen and H. Fjellvåg (2007). "Growth of Thin Films of Co3O4 by Atomic Layer Deposition." *Thin Solid Films* **515**(20-21): 7772-7781.

Kosola, A., M. Putkonen, L.-S. Johansson and L. Niinistö (2003). "Effect of annealing in processing of strontium titanate thin films by ALD." *Applied Surface Science* **211**(1): 102-112.

Kozodaev, M. G., A. G. Chernikova, E. V. Korostylev, M. H. Park, U. Schroeder, C. S. Hwang and A. M. Markeev (2017). "Ferroelectric properties of lightly doped La:HfO2 thin films grown by plasma-assisted atomic layer deposition." *Applied Physics Letters* **111**(13): 132903.

Kryder, M. H. and K. C. Soo (2009). "After Hard Drives-What Comes Next?" *Magnetics, IEEE Transactions* **45**(10): 3406-3413.

Kubel, F. and H. Schmid (1990). "Structure of a ferroelectric and ferroelastic monodomain crystal of the perovskite BiFeO3." *Acta Crystallographica Section B* **46**(6): 698-702.

Künneth, C., R. Materlik, M. Falkowski and A. Kersch (2017). "Impact of Four-Valent Doping on the Crystallographic Phase Formation for Ferroelectric HfO2 from First-Principles: Implications for Ferroelectric Memory and Energy-Related Applications." *ACS Applied Nano Materials*.

Kwon, D., K. Chatterjee, A. J. Tan, A. K. Yadav, H. Zhou, A. B. Sachid, R. dos Reis, C. Hu and S. Salahuddin (2017). "Improved Subthreshold Swing and Short Channel Effect in FDSOI n-Channel Negative Capacitance Field Effect Transistors." *IEEE Electron Device Letters*: 1-1.

Langereis, E., R. Roijmans, F. Roozeboom, M. C. M. van de Sanden and W. M. M. Kessels (2011). "Remote Plasma ALD of SrTiO[sub 3] Using Cyclopentadienlyl-Based Ti and Sr Precursors." *Journal of The Electrochemical Society* **158**(2): G34.

Laukhin, V., V. Skumryev, X. Martí, D. Hrabovsky, F. Sánchez, M. García-Cuenca, C. Ferrater, M. Varela, U. Lüders, J. Bobo and J. Fontcuberta (2006). "Electric-Field Control of Exchange Bias in Multiferroic Epitaxial Heterostructures." *Physical Review Letters* **97**(22).

Lawes, G. and G. Srinivasan (2011). "Introduction to magnetoelectric coupling and multiferroic films." *Journal of Physics D: Applied Physics* **44**(24): 243001.

Lebeugle, D., D. Colson, A. Forget, M. Viret, A. M. Bataille and A. Gukasov (2008). "Electric-Field-Induced Spin Flop in BiFeO_{3} Single Crystals at Room Temperature." *Physical Review Letters* **100**(22).

Lee, C.-C. and J.-M. Wu (2007). "Thickness-dependent retention behaviors and ferroelectric properties of BiFeO3 thin films on BaPbO3 electrodes." *Applied Physics Letters* **91**(10): 102906.

Lee, G., E. M. A. Fuentes-Fernandez, G. Lian, R. S. Katiyar and O. Auciello (2015). "Hetero-epitaxial BiFeO3/SrTiO3 nanolaminates with higher piezoresponse performance over stoichiometric BiFeO3 films." *Applied Physics Letters* **106**(2): 022905.

Lee, J. H., Y. J. Cho, Y. S. Min, D. Kim and S. W. Rhee (2002). "Plasma enhanced atomic layer deposition of SrTiO[sub 3] thin films with Sr(tmhd)[sub 2] and Ti(i-OPr)[sub 4]." *Journal of Vacuum Science & Technology A: Vacuum, Surfaces, and Films* **20**(5): 1828.

Leskelä, M. and M. Ritala (2002). "Atomic layer deposition (ALD): from precursors to thin film structures." *Thin Solid Films* **409**(1): 138-146.

Li, X., D. Carka, C.-y. Liang, A. E. Sepulveda, S. M. Keller, P. K. Amiri, G. P. Carman and C. S. Lynch (2015). "Strain-mediated 180° perpendicular magnetization switching of a single domain multiferroic structure." *Journal of Applied Physics* **118**(1): 014101.

Lie, M., H. Fjellvåg and A. Kjekshus (2005). "Growth of Fe2O3 thin films by atomic layer deposition." *Thin Solid Films* **488**(1-2): 74-81.

Lin, Y.-C., F. McGuire and A. D. Franklin (2018). "Realizing ferroelectric Hf0.5Zr0.5O2 with elemental capping layers." *Journal of Vacuum Science & Technology B, Nanotechnology and Microelectronics: Materials, Processing, Measurement, and Phenomena* **36**(1): 011204.

Liu, F., I. Fina, R. Bertacco and J. Fontcuberta (2016). "Unravelling and controlling hidden imprint fields in ferroelectric capacitors." *Scientific Reports* **6**(1).

Liu, H., Y. Sun and X. Wang (2008). "Study of the electric properties of PbTiO 3 –BiFeO 3 multilayer film structure." *Journal of Physics D: Applied Physics* **41**(9): 095302.

Liu, M., O. Obi, J. Lou, Y. Chen, Z. Cai, S. Stoute, M. Espanol, M. Lew, X. Situ, K. S. Ziemer, V. G. Harris and N. X. Sun (2009). "Giant Electric Field Tuning of Magnetic Properties in Multiferroic Ferrite/Ferroelectric Heterostructures." *Advanced Functional Materials* **19**(11): 1826-1831.

Liu, M., Z. Zhou, T. Nan, B. M. Howe, G. J. Brown and N. X. Sun (2013). "Voltage tuning of ferromagnetic resonance with bistable magnetization switching in energy-efficient magnetoelectric composites." *Adv Mater* **25**(10): 1435-1439.

Liu, Y. T., C. S. Ku, S. J. Chiu, H. Y. Lee and S. Y. Chen (2014). "Ultrathin oriented BiFeO3 films from deposition of atomic layers with greatly improved leakage and ferroelectric properties." *ACS Appl Mater Interfaces* **6**(1): 443-449.

Lomenzo, P. D., Q. Takmeel, S. Moghaddam and T. Nishida (2016). "Annealing behavior of ferroelectric Si-doped HfO2 thin films." *Thin Solid Films* **615**: 139-144.

Lomenzo, P. D., P. Zhao, Q. Takmeel, S. Moghaddam, T. Nishida, M. Nelson, C. M. Fancher, E. D. Grimley, X. Sang, J. M. LeBeau and J. L. Jones (2014). "Ferroelectric phenomena in Si-doped HfO2 thin films with TiN and Ir electrodes." *Journal of Vacuum Science & Technology B: Microelectronics and Nanometer Structures* **32**(3): 03D123.

Longo, V., N. Leick, F. Roozeboom and W. M. M. Kessels (2012). "Plasma-Assisted Atomic Layer Deposition of SrTiO3: Stoichiometry and Crystallinity Studied by Spectroscopic Ellipsometry." *ECS Journal of Solid State Science and Technology* **2**(1): N15-N22.

Lou, J., M. Liu, D. Reed, Y. Ren and N. X. Sun (2009). "Giant Electric Field Tuning of Magnetism in Novel Multiferroic FeGaB/Lead Zinc Niobate-Lead Titanate (PZN-PT) Heterostructures." *Advanced Materials* **21**: 4711-4715.

Marchand, B., P. Jalkanen, V. Tuboltsev, M. Vehkamäki, M. Puttaswamy, M. L. Kemell, K. Mizohata, T. Hatanpää, A. M. Savin, J. Räisänen, M. Ritala and M. Leskelä (2016). "Electric and Magnetic Properties of ALD Grown BiFeO3Films." *The Journal of Physical Chemistry C*.

Martin, D., J. Muller, T. Schenk, T. M. Arruda, A. Kumar, E. Strelcov, E. Yurchuk, S. Muller, D. Pohl, U. Schroder, S. V. Kalinin and T. Mikolajick (2014). "Ferroelectricity in Si-doped HfO2 revealed: a binary lead-free ferroelectric." *Adv Mater* **26**(48): 8198-8202.

Martin, L. W., Y. H. Chu and R. Ramesh (2010). "Advances in the growth and characterization of magnetic, ferroelectric, and multiferroic oxide thin films." *Materials Science and Engineering: R: Reports* **68**(4-6): 89-133.

Matero, R., A. Rahtu, S. Haukka, M. Tuominen, M. Vehkamäki, T. Hatanpää, M. Ritala and M. Leskelä (2006). "Scale-up of the BaTiO3 ALD Process onto 200 mm Wafer." *ECS Transactions* **1**(10): 137-141.

Matsushita, N., S. Nakagawa and M. Naoe (1992). *Preparation of Co ferrite thin films with large perpendicular and in-plane coercivities by facing targets sputtering*. 1992. Digests of Intermag. International Magnetics Conference.

McDaniel, M. D., C. Hu, S. Lu, T. Q. Ngo, A. Posadas, A. Jiang, D. J. Smith, E. T. Yu, A. A. Demkov and J. G. Ekerdt (2015). "Atomic layer deposition of crystalline SrHfO3 directly on Ge (001) for high-k dielectric applications." *Journal of Applied Physics* **117**(5): 054101.

McDaniel, M. D., T. Q. Ngo, S. Hu, A. Posadas, A. A. Demkov and J. G. Ekerdt (2015). "Atomic layer deposition of perovskite oxides and their epitaxial integration with Si, Ge, and other semiconductors." *Applied Physics Reviews* **2**(4): 041301.

McDaniel, M. D., A. Posadas, T. Q. Ngo, A. Dhamdhere, D. J. Smith, A. A. Demkov and J. G. Ekerdt (2013). "Epitaxial strontium titanate films grown by atomic layer deposition on SrTiO3-buffered Si(001) substrates." *Journal of Vacuum Science & Technology A: Vacuum, Surfaces, and Films* **31**(1): 01A136.

McKee, R. A., F. J. Walker and M. F. Chisholm (1998). "Crystalline Oxides on Silicon: The First Five Monolayers." *Physical Review Letters* **81**(14): 3014-3017.

Moazzami, R., C. Hu and W. H. Shepherd (1992). "Electrical characteristics of ferroelectric PZT thin films for DRAM applications." *IEEE Transactions on Electron Devices* **39**(9): 2044-2049.

Molegraaf, H. J. A., J. Hoffman, C. A. F. Vaz, S. Gariglio, D. van der Marel, C. H. Ahn and J.-M. Triscone (2009). "Magnetoelectric Effects in Complex Oxides with Competing Ground States." *Adv Mater* **21**(34): 3470-3474.

Moore, G. E. (1965). "Cramming more components onto integrated circuits." *Electronics* **38**.

Morales, R., A. C. Basaran, J. E. Villegas, D. Navas, N. Soriano, B. Mora, C. Redondo, X. Batlle and I. K. Schuller (2015). "Exchange-Bias Phenomenon: The Role of the Ferromagnetic Spin Structure." *Physical Review Letters* **114**(9).

Moriya, T. (1960). "Anisotropic superexchange interaction and weak ferromagnetism." *Physical Review* **120**(1): 91.

Mostovoy, M. (2006). "Ferroelectricity in Spiral Magnets." *Physical Review Letters* **96**(6): 067601.

Mueller, S., C. Adelmann, A. Singh, S. Van Elshocht, U. Schroeder and T. Mikolajick (2012). "Ferroelectricity in Gd-Doped HfO2 Thin Films." *ECS Journal of Solid State Science and Technology* **1**(6): N123-N126.

Mueller, S., J. Mueller, A. Singh, S. Riedel, J. Sundqvist, U. Schroeder and T. Mikolajick (2012). "Incipient Ferroelectricity in Al-Doped HfO2 Thin Films." *Advanced Functional Materials* **22**(11): 2412-2417.

Mulaosmanovic, H., J. Ocker, S. Muller, U. Schroeder, J. Muller, P. Polakowski, S. Flachowsky, R. van Bentum, T. Mikolajick and S. Slesazeck (2017). "Switching Kinetics in

Nanoscale Hafnium Oxide Based Ferroelectric Field-Effect Transistors." *ACS Appl Mater Interfaces* **9**(4): 3792-3798.

Murugavel, P., M. P. Singh, W. Prellier, B. Mercey, C. Simon and B. Raveau (2005). "The role of ferroelectric-ferromagnetic layers on the properties of superlattice-based multiferroics." *Journal of Applied Physics* **97**(10): 103914.

Nan, C.-W. (1994). "Magnetoelectric effect in composites of piezoelectric and piezomagnetic phases." *Physical Review B* **50**(9): 6082-6088.

Nan, C.-W., G. Liu, Y. Lin and H. Chen (2005). "Magnetic-Field-Induced Electric Polarization in Multiferroic Nanostructures." *Physical Review Letters* **94**(19).

Nan, C. W., M. I. Bichurin, S. X. Dong, D. Viehland and G. Srinivasan (2008). "Multiferroic magnetoelectric composites: Historical perspective, status, and future directions." *Journal of Applied Physics* **103**(3).

Ngo, T. Q., A. B. Posadas, M. D. McDaniel, C. Hu, J. Bruley, E. T. Yu, A. A. Demkov and J. G. Ekerdt (2014). "Epitaxial c-axis oriented BaTiO3 thin films on SrTiO3-buffered Si(001) by atomic layer deposition." *Applied Physics Letters* **104**(8): 082910.

Nguyen, M. D., H. Nazeer, K. Karakaya, S. V. Pham, R. Steenwelle, M. Dekkers, L. Abelmann, D. H. A. Blank and G. Rijnders (2010). "Characterization of epitaxial Pb(Zr,Ti)O 3 thin films deposited by pulsed laser deposition on silicon cantilevers." *Journal of Micromechanics and Microengineering* **20**(8): 085022.

Niinistö, J., K. Kukli, M. Heikkilä, M. Ritala and M. Leskelä (2009). "Atomic Layer Deposition of High-kOxides of the Group 4 Metals for Memory Applications." *Advanced Engineering Materials* **11**(4): 223-234.

Nishimura, T., L. Xu, S. Shibayama, T. Yajima, S. Migita and A. Toriumi (2016). "Ferroelectricity of nondoped thin HfO2films in TiN/HfO2/TiN stacks." *Japanese Journal of Applied Physics* **55**(8S2): 08PB01.

Nogués, J., J. Sort, V. Langlais, V. Skumryev, S. Suriñach, J. S. Muñoz and M. D. Baró (2005). "Exchange bias in nanostructures." *Physics Reports* **422**(3): 65-117.

Oh, Y. S., S. Crane, H. Zheng, Y. H. Chu, R. Ramesh and K. H. Kim (2010). "Quantitative determination of anisotropic magnetoelectric coupling in BiFeO[sub 3]–CoFe[sub 2]O[sub 4] nanostructures." *Applied Physics Letters* **97**(5): 052902.

Ojha, S., W. C. Nunes, N. M. Aimon and C. A. Ross (2016). "Magnetostatic Interactions in Self-Assembled CoxNi1-xFe2O4/BiFeO3 Multiferroic Nanocomposites." *ACS Nano*.

Park, J. H., H. M. Jang, H. S. Kim, C. G. Park and S. G. Lee (2008). "Strain-mediated magnetoelectric coupling in BaTiO3-Co nanocomposite thin films." *Applied Physics Letters* **92**(6): 062908.

Park, K. I., S. Xu, Y. Liu, G. T. Hwang, S. J. Kang, Z. L. Wang and K. J. Lee (2010). "Piezoelectric BaTiO(3) thin film nanogenerator on plastic substrates." *Nano Lett* **10**(12): 4939-4943.

Park, M. H., H. J. Kim, Y. J. Kim, Y. H. Lee, T. Moon, K. D. Kim, S. D. Hyun, F. Fengler, U. Schroeder and C. S. Hwang (2016). "Effect of Zr Content on the Wake-Up Effect in Hf1-xZrxO2 Films." *ACS Appl Mater Interfaces* **8**(24): 15466-15475.

Park, M. H., H. J. Kim, Y. J. Kim, Y. H. Lee, T. Moon, K. D. Kim, S. D. Hyun and C. S. Hwang (2015). "Study on the size effect in Hf0.5Zr0.5O2 films thinner than 8 nm before and after wake-up field cycling." *Applied Physics Letters* **107**(19): 192907.

Park, M. H., H. J. Kim, Y. J. Kim, T. Moon and C. S. Hwang (2014). "The effects of crystallographic orientation and strain of thin Hf0.5Zr0.5O2 film on its ferroelectricity." *Applied Physics Letters* **104**(7): 072901.

Park, M. H., Y. H. Lee, H. J. Kim, Y. J. Kim, T. Moon, K. D. Kim, J. Muller, A. Kersch, U. Schroeder, T. Mikolajick and C. S. Hwang (2015). "Ferroelectricity and antiferroelectricity of doped thin HfO2-based films." *Adv Mater* **27**(11): 1811-1831.

Peng, J.-h., M. Hojamberdiev, H.-q. Li, D.-l. Mao, Y.-j. Zhao, P. Liu, J.-p. Zhou and G.-q. Zhu (2015). "Electrical, magnetic, and direct and converse magnetoelectric properties of (1−x)Pb(Zr0.52Ti0.48)O3−(x)CoFe2O4 (PZT–CFO) magnetoelectric composites." *Journal of Magnetism and Magnetic Materials* **378**: 298-305.

Pešić, M., F. P. G. Fengler, L. Larcher, A. Padovani, T. Schenk, E. D. Grimley, X. Sang, J. M. LeBeau, S. Slesazeck, U. Schroeder and T. Mikolajick (2016). "Physical Mechanisms behind the Field-Cycling Behavior of HfO2-Based Ferroelectric Capacitors." *Advanced Functional Materials* **26**(25): 4601-4612.

Pham, C. D., J. Chang, M. A. Zurbuchen and J. P. Chang (2015). "Synthesis and Characterization of BiFeO3Thin Films for Multiferroic Applications by Radical Enhanced Atomic Layer Deposition." *Chemistry of Materials* **27**(21): 7282-7288.

Pham, C. D., J. Chang, M. A. Zurbuchen and J. P. Chang (2017). "Magnetic Properties of CoFe2O4 Thin Films Synthesized by Radical Enhanced Atomic Layer Deposition." *ACS Appl Mater Interfaces*.

Plokhikh, A. V., M. Falmbigl, I. S. Golovina, A. R. Akbashev, I. A. Karateev, M. Y. Presnyakov, A. L. Vasiliev and J. E. Spanier (2017). "Formation of BiFeO3 from a Binary Oxide Superlattice Grown by Atomic Layer Deposition." *Chemphyschem*.

Polakowski, P. and J. Müller (2015). "Ferroelectricity in undoped hafnium oxide." *Applied Physics Letters* **106**(23): 232905.

Powell, C. J. and A. Jablonski (2000). "Evaluation of electron inelastic mean free paths for selected elements and compounds†." *Surface and Interface Analysis* **29**(2): 108-114.

Profijt, H. B., S. E. Potts, M. C. M. van de Sanden and W. M. M. Kessels (2011). "Plasma-Assisted Atomic Layer Deposition: Basics, Opportunities, and Challenges." *Journal of Vacuum Science & Technology A: Vacuum, Surfaces, and Films* **29**(5): 050801.

Puttaswamy, M., M. Vehkamäki, K. Kukli, M. C. Dimri, M. Kemell, T. Hatanpää, M. J. Heikkilä, K. Mizohata, R. Stern, M. Ritala and M. Leskelä (2016). "Bismuth iron oxide thin films using atomic layer deposition of alternating bismuth oxide and iron oxide layers." *Thin Solid Films* **611**: 78-87.

Ramesh, R. and N. A. Spaldin (2007). "Multiferroics: progress and prospects in thin films." *Nat Mater* **6**(1): 21-29.

Richter, C., T. Schenk, M. H. Park, F. A. Tscharntke, E. D. Grimley, J. M. LeBeau, C. Zhou, C. M. Fancher, J. L. Jones, T. Mikolajick and U. Schroeder (2017). "Si Doped Hafnium Oxide-A "Fragile" Ferroelectric System." *Advanced Electronic Materials*: 1700131.

Rigato, F., J. Geshev, V. Skumryev and J. Fontcuberta (2009). "The magnetization of epitaxial nanometric CoFe[sub 2]O[sub 4](001) layers." *Journal of Applied Physics* **106**(11): 113924.

Rondinelli, J. M., M. Stengel and N. A. Spaldin (2008). "Carrier-mediated magnetoelectricity in complex oxide heterostructures." *Nat Nano* **3**(1): 46-50.

Roy, S. and S. B. Majumder (2012). "Recent advances in multiferroic thin films and composites." *Journal of Alloys and Compounds* **538**(0): 153-159.

Sang, X., E. D. Grimley, T. Schenk, U. Schroeder and J. M. LeBeau (2015). "On the structural origins of ferroelectricity in HfO2 thin films." *Applied Physics Letters* **106**(16): 162905.

Scheffe, J. R., M. D. Allendorf, E. N. Coker, B. W. Jacobs, A. H. McDaniel and A. W. Weimer (2011). "Hydrogen Production via Chemical Looping Redox Cycles Using Atomic Layer Deposition-Synthesized Iron Oxide and Cobalt Ferrites." *Chemistry of Materials* **23**(8): 2030-2038.

Schindler, P., Y. Kim, D. Thian, J. An and F. B. Prinz (2016). "Plasma-enhanced atomic layer deposition of BaTiO3." *Scripta Materialia* **111**: 106-109.

Schulthess, T. C. and W. H. Butler (1998). "Consequences of Spin-Flop Coupling in Exchange Biased Films." *Physical Review Letters* **81**(20): 4516-4519.

Shen, Y. D., Y. W. Li, W. M. Li, J. Z. Zhang, Z. G. Hu and J. H. Chu (2012). "Growth of Bi2O3Ultrathin Films by Atomic Layer Deposition." *The Journal of Physical Chemistry C* **116**(5): 3449-3456.

Smolenskiĭ, G. A. and I. E. Chupis (1982). "Ferroelectromagnets." *Soviet Physics Uspekhi* **25**(7): 475.

Sone, K., H. Naganuma, M. Ito, T. Miyazaki, T. Nakajima and S. Okamura (2015). "100-nm-sized magnetic domain reversal by the magneto-electric effect in self-assembled BiFeO3/CoFe2O4 bilayer films." *Sci Rep* **5**: 9348.

Spaldin, N. A. (2003). *Magnetic materials, fundamentals and device applications*.

Spaldin, N. A. and M. Fiebig (2005). "The Renaissance of Magnetoelectric Multiferroics." *Science* **309**(5733): 391-392.

Tang, Z. H., M. H. Tang, X. S. Lv, H. Q. Cai, Y. G. Xiao, C. P. Cheng, Y. C. Zhou and J. He (2013). "Enhanced magnetoelectric effect in La0.67Sr0.33MnO3/PbZr0.52Ti0.48O3 multiferroic nanocomposite films with a SrRuO3 buffer layer." *Journal of Applied Physics* **113**(16): 164106.

Teherani, F. H., D. C. Look, D. J. Rogers, E. L. Lin, S. Hu and J. G. Ekerdt (2017). "Monolithic integration of metal-ferroelectric-semiconductor heterostructure using atomic layer deposition." **10105**: 1010519.

Thang, P. D., G. Rijnders and D. H. A. Blank (2007). "Stress-induced magnetic anisotropy of CoFe2O4 thin films using pulsed laser deposition." *Journal of Magnetism and Magnetic Materials* **310**(2): 2621-2623.

Thiele, C., K. Dörr, O. Bilani, J. Rödel and L. Schultz (2007). "Influence of strain on the magnetization and magnetoelectric effect inLa0.7A0.3MnO3 ∕ PMN−PT(001)(A=Sr,Ca)." *Physical Review B* **75**(5).

Thomas, R., J. F. Scott, D. N. Bose and R. S. Katiyar (2010). "Multiferroic thin-film integration onto semiconductor devices." *J Phys Condens Matter* **22**(42): 423201.

Tian, X., S. Shibayama, T. Nishimura, T. Yajima, S. Migita and A. Toriumi (2018). "Evolution of ferroelectric HfO2 in ultrathin region down to 3 nm." *Applied Physics Letters* **112**(10): 102902.

Trassin, M., J. D. Clarkson, S. R. Bowden, J. Liu, J. T. Heron, R. J. Paull, E. Arenholz, D. T. Pierce and J. Unguris (2013). "Interfacial coupling in multiferroic/ferromagnet heterostructures." *Physical Review B* **87**(13).

Uusi-Esko, K. and M. Karppinen (2011). "Extensive Series of Hexagonal and Orthorhombic RMnO3 (R = Y, La, Sm, Tb, Yb, Lu) Thin Films by Atomic Layer Deposition." *Chemistry of Materials* **23**(7): 1835-1840.

Uusi-Esko, K., J. Malm and M. Karppinen (2009). "Atomic Layer Deposition of Hexagonal and Orthorhombic YMnO3 Thin Films." *Chemistry of Materials* **21**(23): 5691-5694.

van den Brink, J. and D. I. Khomskii (2008). "Multiferroicity due to charge ordering." *Journal of Physics: Condensed Matter* **20**(43): 434217.

Van, T. T. and J. P. Chang (2005). "Radical-enhanced atomic layer deposition of Y2O3 via a β-diketonate precursor and O radicals." *Surface Science* **596**(1-3): 1-11.

Van, T. T. and J. P. Chang (2005). "Surface Reaction Kinetics of Metal ♌-diketonate Precursors with O Radicals in Radical-Enhanced Atomic Layer Deposition of Metal Oxides." *Applied Surface Science* **246**(1-3): 250-261.

Vaz, C. A., J. Hoffman, C. H. Ahn and R. Ramesh (2010). "Magnetoelectric coupling effects in multiferroic complex oxide composite structures." *Adv Mater* **22**(26-27): 2900-2918.

Vehkamäki, M., T. Hatanpää, M. Ritala, M. Leskelä, S. Väyrynen and E. Rauhala (2007). "Atomic Layer Deposition of BaTiO3 Thin Films—Effect of Barium Hydroxide Formation." *Chemical Vapor Deposition* **13**(5): 239-246.

Wan, J. G., Y. Weng, Y. Wu, Z. Li, J. M. Liu and G. Wang (2007). "Controllable phase connectivity and magnetoelectric coupling behavior in CoFe(2)O(4)-Pb(Zr,Ti)O(3) nanostructured films." *Nanotechnology* **18**(46): 465708.

Wang, G., Z. Gao, S. Tang, C. Chen, F. Duan, S. Zhao, S. Lin, Y. Feng, L. Zhou and Y. Qin (2012). "Microwave Absorption Properties of Carbon Nanocoils Coated with Highly Controlled Magnetic Materials by Atomic Layer Deposition." *ACS Nano* **6**(12): 11009-11017.

Wang, J., J. B. Neaton, H. Zheng, V. Nagarajan, S. B. Ogale, B. Liu, D. Viehland, V. Vaithyanathan, D. G. Schlom, U. V. Waghmare, N. A. Spaldin, K. M. Rabe, M. Wuttig and R. Ramesh (2003). "Epitaxial BiFeO3 Multiferroic Thin Film Heterostructures." *Science* **299**(5613): 1719-1722.

Wang, J. J., J. M. Hu, T. N. Yang, M. Feng, J. X. Zhang, L. Q. Chen and C. W. Nan (2014). "Effect of strain on voltage-controlled magnetism in BiFeO(3)-based heterostructures." *Sci Rep* **4**: 4553.

Wang, K. L. and P. K. Amiri (2012). "Nonvolatile Spintronics: Perspectives on Instant-on Nonvolatile Nanoelectronic Systems." *Spin* **02**(02): 1250009.

Wang, Y., J. Hu, Y. Lin and C.-W. Nan (2010). "Multiferroic magnetoelectric composite nanostructures." *NPG Asia Materials* **2**(2): 61-68.

Watts, J. F. and J. Wolstenholme (2003). *An Introduction to Surface Analysis by XPS and AES*, Wiley.

Weisheit, M., S. Fähler, A. Marty, Y. Souche, C. Poinsignon and D. Givord (2007). "Electric field-induced modification of magnetism in thin-film ferromagnets." *Science* **315**(5810): 349-351.

Weon Hwang, G., H. Ju Lee, K. Lee and C. Seong Hwang (2007). "Atomic Layer Deposition and Electrical Properties of PbTiO3 Thin Films Using Metallorganic Precursors and H2O." *Journal of The Electrochemical Society* **154**(3): G69-G76.

Wu, G., T. Nan, R. Zhang, N. Zhang, S. Li and N. X. Sun (2013). "Inequivalence of direct and converse magnetoelectric coupling at electromechanical resonance." *Applied Physics Letters* **103**(18): 182905.

Wu, P.-H. and S.-Y. Huang (2016). "Noncollinear magnetization between surface and bulk ${\mathrm{Y}}_{3}\mathrm{F}{\mathrm{e}}_{5}{\mathrm{O}}_{12}$." *Physical Review B* **94**(2): 024405.

Yan, L., Z. Xing, Z. Wang, T. Wang, G. Lei, J. Li and D. Viehland (2009). "Direct measurement of magnetoelectric exchange in self-assembled epitaxial BiFeO[sub 3]–CoFe[sub 2]O[sub 4] nanocomposite thin films." *Applied Physics Letters* **94**(19): 192902.

Yang, S. Y., F. Zavaliche, L. Mohaddes-Ardabili, V. Vaithyanathan, D. G. Schlom, Y. J. Lee, Y. H. Chu, M. P. Cruz, Q. Zhan, T. Zhao and R. Ramesh (2005). "Metalorganic chemical vapor deposition of lead-free ferroelectric $BiFeO_3$ films for memory applications." *Applied Physics Letters* **87**(10): 102903.

Yim, C. J., S. U. Kim, Y. S. Kang, M. H. Cho and D. H. Ko (2011). "Enhanced Electrical Properties of SrTiO3 Thin Films Grown by Plasma-Enhanced Atomic Layer Deposition." *Electrochemical and Solid-State Letters* **14**(10): G45.

Zaliznyak, I. A. (2007). Spin Structures and Spin Wave Excitations. *Handbook of Magnetism and Advanced Magnetic Materials*, John Wiley & Sons, Ltd.

Zavaliche, F., H. Zheng, L. Mohaddes-Ardabili, S. Y. Yang, Q. Zhan, P. Shafer, E. Reilly, R. Chopdekar, Y. Jia, P. Wright, D. G. Schlom, Y. Suzuki and R. Ramesh (2005). "Electric field-induced magnetization switching in epitaxial columnar nanostructures." *Nano Lett* **5**(9): 1793-1796.

Zeng, M. (2004). "Resonance magnetoelectric effect in bulk composites of lead zirconate titanate and nickel ferrite." *Journal of Applied Physics* **95**(12): 8069.

Zhai, J. (2004). "Coupled magnetodielectric properties of laminated PbZr[sub 0.53]Ti[sub 0.47]O[sub 3]/NiFe[sub 2]O[sub 4] ceramics." *Journal of Applied Physics* **95**(10): 5685.

Zhai, J. Y., N. Cai, L. Liu, Y. H. Lin and C. W. Nan (2003). "Dielectric behavior and magnetoelectric properties of lead zirconate titanate/Co-ferrite particulate composites." *Materials Science and Engineering: B* **99**(1–3): 329-331.

Zhang, F., G. Sun, W. Zhao, L. Wang, L. Zheng, S. Liu, B. Liu, L. Dong, X. Liu, G. Yan, L. Tian and Y. Zeng (2013). "Atomic Layer Deposition of BiFeO3 Thin Films Using β-Diketonates and H2O." *The Journal of Physical Chemistry C* **117**(46): 24579-24585.

Zhang, F., G. Sun, W. Zhao, L. Wang, L. Zheng, S. Liu, B. Liu, L. Dong, X. Liu, G. Yan, L. Tian and Y. Zeng (2013). "Atomic Layer Deposition of BiFeO3Thin Films Using β-Diketonates and H2O." *The Journal of Physical Chemistry C* **117**(46): 24579-24585.

Zhao, J. L., H. X. Lu, J. R. Sun and B. G. Shen (2012). "Thickness dependence of piezoelectric property of ultrathin BiFeO3 films." *Physica B: Condensed Matter* **407**(12): 2258-2261.

Zhao, T., A. Scholl, F. Zavaliche, K. Lee, M. Barry, A. Doran, M. P. Cruz, Y. H. Chu, C. Ederer, N. A. Spaldin, R. R. Das, D. M. Kim, S. H. Baek, C. B. Eom and R. Ramesh (2006). "Electrical control of antiferromagnetic domains in multiferroic BiFeO3 films at room temperature." *Nat Mater* **5**(10): 823-829.

Zheng, H., F. Straub, Q. Zhan, P. L. Yang, W. K. Hsieh, F. Zavaliche, Y. H. Chu, U. Dahmen and R. Ramesh (2006). "Self-Assembled Growth of BiFeO3–CoFe2O4 Nanostructures." *Advanced Materials* **18**(20): 2747-2752.

Zheng, H., J. Wang, S. E. Lofland, Z. Ma, L. Mohaddes-Ardabili, T. Zhao, L. Salamanca-Riba, S. R. Shinde, S. B. Ogale, F. Bai, D. Viehland, Y. Jia, D. G. Schlom, M. Wuttig, A. Roytburd and R. Ramesh (2004). "Multiferroic BaTiO3-CoFe2O4 Nanostructures." *Science* **303**(5658): 661-663.

Zheng, R. Y., J. Wang and S. Ramakrishna (2008). "Electrical and magnetic properties of multiferroic BiFeO3/CoFe2O4 heterostructure." *Journal of Applied Physics* **104**(3): -.

Zhou, D., L. Hao, S. Gong, Q. Fu, F. Xue and G. Jian (2012). "Magnetoelectric effect of the multilayered CoFe2O4/BaTiO3 composites fabricated by tape casting." *Journal of Materials Science: Materials in Electronics* **23**(12): 2098-2103.

Zhou, Z., M. Trassin, Y. Gao, D. Qiu, K. Ashraf, T. Nan, X. Yang, S. R. Bowden, D. T. Pierce, M. D. Stiles, J. Unguris, M. Liu, B. M. Howe, G. J. Brown, S. Salahuddin, R. Ramesh and N. X. Sun (2015). "Probing electric field control of magnetism using ferromagnetic resonance." *Nature communications* **6**: 6082.